City Research Online

City, University of London Institutional Repository

Citation: Somasiri, N. (2003). Finite element modelling of polarization issues in optoelectronic systems. (Unpublished Doctoral thesis, City, University of London)

This is the accepted version of the paper.

This version of the publication may differ from the final published version.

Finite Element Modelling of Polarization Issues in Optoelectronic Systems

By

Niranthi Somasiri

A thesis submitted to the City University in fulfilment of the requirements for the Degree of Doctor of Philosophy

City University

Photonics Research Group
School of Engineering & Mathematical Sciences
Northampton Square, London EC1V 0HB, UK.

December 2003

To My Father & Mother,

With Love

Table of Contents

List of Tables

List of Figures

Acknowledgements

Throughout this work many people have contributed in many different ways, without whom this thesis would not have been possible. The following words of gratitude are dedicated to all those who helped me.

First of all, I would like to gratefully thank Prof. B. M. A. Rahman for being an excellent and patient supervisor, and also for providing continual support and encouragement over the last three or so years. I would also like to thank Prof. K. T. V. Grattan for his creative influence and valuable advice throughout this research.

I am extremely appreciative of Dr. M. Rajarajan for advising and assisting with computer problems at all times and Dr. S. S. A. Obayya for helping me with relevant discussions and advise. I am also grateful to the staff at the departmental office, Joan Rivellini and Linda Carr, for being very helpful and making my working time more pleasant.

Sincere thanks to all my colleagues, Shyqyri, Femi, Najm and Fethi in the Photonics Modelling Group, for the friendly and joyful atmosphere during the many years I stayed there. Special thanks to all my friends I've made outside the university research environment for their continued moral support and my deepest gratitude is devoted to my fiancé, Prakash, for always supporting me and standing by me in both good and bad times.

Finally, I am forever indebted to my father, mother, brother and Anusha for their love, endless patience and encouragement without whom I would never have got this far.

Declaration

I grant powers of discretion to the University Librarian to allow this thesis to be copied in whole or in part without further reference to me. This permission covers only single copies made for study purposes, subject to normal conditions of acknowledgement.

Abstract

Many integrated optical subsystems incorporate guided wave photonic devices and connecting optical waveguides with two-dimensional confinement and a high index contrast between the core and the cladding. The modes present in such waveguides are not purely of the TE or TM type but are hybrid in nature, with all six components of the electric and magnetic fields being present, which makes the overall system to be polarization dependent. In present high-performance photonic components and optoelectronic subsystems, this polarization issue is a major issue to be tackled with for further enhancement of their performances.

This thesis describes the design, analysis and optimisation of such polarization-based waveguide devices such as polarization rotators, polarization splitters and polarization controllers. To characterize the polarization properties of such devices a fully vectorial approach is necessary. In this work, the most versatile and accurate full vectorial **H**-field based finite element method (FEM) is used to simulate complex waveguide structures in order to optimize and evaluate novel devices, prior to fabrication. This method can accurately calculate the propagation constants of both polarized modes and consequently these are used to calculate the half-beat length, which is an important parameter when designing waveguide devices involving polarization issues. Many important photonic devices, such as polarization splitters, polarization rotators and polarization controllers may be fabricated by combining several butt-coupled uniform waveguide sections. The least squares boundary residual (LSBR) method is used to obtain both the transmission and the reflection coefficients of all the polarized modes by considering both the guided and radiated modes.

In this work, a combination of the FEM and LSBR methods has been extensively used to obtain the TE to TM or TM to TE polarized power transfer efficiency in semiconductor waveguides and the polarization crosstalk in high index contrast silica waveguides. When designing polarization rotators or identifying the possible polarization crosstalk, it is necessary to calculate the modal 'hybridity' of a mode. In this study, it is identified that when the waveguide lacks structural symmetry, the modal hybridity is enhanced, and thereby a considerably high polarization conversion is expected. A compact 400μm long passive polarization rotator (PR) with cascaded asymmetrical waveguide sections is designed with a very low insertion loss of 0.2dB. A more compact 320μm long, much improved PR is designed and analysed by using only a single slanted walled rib waveguide section. Furthermore, an extensive study of fabrication tolerances of a compact, single-stage PR is undertaken. A 99.8% polarization conversion is achieved with a very low crosstalk value of − 29dB. The design of a compact 1.6mm long single-section polarization splitter in a deeply etched semiconductor MMI waveguide is also presented. An extensive analysis of polarization crosstalk is carried out using high index contrast planar silica waveguides. The origin of polarization crosstalk in silica waveguides is explained and it is shown that a significant polarization conversion can take place in a long, high index contrast silica waveguide. It is also learnt that non-verticality of the sidewalls causes the significant polarization crosstalk in many silica-based components. Finally a novel design concept of an active polarization controller is presented using twin electrodes with both biasing and controlling signals. The asymmetry is introduced by incorporating a non-symmetric modulating electric field in order to control the polarization conversion. Both the phase matching and polarization conversion are achieved simultaneously.

Symbols and Abbreviations

LED	Light Emitting Diode
VCSEL	Vertical Cavity Surface Emitting Laser
IC	Integrated Circuit
OEIC	Optical-Electronic Integrated Circuit
WDM	Wavelength Division Multiplexing
EDFA	Erbium Doped Fibre Amplifier
PDFA	Praseodymium Doped Fibre Amplifier
DWDM	Dense Wavelength Division Multiplexing
TDFA	Thulium Erbium Doped Fibre Amplifier
ATM	Asynchronous Transfer Mode
SONET	Synchronous Optical Network
OC	Optical Carrier
EIC	Electrical Integrated Circuit
IOC	Integrated Optical Circuit
AWG	Arrayed Waveguide Grating
PIC	Photonic Integrated Circuit
CATV	Cable Television
FTTH	Fibre-To-The-Home
DBR	Distributed Bragg Reflector
DFB	Distributed Feedback
TE	Transverse Electric
TM	Transverse Magnetic
k	Wave number
ω	Angular frequency
λ	Wavelength
c	Velocity of light in vacuum

β	Propagation constant
RAM	Ray Approximation Method
WKB	Wentzel, Kramers and Brillouin
MM	Marcatili's Method
EIM	Effective Index Method
FEM	Finite Element Method
FDM	Finite Difference Method
VM	Variational Method
MAM	Multilayer Approximation Method
BEM	Boundary Element Method
PMM	Point Matching Method
MMM	Mode Matching Method
ENM	Equivalent Network Method
SI	Spectral Index
BPM	Beam Propagation Method
FFT	Fast Fourier Transform
VBPM	Vector Beam Propagation Method
LSBR	Least Squares Boundary Residual
VFEM	Vector Finite Element Method
ε	Permittivity
μ	Permeability
μ_r	Relative Permeability
MMI	Multimode Interference
PR	Polarization Rotator
PRW	Polarization Rotating Waveguide
IW	Input Waveguide
OW	Output Waveguide
PLC	Planar Lightwave Circuit
PMD	Polarization Mode Dispersion
SOP	State Of Polarization
LO	Local Oscillator
PDM	Polarization Division Multiplexing
DGD	Differential Group Delay

Chapter 1

Introduction

1.1 Innovation of lightwave technology

Communication using light waves is not a new science, and dates back more than two centuries. Even before that, old Roman records indicate that polished metal plates were sometimes used as mirrors to reflect sunlight for long range signalling. In 1790s the French engineer Claude Chappe invented the "optical telegraph". His system relied on a series of semaphores mounted on towers, where human operators relayed messages from one tower to the next. The U.S. military used sunlight-powered devices to send telegraph information from mountain top to mountain top in the early 1800s. For centuries the navies of the world have been using, and, still use flashing lights to send messages from one ship to another.

In 1880, after inventing the telephone, Alexander Graham Bell built what he believed was his greatest invention, the "photophone". It was patented in 1889, and it was the world's first optical transmission system that could transmit voices over a short distance range of about 200 m. The so-called photophone used sunlight reflected off a vibrating mirror and a selenium photocell.

However, sending signals through the air was not so reliable since the atmosphere did not transmit light as reliably as wires carried electricity. The main factor that could influence the ability of an optical communications system to send information through the air is the variability of the weather. Fog, heavy rain and snow can be severe enough to block the light path and interrupt communications. Another limitation of light beam communications is that since light cannot penetrate trees, hills or buildings, a clear line-of-sight path must exist between the light transmitter and the receiver. Arising from these reasons, in the decades that followed, light was used for a few special applications, such as signalling between ships, but otherwise optical communications, like the experimental photophone which Bell donated to the Smithsonian Institution, languished on the shelf. However, the corporation Bell co-founded – the Bell Telephone Company, remained focused on commercialising the telephone.

During both world wars some lightwave communications experiments were conducted, but radio and radar had more success and took the spotlight. It wasn't until the invention of the laser, some new semiconductor devices and optical fibres in the 1960s that optical communications finally began getting some real attention to practical devices.

In the intervening years, a new technology slowly took root that would ultimately solve the problem of optical transmission, although it was a long time before optics was adapted effectively for communications. It was basically depended on the phenomenon of total internal reflection, which can confine light in a material surrounded by other materials with lower refractive index, such as glass in air. In the 1840s, Swiss physicist Daniel Collodon and French physicist Jacques Babinet showed that light could be guided along jets of water for fountain displays. By the turn of the century, inventors realised that bent quartz rods could carry light, and patented them as dental illuminators.

However, optical fibres went a step further and the scientists around the world were closing in on lightwave communications - a technology with a stunning array of applications still emerging today. Optical fibres are essentially transparent rods of glass or plastic stretched into long and flexible wires. During the 1920's John Logie

Baird in England and Clarence W. Hansel in U.S. patented the idea of using arrays of hollow pipes or transparent rods to transmit images for television or facsimile systems. The first person known to have demonstrated image transmission through a bundle of optical fibres was Heinrich Lamm. The goal was to look inside inaccessible parts of the body, and he reported the transmitted image of a light bulb filament through a short bundle. However, the fibres transmitted images poorly due to the unclad nature of the fibres.

All earlier fibres were "bare", with total internal reflection at a glass-air interface. A crucial invention was made by van Heel, in order to protect the total-reflection surface from contamination and to greatly reduce the crosstalk between fibres. The procedure was to cover the bare fibre or glass or plastic with a transparent cladding of lower refractive index. The development of glass-clad fibres was the next innovative and key step. By 1960, the first glass-clad fibres were made by melting a tube onto a rod of higher index glass. These glass-clad fibres had an attenuation of about 1 dB/m, which was fine for medical imaging, but much too high for communication systems.

Throughout the history of radio and carrier telephony on cables there has been a continuous trend towards the use of higher frequencies, since the radio (kHz / MHz) and microwave (3-30 GHz) frequencies were in heavy use. It is generally more economic to obtain additional capacity by exploiting the higher frequencies than to have a number of co-routed lower capacity systems. A major breakthrough came in 1960 – the invention of the laser, the first light source powerful enough to transmit information. The invention of the laser made an enormous impact on the carrier frequency by increasing by 3 to 4 order of magnitudes that of millimetre waves (30-300 GHz).

1.1.1 Optical communications systems

The early research in optical communication systems is very much related to the development of suitable optical sources and channels. The invention of the laser in 1960 (Maiman, 1960) opened the way for the coherent sources of electromagnetic radiation to reach the visible spectrum. Since the demonstration of the laser, the

transmission and the processing of signals has been an important challenge for the scientists. Although the laser offered a tremendous potential bandwidth, some experimental factors such as, attenuation due to rain, fog, and snow limited the laser being used in the development of free space communications. Therefore the need for suitable and reliable transmission media became a crucial factor. Although it had been known for a long time that light can be guided in thin fibres made of transparent dielectric materials, the first concept of using glass fibres as a transmission medium was suggested by Kao and Hockham (Kao and Hockham, 1966) of Standard Telephone Laboratories (STL), U.K. With this invention, an important principle in physics became the theoretical foundation for optical fibre communications: light in a glass medium can carry more information over longer distances than electrical signals can carry in a copper or coaxial medium.

The development of techniques for making low loss optical fibres became the next major challenge for researchers. The first challenge undertaken by scientists at that time was to develop a glass so pure that one percent of the light would be retained at the end of one kilometre, the existing unrepeated transmission distance for copper-based telephone systems. In terms of attenuation, this one percent of light retention translated to an attenuation of 20 dB/km of the glass material. In the 1960s, enormous effort had been undertaken to improve the loss reduction and in 1966 Kao and Hockham of STL labs proposed a loss reduction to 20 dB/km by the removal of metal impurities in the glass material. However the breakthrough came in 1970, when scientists at Corning glass works (USA), Kapran, Keck and Maurier (Kapron *et al.*, 1970) created a fibre with a measured attenuation of less than 20 dB/km. It was the purest glass ever made at that time.

Since then, the technology has advanced tremendously in terms of performance, quality, consistency, and with that the range of applications. Multimode fibre was the first type to be commercialised. It has a much larger core than the single mode fibre, allowing hundreds of modes of light to propagate through the fibre simultaneously. Additionally, the larger core diameter of multimode fibre facilitates the use of lower cost optical transmitters such as light emitting diodes (LEDs) or vertical cavity surface emitting lasers (VCSELs) and connectors. Therefore, in the early 1970s, multimode optical fibres were used to transmit light from light emitting diode sources operating

at visible wavelengths near 800 nm as shown in **Fig. 1.1**. These systems were created with a loss limit of 3 dB/km, which provided a much better performance than the best coaxial cable (10 – 20 dB/km) available.

These first generation systems could transmit light at data rates of about 100 Mbit/s over a single fibre span of about 10 km. In reality, a standard telephone conversation requires 64 kbit/s data rate. So a 100 Mbit/s signal can carry virtually ~1500 simultaneous telephone calls, showing the enormous information capacity an optical system could transmit. The FT3C metropolitan lightwave system from AT&T (Stauffer, 1983) is a good example of such technology.

A huge improvement in the fibre optic communications system performance came with the introduction of single-mode fibres operating at the 1.3 μm wavelength band. At this wavelength the optical signal attenuation in glass is quite low (at 0.5 dB/km) and shows a zero material dispersion for fused silica fibres (Imoto *et al.*, 1980). Single mode fibre has a much smaller core that allows only one mode of light at a time to propagate through the core. It might appear that the multimode fibres have higher capacity, but infact the opposite is true. Single-mode fibres are designed to maintain the spatial and spectral integrity of each optical signal over long distances, allowing more information to be transmitted and decoded. Its tremendous information carrying capacity, low intrinsic loss and the zero modal dispersion have made single mode fibre the ideal transmission medium for a multitude of applications. These types of fibres are mainly used for longer distance and higher bandwidth applications. For example, these second generation systems could be used to transmit light at a rate of about 400 Mbit/s a distance of over 40 km via a fibre link. Suitable semiconductor laser sources such as InGaAsP sources and Ge detectors for the 1.3 μm wavelength window have been developed. In 1980 Bell Labs publicly committed to the single mode 1.3 μm technology for the first transatlantic fibre-optic cable, and in December 1988 TAT – 8(as it was named) began service.

Development of hardware for the first transatlantic fibre cable showed that single mode systems were feasible, so when deregulation opened the long-distance phone market in the early 1980s, the carriers built national backbone systems of single-mode

fibre with 1.3 μm sources. That technology has spread into other telecommunication applications, and it remains the standard for most fibre systems.
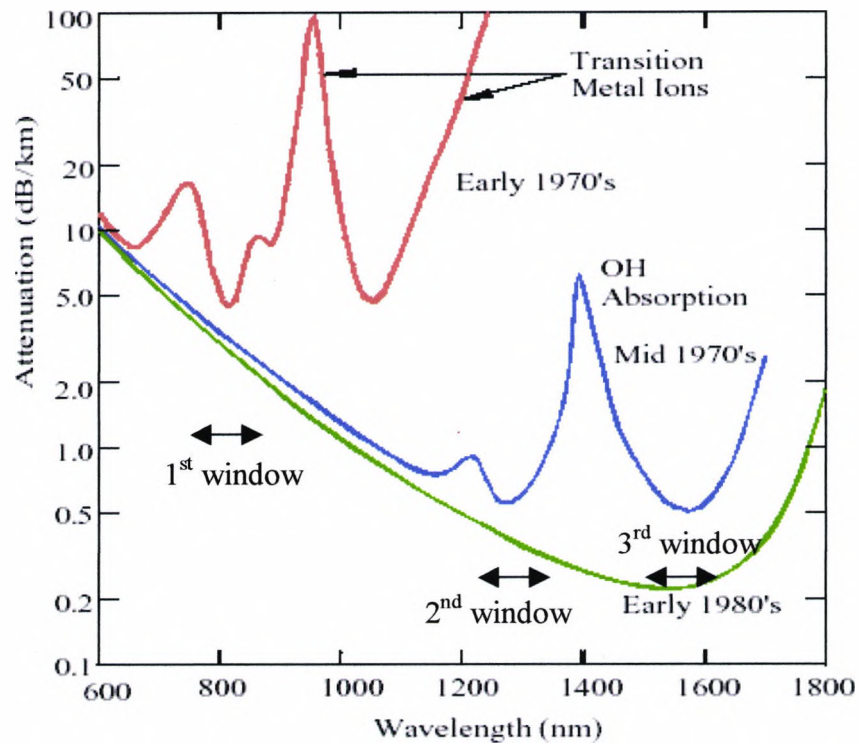
Fig. 1.1 Wavelength dependence of attenuation in optical fibre.

Today, fibre optical performance is approaching the theoretical limits of silica-based glass materials. This purity, combined with improved system electronics, enables modern fibre to transmit digitised light signals well beyond 10 km without amplification. The 3rd generation of optical communications emerged in the mid 1980s to find applications in submarine cables and systems serving large numbers of subscribers. They operate at the 1.55 μm wavelength window, where fibre attenuation is minimum at 0.2 to 0.3 dB/km (as shown in **Fig. 1.1**), allowing even longer repeater spacings than before. Since this wavelength does not correspond to zero dispersion, special dispersion compensation fibres and single frequency laser sources must be utilized to implement single-mode fibre transmission rates up to the Gbits/s range, over an optical fibre link measured on the scale of hundreds of kilometres.

To understand why the world has shifted to optical transmission requires an explanation of the shift from metal to glass and the reason is clearly shown in **Fig. 1.2**. 1 km of one of the most popular coaxial cable suffers from severe attenuation at 20 dB/km at 100 MHz and however, 1 km single mode fibre is capable of transmitting at a rate of about 2000 GHz with very low loss. Optical fibre systems have other significant advantages over either free space radio, or coaxial cable transmission systems. i.e.:

- High immunity to electromagnetic interference
- No radiation with complete electrical isolation (low loss)
- Very large information bandwidth and therefore high transmission capacity
- Very low material cost
- Small, light and flexible
- No crosstalk between fibres
- Larger repeater spacings than for the equivalent coaxial cables
  - 2 to 3 km spacing for coaxial cable system.
  - 30 to >100 km spacing for optical fibre.
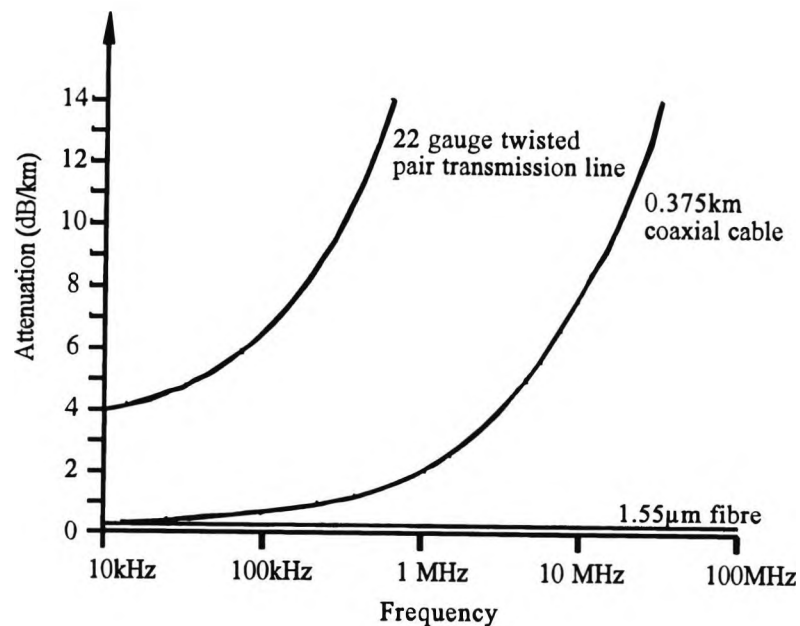
Fig.1.2   Graph of attenuation versus frequency for a twisted pair, one of the most popular coaxial cables and a state of the art optical fibre operating at a wavelength of 1.55 μm.

1.1.2 New generation systems

By the early 1990s, the transmission rate of fast silicon multiplexer/demultiplexer integrated circuits (ICs) of around 30 Gbit/s seemed to have been reached (Rein *et al.*, 1992), with hybrid optical – electronic integrated circuits (OEICs) reported, operating up to 10 Gbit/s.

The demand for network bandwidth in today's world is surging, brought about by the growth of the Internet, the rapidly increasing number of users, and the use of rich media, such as audio, video, and high resolution graphics. Such growing demand for telecommunication capacity is already making the first generation optical systems with one optical wavelength per fibre seem inadequate. Their limitations are, for example, the causes of why it takes so long to transmit the huge amounts of data associated with video images.

In order to overcome these limitations, and thus increase the transmission capacity it was suggested to exploit the fibre bandwidth by introducing wavelength division multiplexing (WDM). The WDM transmission systems have been developed to "multiplex" optical signals effectively using the existing optical fibre infrastructure more effectively, i.e. sending several optical signals with different wavelengths simultaneously, down the same, single optical fibre. Early WDM experiments at 10, 16, and 100 channels achieved aggregated capacities of 20, 32, and 62 Gbit/s respectively (Lin *et al.*, 1988; Toba *et al.*, 1990).

Another most notable advancement has also made the WDM even more attractive. This is the introduction of rare-earth doped optical fibre amplifiers. Since the first announcement in 1987 of a high gain fibre amplifier (Mears *et al.*, 1987), a huge amount of research has been devoted to the optical amplifiers, especially erbium-doped fibre amplifiers (EDFAs) for 1.55 μm and more recently the praseodymium-doped fibre amplifiers (PDFAs) for 1.3 μm. Fibre amplifiers have relatively large bandwidth (around 30 nm), low channel crosstalk, are polarization insensitive and bi-directional. They are used as high-power low-gain amplifiers to boost signals from laser transmitters, as in-line moderate-power cascaded devices, as repeaters to amplify periodically the signal in long distance systems (Gordon and Mollenauer, 1991) and as

low-power low-noise receiver preamplifiers to enhance receiver sensitivity.

The transatlantic TAT 12/13 (Balland *et al.*, 1993) and the transpacific TPC 5 (Runge, 1992) submarine cable networks which began to carry traffic in 1996, are remarkable examples of transmission systems involving hundreds of EDFAs. TAT 12 cable network has a capacity of 25 Gbit/s over a length of 360 km and TAT 13 operates at 25 Gbit/s over a length of 2173 km. TAT 12/13 has a capacity equivalent to about 300000 simultaneous voice channels. TPC 5 is the first transpacific fibre optic system that uses optical amplifiers and it links the U.S. mainland with Hawaii, Guam and Japan covering a distance of around 25000 km. It can transmit 5 Gbit/s over one working fibre pair and a spare fibre for restoration. This results in a capacity equivalent to about 320000 simultaneous phone calls.

The current, unprecedented demand for network capacity is mostly driven by the rapidly growing demand for Internet applications. A conservative estimate of Internet traffic growth is that it doubles every 6 to 12 months. If this growth rate continues, the aggregate bandwidth required for the Internet by 2005 will be in excess of hundreds of Terabits per second. To facilitate this enormous demand, WDM systems have moved further to Dense Wavelength Division Multiplexing (DWDM) systems. Such a system uses EDFAs as well as Thulium Erbium doped fibre amplifiers (TDFAs). In such a DWDM optical system, each fibre amplifier provides the gain for more than a hundred signal carriers separated by a frequency difference of 100 GHz or 50 GHz.

The TAT 14 transatlantic cable system started full service in 2001, connecting the U.S. to the U.K., France, The Netherlands, Germany and Denmark. This cable system is a dual bi-directional ring configuration and uses the DWDM technology. The system also utilizes reverse direction protection switching in the event of failure of the service fibre. It has a dual route, transatlantic capacity of 640 Gbit/s over a length of around 15300 km.

Another important transmission mechanism, soliton transmission, became a reality with the advent of fibre amplifiers, providing the gain for keeping the pulse peak power through the link. A soliton is a type of narrow pulse of light that retains its shape as it travels long distances along the fibre. The soliton's ability to keep its shape

helps it to overcome the problem of light wave dispersion, and the consequent loss of data integrity, as the data-carrying light wave travels over long distances. Soliton-based systems have established high-speed transmission in long haul transoceanic distances: a single channel 10 Gbit/s system over 20000 km, and a two-channel 20 Gbit/s WDM system over 13000 km (Mollenauer *et al.*, 1993), and virtually infinite distances at 10 Gbit/s over $180 * 10^6$ km (Nakazawa *et al.*, 1993).

Fibre optic communication-system speeds have increased from asynchronous-transfer-mode (ATM) rates of 155 Mbit/s and synchronous optical network (SONET) rates of 622 Mbit/s to the optical carrier (OC) standard of OC-48 of 2.5 Gbit/s over the past years. With increasing demands for wireless data transfer, networking, graphics, and high-speed communications using the Internet World Wide Web, OC-192 of 10 Gbit/s has become the standard fibre optic operating speed. New technologies and systems concepts are still being developed for ultra high-speed long haul systems operating at channel bit rates in excess of 40 Gbit/s with aggregate throughputs excess of around 1 Tb/s.

1.2   Integrated optics

The parallel development of semiconductor lasers, which gave the birth to the field of 'Photonics' has seen the subsequent availability of low-loss optical fibres and made possible the implementation of completely optical systems for communications, signal processing and other applications that had used only electronic circuitry in the past. The first electronic semiconductor devices, such as transistors, that came to market were discrete and had to be assembled in to functions and systems by connecting them together with wire and solder. As the material and fabrication technologies became more sophisticated, the manufacturers began to combine functions on to a single substrate. The interconnections were fabricated on the board itself with the devices. These were called electronic integrated circuits (EICs).

However towards the end of the sixties, guided-wave-optical components became sufficiently effective to herald the beginning of a highly promising and sophisticated technology called 'integrated optics'. The concept of integrated optics was first

proposed by S.E. Miller (Miller, 1969). The idea behind it was that using well-established processes from the integrated electronics industry, planar lightwave circuits containing passive and active guided wave optical components could be fabricated. Simply, the goal of integrated optics is to develop miniaturised optical circuits of high functionality on a common substrate.

Integrated optics, sometimes informally described as planar-optic technology deals with the transmission, switching and routing of guided optical beams in a plane, allowing the possibilities of integrating the three functions on a single substrate in a compact device. These are the photonics-equivalent of microelectronic chips, which integrate two or more transistors on a chip to form electronic integrated circuit. However, instead of guiding electricity, an integrated optical circuit (IOC) routes light waves. Waveguides, usually made of silica, polymer or semiconductors (Marcatili, 1969), act as the photonic analogue of copper circuits, serving as interconnects among various discrete components on a chip. The refractive index of an active or core layer, which is sandwiched between two cladding layers with a lower index of refraction, applies total internal reflection to continue and route a particular wavelength of light.

Optical telecommunication systems continue to be the leading force behind the recent developments of integrated optics, because the area of telecommunications is expected to require huge bandwidths in the future. Practical integrated optics can be classified as active and passive devices. Passive components are involved in the transport, splitting, and combining of light including arrayed waveguide gratings (AWGs), beam splitters, polarization converters and controllers, variable optical attenuators, switches and other passive waveguide wavelength management devices such as wavelength division multiplexers. Active components have both optical and electrical properties and require electrical power to emit, receive, and convert light signals. These include lasers, detectors, transmitters, modulators, transceivers, and amplifiers. Above are some of the most commonly required components and devices, and these have been made on silica (SiO_2), lithium niobate ($LiNbO_3$), polymer and other semiconductor materials.

The advantages provided by integrated optics can benefit areas other than telecommunications. Thus, integrated-optics components have been developed for

spectrum analysers, gyroscopes, digital correlators, and analogue to digital converters. Other application areas, however, are also growing: for instance, displays, signal processing, and sensing can all benefit from innovative integrated optic (IO) devices. At the same time, more foundries (e.g. for silica-on-silicon devices and circuits) are available, and an increasing number of IO devices are on the market.

The fabrication of photonic integrated circuits (PICs) involves building devices in or on a substrate using high-yield, batch semiconductor manufacturing processes, such as deposition, photolithography, and etching techniques. As Dense Wavelength Division Multiplexing (DWDM) speeds rise to 40 Gbit/s and beyond, system builders employing traditional optical components and equipment building techniques face severe technical problems such as light scattering, pulse break-up and crosstalk, as well as the issues raised by increasingly complex systems assembly and integration. Multi-function devices are the key to progress. They make it possible to realise higher performance communities reliably and repeatably, and to provide the dynamically adjustable and lower-cost features needed to create the new peripherals and architectures for all-optical networking markets.

Monolithic integration is ideally suited to support this transition. By integrating functions within a photonic integrated circuit (PIC), the number of links in the signal transmission/reception chain can be reduced substantially. That cuts the levels of cost, manufacturing difficulties, and optical losses associated with high-precision system assembly.

1.2.1 Guided wave devices – Market and technology

Within the past decade, guided wave, or integrated optical (IO), components in various materials have become available from a variety of vendors worldwide and are now being deployed in commercial systems (Tamir, 1990). These devices are the key to advanced transmitters in many fibre-optic based cable television (CATV) and long-haul telecommunications systems and also instrumentation. The basic devices are based on planar optical waveguides, in which light is confined to channels at the substrate surface and routed on the chip. These channels are typically less than 10

microns and are patterned using micro lithography techniques.

Applications for integrated optics have historically been in niches of the analogue, digital, and sensor fibre-optic markets; at present, however, major new markets are emerging. The largest new market is telecommunications, where IO devices will be used for multigigabit data transmission, signal splitting and loop distribution, and in bi-directional communication modules. A second new market is CATV, where IO modules will be used for external modulation in fibre-optic-based signal distribution systems. In both telecommunications and CATV, IO devices enable signal transmission of higher data rates and over long distances. In a third market, instrumentation, a major application is fibre-optic gyroscopes. High-speed telecommunication and fibre gyro applications are common to world's markets today, and there has been high interest in CATV and also other analogue fibre-optic link applications of IO technologies. In Japan, NTT's push for fibre-to-the-home (FTTH) is driving telecommunications loop applications. The global consumption value of integrated optical modulators will increase at a pace of about 40.3 percent per year over the coming years to $1.37 billion in 2006, according to new market research data (ElectroniCast Corp.).

A closely related area that is in the research stage is photonic integrated circuits (PICs), in which a variety of semiconductor integrated optical circuits (IOCs) are monolithically integrated and interconnected with waveguides such as lasers and modulators. The market for PICs has reached a critical commercial threshold. Since the introduction of PICs in 1997, the optical component industry has slowly been migrating from the manual assembly of discrete optical devices to automated, semiconductor wafer-processing techniques and single-chip solutions. Ultimately, each major optical networking function (e.g. amplification, mux/demux, switching, transmitting/receiving) will be performed by a single chip. Until recently, though, factors such as low cost-to-performance ratios, material limitations, and the absence of a large end-market made it difficult to justify the exorbitant capital expenditures of semiconductor processing.

However, with the demand for high-volume, low-cost components in the metro market and compact, advanced components in all-optical and higher-speed networks,

the economics now make sense. The market for photonic integrated circuits (PICs) subsystems and components is currently estimated at $4.3 billion (IC Industry Market Reports, 2003, Electronics.ca publications Inc.). It is expected to grow at an AAGR (average annual growth rate) of 20.5% to reach almost $11 billion by 2006.

The preponderance of growth for photonic chips is expected to take place beyond 2003. Simultaneous upgrades to both network architecture and bandwidth, specifically the all-optical and 40-Gbps networks will establish sizable end markets for advanced optical components. Both are conspiring to eliminating the optical-electronic-optical (OEO) bottleneck, a necessary step to enabling the dynamic routing of photons at higher speeds. The wide scale commercialisation of photonic switches and subsystems, optical add-drop multiplexers, and optical crossconnects will help accomplish this.

1.3   Optical waveguides

Optical waveguides trap light locally and guide it in a specific direction. They can be classified into optical waveguides for optical integrated circuits and for optical fibres, (which have a filamentary appearance and are mainly used in optical communications.) Since all the waveguides considered in the thesis are for use in integrated optical devices, a brief discussion of the principles of these waveguides will be presented next.

An optical waveguide that is uniform in the direction of propagation is the most basic type of waveguide. However this alone is not sufficient for achieving the desired features in an optical integrated circuit. Corner-bent waveguides, S-shaped waveguides, and bent waveguides are used to change the direction of light waves. Tapered waveguides are used to change the width of the waveguides. Other non-uniform waveguides like branching and crossed waveguides are used for splitting, combining and intereference. Waveguide gratings, with a periodic structure in the direction of propagation, plays many important roles in the optical integrated circuit, such as wavelength filters, mode converters, reflectors, resonators and demultiplexers

etc. These waveguide gratings can also be used widely as laser elements such as distributed bragg reflector (DBR) lasers or distributed feedback (DFB) lasers.

The simplest and the most basic type of optical waveguide is known as the three layer dielectric waveguide or an asymmetric slab waveguide which is shown in **Fig. 1.3.**
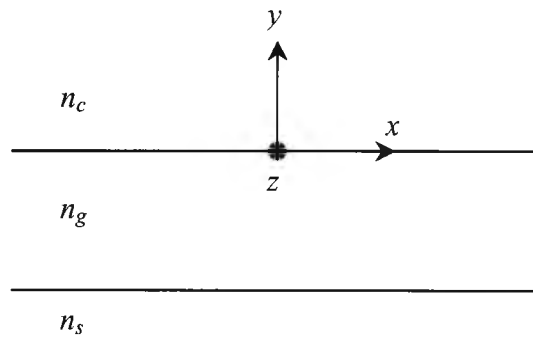
Fig. 1.3 Schematic three-layer dielectric waveguide.

Here n_g, n_s and n_c represent the refractive indices of the guide, substrate and the upper cladding, respectively. By loading a thin film with a higher refractive index than either the substrate or the upper cladding on the substrate surface, the light can be trapped inside this film, which is often called the guide. So the relationship among the refractive indices is $n_c < n_s < n_g$. However, in most cases, the upper cladding is air, giving $n_c = 1$. When $n_s = n_c$, the waveguide is called a symmetric slab waveguide.

A three-layer dielectric optical waveguide is shown in **Fig. 1.4**, and it may be assumed that z is the direction of propagation and the waveguide structure is homogeneous in the z-direction. n_g, n_s and n_c are the guide, substrate and cladding indices, respectively, and t is the guide thickness. In general the relationship among the refractive indices is $n_g > n_s > n_c$.
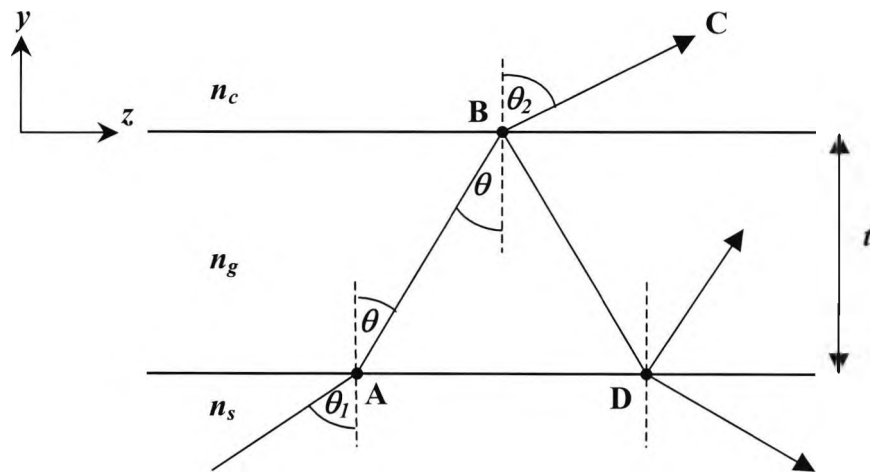
Fig. 1.4 Ray diagram showing refraction and reflection in a slab waveguide.

A feature of visible light is its comparatively short wavelength. In all cases where the wavelength of light is much shorter than the dimensions of any obstacle that the light encounters, it is possible to utilise the short wavelength of light to solve the problem of light propagation in an approximate way. The approximation that is valid for short wavelength of light is known as the '*geometrical or ray*' optics. In order to analyse the propagation problem of the three-layer slab waveguide, Maxwell's equations or the wave equation can be utilised. However, the geometrical optics treats the light propagation problem in a way far simpler than would be possible by solving Maxwell's equations.

Consider a coherent light wave incident at an angle θ_l between the wave normal and the normal to the substrate-guide interface, as shown in **Fig. 1.4.** By using Snell's law the refraction can be expressed as (Kogelnik, 1990),

$$\frac{n_g}{n_s} = \frac{\sin\theta_1}{\sin\theta} \tag{1.1}$$

where θ is the exit angle of the refracted wave AB.

Similarly, for the guide-cladding interface, the Snell's law gives,

$$\frac{n_c}{n_g} = \frac{\sin\theta}{\sin\theta_2}$$

(1.2)

where θ_2 is the angle of the refracted ray BC, with the normal to the guide-cladding interface.

The so-called critical angles θ_s and θ_c at the guide-substrate and at the guide-cladding interfaces, respectively, are determined by (Koshiba, 1992),

$$\sin\theta_s = \frac{n_s}{n_g}$$

(1.3)

$$\sin\theta_c = \frac{n_c}{n_g}$$

(1.4)

Here, $\theta_c < \theta_s$, based on the assumption that $n_c < n_s < n_g$. If the angles of incidence to these two interfaces exceed the critical angles, then the total internal reflection phenomenon occurs and the light can be guided inside the material.

Since $n_g > n_s$, the incident ray is refracted into the guide region, following the path AB and when $\theta < \theta_c$, total reflection conditions are not met at the guide-cladding interface, and thereby the ray is refracted to the cladding side. There is essentially no confinement of light and the electromagnetic mode corresponding to this is called a *"radiation mode"*.

When the incident angle θ is greater than the critical angle, θ_c, then the total reflection occurs and the light ray will follow the path BD. At the guide-substrate interface, if the incident angle $\theta < \theta_s$, then the light ray may refract back in to the substrate through which the light escapes from the structure. These are called *"substrate radiation modes"*.

Finally when θ is large enough, i.e. θ_s; $\theta_c < \theta$, total internal reflection occurs at both interfaces. Then the light, once it is inside, is trapped and confined in the guide and propagates in a zig-zag path along the $+z$ direction. These modes are called the '*guided*' or '*bound*' modes as shown in **Fig. 1.5**.
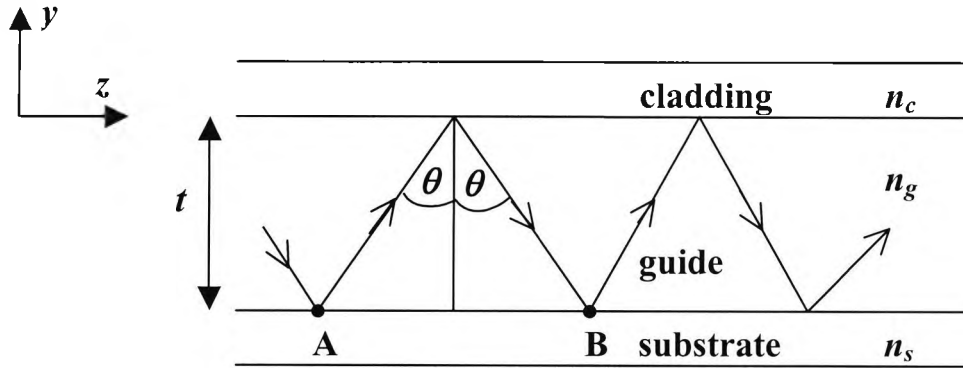
Fig. 1.5 Wave normals of the zig-zag waves corresponding to a guided mode in a slab waveguide.

These modes can be classified as either Transverse Electric (TE) or Transverse Magnetic (TM) modes. In the TE mode, the electric fields are perpendicular to the plane of incidence and in TM mode the magnetic fields are perpendicular to the plane of incidence. These waves travel with a wave vector kn_g in the direction of the wave normal where the absolute value of k is,

$$k = \frac{2\pi}{\lambda} = \frac{\omega}{c} \tag{1.5}$$

k is called the wave number and ω, λ and c are the angular frequency, free-space wavelength and the velocity of light in vacuum, respectively.

The propagation constant β in the direction of propagation, and the phase velocity v_p can be defined by (Kogelnik, 1990),

$$\beta = \frac{\omega}{v_p} = kn_g \sin\theta \tag{1.6}$$

However not all the values of θ are allowed and only discrete values of θ will yield the "guided mode". The condition for the existence of a guided mode is that the total phase shift in the *y*-direction during one cycle (from point A to point B in **Fig. 1.5**) of the plane wave must equal an integral multiple of 2π. The phase change for the plane wave to cross the thickness *t* of the guide twice (i.e. up and down) is $2kn_g t \cos\theta$ (Tien, 1971). In addition the wave suffers a phase change of $-2\phi_c$ due to the total reflection at the guide-cladding interface, and similarly a phase shift of $-2\phi_s$ on total relection at the guide-substrate boundary. Thus, the self-consistency condition can be expressed as follows:

$$2kn_g t\cos\theta - 2\phi_s - 2\phi_c = 2m\pi \tag{1.7}$$

where *m* is the order of the mode which is an integer. This expression is also referred to as the eigen value or transcendental equation. According to the theory of total reflection and by employing the Fresnel formulas (Kogelnik, 1990), the phase shifts ϕ_s and ϕ_c can be derived in terms of the angle θ, for each polarization;

$$tan\phi_s = \frac{\sqrt{n_g^2 \sin^2\theta - n_s^2}}{n_g \cos\theta}$$

$$tan\phi_c = \frac{\sqrt{n_g^2 \sin^2\theta - n_c^2}}{n_g \cos\theta} \tag{1.8}$$

for the TE waves, and,

$$tan\phi_s = \frac{n_g^2 \sqrt{n_g^2 \sin^2\theta - n_s^2}}{n_s^2 n_g \cos\theta}$$

$$tan\phi_c = \frac{n_g^2 \sqrt{n_g^2 \sin^2\theta - n_c^2}}{n_c^2 n_g \cos\theta} \tag{1.9}$$

for the TM waves.

From the above eigenvalue equation (1.7), the propagation constant β of a guided mode at a given angular frequency ω can be calculated. Since the angle of incidence, θ is discrete, only a limited number of discrete values are allowed for β. Therefore the

guided mode is sometimes called the discrete mode or discrete spectrum. On the other hand in the radiation mode, the angle of incidence θ and the propagation constant β are continuous quantities. For this reason it is called the continuous mode or the continuous spectrum.

For guided modes, β is bounded by the plane wave propagation constants of substrate and guide (Kogelnik, 1990).

$$kn_s < \beta < kn_g \tag{1.10}$$

From (1.10) it is convenient to define an *"effective refractive index"* (Koshiba, 1992);

$$n_{eff} = \frac{\beta}{k} = n_g Sin\theta \tag{1.11}$$

which is bounded by,

$$n_s < n_{eff} < n_g \tag{1.12}$$

1.4 Analysis of optical waveguides

The analysis of the optical waveguides means finding the propagation constants and field profiles of all the modes that the waveguide supports. In order to calculate these propagation characteristics the well-known Maxwell's equations have to be used with necessary boundary conditions. However, employing of Maxwell's equations is not an easy task and a precise analysis of optical waveguides is generally considered to be difficult. Some of the major reasons are that the optical waveguides may have complex structures, arbitrary refractive index distribution (graded optical waveguides), anisotropic and non-linear optical materials as well as materials with complex refractive index such as semiconductors and metals. To overcome these difficulties, various methods of optical waveguide analysis have been developed. These methods can be broadly classified into two groups, namely the analytical approximation solutions and the numerical solutions.

An exact analytical solution can be obtained for stepped 2-D optical waveguides (i.e. slab waveguides) and stepped optical fibre. However, if the waveguide has an arbitrary refractive index distribution, then the exact solutions may not be possible. Therefore various types of analytical approximation solutions have been developed for 2-D stepped optical waveguides which have a gradually changing refractive index distribution in the thickness direction of the waveguide. For example, the ray approximation method (RAM) (Qiao and Wang, 1992) and the Wentzel, Kramers and Brillouin (WKB) method (Srivastava *et al.*, 1987) are typically known analytical approximation solution techniques for such optical waveguides.

In the case of 3-D optical waveguides for optical integrated circuits, hybrid mode analysis is required in order to satisfy the boundary conditions. However, the analytical approximation solutions developed for these guides do not treat them as hybrid mode and therefore, they are not suitable for accurately analysing the practically used 3-D optical waveguides. Marcatili's method (MM), and the effective index method (EIM) can be treated as the typical analytical approximation solutions for 3-D optical waveguides.

Numerical solutions can also be grouped into two categories, i.e. the domain solution and the boundary solution. The domain solution includes the whole domain of the optical waveguide structure as the operational area, where as the boundary solution includes only the boundaries as the operational area. The former is also called a differential solution, and the latter, an integral solution. Some of the examples of the domain solutions include the finite element method (FEM), finite difference method (FDM), variational method (VM), and multilayer approximation method (MAM). The boundary solutions include the boundary element method (BEM), point-matching method (PMM) and mode-matching method (MMM).

In the next sections, a brief description of the most commonly used analytical and numerical solution techniques for modelling in opto-electronics will be presented.

1.5   Analytical approximation solution methods

Analytical approximation methods are widely used in the modelling of opto-electronic waveguides such as buried waveguides, rib waveguides, tapers and directional couplers. This group of methods has always been very popular with the opto-electronic circuit designers, especially before the advent of modern computers. Some of the methods will be briefly discussed in the next sub-sections.

1.5.1 Marcatili's method

One of the first analytical approximation methods to be developed for the analysis of buried waveguides and couplers is Marcatili's method (Marcatili, 1969). This is a method which was developed for guiding structures with large dimensions and a small refractive index difference (less than 5%) between the guiding and cladding materials. According to these assumptions, the field is assumed to exist in the rectangular waveguide core region and also in the four neighbouring cladding regions, which are obtained by extending the width and the height of the waveguide to infinity. Furthermore, the field is assumed to vary sinusoidally in the core region and exponentially in the four cladding regions and the field is approximated to the field in two slab waveguides, one vertical and the other horizontal. Two transcendental or eigenvalue equations for each slab waveguide are solved simultaneously to give the axial propagation constant.

Marcatili's method (MM) works well in the regions far from cut-off, but does not operate close to cut-off region (Chiang, 1994).

1.5.2 The effective index method

The effective index (EI) method was first proposed by Knox and Toulios in 1970 (Knox and Toulios, 1970) with a view of extending Marcatili's method (Marcatili, 1969) for the fundamental mode of a simple rectangular-core waveguide. Soon after, this method became one of the most popular methods for the analysis of optical waveguides. In this approach, the rectangular structure is replaced by an equivalent slab with an effective refractive index obtained from another slab. The rectangular

dielectric waveguide is divided into two slab waveguides in each transverse direction. The first step solves the transcendental equation for a vertical slab waveguide by applying the appropriate boundary conditions. The effective index which is calculated is used as the refractive index of the horizontal slab waveguide, and by solving the eigenvalue equation gives a good approximation to the effective index of the original waveguide structure. As only the solutions for slab waveguides are required, this method is significantly more efficient than those methods that solve the rectangular structure directly.

The advantage of the EI method is that it can be applied to a wide variety of structures, including channel waveguides, strip waveguides and arrays of such waveguides (Chiang *et al.*, 1996) and also for various types of optical fibres and fibre devices (Chiang, 1986*a*; Van de Velde *et al.*, 1988). The weakness of the method is that it does not give good results when the structure operates near cut-off region. The simplicity and speed of the method have encouraged many engineers to search for different approaches that will improve the accuracy of the EI method. Consequently, many different variants of the EI have been developed such as the EI method based on linear combinations of solutions (Chiang, 1986*b*; Van Der Tol and Baken, 1988), or the EI method with perturbation correction (Chiang *et al.*, 1996).

1.6   Numerical solution methods

The rapid growth in the millimetre-wave, optical fibre, and integrated optics fields has included the use of arbitrarily shaped dielectric waveguides, which in many cases also happened to be arbitrarily inhomogeneous and/or arbitrarily anisotropic. Most of such cases of waveguide arbitrariness do not lend themselves to analytical solutions. Therefore many scientists have given their attention to construct numerical methods to solve such waveguides. Numerical methods may be used to solve Maxwell's equations exactly and the results they provide are accurate enough for the characterisation of most of the devices.

Since the advent of computers with large memories, considerable attention has been paid to methods of obtaining numerical solutions of the boundary and initial value

problems. Methods are usually evaluated in terms of their generality, accuracy, efficiency and complexity. It is evident from the review methods (Chiang, 1994; Vassalo, 1997) that every method represents some sort of compromise between these aspects. No method is superior to the other in all aspects. The optimal method should be the one that can solve the problem with acceptable accuracy but requires the minimum effort to implement and run in terms of man-power and computer capacity. The continuing improvement in computer power will make computational efficiency less of an issue in the future.

Some factors with regard to the selection of methods for analysing optical waveguide problems, based on reviews (Davies, 1972; Ng, 1974; Saad, 1985) are given, as follows:

(a)   the shape of the cross section of the structure, whether it is curved or polygonal or whether it is convex or non-convex.

(b)   whether a method that can be realised as a computer program suitable for the automatic solution of a wide range of structures is needed.

(c)   whether a computer program requiring human intervention or some exploratory work with the computer is needed.

(d)   the method should be programmable and it has to be written specially for each region of the structure separately.

(e)   whether the dominant mode only, or a number of the higher order modes are required.

(f)   whether the field distribution, or the cut-off frequency is needed, or the both are needed.

(g)   the requirement of accuracy needed for eigenvalues and perhaps eigen functions.

(h)   the accuracy of the method in modelling the dielectric boundaries and regions.

(i)   the accuracy of the method in specific frequency ranges as an example, near the cut-off frequency.

(j)   whether the method has a mechanism of generating spurious numerical solutions and if so whether the method can identify and/or eliminate them.

(k)   the computational efficiency of the method, including its computer storage requirements.

In this section, a short overview of these commonly used numerical solution techniques is given.

1.6.1 The Boundary Element method

The boundary element method (BEM) is interpreted as a combination technique of the conventional boundary integral equation method and a discretisation technique, such as the finite element method (Kagami and Fukai, 1984). The BEM is a boundary solution method and therefore the fields are needed only for the nodes which are on the boundaries of the region. The derivation of the integral equations with respect to the unknown fields at boundaries is obtained by using the method of weighted residuals or Green's formula. These integral equations are then discretised to a set of linear equations to be solved for the numerical solutions.

The BEM can be used for the analysis of arbitrarily shaped discontinuities as FEM, but the BEM can be performed using far fewer nodes than by the FEM. Koshiba and Suzuki have reported (Koshiba and Suzuki, 1986*a*) a numerical approach based on the BEM for analysis of discontinuity problems of TE and TM modes in a dielectric slab waveguide. Moreover, the BEM can handle unbounded field problems easily and therefore has the possibility of modelling domains extending to infinity without an infinite element analysis which is often performed in FEM. However, the BEM can only be applied to homogeneous structures (Hirayama and Koshiba, 1989), and also it has been known that the matrices involved are dense matrices unlike those in FEM which are sparse. Therefore the FE method can be treated as more numerically efficient.

1.6.2 The Point Matching method

The point matching method (PMM) is one of the oldest and simplest 'boundary solution' techniques for the analysis of isotropic homogeneous dielectric waveguides. Its application was first shown by Goell (Goell, 1969) to investigate the propagation characteristics in rectangular cross section dielectric waveguides. Goell's numerical analysis is based on expressing the internal and external fields in terms of circular

harmonics. The fields inside the dielectric and outside the dielectric are expressed by a sum of Bessel functions and modified Bessel functions multiplied by trigonometric functions, respectively, and their derivatives. By matching the tangential fields at optimally selected points around the boundary called 'matching points', a system of linear equations is obtained. By applying the condition of nontrivial solution, a characteristic equation including the propagation constant is obtained and solved for the appropriate eigenvalues. The original matrix equation is then solved for each mode eigenfunction by standard matrix techniques.

The PMM is capable of use for analysing dielectric waveguides with arbitrary cross sections and composite structures, and also computing coupling coefficients between two rectangular rods. Improved results for the PMM were reported (Cullen *et al.*, 1971), by rotating the grid of equiangularly spaced matching points in order to place a matching point at the corner of a rectangular dielectric waveguide. However, the PM method is not suitable for the analysis of 3- dimensional waveguide structures (as shown in **Fig. 2.2**) with inhomogeneous index distribution, such as graded index fibres.

1.6.3 The Mode Matching method

The mode matching method (MMM), which is also known as the equivalent network method (ENM), is an approximate solution method for the analysis of open dielectric waveguides (Peng and Oliner, 1981). In this approach the structure is artificially bounded, and the waveguide cross section is viewed in terms of constituent parts or building blocks, which are usually portions of uniform dielectric layered structures interfaced by the dielectric step discontinuities. Then each constituent is analysed separately and all the parts are put together to comprise the final structure of interest. A transverse equivalent network for the structure is obtained by representing the uniform dielectric regions as uniform transmission lines and by characterising the step discontinuities as transformers. From this, the dispersion relation can be derived to obtain the waveguide propagation characteristics.

In the earlier analysis of the MMM, due to the artificial bounding of the structure, the continuous spectrum (Peng and Oliner, 1981) and TE to TM coupling at the sides of the waveguide are neglected. Dagli and Fonstad (Dagli and Fonstad, 1986) reported a modified approach, which takes into account the continuous spectra. Rather than artificially bounding the structure to discretise the continuous modal spectrum, here, they are discretised by converting integrals into summations using suitable basis function expansions. Koshiba and Suzuki (Koshiba and Suzuki, 1985; 1986*b*) reported a vectorial wave analysis of rectangular optical waveguides using the ENM, by taking the TE-TM coupling and the discrete-continuous spectrum coupling into account.

1.6.4 The Spectral Index method

The spectral index (SI) method may be used to find quickly and easily the guided modes and propagation constants of semiconductor rib waveguides (Kendall *et al.*, 1989; Stern *et al.*, 1990). Here the true open structure is replaced by slightly larger, partially closed one, which is simpler to analyse, in order to model the penetration of the optical field into the cladding. The spectral index method can be expressed as the following combination.

(a)   In the region below the rib, the Fourier transform is applied in order to reduce the dimensionality of the problem to a one-dimensional structure, and the field is expressed in spectral space using Fourier transform.

(b)   In the rib region the wave equation is exactly expressed using Fourier series in terms of cosine and sine functions.

(c)   The two solutions are linked by employing a transfer relationship and consequently, giving a transcendental equation which can be solved for the propagation constant of the original rib structure.

The presence of the strong discontinuities at the dielectric interfaces is dealt with by using an effective rib width and an effective outer slab depth.

The SI method has been extended to include rib coupler problems (Burke, 1989; 1990), cases with loss and gain (Burke, 1994) and also it has been used to analyse multiple rib waveguides (Pola *et al.*, 1996).

1.6.5 The Beam Propagation method

The beam propagation method (BPM) describes the evolution of the total field propagating along a waveguide and it is the most widely used tool in the study of light propagation in longitudinally varying waveguides such as, tapers, Y-junctions, bends and gratings. The BPM was first applied to optoelectronics in 1980 (Feit and Fleck, Jr., 1980) and the solutions for optical waveguides can be made to generate mode-related properties such as propagation constants, relative mode powers and group delays with high precision and considerable flexibility. The initial BPM is based on the fast Fourier transform (FFT) and only solves the scalar wave equations under paraxial approximation. Therefore the FFT-BPM was only developed for the case of weakly guiding structures, neglecting the vectorial properties of the field. Several numerical algorithms to treat the vectorial wave propagation (vector BPM) using the finite difference (FD) method, have been reported (Huang *et al.*, 1992; Chung *et al.*, 1991; Huang and Xu, 1992). The VBPMs are capable of simulating polarized or even hybrid wave propagation in strongly guiding structures. Recently, the finite element (FE) method has been utilised to develop BPM approaches. A unified finite element beam propagation method has been reported (Tsuji and Koshiba, 1996) for both TE and TM waves propagating in strongly guiding longitudinally varying optical waveguides. Obayya *et al.* (Obayya *et al.*, 2000) has reported a full-vectorial BPM algorithm based on the FEM to characterise 3-dimensional optical guided-wave devices.

1.6.6 The Finite Difference method

The finite difference method (FDM) is one of the oldest and perhaps the most commonly used numerical technique in analysing dielectric waveguide problems. Its application to the modelling of optical waveguides dates from the early eighties, originally evolving from previous finite difference models for metal waveguides (Davies and Muilwyk, 1966). The FDM discretises the cross section of the device being analysed and is therefore suitable for modelling inhomogeneous media and complicated boundaries.

In this method, its necessary to define a finite cross section, by enclosing the dielectric guide in a rectangular "box" with the side walls are either electric or magnetic walls and the field at these boundaries are assumed to be very small. The enclosed cross section is divided into a rectangular mesh allowing for the material discontinuities only along mesh lines (Bierwirth *et al.*, 1986). The nodes are placed on mesh points so that each node can be associated to maximum of four different refractive indices. By using the five point finite difference form, the differential vector, semi-polarized or scalar wave equation can be approximated in terms of the fields at the neighbouring nodes of the mesh. Taking into account the continuity and discontinuity conditions of the electric and magnetic components at the grid interfaces, an eigen value problem is generated which can be solved in order to obtain the modal propagation constants and their modal field profiles.

The accuracy of the method depends on the mesh size, the assumed nature of the electromagnetic field (scalar, polarized or vector) and the order of the finite difference scheme used. When the device operates near cut-off, the size of the box has to be sufficiently large to allow for substantial penetration of the field into the substrate. If a uniform mesh is used, then it can result in a very large number of nodes and large matrices and therefore the disadvantages like long run times and high memory requirements may become apparent.

1.6.7 The Finite Element method

The finite element method (FEM) is a well established numerical method for the solution of a wide range of guided wave problems. It can be very easily applied not only to optical waveguides of any shape, but also to optical waveguides with any refractive index distribution and to those with any anisotropic materials or non linear materials. This method is based upon dividing the problem region into non-overlapping patchwork of polygons, usually triangular elements. The field over each element is then expressed in terms of polynomials weighted by the field values at the nodes of each element. The total field is found by the linear summation of the fields over each element. By applying the variational principle to the system functional, and thereby differentiating the variational functional with respect to each nodal value, the

problem reduces to a standard eigen value matrix equation. This is solved using iterative techniques to obtain the propagation constants and the field profiles (Rahman and Davies, 1984*a*; Koshiba and Inoue, 1992).

The accuracy of the FEM can be increased by using finer mesh. Number of formulations have been proposed, however, the full vectorial **H**-field formulation is the most commonly used and versatile method in modelling optical waveguides due to much easier treatment of boundary conditions. This method can accurately solve the open type waveguide problems near the cut-off region and much better results were obtained by introducing infinite elements to extend the region of explicit field representation to infinity (Rahman and Davies, 1984*b*). One drawback associated with this powerful vector formulation is the appearance of spurious or non-physical solutions. Suppression of these spurious solutions can be achieved by introducing a penalty term into the variational expression (Rahman and Davies, 1984*c*). In order to eliminate the spurious solutions completely, another approach is employed using the edge elements (Bossavit and Mayergoyz, 1989; Koshiba and Inoue, 1992).

In modelling more complex structures, the FE method is considered to be more flexible than the FD method, due to the ability of employing irregular mesh. A more detailed study of the FE method is presented in the next chapter.

1.7   Aims and objectives of the thesis

The discussion given so far explains the remarkable technological achievements gained in the field of communication of information in recent years and discusses the role of integrated optics within the broad field of communication in facilitating an efficient dissemination of information. Thus the introductory information presented, serves as an important background to the research work reported in this thesis. The primary aims and objectives of this research work can be summarised as follows;

(1)   To develop and accurately implement the rigorous and efficient finite element method based on vector **H**-field variational formulation for the analysis of optical waveguides with arbitrary cross sectional shapes.

(2)   To implement the least squares boundary residual (LSBR) method together with the exploitation of the accurate modal solutions obtained from the finite element method in order to achieve an accurate waveguide junction analysis and to account for power conversion phenomenon.

(3)   To apply the full vectorial numerical techniques implemented in (1) and (2) in the study of designing and characterising various optical waveguides involved in polarization-based issues in optoelectronics;

   a) To design an efficient passive polarization splitter which splits transverse electric (TE) and transverse magnetic (TM) polarizations into two separate ports, fabricated using a deeply etched semiconductor waveguide based on the multimode interference mechanism.

   b) To design and characterise various types of passive polarization rotators in semiconductors, including a cascaded multi-sectioned waveguide rotator and a single waveguide sectioned rotator. It is shown that nearly 100% TE to TM polarization conversion can be achieved with very short device lengths.

   c) To optimise novel single stage polarization rotators and also to undertake a thorough sensitivity study of the fabrication tolerances on the performance of the single sectioned polarization rotators.

   d) To investigate the origin of the polarization crosstalk in planar silica waveguide with high index contrast and to show the critical effect of such polarization crosstalk in considerably longer silica waveguides when the side walls are not perfectly vertical.

(4)   To design and optimise a novel semiconductor based (AlGaAs-GaAs) active polarization controller by using full vectorial numerical methods implemented in (1) and (2) along with the finite element based solution of the Laplace equation. A novel design concept has been used with two electrodes inducing an asymmetric electric field to show the effect on polarization controllability.

1.8   Structure of the thesis

The work presented in this thesis is based on the research carried out by the author in the use of the versatile finite element method and the least squares boundary residual approach in the analysis of various types of semiconductor waveguide devices. The work reported here has been mainly devoted to the study of polarization issues in optoelectronic systems. The discussion given here is an outline of the structure of the thesis, beginning with a general introduction. This first chapter gives a brief historical view of the lightwave technology followed by the development of the integrated optical devices and its economic and technological impact on present day society. A theoretical explanation of optical waveguides is given and it also covers the basis of some analytical and numerical solution techniques which are used to analyse various types of optical waveguides. The subsequent chapters give the basis of theory of the numerical methods used followed by various polarization-based design aspects achieved, and the presentation of the numerical results.

The theoretical formulation of the finite element method as a powerful numerical tool in analysing optical waveguides is described in Chapter 2. First a brief history of the finite element method is presented with its importance in analysing any type of waveguide. The fundamental mathematical relations derived from Maxwell's equations for the application of this approach in the solution of optical waveguides is derived. Also a comparison of several variational formulations is presented with an emphasis on the vector **H**-field finite element formulation. The utilisation of triangular elements, the shape functions, and the infinite elements is undertaken in order to obtain the propagation constants and the field profiles of different modes propagating through a uniform optical waveguide. The problem of spurious modes is investigated and the penalty function method is introduced to avoid the appearance of the spurious modes.

Chapter 3 deals with the theoretical foundation of a rigorously convergent, junction analysis approach called the least squares boundary residual (LSBR) method. The chapter starts with a brief introduction of waveguide discontinuity analysis and an abrupt discontinuity problem in the transverse plane $z = 0$, is considered. The use of the finite element output data in the LSBR approach is also explained. The final part

of this chapter is devoted to the losses in optical waveguides, mainly the insertion loss which can be obtained by using the scattering coefficients calculated by employing the LSBR method.

Chapters 4, 5, 6 and 7, are devoted to the application of these methods to undertake a detailed study of polarization issues of different optical waveguides. In Chapter 4, a design of a single section polarization splitter, in a deeply etched semiconductor MMI waveguide is presented. Polarization splitter separates the two orthogonal states of polarization of an optical signal, allowing the further processing of the polarized fields. The design considerations such as, the quadrature relationship and the coupling length calculations are explained. Modal simulation results of the deeply etched InP-InGaAsP MMI ridge waveguide structure are accurately obtained by employing the vector **H**-field finite element method. The input-output waveguides were placed appropriately in order to design the devices with restricted and general interference mechanisms. The rigorous LSBR method is employed to calculate the excited modal coefficients of the modes in the MMI section and also the optical power intensity contours along the propagation direction (z) are obtained for both TE and TM polarizations. The TE and TM optical power transfer characteristics in the bar and cross ports, with the axial direction (z) are presented and the effect of the operating wavelength on the device performance is also investigated.

In Chapter 5, a number of passive polarization rotator designs are proposed and simulated with the use of the vector **H**-field finite element (VFEM) and the LSBR method. Firstly, different types of waveguides such as, semiconductor rib waveguides with vertical side walls, both slanted side walls and one slanted side wall are analysed to achieve their modal characteristics. The modal field profiles are thoroughly examined and other characteristics, such as, the hybridity, the overlap integral and the half-beat length are obtained by using the VFEM for all the shapes of waveguides considered. The hybridity is defined as the field ratio of the non-dominant to the dominant field. Next, a cascaded polarization rotator design is presented using the rib waveguides with one slanted side wall. The butt junction between the two waveguides are analysed by the LSBR method and the results of the power conversion from TE to TM are obtained. The transmission coefficients of the excited TE and TM modes at he junction interface when TE mode is incident, are obtained and the variation of these

and the insertion loss with the lateral offset between the guides is shown. The optimum offset is then obtained to achieve the maximum power conversion.

Also in this chapter, the design and the simulation of a single section passive polarization rotator is presented. The importance of the numerical approaches used in the analysis is explained followed by the presentation of the results of the input-output waveguide characteristics. The polarization rotator waveguide is analysed next. The effects of the waveguide width, the slant angle and the index contrast on the hybridity and the half beat length are thoroughly investigated with the aim to design a short low loss polarization rotator. Finally, the evolution of power and the insertion loss at the junction between the input vertical wall rib waveguide and the polarization rotator waveguide are evaluated.

The next part of the Chapter 5 deals with a detailed study of the fabrication tolerances of a compact passive, single section polarization rotator. The effects of the waveguide width, slant angle, the etch depth, and refractive index variations during its fabrication on the overall polarization conversion and polarization crosstalk are reported. The behaviour of the polarization conversion is investigated over a range of operating wavelengths. Finally in this chapter, some novel polarization rotator designs in shallow-etched waveguides are presented with a detailed study of effects of the waveguides parameters on the device performance.

Chapter 6 discusses the numerically simulated results by using the full vectorial approaches to indicate the possibility of significant polarization crosstalk in a high index contrast planar silica waveguide, particularly when it consists of slanted side walls. A square shaped planar silica waveguide is considered and the width is varied in order to understand its effect on the modal hybridity and the field profiles for different slant wall angles. The variation of the half beat length is also obtained for different slant angles when the refractive index difference is 1.5%. The final section of the chapter discusses the results of the junction analysis between the square shaped input silica waveguide and the slanted waveguide. The transmission coefficients of the excited TE and TM modes are obtained when TE is incident for different slant angles. Consequently, the polarization conversion is analysed along the propagation distance for different waveguide widths and different slant angles. Finally, a detailed study of

the polarization crosstalk at various waveguide lengths is investigated for different slant angles.

In Chapter 7, a novel polarization controller design using a semiconductor deeply etched rib waveguide is introduced. The waveguide is implemented in AlGaAs-GaAs based material and here the design concept is to achieve polarization conversion by inducing the electro-optic effect via a voltage applied to two electrodes placed on the top of a deeply etched rib waveguide. First, the simulations are carried out considering a symmetric passive waveguide in order to show the disadvantages, such as, poor polarizability and the extensively long device lengths. Consequently, the simulations are carried out for the active polarization controller waveguide including both symmetrical and non-symmetrical voltages. The phase matching voltage is achieved for the symmetrical case for different waveguide core heights. Although the maximum hybridity occurs at the phase matching instance, it is extremely sensitive with the fabrication processes. However, it is clearly shown that by introducing asymmetry in the voltages the polarization rotation can be achieved by mode coupling via the change in the off diagonal permittivity tensor. The variation of the modal hybridity with the applied average voltage is shown for different core heights. The applied E-field profiles and the change on the refractive indices are also clearly presented. Finally the polarization conversion from TE to TM power along the length of the waveguide is analysed for different waveguide parameters and applied average voltages when the voltage difference between the electrodes is maintained at a constant value.

Finally in Chapter 8, general conclusions gained from this research work are summarised and explored. Possible future prospects for this work are also suggested. The thesis concludes with a list of relevant publications by the author followed by a list of references cited.

Chapter 2

The Finite Element Method

2.1 Introduction

In essence, the finite element method is a numerical technique which solves the governing equations of a complicated system through a discretisation process. The system of interest can be either physical or mathematical. The governing equations can be given in differential form or be expressed in terms of variational integrals. Although this method was first developed for applications in structural mechanics, now it is widely used in many branches of science and engineering. The use of piecewise continuous functions defined over a subdomain to approximate the unknown function dates back to the work of Courant (1943), who used an assemblage of triangular elements as a way to get approximate numerical solutions. Although certain key features of the finite element can be found in the work of Courant (1943), the formal presentation of the finite element method is attributed to Turner, Clough, Martin and Topp (1956) at the Boeing Aircraft Company. They used finite element method to calculate the stress-strain relations for complicated aircraft structures for which no known solutions existed. With this piece of work, together with many others, an explosive development of the finite element method in engineering applications began. However the name "finite element" was first introduced by

Clough in 1960 to describe the new technique for plane stress analysis. The method was soon recognised as a general method of solution for partial differential equations, and its applicability to non-linear and dynamic structural problems was amply demonstrated. Subsequent development has been rapid, and the techniques are now extended in many other domains, such as, soil mechanics, fluid mechanics, thermodynamics, electromagnetism, biomedical engineering, etc.

The basic idea of the finite element method is the piecewise approximation of a smooth function by means of simple polynomials, each of which is defined over a small region (element) of the domain of the function. Instead of expressing the value of the function as a whole, it is expressed in terms of the values of the functions at several points of the domain called element nodes.

The finite element method can be considered as an extension to the variational methods such as the Rayleigh-Ritz and Galerkin methods or the weighted residual techniques (Zienkiewicz, 1977; Desai, 1979). The earliest mathematical formulations for finite element models were based on variational techniques. These techniques have been applied to yield approximate solutions for variationally formulated problems in many areas in physics and engineering such as solid mechanics and fluid mechanics. The approximate solution is assumed to be a combination of given approximation functions called trial functions. The weighted residual techniques are important in the solution of differential equations and other non-structural applications. It starts with the governing differential equation and assumes an approximate solution which in turn is substituted into the differential equation. However, these methods suffer from disadvantages which prevent them from being used in wider class of problems. The main disadvantage of the variational methods is that there is no specific way of choosing the trial functions used in the approximation and, it is difficult to construct the approximate functions for problems with arbitrary domains with changes in material properties.

On the other hand, there are other difficulties suffered by the variational techniques, since the approximation is applied over the whole domain. As a result, very high degree polynomials have to be used in order to describe the unknown function accurately. This creates a more complicated problem if the domain consists of

interfaces which have abrupt material changes. Also for irregular shaped boundaries, it can be really difficult to impose the boundary conditions on the complicated trial functions.

The finite element method overcomes the above mentioned difficulties. The method is endowed with two basic features which account for its superiority over other competing methods. First a geometrically complex domain of the problem is represented as a collection of geometrically simple sub domains, called finite elements, avoiding the difficulties associated with the 'whole domain' techniques. Second, over each finite element the approximation functions are derived using the basic idea that any continuous function can be represented by a linear combination of algebraic polynomials.

2.2   Important characteristics

Generality and versatility are perhaps the most outstanding features of the finite element method. The present-day application of the method includes almost all physical problems that are governed by differential equations. Several advantageous properties of the method have contributed to its extensive use. Some of the more important characteristics are listed below:

- The material properties of adjacent elements need not be the same, allowing the application to bodies composed of several types of materials.
- Irregular shaped boundaries can be approximated using elements of straight edges or matched exactly using elements with curved boundaries.
- Various shapes, sizes, and types of elements can be used within the same region allowing the method to make optimal use of the finite elements available.
- Boundary conditions such as discontinuous surface loading and mixed boundary conditions can be handled easily in a natural way.
- The size of the elements can be made smaller and consequently the mesh can be refined in regions where the unknown parameter is expected to vary rapidly.

- The technique can easily lend itself to computer implementation as it involves a large number of repetitive steps.

2.3   Application to optical waveguides

The electromagnetic waveguide problems can be classified into two categories according to their cross-sectional shape.

     (a)   one dimensional
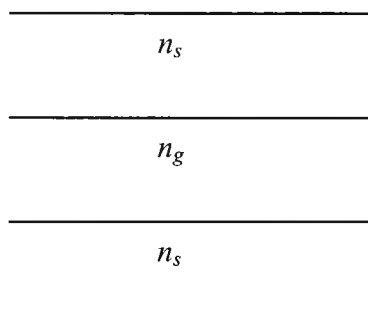
     (b)   two dimensional

Fig. 2.1 *(a)* Planar waveguide   *(b)* Arbitrarily-shaped waveguide
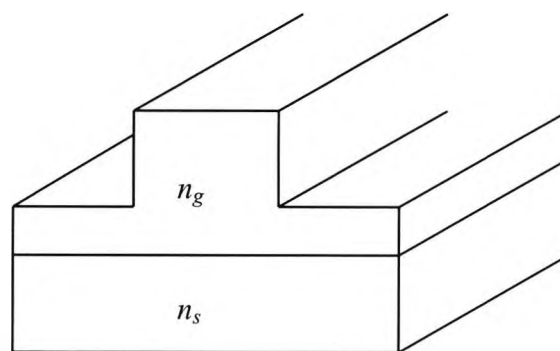
Fig. 2.1*(a)* shows a planar waveguide or an axially symmetrical waveguide which can be treated as a one dimensional problem. **Fig. 2.1***(b)* shows an arbitrary shaped waveguide and it is generally considered as a two dimensional problem. However, choosing the waveguide analysis method as either scalar or vector depends upon the eigenmode property of the waveguide. Hence the scalar wave analysis can be employed for both one and two dimensional problems, but the vector analysis is more accurate and versatile when considering the two dimensional problems. For the planar structures, the scalar analysis will be sufficient. On the other hand, since the guided modes of the waveguide shown in **Fig. 2.1***(b)*, are hybrid modes, vector wave analysis is required for a precise evaluation of their propagation characteristics. Also when evaluating the polarization issues, the more rigorous vector wave analysis is crucial.

Consider the optical waveguide with arbitrary cross-sectional shape, composed of several different materials as shown in **Fig. 2.2**. The materials can be described as

having arbitrary permittivity and permeability tensors ε and μ respectively and they could be linear, nonlinear, isotropic, nonisotropic, or loss less. The waveguide is assumed to be uniform along the propagation direction (*z* axis). Consider light with angular frequency, ω, and propagation constant, β, propagated by such a waveguide whose structure and refractive index are constant in the direction of propagation, i.e. in the positive *z* direction. Assuming the time (*t*) and *z* variation are given by exp(*jωt*) and exp(*-jβz*) functions, respectively, the electric field *E* and the magnetic field *H* can be expressed in the form:

$$E(x,y,z,t) \;=\; E(x,y) \; exp[j(\omega t - \beta z)] \tag{2.1}$$

$$H(x,y,z,t) \;=\; H(x,y) \; exp[j(\omega t - \beta z)] \tag{2.2}$$

E(x,y) and *H(x,y)* are the spatial variations of the electric and magnetic fields, respectively.
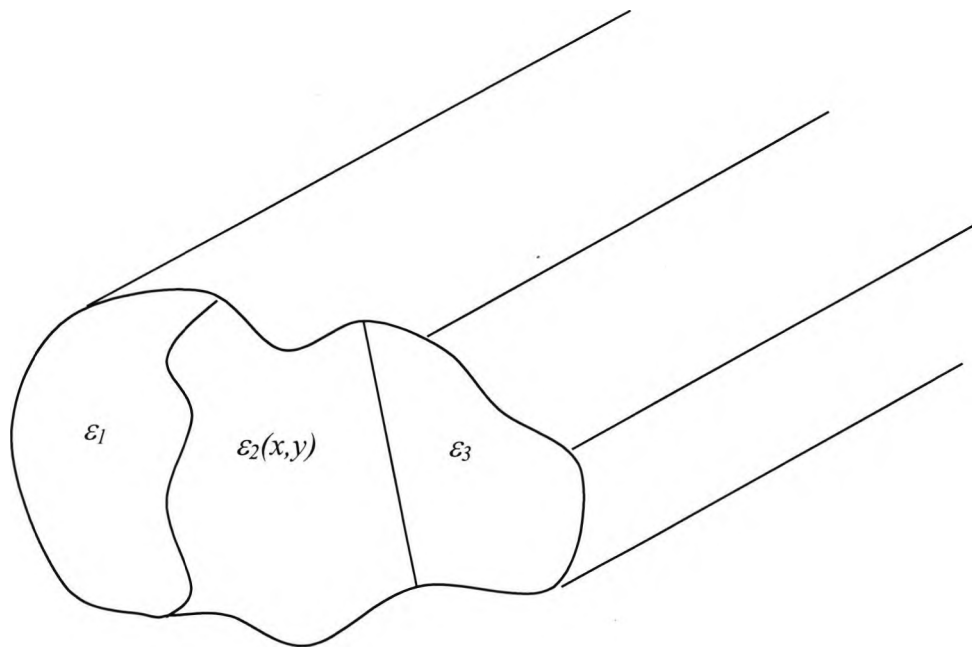
Fig. 2.2 Waveguide with arbitrary cross-sectional shape, consisting of several regions of different materials.

2.4 Basic equations for lightwaves

This section discusses the fundamentals of Maxwell's equations and the boundary conditions, which govern the optical waveguide phenomenon. Also, in order to employ the finite element method in the optical waveguide analysis problems, the consideration of above mentioned equations is necessary.

2.4.1 Maxwell's equations

Light is an electromagnetic wave phenomenon. Its magnetic field is represented by four electromagnetic field vectors and they can be expressed by Maxwell's equations. The equations can be written in both differential and integral forms. However, in this thesis they are presented only in differential form, as they lead to differential equations to be used by the finite element method.

For general time-varying electromagnetic fields, the differential form of Maxwell's equations:

$$\nabla \times \boldsymbol{E} = \frac{-\partial \boldsymbol{B}}{\partial t} \qquad \text{(Faraday's law)} \qquad (2.3)$$

$$\nabla \times \boldsymbol{H} = \frac{\partial \boldsymbol{D}}{\partial t} + \boldsymbol{J} \qquad \text{(Ampere's law)} \qquad (2.4)$$

$$\nabla \cdot \boldsymbol{D} = \rho \qquad \text{(Gauss's law)} \qquad (2.5)$$

$$\nabla \cdot \boldsymbol{B} = 0 \qquad \text{(Gauss's law for magnetics)} \qquad (2.6)$$

$\boldsymbol{E}$ = electric field intensity (volts/meter)

$\boldsymbol{H}$ = magnetic field intensity (amperes/meter)

$\boldsymbol{D}$ = electric flux density (coulombs/meter^2)

$\boldsymbol{B}$ = magnetic flux density (webers/meter^2)

$\boldsymbol{J}$ = electric current density (amperes/meter^2)

ρ = electric charge density (coulombs/meter^3)

The following current continuity equation (or the conservation of charge equation) holds for J and the charge density, ρ:

$$\nabla \cdot J = \frac{-\partial \rho}{\partial t} \tag{2.7}$$

The associated constitutive relations for the medium can be written as:

$$D = \varepsilon E \tag{2.8}$$

$$B = \mu H \tag{2.9}$$

where ε is the permittivity and μ is the permeability of the medium.

Let the time dependence be assumed to be $\exp(j\omega t)$ for convenience, where j is the imaginary unit, ω is the radian (angular) frequency, and t is the time. Then with this assumption, all the time derivatives may be replaced by $j\omega$ and the factor $\exp(j\omega t)$ will not be included as this factor always occurs as a common factor in all terms. Hence the differential form of Maxwell's equations becomes:

$$\nabla \times E = -j\omega B \tag{2.10}$$

$$\nabla \times H = j\omega D + J \tag{2.11}$$

$$\nabla \cdot D = \rho \tag{2.12}$$

$$\nabla \cdot B = 0 \tag{2.13}$$

and the continuity equation becomes:

$$\nabla \cdot J = -j\omega \rho \tag{2.14}$$

2.4.2 Boundary conditions

Boundary conditions are conditions that must be met at the boundary surface where two different media come into contact. It is necessary to subject the Maxwell's equations to boundary conditions at surfaces where abrupt changes of the material constants occur. **Fig. 2.3** shows a sketch of such a boundary between two media distinguished by the indices 1 and 2, with the unit normal vector *n* directed from medium 1 to medium 2.

ε_2, μ_2, E_2, H_2 **medium 2**

ε_1, μ_1, E_1, H_1 **medium 1**
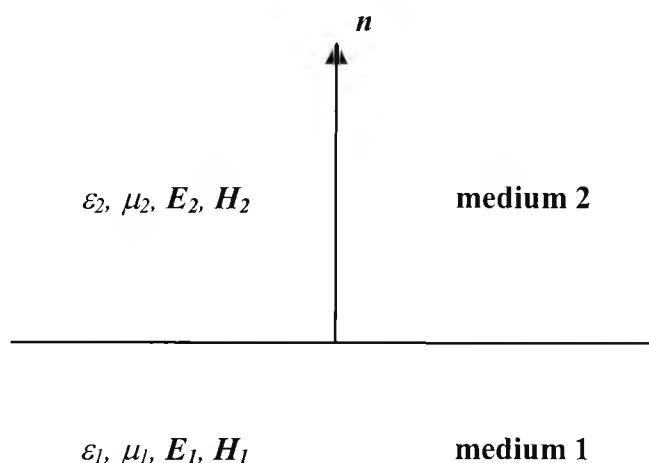
Fig. 2.3 Boundary between two media.

In the absence of surface charges ($\rho = 0$) and surface currents ($J = 0$), the boundary conditions are given as below.

1) The tangential components of the electric field must be continuous.

$$n \times (E_1 - E_2) = 0 \tag{2.15}$$

$$\therefore E_{t1} = E_{t2}$$

2) The tangential components of the magnetic field must be continuous.

$$n \times (H_1 - H_2) = 0 \tag{2.16}$$

$$\therefore H_{t1} = H_{t2}$$

3)   The normal components of the electric flux density must be continuous.

$$\boldsymbol{n} \cdot (\boldsymbol{D}_1 - \boldsymbol{D}_2) = 0 \tag{2.17a}$$

$$\therefore D_{n1} = D_{n2}$$

$$\therefore \varepsilon_1 E_{n1} = \varepsilon_2 E_{n2} \quad \Rightarrow \quad \therefore E_{n1} \neq E_{n2} \tag{2.17b}$$

4)   The normal components of the magnetic flux density must be continuous.

$$\boldsymbol{n} \cdot (\boldsymbol{B}_1 - \boldsymbol{B}_2) = 0 \tag{2.18a}$$

$$\therefore B_{n1} = B_{n2}$$

$$\therefore \mu_1 H_{n1} = \mu_2 H_{n2}$$

since, for most of the optical waveguides, $\mu_{r1} = \mu_{r2} = 1$, where μ_{r1} and μ_{r2} are the relative permeabilities in medium 1 and 2, respectively.

$$\therefore H_{n1} = H_{n2} \tag{2.18b}$$

which implies equality of the magnetic field vectors at the boundary.

There is another boundary condition, which is often used in the idealised case of a perfect electric conductor. This can be considered as an 'electric wall' boundary condition:

$$\boldsymbol{n} \times \boldsymbol{E} = 0 \qquad \text{or} \qquad \boldsymbol{n} \cdot \boldsymbol{H} = 0 \tag{2.19}$$

This boundary condition requires that the magnetic field vector, $\boldsymbol{H}$, must vanish, and ensures the continuity of the electric field vector, $\boldsymbol{E}$, at the boundary.

When one of the two media becomes a perfect magnetic conductor, a 'magnetic wall' condition is imposed as:

$$\boldsymbol{n} \times \boldsymbol{H} = 0 \qquad \text{or} \qquad \boldsymbol{n} \cdot \boldsymbol{E} = 0 \tag{2.20}$$

This condition will ensure the continuity of the magnetic field component, $\boldsymbol{H}$, at the boundary and it vanishes the electric field vector, $\boldsymbol{E}$.

2.5   Variational formulations

Finite element formulations are usually based on the variational or weighted residual approach. The weighted residual approach is more straightforward but however, the variational approach is more advantageous, when only one global parameter, such as the propagation constant is needed. Most of the solutions reported in the literature for a wide variety of electromagnetic field problems have been based on the variational approach. Only this form of formulation will be discussed in this chapter.

There are mainly two types of variational formulations, which can be utilised in finite element method, namely, scalar (Koshiba *et al.*, 1982) and vector formulations (Morishita and Kumagai, 1977; Rahman and Davies, 1984*b*; Koshiba *et al.*, 1985*a*).

2.5.1 The scalar approximation analysis

The scalar approximation formulation is the simplest form of the different variational formulations. This type of formulation gives the waveguide mode by only one field component and it is only valid in situations where the modes can be described as predominantly TE and TM modes. Koshiba *et al.* (Koshiba *et al.*, 1982) described an approximate scalar finite-element program for the analysis of anisotropic waveguides. According to Mabaya *et al.*, (Mabaya *et al.*, 1981) the scalar approximation for the TE modes is based on the following functional:

$$J(\phi) = \iint_{\Omega} \left[\left(\frac{\partial \phi}{\partial x} \right)^2 + \left(\frac{\partial \phi}{\partial y} \right)^2 + \left(\beta^2 - k_0^2 n^2 \right) \phi^2 \right] dxdy \qquad (2.21)$$

where, β is the propagation constant

      n is the refractive index profile

      k_0 is the free-space wavenumber

Here Ω represents the cross sectional domain and the integration is carried out over the domain, Ω. A finite element program based on the above mentioned functional yields β^2 as the eigenvalue of the matrix equation for a given k_0. The eigenvector,

$\phi(x,y)$ is the transverse field distribution, i.e. E_x component for the TE modes.

The scalar approximation for the TM modes is based on the following functional:

$$J(\psi) = \iint_\Omega \frac{1}{n^2}\left[\left(\frac{\partial \psi}{\partial x}\right)^2 + \left(\frac{\partial \psi}{\partial y}\right)^2 + \left(\beta^2 - k_0^2 n^2\right)\psi^2\right]dxdy \qquad (2.22)$$

$\psi(x,y)$ is the transverse field distribution, i.e. H_x field component for the quasi-TM modes. A finite element program based on this functional yields k_0^2 as the eigenvalue of the matrix equation for a given propagation constant, β.

In order to implement the finite element analysis, the primary variables are replaced by a system of discretised variable over the domain of consideration. This is generally done by dividing the entire waveguide cross section into a patchwork of sub regions, called 'elements' usually triangles or quadrilaterals. The finite element mesh (discretisation) consists of elements of various shapes, such as triangles or rectangles of different sizes, that are connected to each other at nodal points on the boundaries of the elements. However, the triangular elements are the basic and much preferred element when analysing electromagnetic waveguide problems, as they are easily adapted to complex shapes. Using many elements, any continuum with a complex boundary and with an arbitrary index distribution can be approximated to such a degree that an accurate analysis can be carried out. The simplest triangular element imposes a linear interpolation between the field values of the vertices of the triangle. However the higher order polynomial interpolation functions can also be used, but the drawback is that the programming effort for those higher order elements is quite large. The unknown field functions at a nodal point are defined by a set of algebraic polynomials over each element, and the field over the guide will be determined by those nodal field values and assumed shape functions. By expressing the fields in terms of nodal values, the resulting field components can be continuous over the whole domain.

To obtain the nodal field values, the usual Rayleigh-Ritz procedure is employed for the stationary solution of the functions with respect to each of the nodal variables. This can be written in a matrix eigenvalue equation:

$$[\mathbf{A}]\{x\} - \lambda[\mathbf{B}]\{x\} = 0 \tag{2.23}$$

where $[\mathbf{A}]$ and $[\mathbf{B}]$ are real symmetric matrices, and $[\mathbf{B}]$ is also positive definite matrix. The eigenvalue λ may be k_0^2 or β^2 depending on the variational formulation and $\{x\}$ is the eigenvectors representing the unknown nodal field values. It is most desirable for the resulting matrix equation to be of this canonical form, to allow for an efficient and robust solution. This equation (2.23) can be solved by one of various standard subroutines to obtain different eigenvectors and eigenvalues.

The most serious difficulty in using the finite element method for open dielectric waveguides is the appearance of the spurious or non physical modes. That means the eigenvectors and eigenvalues of the matrix eigenvalue problem do not represent physical modes of the waveguide but are spurious results introduced by the employed numerical technique. The reason for the appearance of spurious modes is probably the fact that the functional is not positive definite (Csendes and Silvester, 1970). The appearance of these spurious modes does not affect the calculation of the lowest propagating mode, since the lowest order mode usually corresponds to the first positive eigenvalue of the matrix equation. However, to compute higher order modes, it becomes more difficult and very cumbersome to distinguish between the spurious and the physical modes of the guide.

On the other hand, the scalar approximation does not suffer from this difficulty, since the two scalar functionals are positive definite and therefore all the eigenvalues are positive, each one corresponding to a physical mode of the guide. Consequently, the higher order modes of the guide can be easily computed without any difficulty. Another advantage is that with this method the number of matrix elements to be solved is reduced compared to vector finite element method and therefore a reduction of the computer time can be achieved.

2.5.2 The vector formulations

Vector formulations of the Maxwell equations provide a means for solving wave propagation problems where all six electromagnetic field components are present. The single scalar formulation is inadequate for the inherently hybrid mode situation of anisotropic or inhomogeneous waveguide problems. Since the guided modes of a 3-D optical waveguide (**Fig. 2.1(*b*)**) are hybrid modes, vector wave analysis is required for a precise evaluation of their propagation characteristics. They also provide better solution convergence for some modal types as compared to corresponding scalar formulations. However, as will be seen later, in some vector wave analysis formulations, the so-called spurious or non-physical solutions, which appear mixed with the correct solutions, are inevitably generated.

There are many types of finite element methods for such vector wave analysis, depending on which electromagnetic field component is used for formulation. They include:

- Finite element method using longitudinal (axial) electromagnetic (**E** and **H**) field components, $(E_z + H_z)$,

- Finite element method using transverse electromagnetic field components, $(E_t + H_t)$,

- Finite element method using transverse electric field components, (E_t),

- Finite element method using transverse magnetic field components, (H_t),

- Finite element method using the three electric field components, (**E**),

- Finite element method using the three magnetic field components, (**H**),

- Finite element method using the six electromagnetic field components, (**E+H**).

The finite element formulation using the axial component of the fields, E_z and H_z, was the first vector finite element method to be developed and it has been used to solve many different types of guiding structures problems (Csendes and Silvester, 1970; Ikeuchi *et al.*, 1981; Ahmed and Daly, 1969; Wu and Chen, 1985). This E_z-H_z formulation (Mabaya *et al.*, 1981) cannot treat general anisotropic problems without destroying the canonical form of the eigenvalue equation (2.23). Also for a waveguide with arbitrary dielectric distribution, satisfying the boundary conditions using this formulation can be quite difficult. This formulation was developed for microwave

guides where TE or TM modes can have either H_z or E_z. However, the fundamental disadvantage of this method for optical waveguide problems is that it considers the axial E_z-H_z components of the fields, which are the least important components of the six-vector field. This formulation is also affected by the spurious solutions and a possible solution to the problem is presented by Mabaya *et al.* (Mabaya *et al.*, 1981) by explicitly enforcing the continuity of the tangential components of the transversal fields, at the interfaces. However, the complexity of the numerical operations that have to be done for enforcing those continuity conditions is enormous.

Angkaew *et al.* (Angkaew *et al.*, 1987) formulated a variational expression suited for the finite element method in terms of the transverse electric (**E**) and magnetic (**H**) field components. Although a complete discrimination of the spurious mode solutions from guided mode solutions was confirmed, this transverse formulation is computationally costly as this involves additional differentiation (Ohtaka *et al.*, 1976), which in turn would be particularly disadvantageous with finite element approach.

Berk (Berk, 1956) derived a number of vector variational formulations in the form of a Rayleigh quotient for loss-free anisotropic microwave waveguides and resonators in terms of the **H** field, the **E** field or a combination of both. Later, Morishita and Kumagai (Morishita and Kumagai, 1977) derived similar vector variational formulations.

A vector **E** field formulation (3 component formulation) of the Maxwell's equations has been applied by English and Young (English and Young, 1971) to analyse cylindrical waveguide problems. The vector **E** formulation is valid for general anisotropic loss-less waveguide problems, and has been applied for the solution of various types of optical waveguides (Hano, 1984; Koshiba *et al.*, 1985*a*; Koshiba *et al.*, 1986). But for this **E**-field formulation (English and Young, 1971) the natural boundary condition is that of a magnetic wall, which cannot be left free for an electric wall boundary. So for the electric wall situation it needs to be specifically implemented (i.e. *n* × **E** = 0). As this necessary boundary condition must be imposed on any conducting boundaries, it is an added difficulty to implement that boundary condition on arbitrarily shaped guide walls. Another disadvantage is that it needs

special consideration to enforce the continuity of the tangential field components at the dielectric interface.

A vector formulation, which is formulated in terms of all three components of **H**, has the advantage over all other formulations. This vector **H**-field formulation (Rahman and Davies, 1984*b*; Rahman and Davies, 1984*c*; Koshiba *et al.*, 1985*b*) is valid for general anisotropic problems with a non-diagonal permittivity tensor. The natural boundary condition is that of an electric wall ($n \times \mathbf{E} = 0$, $n \cdot \mathbf{H} = 0$), so for the arbitrary conducting guide walls it can be left free. In dielectric waveguides, the permeability is always assumed to be that of free space. Therefore, each component of **H** is continuous in the whole region and thus the variation of the refractive index over the waveguide cross section does not need to impose interface boundary conditions. The total vector **E**+**H** formulation (Svedin, 1989) does not have much advantage over the vector **H** field formulation since all the six components are needed for the formulation giving rise to a complicated problem.

2.5.3 The vector H-field formulation

For general optical waveguide problems, where the modes are hybrid, the transverse components are the dominant and the materials have general anisotropy, the vector **H**-field formulation appears to be the most accurate and versatile method (Rahman and Davies, 1984*b*). On the other hand, various ways of suppressing or eliminating spurious solutions have been discovered for this method. For an abrupt discontinuity in the permittivity in an inhomogeneous medium there is an abrupt change in the electric field, **E**. In such cases, it is advantageous to solve for the values of **H** at the nodal points. This formulation is also very important and useful when analysing various active and passive integrated optic structures.

The full vector **H**-field formulation can be written as (Rahman and Davies, 1984*a*; Berk, 1956):

$$\omega^2 = \frac{\int (\nabla \times \mathbf{H})^* \cdot \hat{\varepsilon}^{-1} \cdot (\nabla \times \mathbf{H}) \, d\Omega}{\int \mathbf{H}^* \cdot \hat{\mu} \cdot \mathbf{H} \, d\Omega} \qquad (2.24)$$

where $\overset{\wedge}{\varepsilon}$ and $\overset{\wedge}{\mu}$ are the general anisotropic permittivity and permeability of the loss-free medium, respectively, and the integration is carried out over the waveguide cross section, Ω. To obtain a stationary solution of the functional (2.24), this is minimised with respect to each of the variables, which are the unknown nodal field components H_x, H_y and H_z. This minimisation leads to a matrix eigenvalue equation as stated in equation (2.23), where [**A**] is a complex Hermitian matrix and [**B**] is a real symmetric and positive-definite matrix. Because of the general 90° phase difference between the axial and transverse components of **H** (Konrad, 1977) the Hermitian matrix [**A**] can be transformed to a real symmetric matrix for a loss-less problem. In general, the matrices [**A**] and [**B**] are quite sparse. The eigenvectors $\{x\}$ represent the unknown field components at the nodal points for different modes with λ as their corresponding eigenvalues and also λ is proportional to ω^2. In order to obtain a solution for a given wavelength, the propagation constant, β value has to be changed iteratively until the output eigenvalue corresponds to that wavelength. By varying β over the range of interest, it is possible to calculate the dispersion characteristics for the various modes. However, the appearance of spurious solution is a disadvantage and how these spurious solutions can be avoided will be discussed later.

2.5.4 Natural boundary conditions

The term "natural boundary condition" usually arises in the calculus of variations, and since the finite element method is fundamentally one of minimisation of an error functional, the term arises also in this context. The boundary condition, which is automatically satisfied in the variational procedure, is called the 'natural boundary condition'. In variational formulations these can be automatically satisfied, if left free.

The scalar functional defined in equation (2.21) has the continuity of $\dfrac{\partial \phi}{\partial \hat{n}}$ as the natural boundary condition, and the functional (2.22) has the continuity $\left(\dfrac{1}{n^2}\right)\left(\dfrac{\partial \psi}{\partial \hat{n}}\right)$ as the natural boundary condition, where $\hat{n}$ is the outward normal unit vector.

The vector **H**-field formulation described in equation (2.24), has the natural boundary condition of an electric wall, i.e. $n \cdot \mathbf{H} = 0$. Therefore there is no need to force any boundary condition on conducting guide walls. But for regular shaped waveguides, and at the symmetric walls (if applicable) we may enforce the natural boundary condition to reduce matrix problem size. However, it may be necessary to analyse the structure with complementary symmetry conditions to obtain all the modes, although the exploitation of the symmetry greatly reduces the computational cost.

2.6 Formulation of the finite element method

The basic idea of the finite element method is to find the solution of a complicated problem by replacing it by a simpler one. The differential operator equations which describe the physical problem are replaced by an appropriate extremum functional *J*, which is the variational for the desired quantity. The problem can be regarded as obtaining the solution **H** over a specified region in the transverse plane so that the boundary conditions and also the extremum requirement are satisfied. The axial dependence is assumed in the form exp(*-jβz*), and the transverse plane is used for the discretisation.

2.6.1 Discretisation of the domain

The discretisation of the domain into sub-regions (finite elements) is the first step in the finite element method. The shapes, sizes, number and configurations of the elements have to be chosen carefully such that the original body or domain is simulated as closely as possible without increasing the computational effort needed for the solution. Each element is essentially a simple unit within which the unknown can be described in a simple manner. There are various types of elements available for use in finite element formulations. These elements can be classified as one, two and three dimensional elements. When the geometry and material properties can be described in terms of only one spatial coordinate, then the one-dimensional element can be used. However, when the configuration and other details of the problem can be described in terms of two independent spatial coordinates, the two-dimensional elements shown in **Fig. 2.4** can be used. The basic and the simplest element useful for

two-dimensional analysis is the triangular element. The smaller the size of the element, the more accurate is the final solution. Finite element discretisation of an irregular waveguide, using triangular elements is shown in **Fig. 2.5**.

By dividing the waveguide cross section into triangular elements, the unknown **H** is also considered as to be discretised into corresponding sub-regions. These elements are easier to analyse rather than analysing the distribution over the whole cross section. As shown in **Fig. 2.5** the transverse plane is covered with a grid of discrete nodes which are the vertices of each triangular element. The values of **H** at these nodal points are the basic unknowns. The intersections of the sides of the triangular elements are called the nodal lines.

triangle   rectangle

quadrilateral   parallelogram
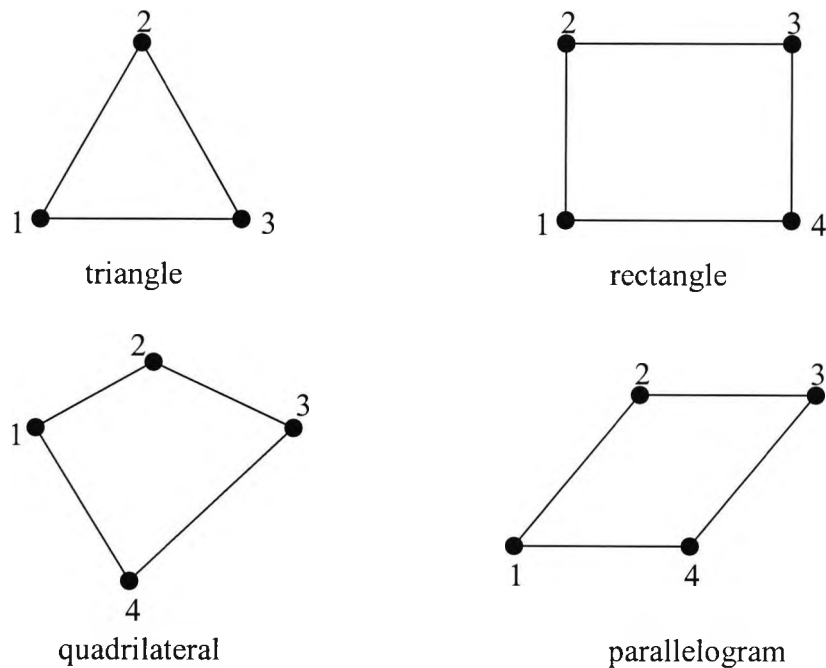
Fig. 2.4 Finite elements in two dimensions.
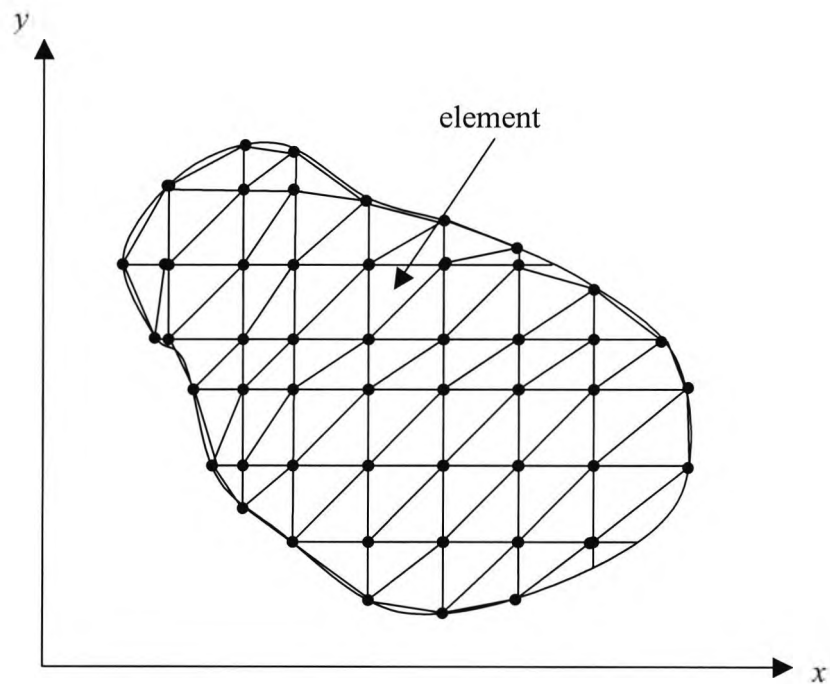
Fig. 2.5 Waveguide cross section subdivided into finite elements.

2.6.2 Shape functions

In two-dimensional problems, the element assumes a linear interpolation between the field values at the vertices of the triangle. Within each element the unknown field **H**, is approximated by means of suitably chosen set of polynomials. These functions are called "shape functions". For the simplest triangular element the interpolation polynomial should include terms containing both x and y, but not only one of them, in addition to the constant term, giving a first order degree 'complete' polynomial. Omitting any term from the polynomial would yield an 'incomplete' polynomial. The field variable representation within an element, and hence the polynomial, should not change with a change in the local coordinate system. In order to achieve this 'geometric isotropy', the polynomial should be complete according to the Pascal's triangle shown in **Fig. 2.6**.

The final consideration in selecting the order of the interpolation polynomial is to make the total number of terms involved in the polynomial equal to the number of nodal degrees of freedom of the element. For example, the first degree polynomial

involves three coefficients and so can be expressed in terms of three nodal values at the triangle vertices. The second degree polynomial needs six coefficients and can similarly be expressed in terms of values of six nodes as shown in **Fig. 2.6**.

	Degree of Polynomial	No. of terms in the polynomials	Element with nodes
1	1	3	
$x \quad y$			
$x^2 \quad xy \quad y^2$	2	6	
$x^3 \quad x^2y \quad xy^2 \quad y^3$	3	10	
$x^4 \quad x^3y \quad x^2y^2 \quad xy^3 \quad y^4$	4	15	
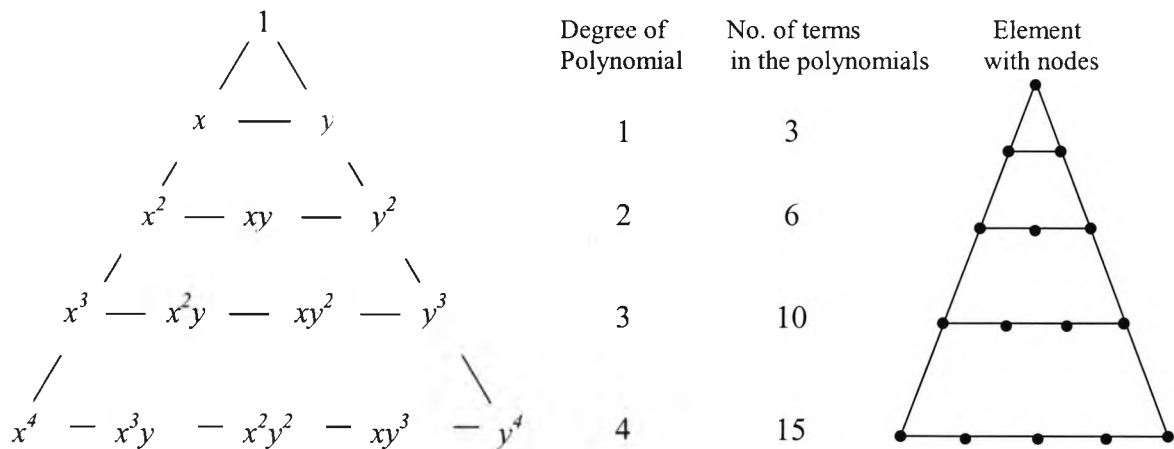
Fig. 2.6 Pascal's triangle for complete polynomials in two dimensions.

The continuous field function $\phi(x,y)$ in the problem domain may be replaced by a set of discrete values (ϕ_i, $i = 1,2,3,\ldots,m$), where m is the total number of nodes. This function will be continuous across the adjacent triangles. To be admissible functions, they must satisfy some specific conditions between the elements; usually the continuity of the field across the boundaries is preferred.

Fig. 2.7 shows a typical first order triangular element. Inside each first order triangular element ϕ is interpolated continuously. This can be achieved by introducing the interpolation functions, $N_i(x,y)$. Let $\phi_e(x,y)$ is the field inside an element. Using these interpolation functions, for $i = 3$, it can be written as:

$$\phi_e(x,y) = \sum_{i=1}^{3} N_i(x,y) \cdot \phi_i \tag{2.25}$$

where ϕ_i are the nodal field values.

Since eq. (2.25) describes the shape of an element, and therefore, the $N_i(x,y)$ are called 'shape functions'. Eq. (2.25) can also be written in matrix form:

$$\phi_e(x,y) = \begin{bmatrix} N_1 & N_2 & N_3 \end{bmatrix} \begin{Bmatrix} \phi_1 \\ \phi_2 \\ \phi_3 \end{Bmatrix} \qquad (2.26)$$

$$\phi_e(x,y) = [N]\{\phi_e\} \qquad (2.27)$$

where $[N]$ is the shape function matrix and the column vector $\{\phi_e\}$ is the vector corresponding to the field values at the 3 vertices of the triangular element (i.e. the nodal field values).
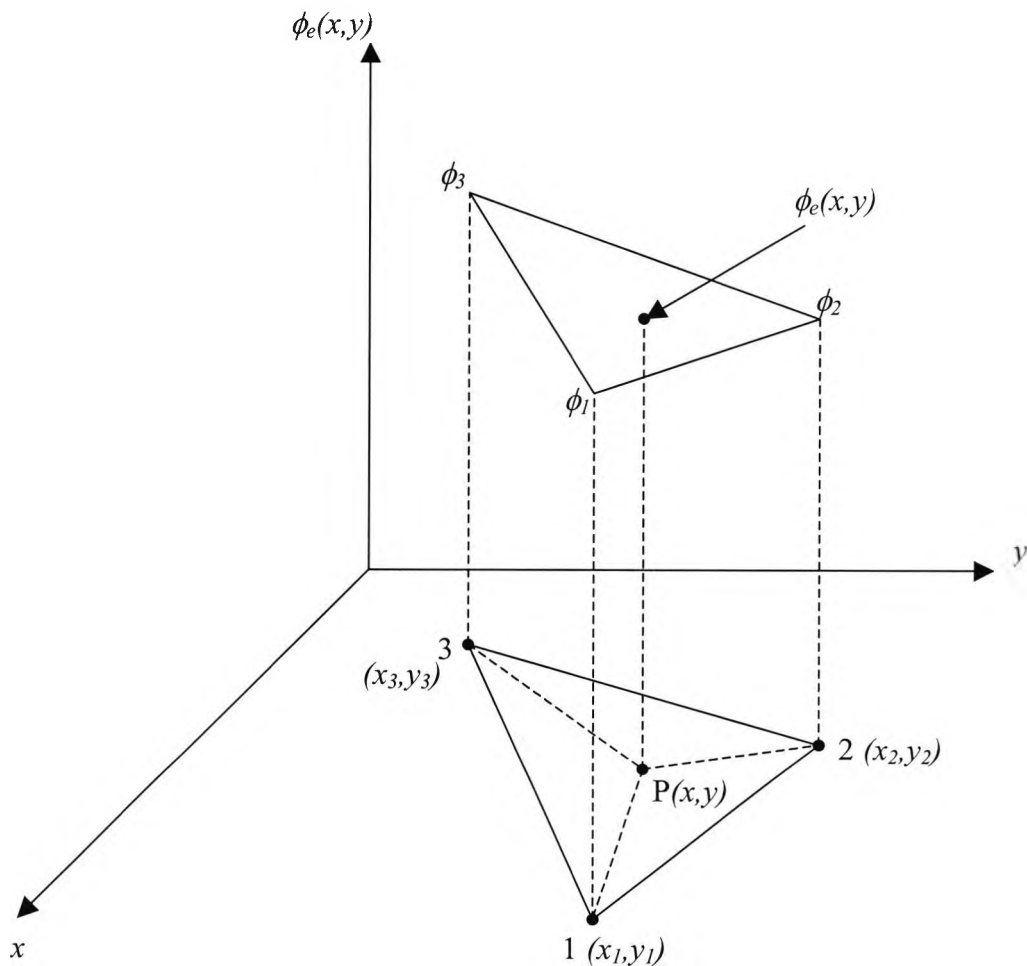
Fig. 2.7 First order triangular element.

In order to obtain the shape functions, $N_i(x,y)$, $i = 1,2,3$, first a linear approximation of the field inside an element is considered:

$$\phi_e(x, y) = \alpha_1 + \alpha_2 x + \alpha_3 y \tag{2.28}$$

where α_1, α_2, α_3 are constants.

By rewriting the approximation (2.28), such that it satisfies the conditions:

$$\phi_e(x_i, y_i) = \phi_i \qquad i = 1,2,3 \tag{2.29}$$

where (x_i, y_i) ($i = 1,2,3$) are the (global) coordinates of the three vertices of the triangle.

Then, the nodal field values ϕ_i can be expressed as:

$$\phi_1 \equiv \phi_e(x_1, y_1) = \alpha_1 + \alpha_2 x_1 + \alpha_3 y_1$$

$$\phi_2 \equiv \phi_e(x_2, y_2) = \alpha_1 + \alpha_2 x_2 + \alpha_3 y_2 \tag{2.30}$$

$$\phi_3 \equiv \phi_e(x_3, y_3) = \alpha_1 + \alpha_2 x_3 + \alpha_3 y_3$$

In matrix form:

$$\begin{Bmatrix} \phi_1 \\ \phi_2 \\ \phi_3 \end{Bmatrix} = \begin{bmatrix} 1 & x_1 & y_1 \\ 1 & x_2 & y_2 \\ 1 & x_3 & y_3 \end{bmatrix} \begin{Bmatrix} \alpha_1 \\ \alpha_2 \\ \alpha_3 \end{Bmatrix} \tag{2.31}$$

By solving the above matrix, the constants α_1, α_2, α_3 can be determined in terms of ϕ_i, $i = 1,2,3$:

$$\alpha_1 = \frac{1}{2A_e} [\phi_1(x_2 y_3 - x_3 y_2) + \phi_2(x_3 y_1 - x_1 y_3) + \phi_3(x_1 y_2 - x_2 y_1)]$$

$$\alpha_2 = \frac{1}{2A_e} [\phi_1(y_2 - y_3) + \phi_2(y_3 - y_1) + \phi_3(y_1 - y_2)] \tag{2.32}$$

$$\alpha_3 = \frac{1}{2A_e} [\phi_1(x_3 - x_2) + \phi_2(x_1 - x_3) + \phi_3(x_2 - x_1)]$$

where A_e is the area of the triangular element given by,

$$A_e = \frac{1}{2} \begin{vmatrix} 1 & x_1 & y_1 \\ 1 & x_2 & y_2 \\ 1 & x_3 & y_3 \end{vmatrix} = \frac{1}{2}(x_2 y_3 - x_3 y_2) + (x_3 y_1 - x_1 y_3) + (x_1 y_2 - x_2 y_1) \qquad (2.33)$$

Substituting for α_i from eq. (2.32) into eq. (2.28) and rearranging yields the following equation,

$$\phi_e(x, y) = N_1(x, y).\phi_1 + N_2(x, y).\phi_2 + N_3(x, y).\phi_3$$

or

$$\phi_e(x, y) = [N]\ \{\phi_e\} \qquad (2.34)$$

which is exactly the same matrix equation given by eq. (2.27), and $N_i(x,y)$, $i = 1,2,3$, are shape functions given by the matrix notation (Reddy, 1984; Davies, 1989):

$$\{N\}^T = \begin{bmatrix} N_1 \\ N_2 \\ N_3 \end{bmatrix} = \frac{1}{2A_e} \begin{bmatrix} x_2 y_3 - x_3 y_2 & y_2 - y_3 & x_3 - x_2 \\ x_3 y_1 - x_1 y_3 & y_3 - y_1 & x_1 - x_3 \\ x_1 y_2 - x_2 y_1 & y_1 - y_2 & x_2 - x_1 \end{bmatrix} \begin{bmatrix} 1 \\ x \\ y \end{bmatrix} \qquad (2.35)$$

where T denotes the transpose. This shape function matrix can also be written as:

$$\{N\}^T = \begin{bmatrix} N_1 \\ N_2 \\ N_3 \end{bmatrix} = \begin{bmatrix} a_1 + b_1 x + c_1 y \\ a_2 + b_2 x + c_2 y \\ a_3 + b_3 x + c_3 y \end{bmatrix} \qquad (2.36)$$

and a_i, b_i, c_i ($i = 1,2,3$) are the constants calculated as:

$$a_1 = \frac{x_2 y_3 - x_3 y_2}{2A_e} \qquad (2.37)$$

$$b_1 = \frac{y_2 - y_3}{2A_e} \qquad (2.38)$$

$$c_1 = \frac{x_3 - x_2}{2A_e} \qquad (2.39)$$

Similarly, a_2, b_2, c_2, a_3, b_3, and c_3 can be calculated by cyclic exchange of $1 \rightarrow 2 \rightarrow 3$ in equations (2.37) to (2.39).

Consider a typical point $P(x,y)$ inside the triangular element as shown in **Fig. 2.7**. By carefully considering the eq. (2.35), the shape functions N_i can also be denoted by using the areas of the triangles as below:

$$N_1 = \frac{\text{area of the sub triangle P23}}{\text{area of the full traingle 123}} \qquad (2.40)$$

Similarly N_2 and N_3 can be defined, and immediately it follows that N_i has the following property:

$$\sum_{i=1}^{3} N_i = 1 \qquad (2.41)$$

Also it can be noted that, when the shape function N_1 is evaluated at node $1(x_1, y_1)$, it gives the value 1, and the value 0 at nodes 2 and 3 and at all points on the line passing through these nodes. Therefore it is the unique first-degree interpolation function for node 1. Similarly the shape functions N_2 and N_3 gives a value of 1 at nodes 2 and 3 respectively, and 0 at other nodes.

2.6.3 Element and global matrices

This section explains the derivation of the element and global matrices based on the full vectorial **H**-field variational expression eq. (2.24). Within each triangular element, the three unknown **H**-field components, H_x, H_y and H_z of the magnetic field can be expressed as;

$$H_x(x,y) = \begin{bmatrix} N_1 & N_2 & N_3 \end{bmatrix} \begin{Bmatrix} H_{x1} \\ H_{x2} \\ H_{x3} \end{Bmatrix} \tag{2.42a}$$

$$H_y(x,y) = \begin{bmatrix} N_1 & N_2 & N_3 \end{bmatrix} \begin{Bmatrix} H_{y1} \\ H_{y2} \\ H_{y3} \end{Bmatrix} \tag{2.42b}$$

$$H_z(x,y) = \begin{bmatrix} N_1 & N_2 & N_3 \end{bmatrix} \begin{Bmatrix} H_{z1} \\ H_{z2} \\ H_{z3} \end{Bmatrix} \tag{2.42c}$$

where, H_{xi}, H_{yi} and H_{zi} ; $i = 1,2,3$, represents the x, y and z components of the nodal magnetic fields. Hence, the element magnetic field vector $[H]_e$ can be expressed by combining equations (2.42a)-(2.42c);

$$[H]_e = \begin{bmatrix} H_x(x,y) \\ H_y(x,y) \\ H_z(x,y) \end{bmatrix} = \begin{bmatrix} N_1 & N_2 & N_3 & 0 & 0 & 0 & 0 & 0 & 0 \\ 0 & 0 & 0 & N_1 & N_2 & N_3 & 0 & 0 & 0 \\ 0 & 0 & 0 & 0 & 0 & 0 & N_1 & N_2 & N_3 \end{bmatrix} \begin{Bmatrix} H_{x1} \\ H_{x2} \\ H_{x3} \\ H_{y1} \\ H_{y2} \\ H_{y3} \\ H_{z1} \\ H_{z2} \\ H_{z3} \end{Bmatrix}$$

$$\tag{2.43}$$

Equation (2.43) can also be written as;

$$[H]_e = [\mathbf{N}] \{H\}_e \tag{2.44}$$

where $\{H\}_e$ is the column vector representing the three components of the nodal field values in the element and $[\mathbf{N}]$ is the shape function matrix.

Also by substituting (2.44), the $(\nabla \times H)_e$ factor within the element can be written as;

$$\left(\nabla \times H\right)_e = \nabla \times [\mathbf{N}]\{H\}_e = \begin{bmatrix} 0 & \dfrac{-\partial}{\partial z} & \dfrac{\partial}{\partial y} \\[8pt] \dfrac{\partial}{\partial z} & 0 & \dfrac{-\partial}{\partial x} \\[8pt] \dfrac{-\partial}{\partial y} & \dfrac{\partial}{\partial x} & 0 \end{bmatrix} [\mathbf{N}]\{H\}_e = [Q]\{H\}_e \qquad (2.45)$$

where the matrix $[Q]$ can be written as;

$$[Q] = \begin{bmatrix} [0] & \dfrac{-\partial[N]}{\partial z} & \dfrac{\partial[N]}{\partial y} \\[8pt] \dfrac{\partial[N]}{\partial z} & [0] & \dfrac{-\partial[N]}{\partial x} \\[8pt] \dfrac{-\partial[N]}{\partial y} & \dfrac{\partial[N]}{\partial x} & [0] \end{bmatrix} = \begin{bmatrix} [0] & j\beta[N] & \dfrac{\partial[N]}{\partial y} \\[8pt] -j\beta[N] & [0] & \dfrac{-\partial[N]}{\partial x} \\[8pt] \dfrac{-\partial[N]}{\partial y} & \dfrac{\partial[N]}{\partial x} & [0] \end{bmatrix} \qquad (2.46)$$

where $\qquad [0] = \begin{bmatrix} 0 & 0 & 0 \end{bmatrix}$ $\qquad\qquad\qquad\qquad\qquad$ (2.47)

$$[N] = \begin{bmatrix} N_1 & N_2 & N_3 \end{bmatrix} \qquad (2.48)$$

and the following arises by using the differentiations of equation (2.36),

$$\frac{\partial[N]}{\partial x} = \begin{bmatrix} b_1 & b_2 & b_3 \end{bmatrix} \qquad (2.49)$$

$$\frac{\partial[N]}{\partial y} = \begin{bmatrix} c_1 & c_2 & c_3 \end{bmatrix} \qquad (2.50)$$

The values of the constants b_1, b_2, b_3, c_1, c_2 and c_3 were given in equations (2.38) and (2.39).

By substituting the terms in equations (2.44) and (2.45) into the equation (2.24), the vector **H**-field formulation functional for an element can be obtained as;

$$J_e = \int_{\Delta} \{H\}_e^T [Q]^* \stackrel{\wedge}{\varepsilon}{}^{-1} [Q]\{H\}_e \, d\Omega - \omega^2 \int_{\Delta} \{H\}_e^T [\mathbf{N}]^T \stackrel{\wedge}{\mu} [\mathbf{N}]\{H\}_e \, d\Omega \qquad (2.51)$$

Δ represents the integration over the triangular element domain. T and $*$ denote the transpose and the complex conjugate transpose, respectively.

If the material is isotropic, then the ε is a scalar value. Here it is assumed that the ε is a scalar quantity. If ε is a tensor, then it should be represented by a 3×3 matrix and the inverse of the matrix should be implemented.

The total function, J, associated with the whole cross section of the waveguide can be obtained by summing J_e of all the individual elements,

$$J = \sum_{e=1}^{n} J_e \qquad (2.52)$$

where n is the number of elements.

The minimisation of the functional given in equation (2.52) is achieved by differentiating with respect to the field nodal values and equating it to zero as below;

$$\frac{\partial J}{\partial \{H\}_e} = 0 \qquad e = 1,2,\ldots\ldots,n \qquad (2.53)$$

This minimisation leads to the following eigenvalue equation;

$$[\mathbf{A}]\{H\} - \omega^2 [\mathbf{B}]\{H\} = 0 \qquad (2.54)$$

where $\qquad [\mathbf{A}] = \sum_{e=1}^{n} [\mathbf{A}]_e = \sum_{e=1}^{n} \int_{\Delta} \varepsilon^{-1} [Q]^* [Q] \, d\Omega \qquad (2.55)$

$$[\mathbf{B}] = \sum_{e=1}^{n} [\mathbf{B}]_e = \sum_{e=1}^{n} \int_{\Delta} \mu [\mathbf{N}]^T [\mathbf{N}] \, d\Omega \qquad (2.56)$$

Matrix $\{H\}$ contains all the **H**-field nodal values over the whole cross section of the waveguide considered. $[A]_e$ and $[B]_e$ represent the element matrices. The assemblage of all the element matrices $[A]_e$ and $[B]_e$ over the whole cross section result in the so called global matrices of the eigenvalue equation, given by $[\mathbf{A}]$ and $[\mathbf{B}]$, respectively. The calculations of the element matrices, $[A]_e$ and $[B]_e$, are implemented in **Appendix 1**.

When solving waveguide problems by using finite elements, the key factor affecting storage requirements and computational effort is the choice of algorithm to solve the matrix equation. The global matrices $[\mathbf{A}]$ and $[\mathbf{B}]$ shown in equation (2.55) and (2.56) are highly sparse. The sparsity increases with the order of the matrices and decreases with the polynomial order of the shape functions. The main advantage of using the higher order basis functions for the fields is that they give a more accurate solution for a given matrix order, but involves an increased programming effort, particularly when considering anisotropic materials, infinite elements and penalty functions. (A brief explanation of infinite elements and the method of penalty function will be outlined in the next sections.) Another disadvantage when using higher order polynomials for a given matrix order is the increase in the density of the matrix. It must be emphasised here that the trade-off and the optimum choice between low- and high-order polynomials depends crucially on the matrix algorithm used.

2.7   Analysis of infinite elements

In open type integrated optic waveguides, the finite fields exist in the region outside the guide. Outside the guide core, the field decays roughly in an exponential manner. Therefore the region of interest extends to infinity and this extension of the domain is particularly important for the solutions close to cut off. When a waveguide is operating near the cut off region, the fields decay slowly and extend a large distance away from the guide core, and some proper account of these fields must be made. Analysis of unbounded field problems is not possible with orthodox finite elements (as shown in **Fig. 2.8**), as the region of consideration cannot extend up to infinity. Consideration of an artificial electric or magnetic wall boundary condition is the simplest approximation to this problem (Mabaya *et al.*, 1981), but this either

introduces a significant error or needs to consider a large active domain to minimize this perturbation error. Another technique (Ikeuchi *et al.*, 1981) involves shifting the virtual boundary wall to satisfy a given criterion for the maximum field strength at that wall.

Yeh *et al.* (Yeh *et al.*, 1979) have considered an exponential decay outside the core by using some boundary elements. However, because of the mixture of coordinate systems, their method lacks continuity of field over the problem domain. Rahman and Davies (Rahman and Davies, 1984*b*) have developed an infinite element approach, which is found to be very useful when extending the domain of interest to infinity as shown in **Fig. 2.8**. This method is quite simple to implement, and it does not increase the order of the matrices.

An infinite element is a finite element that indeed extends to infinity. The shape functions of such an element, substitutes the shape functions of the outer boundary of the orthodox elements and should decay exponentially in the direction, which the field extends to infinity. The elements can be extended to either one or both transverse directions.
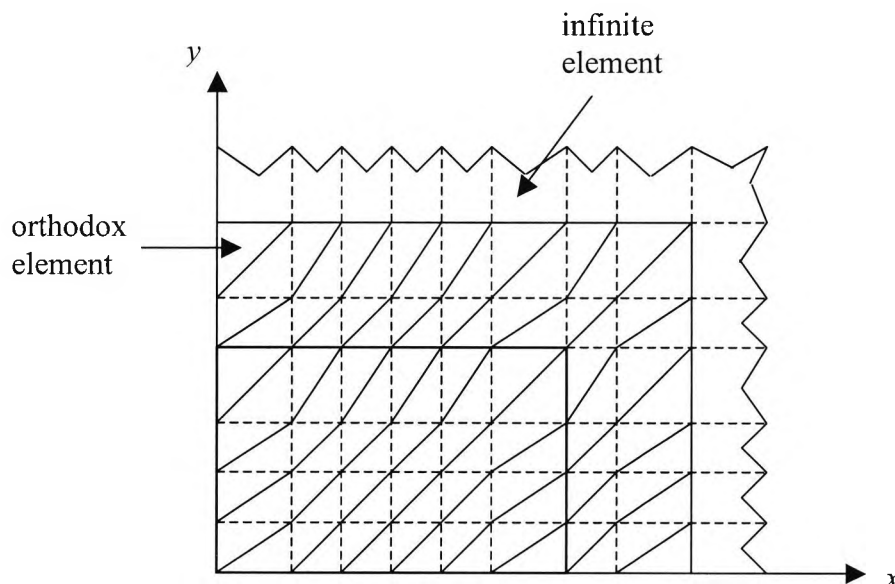
Fig. 2.8 Rectangular dielectric waveguide cross section discretised into orthodox and infinite elements.
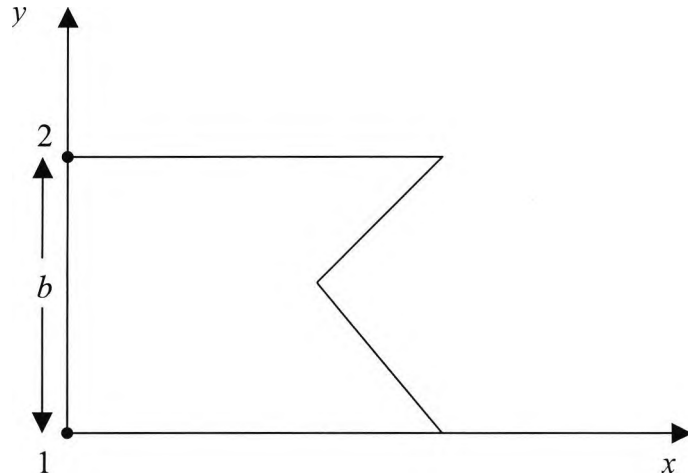
Fig. 2.9 Infinite element extending to infinity in the x-direction.

When extending in one transverse direction, we consider an exponential shape function in that direction and conventional polynomial shape function in the other direction. In Cartesian coordinates, if an infinite element is extending to infinity in the positive x-direction, as shown in **Fig. 2.9**, we can assume exponential decay in x and conventional shape function dependence in the y-direction. The shape function can then be written as follows:

$$N_i(x,y) = f_i(y) \cdot exp\,(-x\,/\mathrm{L}) \tag{2.57}$$

where L is the decay length.

Consider any field component, such as, H_x and it can be expressed as:

$$H_x = f(x,y)H_{xi} = \sum_{i=1}^{2} N_i(x,y).H_{xi} \tag{2.58}$$

where H_{x1} and H_{x2} are the x-components of the magnetic field of nodes 1 and 2, respectively.

$$H_x = f_1(y).e^{(-x/L)}.H_{x1} + f_2(y).e^{(-x/L)}.H_{x2} \qquad (2.59)$$

$$= \begin{bmatrix} N_1 & N_2 \end{bmatrix} \begin{Bmatrix} H_{x1} \\ H_{x2} \end{Bmatrix}$$

For the simplest case, the shape functions, N_1 and N_2 can be written as:

$$N_1 = \frac{y}{b} e^{(-x/L)} \qquad (2.60)$$

$$N_2 = \left(1 - \frac{y}{b}\right) e^{(-x/L)} \qquad (2.61)$$

where b is the width of the infinite element in the y-direction. Similarly, H_y and H_z field components can also be expressed. Also the infinite element can extend to negative x or either direction with y. Similarly, by assuming exponential decay in both x and y, a rectangular or quadrant element extending towards infinity in both x and y directions can be considered, and particularly these are suitable for use at the corners. Integration of these shape functions or their derivatives over the infinite elements are finite and can be carried out easily. Combining all of these infinite elements with the conventional finite element, any open type waveguide cross sectional domain can be represented conveniently with continuous field components over the whole infinite domain.

2.8 Spurious solutions

The most serious problem associated with vector finite element analysis is the appearance of extraneous non-physical or spurious modes. Spurious solutions are found to spread all over the eigenvalue spectrum, some of them appearing below any true modes and some between the physical modes. The cause of appearance of the spurious modes, could be due to various factors such as, enforcement of the boundary conditions, the positive definiteness of the operator or possibly due to the non zero divergence of the trial fields (Rahman and Davies, 1984*a*; 1984*b*).

For electromagnetic waveguide problems, it has been observed (Konrad, 1976; Mabaya *et al.*, 1981; Davies *et al.*, 1982) that spurious modes do not arise if the trial field precisely satisfies **div B** = 0. In the conventional **H**-field finite element formulation, the variational functional (2.24) is consistent with the Maxwell's two curl equations, (2.10) and (2.11), but do not satisfy the $\nabla \cdot$ **B** = 0. Therefore in the full vector formulation it has been found (Davies *et al.*, 1982; Rahman and Davies, 1984*b*) that these spurious modes occur because this divergence-free condition (**div B** = 0) is neither implied nor forced.

To eliminate these spurious solutions, Rahman and Davies (Rahman and Davies, 1984*c*) have utilised the penalty function method, which gives very easy identification of a solution as being either a physical or spurious solution. The logic behind the scheme is the fact that an eigenvector of a physical mode should obey **div B** = 0. Thus **div H** for each eigenvector of interest is calculated over the guide cross section. The value of **div H** is then examined for different solutions, and only solutions with a low value of **div H** will be considered as real modes. In this case, the **div H** is calculated from the discrete nodal field values obtained after the solution of the eigenvalue equation (2.23).

The penalty function method (Rahman and Davies, 1984*c*; Koshiba *et al.*, 1984; Koshiba *et al.*, 1985*b*; Young, 1988) is a useful way of imposing certain constraints on solution variables; and it has been used in structural engineering problems to impose specific boundary conditions (Bathe, 1982). In this method (Rahman and Davies, 1984*c*), an additional integral is added to the original functional (2.24) which satisfies **div H** = 0. The augmented functional can be written as;

$$\omega^2 = \frac{\int \left((\nabla \times H)^* \cdot \hat{\varepsilon}^{-1} \cdot (\nabla \times H)\, d\Omega + \left(\frac{\alpha}{\varepsilon_0} \right) (\nabla \cdot H)^* \cdot (\nabla \cdot H) \right) d\Omega}{\int H^* \cdot \hat{\mu} \cdot H\, d\Omega} \qquad (2.62)$$

where α is the dimensionless penalty number. A separate subroutine can be introduced in order to implement the addition of the penalty term in the numerator of equation (2.62). The value of α can be estimated around $1/\varepsilon_g$, where ε_g is the dielectric constant

of the guide core. Here, the divergence-free constraint is imposed in a least-squares sense, and larger the value of the penalty number the more heavily the constraint is imposed, giving a further reduction of the spurious modes from the spectrum. It is also found that using this penalty function method considerably improves the quality of the field eigenvectors (Rahman and Davies, 1984*c*). Another advantage is that it does not increase the matrix order of the eigenvalue problem and does not need additional storage.

A number of alternative ways of eliminating spurious modes have been suggested, and the problem does not occur at all with the scalar formulation (Mabaya *et al.*, 1981). When appropriate these schemes can be used to flush out spurious modes from the vector formulation. The technique of working with scalars can reduce the amount of computation and eliminate spurious modes, but at the expense of accuracy. A formulation in terms of the transverse **H**-field has been advanced (Hayata *et al.*, 1986) which completely eliminates spurious modes. The H_x and H_y field components are represented to the order of the elemental shape functions, but H_z involves a stage of differentiation and is thus more approximately represented. In this formulation, any artificial parameters such as the penalty coefficient are not included. Davies (Davies, 1993) has shown two successful schemes for the avoidance of spurious modes. The first method solves the difficulty by a new formulation using transverse magnetic field with no need for special new finite elements. The above mentioned spurious modes are described as the non-physical solutions which do not satisfy the divergence free condition. Since all solutions are finite linear combinations of the basis functions, it follows that these spurious solutions will no longer appear if the basis functions are chosen to be divergence free. The second method considers this versatile approach by using the established variational formulation (2.24) but with the application of a more appropriate choice of basis vector functions using new finite elements, - some form of 'vector finite elements'.

2.9   Summary

In this chapter, the finite element method based on the variational principle has been presented for the analysis of optical waveguiding problems. The history and the importance of the method are also described briefly. Various aspects, including different scalar and vector formulations, domain discretisation, natural boundary conditions, shape functions, element and global matrices have been discussed. Finally, the analysis of infinite elements was considered and also the important penalty function method was utilised to eliminate the spurious or non-physical solutions. This chapter, together with the discussion of the least squares boundary residual method presented in the next chapter, forms the basis for the work in the analysis of optical waveguide problems involved in the subsequent chapters of this thesis.

Chapter 3

The Least Squares Boundary Residual Method

3.1 Introduction

There has been a considerable interest in the analysis and design of integrated optical devices in which waveguide parameters vary along the axial direction. They play an important role in designing practical devices, such as, an isolated step discontinuity as in the simple butt-joining of two waveguides of different widths, or as finite cascades of discontinuities as in the bending of an optical waveguide in an integrated optical directional coupler circuit, the tapering of a channel waveguide for efficient coupling to an optical fibre, gratings on dielectric waveguides in certain components like bragg reflectors, or Y- junctions. Various methods for the analysis of the discontinuity problems in a dielectric waveguide have been developed by a number of authours (Clarricoats and Sharpe, 1972; Hockham and Sharpe, 1972; Mahmoud and Beal, 1975; Morishita *et al.*, 1979; Shigesawa and Tsuji, 1986). However, most of the theoretical analyses reported earlier have restricted limitations of practical application, since the radiated and reflected waves have been ignored and also used under the assumption of slight discontinuity.

The problem considered here is an abrupt discontinuity in the transverse plane, $z = 0$, between two arbitrarily shaped uniform waveguides. Each waveguide can have scalar or tensor permittivity that varies arbitrarily with the two transverse directions. The incoming wave incident upon the discontinuity plane is presumes of one mode. In this thesis, the discontinuities in dielectric waveguides are accurately analysed using the least squares boundary residual (LSBR) method (Rahman and Davies, 1988). Consequently, the LSBR method has been used along with the versatile vector finite element method (Rahman and Davies, 1984*a*) in order to calculate the power transfer from a waveguide section to another.

The least squares boundary residual method was introduced as an alternative to the point matching (and Galerkin) methods, of numerically solving problems. The LSBR method satisfies the boundary conditions in the useful least-square sense over the discontinuity interface. In contrast to point matching, the LSBR method is a rigorously convergent procedure, free from the phenomenon of relative convergence. The LSBR method has the flexibility of introducing an electric/magnetic weighting factor and, unlike the point matching, the errors being minimised are global rather than sampled just at discrete points. The method has been widely used to study discontinuity parameters in microwave and optical waveguides (Davies, 1973; Brooke and Kharadly, 1976; Matsumoto *et al.*, 1986; Cullen and Yeo, 1987; Fernandez and Davies, 1988;). The LSBR method matches the continuity of the tangential fields in the least squares sense considering many modes at the discontinuity plane to provide the generalised scattering matrix. In this study, it has been shown that the LSBR method is an accurate and versatile numerical tool to obtain the power transfer between coupled waveguides.

A brief explanation of the theory of the least squares boundary residual method is given in the next section, followed by a discussion of the use of FEM in the numerical analysis of the discontinuity problem.

3.2 Analysis of discontinuity in dielectric waveguides

Consider the abrupt junction of two dielectric waveguides as illustrated in **Fig. 3.1**. It is assumed that the discontinuity junction is excited by an incident wave of one mode from side I. This incoming wave is partly reflected, partly transmitted, and radiated at the junction interface. Let E_t^{in} and H_t^{in} be the transverse components of the electric and magnetic fields of the incident wave, respectively. Some of the incident wave is reflected back into the side I. On the other hand, many modes will be generated at the discontinuity plane to satisfy the boundary conditions. These can be guided or radiated modes in both sides of the discontinuity. The total transverse electric and magnetic fields E_t^I and H_t^I in side I and E_t^{II} and H_t^{II} in side II at the discontinuity plane ($z = 0$), can be expressed in terms of the eigen modes in side I and side II, respectively, as follows:

$$E_t^I = E_t^{in} + \sum_{i=1}^{\infty} a_i \, E_{ti}^I \qquad (3.1)$$

$$H_t^I = H_t^{in} - \sum_{i=1}^{\infty} a_i \, H_{ti}^I \qquad (3.2)$$

$$E_t^{II} = \sum_{i=1}^{\infty} b_i \, E_{ti}^{II} \qquad (3.3)$$

$$H_t^{II} = \sum_{i=1}^{\infty} b_i \, H_{ti}^{II} \qquad (3.4)$$

The modes, which are generated at the discontinuity plane, may be propagating, radiating, or evanescent. Therefore E_{ti}^I and H_{ti}^I represent the transverse field components of the ith mode reflected from the junction in side I and, a_i are the corresponding modal amplitudes of these reflected modes. Similarly, E_{ti}^{II} and H_{ti}^{II} are the transverse field components of the ith mode transmitted in side II and, b_i are the modal amplitudes of those transmitted modes. These scattering coefficients, a_i and b_i have to be determined.
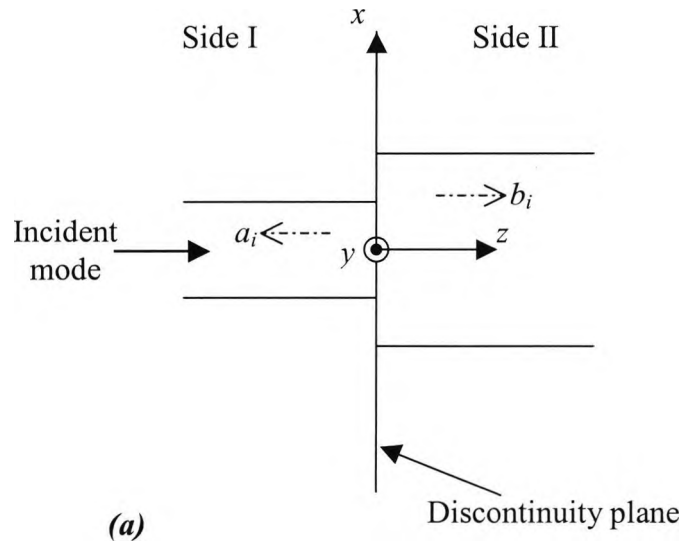
(a)
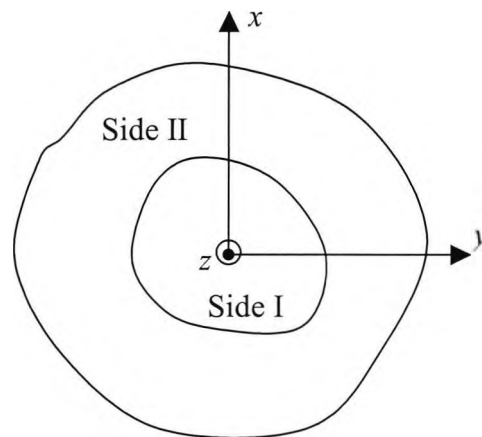
(b)

Fig. 3.1 Discontinuity junction of two dielectric waveguides *(a)* Vertical section of the discontinuity between side I and II. *(b)* Transverse cross section of the discontinuity at the junction of two sides.

Considering the fields in either side of the discontinuity, the mean-square error to the boundary condition in that plane can be defined as the functional:

$$J = \int \left|E_t^I - E_t^{II}\right|^2 + \alpha.Z_0^{\ 2}\left|H_t^I - H_t^{II}\right|^2 d\Omega \qquad (3.5)$$

where α is a convenient, positive and dimensionless weighting factor, and the integral is calculated over the discontinuity plane. Z_0 is the free-space wave impedance.

In the LSBR method, the aim is to look for a stationary solution to satisfy the continuity conditions of the tangential fields in a least square sense by minimising the functional (3.5). To obtain the approximate numerical solution to the problem, the infinite series expansions of (3.1) to (3.4) are truncated, including all relevant propagating modes plus as many radiating and/or evanescent modes as convenient. In this analysis, all the reflection, transmission and radiation fields are determined in such a way that J becomes a minimum. The electromagnetic fields thus obtained are the best approximate fields in the sense of least square error. The condition for eq. (3.5) being minimised is:

$$\frac{\partial J}{\partial a_i} = 0, \qquad \frac{\partial J}{\partial b_i} = 0 \qquad \text{for i} = 1 \dots \dots \infty \qquad (3.6)$$

which results in a set of linear equations:

$$\boldsymbol{C}\boldsymbol{x} = \boldsymbol{v} \qquad (3.7)$$

The solution of this equation gives in $\{x\}$, the required approximate modal coefficients of a_i and b_i. These constitute one column of the scattering matrix, corresponding to the chosen incident mode. $\boldsymbol{C}$ is a square matrix generated from the eigen vectors and $\boldsymbol{v}$ is an array due to the incident mode. The elements of $\boldsymbol{C}$ and $\boldsymbol{v}$ are given by:

$$C_{ij} = \left\langle E_{ti}, E_{tj} \right\rangle + \alpha.Z^2 \left\langle H_{ti}, H_{tj} \right\rangle \qquad (3.8a)$$

$$v_i = \left\langle E_t^{in}, E_{ti} \right\rangle + \alpha.Z^2 \left\langle H_t^{in}, H_{ti} \right\rangle \qquad (3.8b)$$

where $i, j = 1, \dots \dots N$, and N is the total number of modes in side I and II and the vectors E_t and H_t are made up of all the corresponding modal fields in both sides.

The inner products involved in the above expressions are defined as:

$$\langle x_1, x_2 \rangle = \int x_1 \cdot x_2^* \; ds \tag{3.9}$$

where x_1 and x_2 are two field vectors, x_2^* is the complex conjugate of x_2 and integration is carried out over the waveguide cross section.

The above gives a brief outline of the least squares boundary residual technique which will be applied in the next chapters to analyse a series of relevant waveguide problems concerning power transfer between waveguides.

3.3   Numerical analysis using FE output

The vector **H**-field finite element has become a powerful tool for the solution of microwave and optical waveguides as described in the previous chapter. One of the main advantages of **H**-field formulation is that the continuity of **H**-field components is automatically satisfied even with permittivity discontinuities. In this thesis, to analyse the power transfer characteristics of coupled waveguides, the rigorously convergent LSBR method is used along with **H**-field FE program. The elimination of spurious solutions by using the penalty method, particularly improves the eigen vector quality, which is a very important fact for the analysis of discontinuity problems.

By employing the FE program, the nodal values of the complete **H**-field for each mode are obtained for both the waveguides (side I and side II). The **E**-field over each element are calculated using these nodal **H**-field values by means of a Maxwell's equation. Modal eigenvalues and eigenvectors of all the modes in both sides of the discontinuity are used as the input data to the LSBR method. All these eigen values and eigen vectors are easily generated by employing the vector FEM program. The LSBR program reads all the input data and calculates the integral J, and minimises the error criterion of eq. (3.5), with respect to each value of a_i and b_i for any given incidence, by solving a homogeneous linear equation (3.7). There is no need to generate the nodal **E**-fields as the nodal **H**-fields can be directly used to calculate the electric field part of the functional, J. The solution of the eq. (3.7) gives the unknown

vector $\{x\}$ consisting of the reflected and transmitted coefficients of all the modes considered in the analysis. The singular value decomposition algorithm has been used to solve the linear equation (3.7). For numerical efficiency, the FE nodal points of side I are matched with the nodal points of side II across the transverse plane at the discontinuity.

The LSBR method can be applied to a wide range of discontinuity problems, involving abrupt changes at the transverse plane between arbitrary guiding structures of uniform cross section. These include vertical shifts, horizontal misalignments, sudden changes of width or height, change in guide dimensions or materials, or combinations of all these varieties. The method can also be used to guiding structures, such as optical fibres or titanium diffused $LiNbO_3$ channel waveguides with anisotropic or electro optic refractive indices. On the other hand, the LBSR method can be used to find the optimum matching of the two waveguides by controlling the geometries and material properties of the guides. In addition, by choosing the optimum guide parameters the radiation losses resulting from random fluctuations in waveguide geometry and refractive index can also be minimised. The resulting reflection matrix and the transmission matrix give a complete understanding of the discontinuity problem which facilitates better designs of optical and microwave devices.

3.4 Losses in optical waveguides

The source of losses in waveguide devices include, coupling loss, propagation loss, electrode loading loss and if considered, the waveguide bending loss. The propagation loss is generally attributable to three different mechanisms: scattering, absorption and radiation. The scattering loss is usually predominates in glass or dielectric waveguides, while absorption loss is most important in semiconductors and other crystalline materials. Radiation losses become significant when waveguides are bent through a curve. Photons can be either scattered, absorbed or radiated as the optical beam progresses through the waveguide, thus reducing the total power transmitted. To describe quantitatively the magnitude of the scattering loss, the exponential

attenuation coefficient is generally used, and the intensity (power per area) at any point along the length of the waveguide is given by,

$$I(z) = I_0 \, e^{-\alpha z} \qquad\qquad (3.10)$$

where I_0 is the initial intensity at $z = 0$ and α is the power attenuation coefficient.

For most polarization-based applications described in this thesis, the light is coupled in and out of one optical waveguide to another through a butt joint. The LSBR method analyses the waveguide junction efficiently in order to calculate the power transfer from the input guide to the other. When a guided TE or TM mode is incident on the discontinuity plane between two waveguides, some of the incident light energy is lost, called the insertion loss. The method can also be used to calculate this power loss suffered by the TE or TM mode, by utilising the scattering coefficients. If an incident mode of unit power is assumed then the insertion loss in decibels is given by:

$$L = 10 log_{10} \left(\sum_{i=1}^{N} |b_i|^2 \right) \qquad\qquad (3.11)$$

where, b_i are the transmission coefficients of the ith mode and N is the total number of modes considered.

3.5 Summary

In this chapter, a rigorously convergent least squares boundary residual method is described for use to analyse the discontinuities in optical waveguides. The method is also capable of calculating the power transfer between two waveguides, using the scattering coefficients. The role of the FE program in utilising the LSBR technique is also presented briefly, followed by the calculation of the insertion loss. Having established this formulation, the application of the LSBR method will be presented in the next four chapters.

Chapter 4

Polarization Splitters

4.1 Introduction

Guided wave optical TE/TM polarization mode splitters are required in many optical communication systems, such as, polarization diversity heterodyne receivers for coherent detection (Okoshi *et al.*, 1983), optical fibre sensor applications, and also for devices like integrated optic gyroscopes, electro-optic switches and modulators which require a single polarization state for their operation. Several types of optical polarizers have been reported using different operation principles. However, the simplest designs result from exploiting material birefringence in LiNbO$_3$ (Hempelmann *et al.*, 1995) or in polymers (Lee *et al.*, 1998) to radiate out the unwanted polarization. These types of devices can be described as polarization filters rather than the polarization splitters. A polarization splitter differs from a simple polarizer in that no energy is intentionally lost, and the two separated orthogonal states of polarization of the input signal, emerge from the device at two separate ports. In such cases, both the polarized modes are collected, and several design approaches by using asymmetric y-branches in LiNbO$_3$ (Goto and Yip, 1989; Wei and Wang, 1994), or polymers (Garner *et al.*, 1999), or semiconductors with a supper lattice (Suzuki *et al.*, 1994) have been reported, again exploiting the material birefringence. On the

other hand, by using metal-clad waveguides, the propagation characteristics of the quasi-TM polarized modes can be significantly altered, and employing this property, directional couplers in LiNbO$_3$ (Mikami, 1980) or in semiconductors (InGaAsP/InP based (Albrecht *et al.*, 1990; Rajarajan *et al.*, 1997)), and a reversed $\Delta\beta$ directional coupler (Habara, 1987) have also been reported.

Recently, in the design of many important optoelectronic systems, such as phased array demultiplexers (Bissessur *et al.*, 1996), electro-optic modulators and multimode interference (MMI) designs (Heaton *et al.*, 1992), and compact optical bends (Van Dam *et al.*, 1996), deeply etched waveguides have increasingly been used, these being more tolerant to the fabrication approaches used for such devices. However, the directional coupler-based approach is not suitable for such deeply etched semiconductor waveguides as the coupling between the waveguides is generally weak. In recent years, there is a growing interest in the application of multimode interference (MMI) effects in integrated optics. It is generally known that MMI-based devices are polarization independent, so therefore in the design proposed by Soldano *et al.*, (1994), using two 3-dB couplers, one arm of the Mach-Zehnder interferometer was covered by a metal layer to introduce the relative phase differences between the two arms for the two polarizations.

However, simulations carried out using a more rigorous vectorial finite element method (VFEM) (Rahman and Davies, 1984*a*) indicate that a significant level of polarization dependence of MMI-based devices in semiconductor waveguides. In this chapter, a design of a single-section, deeply etched semiconductor MMI-based polarization splitter, which enables the polarization states to be split into two separate ports, is reported.

4.2 Design considerations of an MMI-based device

The MMI waveguides are usually designed to support a large number of modes (typically $\geq$ 3). An MMI-based device consists of a large multimode waveguide section with input and output access waveguides which are placed at its beginning and at its end. Generally, the input and output access waveguides are single-moded waveguides, and used to launch light into and collect light from the central MMI waveguide section. These devices are generally referred to as N×M MMI couplers, where N and M are the number of input and output waveguides, respectively. **Fig. 4.1** shows a schematic of a simple 1×2 MMI-based coupler.
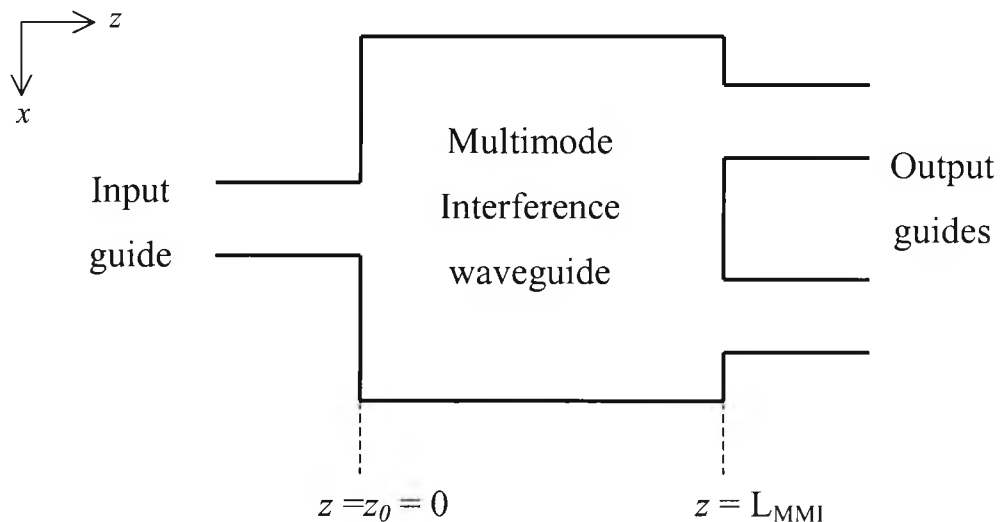
Fig. 4.1 Schematic of a simple 1×2 MMI-based coupler.

The operation of an MMI-based device is based on the so called 'self imaging' principle, which states that, an input field profile is reproduced in single or multiple images at periodic intervals along the propagation direction of the guide. To clarify the origins of self-imaging, the following interpretation can be offered. The input field from a single-mode input access waveguide propagates as linear combination of the allowed modes in the multimode region. At the beginning of the multimode region, the modes are 'in phase' since their addition results in a representation of the input field. As the modes propagate along the multimode region, they move 'out of phase',

since the multiple modes have different propagation constants. This causes the modes to interfere destructively and the sum of the modes at a point in the axial direction, $z >$ z_0, in general no longer results in a faithful representation of the input. The mode phases, however, are periodic and at certain propagation distances a mode-beating phenomenon occurs, where the modes constructively interfere to partially or fully reconstruct the original input field. The result is that at certain propagation lengths in the multimode region, single or multiple self-images of the input field are formed.

Once the incident fundamental mode entering via the input access waveguide excites the modes in the MMI region, they then propagate with different phase velocities and their values may be calculated approximately, through a quadrature relationship given by (Soldano and Pennings, 1995),

$$\beta_0 - \beta_v = \frac{v(v+2)\pi}{3L_\pi} \qquad (4.1)$$

where β_0 is the propagation constant of the fundamental mode of the MMI waveguide, v is an integer and L_π is the coupling length of the two lowest order modes, given by,

$$L_\pi = \frac{\pi}{\beta_0 - \beta_1} \qquad (4.2)$$

If the quadrature relationship holds correctly, then the images will be formed periodically at every odd and even multiple of a specific length, L_i, which is directly related to the coupling length, L_π. At every odd multiple of L_i, the image of the input field will be formed at an anti-symmetric position called the *Cross-port*. At every even multiple of L_i, the image will be formed at an identical position called the *Bar-port*.

A full vectorial numerical approach (Rahman and Davies, 1984*a*), based on the **H-**field formulation (VFEM) has been used to obtain the modal solutions and the propagation constants of all the modes in the input/output and the MMI waveguide section. To calculate the power carried by these excited modes, it is crucial to obtain the excited modal coefficients of the modes in the MMI section. A full vectorial

junction analysis approach, based on the rigorous least squares boundary residual (LSBR) method (Rahman and Davies, 1988) has been considered as a means to find these transmitted and reflected modal coefficients at each junction, thereby to obtain the evolution of the composite modal field along the uniform waveguide sections.

4.2.1 General interference

In the general interference mechanism relating to an MMI coupler, the input waveguide can be placed flexibly at any particular position with respect to the centre of the MMI section. In this study, the input/output waveguides were placed at the side ends as shown in **Fig. 4.2**. In this case of general interference, the corresponding periodic imaging length, L_i is equal to $3L_\pi$. Therefore, direct and mirrored single images of the input optical field will be formed at distances of even and odd multiples of the length, L_i, along the axial direction of the MMI waveguide. At this point, the direct and mirrored single images can be obtained at the bar port and the cross port, respectively.
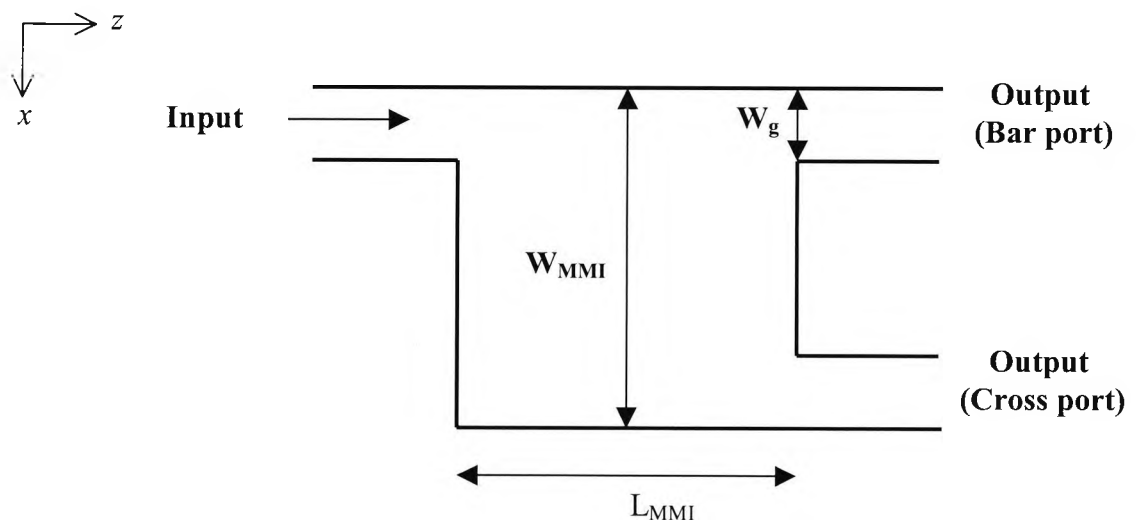
Fig. 4.2 Schematic MMI configuration for general interference mechanism.

4.2.2 Restricted interference

In the restricted interference mechanism, the input and output waveguides are located at predetermined positions, i.e. $\pm W_{MMI}/6$ with respect to the centre of the MMI waveguide section, where, W_{MMI} is the width of the MMI waveguide, there by placing restrictions on the modal excitation in the MMI section. Therefore, as a result, every third mode is not excited in the MMI-region thus reducing the image period significantly to $L_i = L_\pi$. **Fig. 4.3** shows the schematic of the restricted MMI configuration.

Although the image period is much shorter, the separation between the ports is reduced, which could restrict some designs, particularly when the overall MMI width needs to be smaller. On the other hand, in the general interference mechanism, the ports can be placed at the extreme sides of the MMI section, thereby allowing a reduction of the overall width of the MMI, which ultimately may reduce the device length.
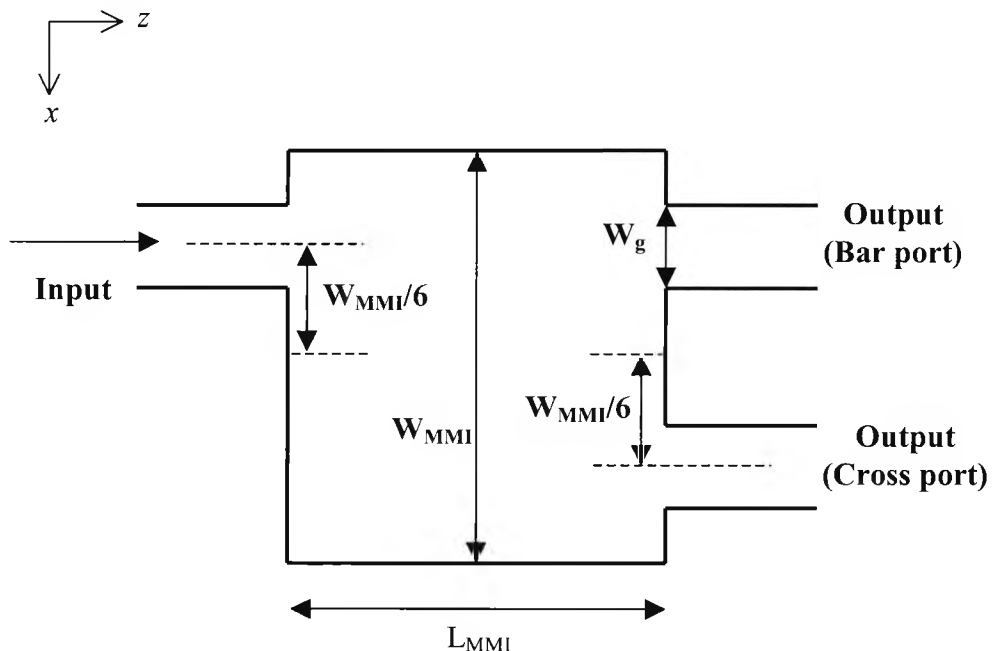
Fig. 4.3 Schematic MMI configuration for restricted interference mechanism.

Although the propagation constants for the TE and TM polarizations differ considerably in semiconductor waveguides it has, however, generally been assumed that MMI-based devices are nearly polarization-independent. Their polarization

dependence may be significantly smaller for silica-based structures, but it has been clearly noticed from this study, that a significant polarization dependence for semiconductor based MMI devices exists. The MMI width can be adjusted to obtain the relationship between the coupling lengths $L_\pi(TE)$ and $L_\pi(TM)$ for the TE and TM polarizations respectively, for the overall length of the device, L_{MMI} to be given by,

$$L_{MMI} = n * L_\pi(TE) = (n\text{-}1) * L_\pi(TM) \qquad (4.3)$$

Here, *n* is an integer.

4.3   Device simulation results

A deeply etched InP-InGaAsP (λ_g=1.3 μm)-InP ridge waveguide structure, with a guiding layer of 0.8 μm height, an upper cap layer of 1.0 μm and a total etch-depth of 2.0 μm, at an operating wavelength of λ=1550 nm, has been considered here for the design of a simple MMI-based optical polarization splitter shown in **Fig. 4.4(a)**. W_{MMI} and W_g are the width of the MMI and the input/output waveguides, respectively. The refractive indices of the core and substrate are taken as 3.38 and 3.17 respectively. **Fig. 4.4(b)** shows the cross section of the input/output waveguide. In the present work, the input/output guides were placed at the extreme side ends of the MMI waveguide, for the general interference mechanism example.
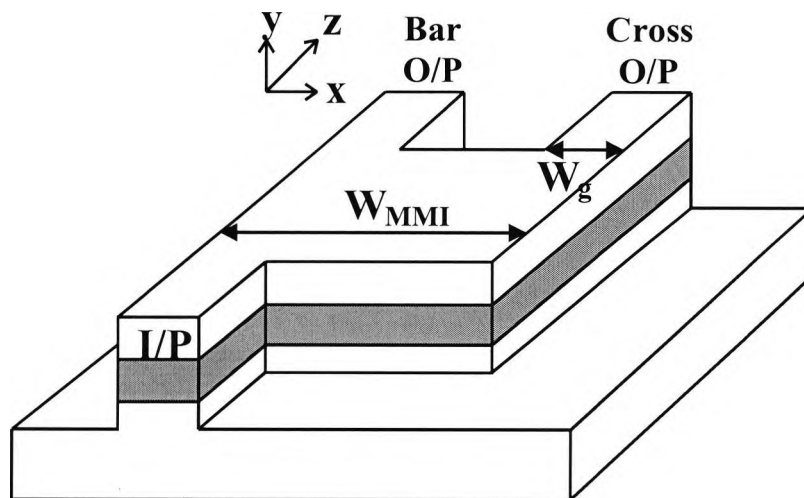
Fig. 4.4(a) MMI-based polarization splitter.
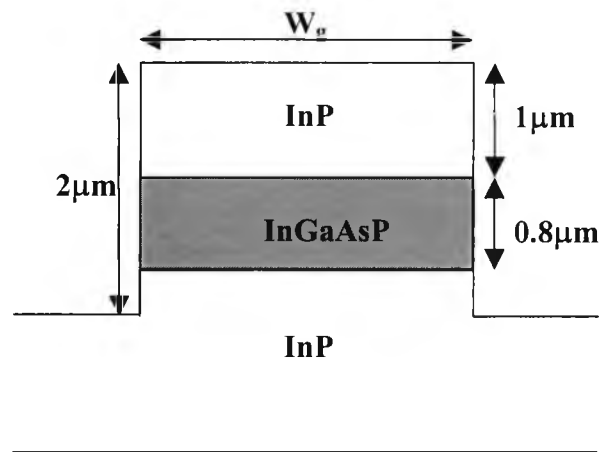
Fig. 4.4*(b)* Cross section of the input/output waveguide.

4.3.1 MMI waveguide characteristics

Initially, the modal characteristics of the MMI waveguide were analysed. The coupling length, L_π, for TE and TM modes of the MMI structure were calculated using equation (4.2), where the propagation constants were obtained using the full vectorial modal solution approach (Rahman and Davies, 1984*a*). **Fig. 4.5** shows the variation of L_π with the MMI width, W_{MMI} and the ratio, $R= L_\pi(TE)/ L_\pi(TM)$. It can be noted that the device length L_{MMI} increases with the MMI width, following a square law. The L_π values for TE and TM modes are very similar, but still a noticeable difference exists. It should be noted here that L_π, for the TM mode, is consistently higher for all the W_{MMI} values considered in this study: however, simple semi-analytical equations (Soldano and Pennings, 1995) incorrectly predict that $L_\pi(TE)$ is larger than $L_\pi(TM)$ for all cases. When $W_{MMI} = 6$ μm, the propagation constants for the TE and TM modes are calculated as 13.45614 and 13.43971, respectively. It can also be noted that R, the L_π ratio, progressively becomes smaller than 1.0 when the MMI width is reduced. The horizontal dashed lines show the specific L_π ratios, for different MMI widths. A lower L_π ratio means a smaller value of *n* and ultimately a smaller overall device length.
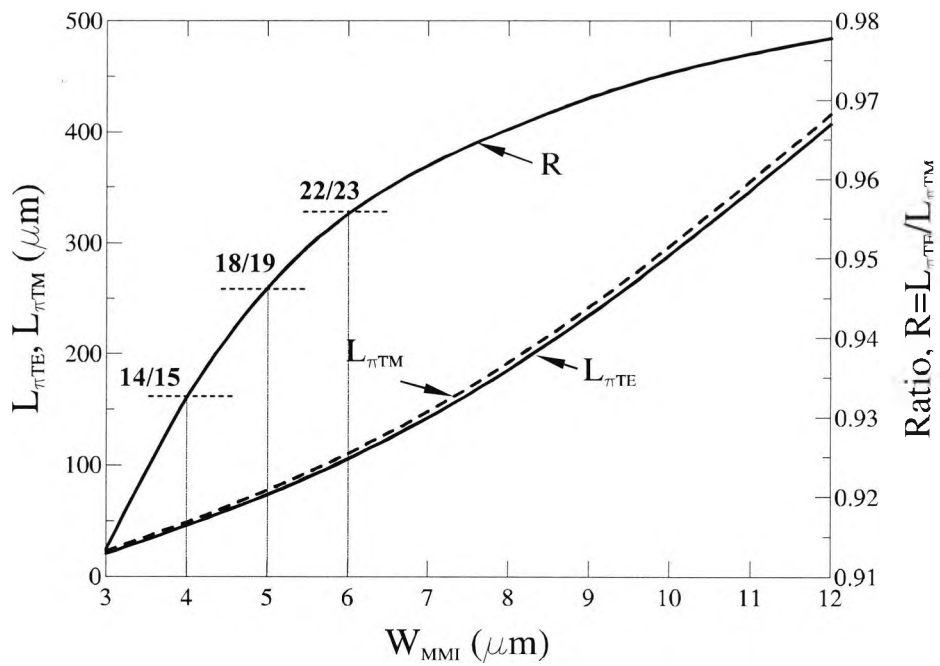
Fig. 4.5 Variation of L_π and L_π ratio, R, for the TE and TM polarizations.

4.3.2 Device performance – Restricted interference mechanism

In the restricted interference mechanism example, the input and the output waveguides are placed at a lateral offset of $\pm W_{MMI}/6$, with respect to the centre of the MMI region, and the structure is shown in **Fig. 4.6**.
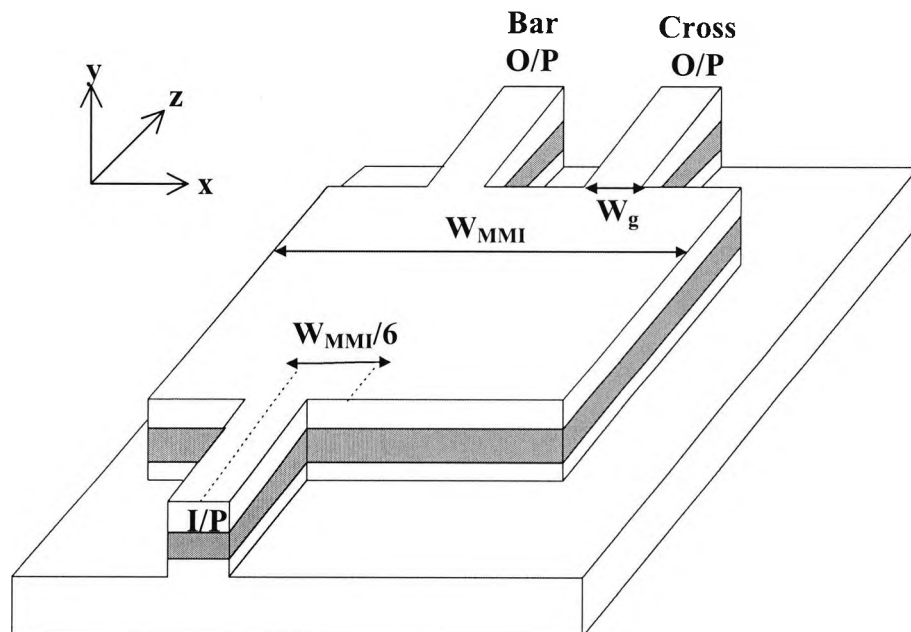
Fig. 4.6 MMI structure for restricted interference.

In this analysis, the MMI waveguide width (W_{MMI}) is taken as 6 μm, and narrower input/output waveguides of 1 μm width (W_g) are considered, which allowed the separation between the guides, *s*, to be only 1 μm. If a wider value of W_g was considered, that would have reduced the waveguide separation further. The resonance length, $L_i = L_\pi = 102.8$ μm for the TE polarization and the corresponding L_π ratio is 21/22. Hence the overall device length is ≈ 2262 μm. When the width of the MMI section, $W_{MMI} = 6$ μm, seven guided modes could be excited, when the input field is incident on the junction interface. However, in this case, due to the restricted interference, only five of the total seven guided modes were excited. Consequently, the rigorous LSBR method is employed by using the modal field profiles and the propagation constants of the modes, which are obtained from the VFEM, to calculate the excited modal transmission coefficients of the modes in the MMI section. It was calculated that only 89% of the input power was coupled to the MMI section. The composite field at the junction of the input guide and the MMI waveguide, i.e. at *z* = 0^+, is shown in **Fig. 4.7.** It can be seen that the field profile is very similar to the input field distribution.
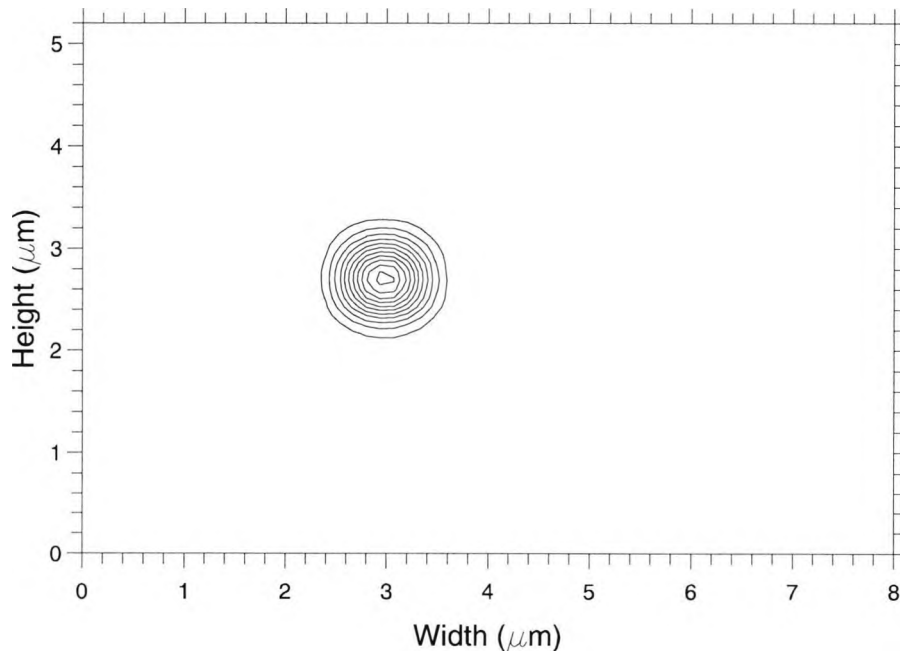
Fig. 4.7 Composite field profile at *z* = 0^+ μm, at the beginning of the MMI section.

The images are formed in the MMI structures, as it is normally assumed that a quadrature relation between the propagation constant spacing is satisfied for such a structure due to the strong lateral confinement. If this relation holds exactly, then perfect images are repeatedly produced for any value of n. However, the numerical simulation carried out indicates that the quadrature relation is obeyed only approximately, and the quadrature error calculations are given in **Table 4.1** when the MMI width is 6.0 μm. As an example, the equivalent value of L_π obtained between the fundamental and the seventh TE modes is 100.7 μm, which represents a significant shift from the L_π value, 102.8 μm obtained from the first two modes. For this reason only subsequent images would deteriorate slowly as the optical power propagates further along the waveguide.

$L_\pi = v(v+2)\pi/3(\beta_0-\beta_v)$		Effective Index Method $L_\pi(\mu m)$	Finite Element Method (140*140 Mesh), $L_\pi(\mu m)$
$v = 1$	$\pi/(\beta_0-\beta_1)$	103.1722	102.8344
$v = 2$	$8\pi/3(\beta_0-\beta_2)$	102.9819	102.5784
$v = 3$	$5\pi/(\beta_0-\beta_3)$	102.7000	102.2454
$v = 4$	$8\pi/(\beta_0-\beta_4)$	102.3528	101.8138
$v = 5$	$35\pi/3(\beta_0-\beta_5)$	101.9184	101.2875
$v = 6$	$16\pi/(\beta_0-\beta_6)$	101.4000	100.6699

Table 4.1 Quadrature error calculation for MMI waveguide with 6 μm width.

The best image is formed at $z = 101$ μm ($n \cong 1$) at the cross port, which is shown in **Fig. 4.8(a)**, and it gives a reasonably good image of the input field. **Fig. 4.8(b)** shows the image at $z = 202$ μm ($n \cong 2$) at the bar port and it shows slight deterioration. The image at the final position, $z = 2255$ μm ($n \cong 22$) is shown in **Fig. 4.9**, which demonstrates significant deterioration of the field.

(a)

(b)
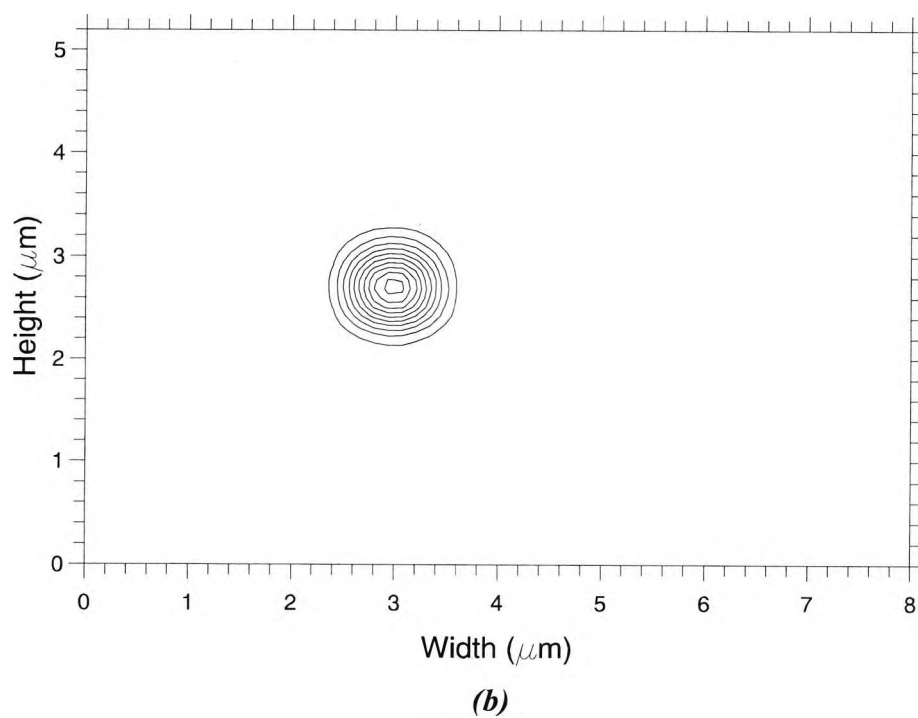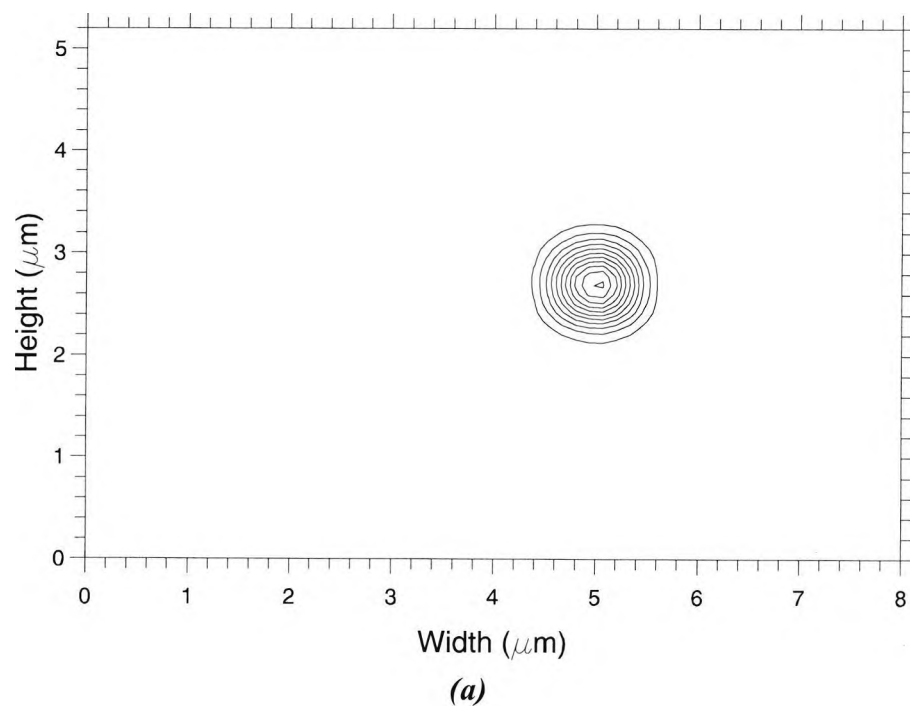
Fig. 4.8 Optical power intensity contours for TE polarization at *(a)* $z = 101\,\mu$m $(n \cong 1)$ and *(b)* at $z = 202\,\mu$m $(n \cong 2)$.
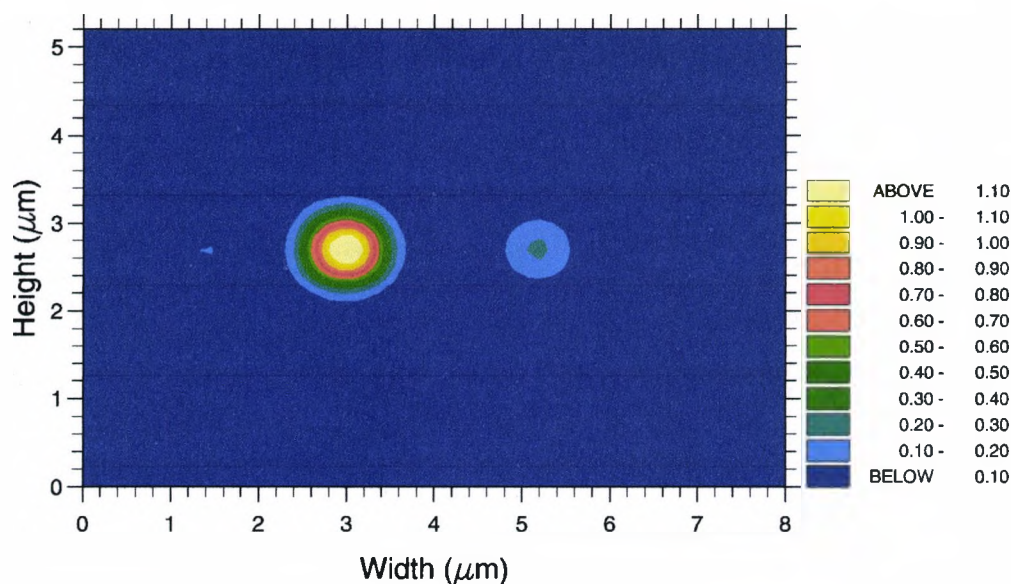
Fig. 4.9 Optical power intensity contours at $z = 2255$ μm ($n \cong 22$) for TE polarization.

When a TM field is launched via the input guide, the final image will appear in the cross port at a distance $z = 2258$ μm ($n \cong 21$) which is shown in **Fig. 4.10**. It can be noted that although the L_π ratio suggests a viable design might be possible, however, due to the build up of the quadrature phase error, the field deterioration is greater for a larger value of n. Besides the building up of the phase errors, the modal loss in a 2.2 mm long structure may also be an issue that has to be considered seriously.
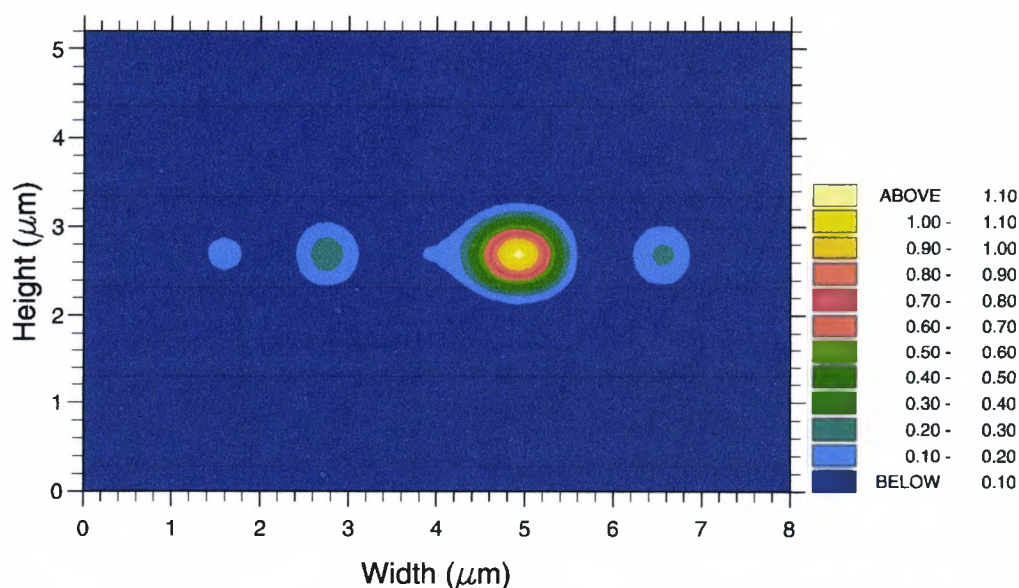
Fig. 4.10 Optical power intensity contours at $z = 2258$ μm ($n \cong 21$) for TM polarization.

4.3.3 Device performance – General interference mechanism

In this section, the performance of the polarization splitter using the general interference mechanism has been analysed. Since, the L_π ratio decreases with a reduction of the MMI waveguide width, W_{MMI}, as was shown in **Fig. 4.5**, a better overall design would be expected for a shorter MMI width than for the wider 6 μm guide, as shown earlier. Hence simulations were carried out for various MMI widths ranging from 3.5 μm to 4.3 μm using the general interference mechanism. Because the two output waveguides are placed at the extreme ends of the MMI waveguide as shown in **Fig. 4.4(a)**, slightly wider input/output waveguides could also be considered. A wider input/output guide (W_g) would be easier to fabricate and it would improve the power coupling with the MMI waveguide sections, yet allow a useful separation between the waveguides to reduce the cross talk between them.

Table 4.2 shows L_π for the TE and TM polarized modes, the L_π ratio, the number of modes in the MMI guide, the transmission coefficients for these modes and the power in the respective output ports for different MMI widths, when the input/output guide width, W_g, is equal to 1.3 μm. Here, P_{yA} and P_{yB} denote the TE-polarized powers in the bar port and cross ports, respectively, and similarly P_{xA} and P_{xB} are for the TM-polarized powers in the bar and cross ports. From **Table 4.2**, it can be noted that, if a wider MMI guide is used, then not only is L_π increased but also, due to the deteriorating L_π ratio, a much longer device would be required. A wider MMI guide would support a greater number of guided modes, however, these simulated results show that the image quality for MMI widths 3.5, 3.7, 4.0 and 4.3 μm are almost similar, but however both the power throughput and the cross talk value were rather improved when $W_{MMI} = 3.7$ μm, that is when a narrower MMI guide is used.

$W_{MMI}(\mu m)$	3.5	3.7	4.0	4.3
$L_{\pi}TE(\mu m)$	35.0977	39.2258	45.8493	52.9958
$L_{\pi}TM(\mu m)$	37.9468	42.2484	49.1104	56.4831
L_{π} ratio	12/13	13/14	14/15	16/17
No. of modes	4	4	5	5
Modal Coefficients, τ_i (Input TE)	$\tau_1 = 0.42485$ $\tau_2 = 0.63317$ $\tau_3 = 0.55784$ $\tau_4 = 0.30759$	$\tau_1 = 0.39506$ $\tau_2 = 0.60797$ $\tau_3 = 0.57053$ $\tau_4 = 0.35338$	$\tau_1 = 0.35573$ $\tau_2 = 0.56930$ $\tau_3 = 0.57565$ $\tau_4 = 0.41449$ $\tau_5 = 0.17944$	$\tau_1 = 0.32241$ $\tau_2 = 0.53217$ $\tau_3 = 0.56998$ $\tau_4 = 0.45402$ $\tau_5 = 0.25948$
Input TE P_{yA} P_{yB}	At $L_i \cong 104\mu m$ 0.004287 0.984289	At $L_i \cong 116\mu m$ 0.005965 0.972089	At $L_i \cong 136\mu m$ 0.002562 0.982635	At $L_i \cong 157\mu m$ 0.003919 0.973830
Input TE P_{yA} P_{yB}	At $13L_i \cong 1363\mu m$ 0.209865 0.740848	At $14L_i \cong 1641\mu m$ 0.792166 0.170773	At $15L_i \cong 2059\mu m$ 0.167573 0.740948	At $17L_i \cong 2700\mu m$ 0.155828 0.710021
Input TM P_{xA} P_{xB}	At $12L_i \cong 1361\mu m$ 0.789412 0.149670	At $13L_i \cong 1643\mu m$ 0.173994 0.737289	At $14L_i \cong 2060\mu m$ 0.625959 0.216454	At $16L_i \cong 2710\mu m$ 0.553306 0.226539

Table 4.2 L_{π}, modal coefficients, output powers for different MMI widths, $W_g = 1.3 \mu m$

A more satisfactory design with $W_g = 1.4$ µm indicates that the TE image is formed at $z = 117$ µm ($n \cong 1$), which gives a reasonably good image of the input field, but it is antisymmetric, as shown in **Fig. 4.11*(a)***. In this case, the $L_{\pi}(TE)$ is 39.22 µm and the corresponding image period, $L_1 = 3 * L_{\pi}(TE) = 117.7$ µm. The first image at the bar port appears at 233 µm ($n \cong 2$), shown in **Fig. 4.11*(b)***, and repeats for even values of n.
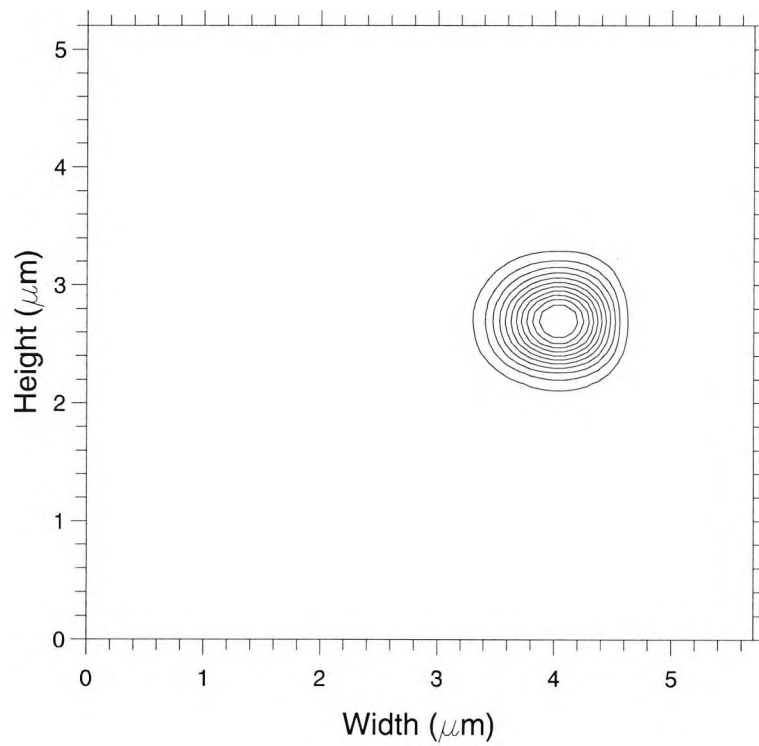
(a)
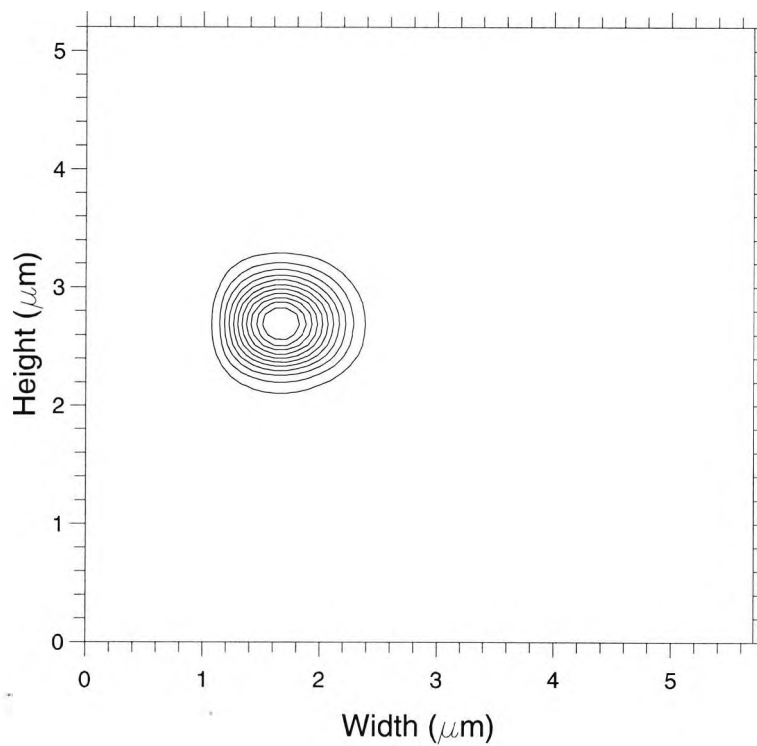
(b)

Fig. 4.11 Optical power intensity contours for general resonance, when W_{MMI} = 3.7 μm and W_g = 1.4 μm *(a)* at $z = L_i$ = 117 μm, and *(b)* at $z = 2L_i$ = 233 μm for TE polarization.

The image at 1641 μm ($n \cong 14$) is shown in **Fig. 4.12**, which shows slight deterioration, due to the build up of cumulative phase error, as the propagation constants did not follow the quadrature rule exactly. Since L_π(TM) is 42.25 μm, at $z =$ 1641 μm, where $n \cong 13$, the resulting field, as shown in **Fig. 13**, indicates that most of the TM power appears in the cross port.
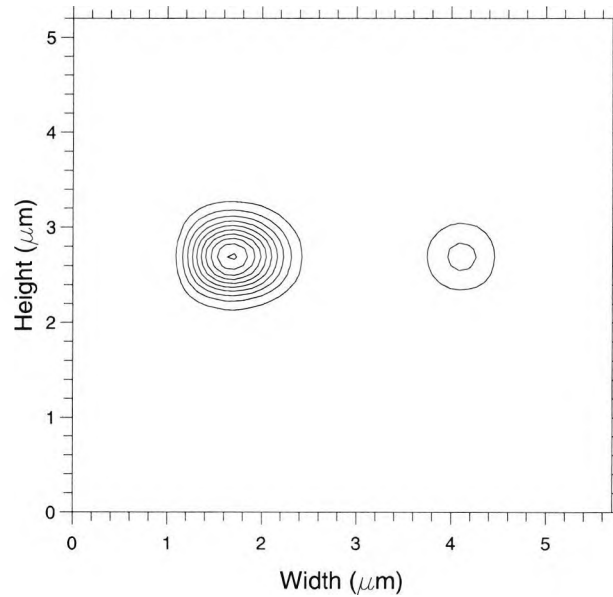
Fig. 4.12 Optical power intensity contour at $z = 1641$ μm ($n \cong 14$) at bar port, for TE polarization.
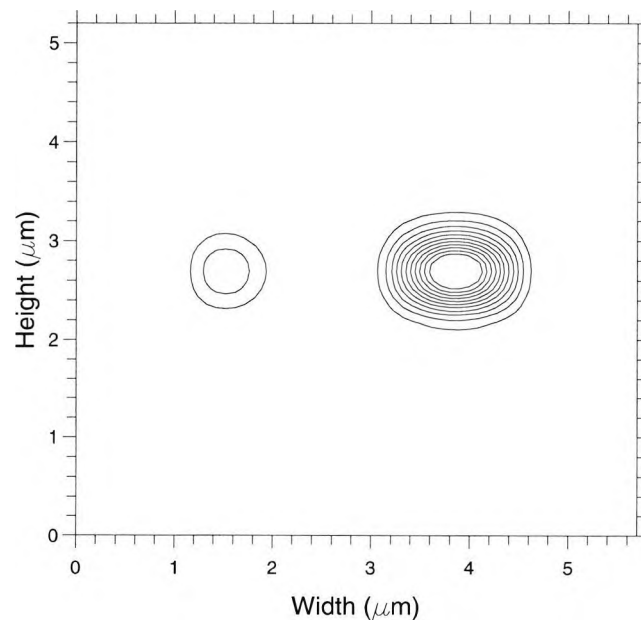
Fig. 4.13 Optical power intensity contour at $z = 1641$ μm ($n \cong 13$) at cross port, for TM polarization.

Due to the quadrature error, the optical power at successive image positions deteriorates and these values at discrete axial positions are shown in **Fig. 4.14**, along with their trends by using continuous curves. It can be seen that, as the TE power in the bar-port reduces, at the same time the TE power in the cross-port increases. Similarly, the TM polarized power in the cross-port gradually reduces and the TM power in the bar port increases. It is also shown that at $z = 1641$ µm, the TE and TM image positions coincide.
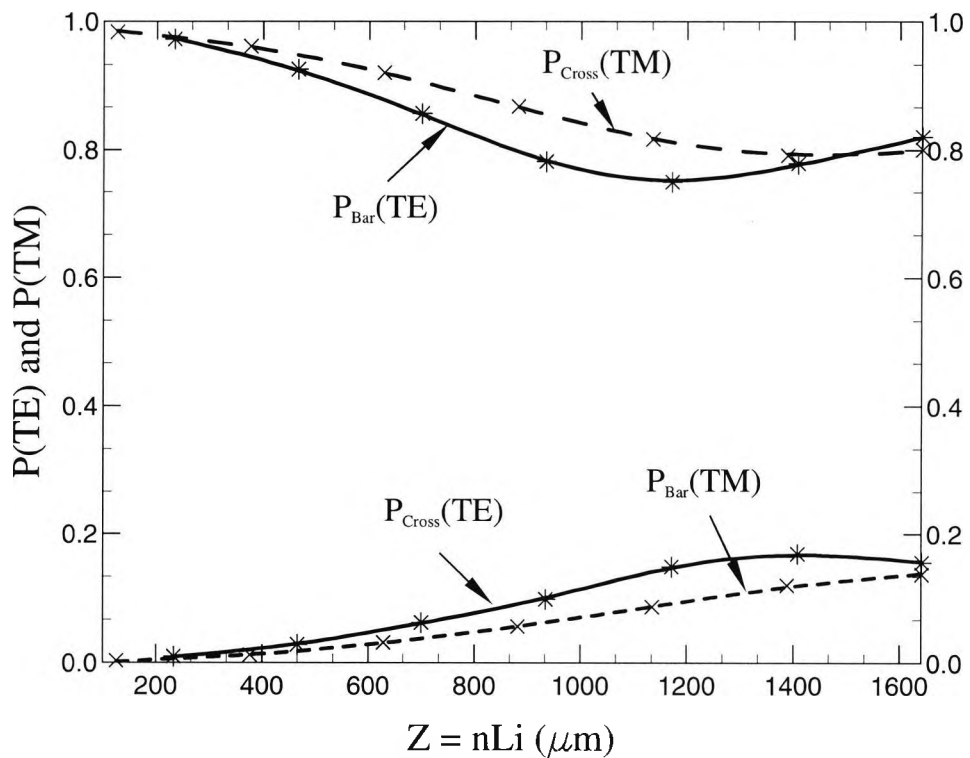
Fig. 4.14 Variation of the TE and TM polarized powers in the bar and cross ports at successive image positions.

The optical power values for both the TE and TM modes are calculated for both the bar and cross-ports around this region as presented in **Fig. 4.15**. It should be noted that 82% of the TE polarized power is available in the bar port and only 15% of total input power remains in the cross port. For the TM polarization, 80% of the input power is in the cross port and again 14% power remains in the bar port. The device length is relatively shorter at 1641 µm, much shorter than value of 2255 µm that occurs when using the 6 µm wide MMI guide with restricted resonance.
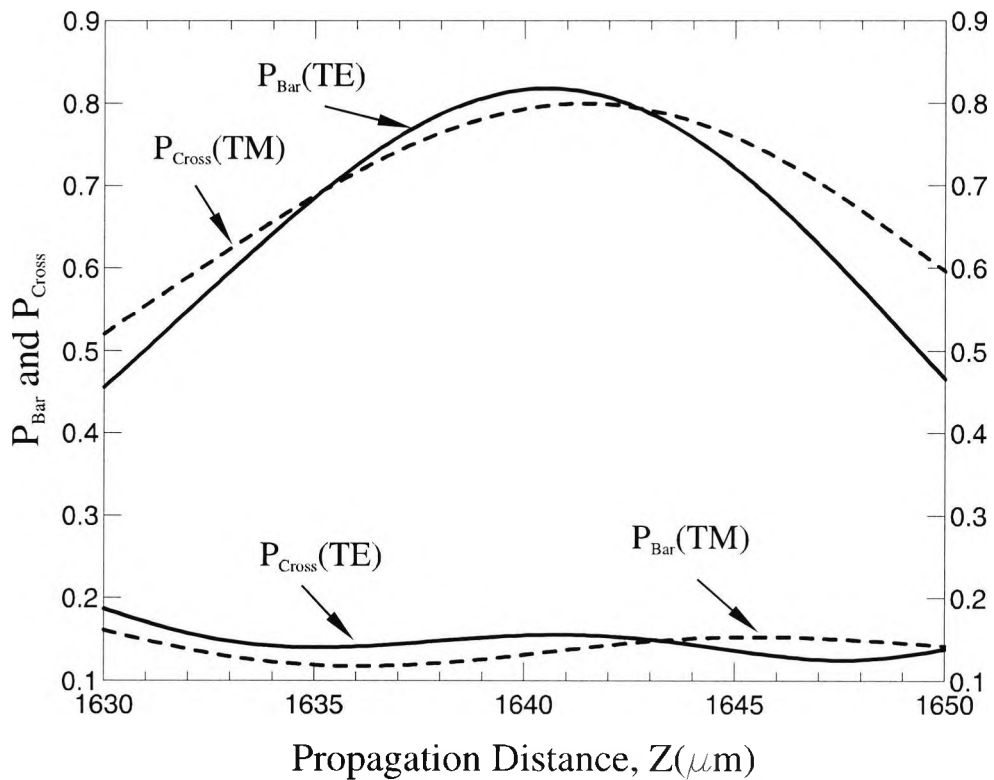
Fig. 4.15 Variation of the TE and TM optical powers in the bar and cross ports with the axial positions (z) near the output plane.

Finally, the effect of the operating wavelength is studied. **Fig. 4.16** shows the variation of the TE and TM optical power values in the bar and cross-ports, respectively, with the propagation distance for two different operating wavelength values, $\lambda = 1.55$ µm and $\lambda = 1.545$ µm. It can be noted that the maximum values of the TE and TM polarized optical powers in the bar and cross-ports, respectively, are very similar for both wavelengths, although the distances at which the maxima occur are different. Hence, a small reduction of the operating wavelength may slightly increase the device length.
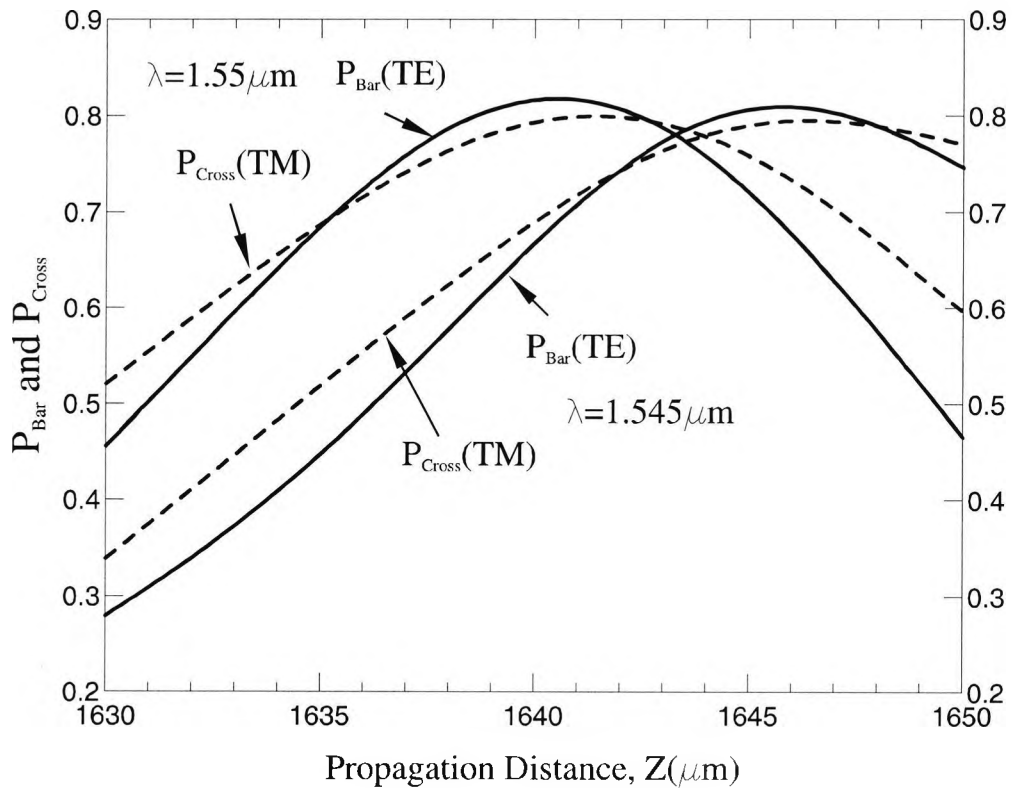
Fig. 4.16 Variation of the TE and TM powers with the axial distance (z) for two different operating wavelengths.

4.4 Summary

In this chapter, a compact, single section polarization splitter in a deeply etched semiconductor MMI waveguide has been designed and analysed using a very simple approach. Numerically simulated results, using rigorous VFEM and LSBR methods, clearly indicate that the performance of MMI-based devices, particularly in semiconductors depend on the polarization state of the input wave. Here, it has also been shown that the coupling length, L_π, for TE polarization is smaller than that for the TM polarization. A compact 1.6 mm long MMI-based polarization splitter has been designed to yield more than 8 dB polarization separation and only 0.11 dB optical loss.

Chapter 5

Polarization Rotators

5.1 Introduction

It is only in recent years that industries that manufacture and use photonic devices have become aware of the unexpected and undesirable polarization rotation, and consequent polarization dependent loss and polarization crosstalk that can occur in optoelectronic systems. In semiconductor optoelectronic systems, the optical modes in practical waveguides with two-dimensional confinement are highly hybrid (i.e. all the six components of the electro-magnetic fields are present), and therefore able to convert power between the polarization states if the modes are nearly phase matched and have an enhanced overlap between them. However, in order to obtain this conversion, some means of discontinuity should also exist along the propagation direction such as junctions, tapers, or bends. An important issue is to understand the physical process in such polarization conversion and to consider an appropriate design approach for its minimisation.

However the knowledge of the origin of such polarization crosstalk can be used in the design of compact low-loss polarization rotators (PRs). Polarization rotators can have different and important uses in the design of communication systems, such as in

polarization modulators (Heismann and Smith, 1996) to avoid polarization hole burning in transoceanic fibre links with concatenated EDFAs, in polarization switches (Morita *et al.*, 1999) for polarization division multiplexing, in polarization controllers (Hayashi *et al.*, 2001) to compensate polarization mode dispersion or in polarization diversity heterodyne receivers to manipulate the polarization states of the optical fields.

Over the last 10 years there has been a great interest in the design of effective polarization rotators. Polarization rotation in optical guided wave devices can be achieved by applying an electric field and exploiting the large electro-optic tensor component in semiconductor material (Schlak *et al.*, 1991) or in LiNbO$_3$-type materials (Alferness and Buhl, 1982). However the design of a *passive* polarization rotator is much preferred and the first such design was based on the pioneering work of Shani *et al.* (Shani *et al.*, 1991), which consisted of a number of butt-coupled and asymmetrically loaded waveguide sections.

In this chapter, some improved designs for various semiconductor passive polarization rotators, their characteristics, and a detailed study of fabrication tolerances are presented.

5.2 Cascaded polarization rotator design using slanted semiconductor rib waveguides

A passive polarization rotator may be made by using a number of uniform periodically butt-coupled waveguide sections to transfer power between the two fundamental TE and TM modes. These passive components may be simple to fabricate and require less processing. In the design of the optical waveguides for polarization rotator structures, it is necessary at the outset that the magnitude of the non-dominant field components of the fundamental TE and TM polarized modes increase and more significantly their field profiles be modified to increase the overlap with the dominant field components. It is also necessary to design optical waveguides with offsets between the sections such that a significant polarization rotation can take place at each junction. If the length of each waveguide section matches the half-beat length, L$_\pi$, of the fundamental

TE and TM modes, a constructive interference may lead to the maximum polarization conversion. Here the half-beat length, L_π, is defined as

$$L_\pi = \pi/(\beta_{TE} - \beta_{TM}) \tag{5.1}$$

where β_{TE} and β_{TM} are the propagation constants for the fundamental TE and TM polarized waves, respectively.

5.2.1 Waveguide Structures

To understand the hybrid nature of the optical modes in semiconductor waveguides, first a simple semiconductor rib waveguide with vertical sidewalls and symmetry along the vertical axis is considered for its evaluation. The schematic of the rib waveguide with vertical sidewalls is shown in **Fig. 5.1**.
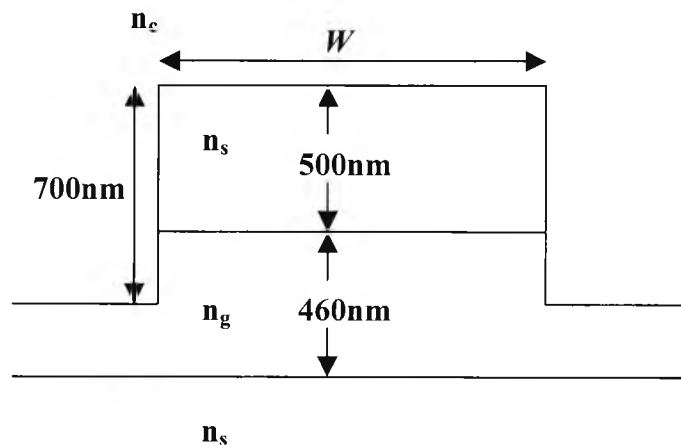
Fig. 5.1 Schematic of the rib waveguide with vertical sidewalls.

An InGaAsP epi-layer with a bandgap of 1.3 μm and a thickness 460 nm and a 500 nm thick InP top layer have been grown on an InP substrate. The guide (n_g), substrate (n_s) and top cladding (n_c) refractive indices are taken as 3.3907, 3.17 and 1.0, respectively, at the operating wavelength of 1.5 μm. The lateral confinement is achieved by etching a ridge of 700 nm high.

The optical modes in semiconductor waveguides are truly hybrid in nature, where the E_x and H_y components of the fundamental quasi-TE mode (H^y_{11}) (Marcatili, 1969) are the dominant field components. Similarly, E_y and H_x are the dominant field components for the quasi-TM (H^x_{11}) mode (Marcatili, 1969). Here, the **H**-field-based Vector Finite Element Method (VFEM) has been used to obtain the propagation constants and the modal field profiles of the uniform guided-wave sections. In this approach, often more than 40000 first order triangular elements with irregular cross sections have been used to accurately represent the waveguide structure.

The dominant H_y field component of the quasi-TE mode is shown in **Fig. 5.2**, when the guide width, W, is 2 μm. It should be noted here that this field profile is naturally symmetric along the vertical axis, due to the symmetry of the structure in that particular direction. **Fig. 5.3** shows the 3-dimensional field profile of the dominant H_y field of the quasi-TE mode, clearly showing the symmetric behaviour.
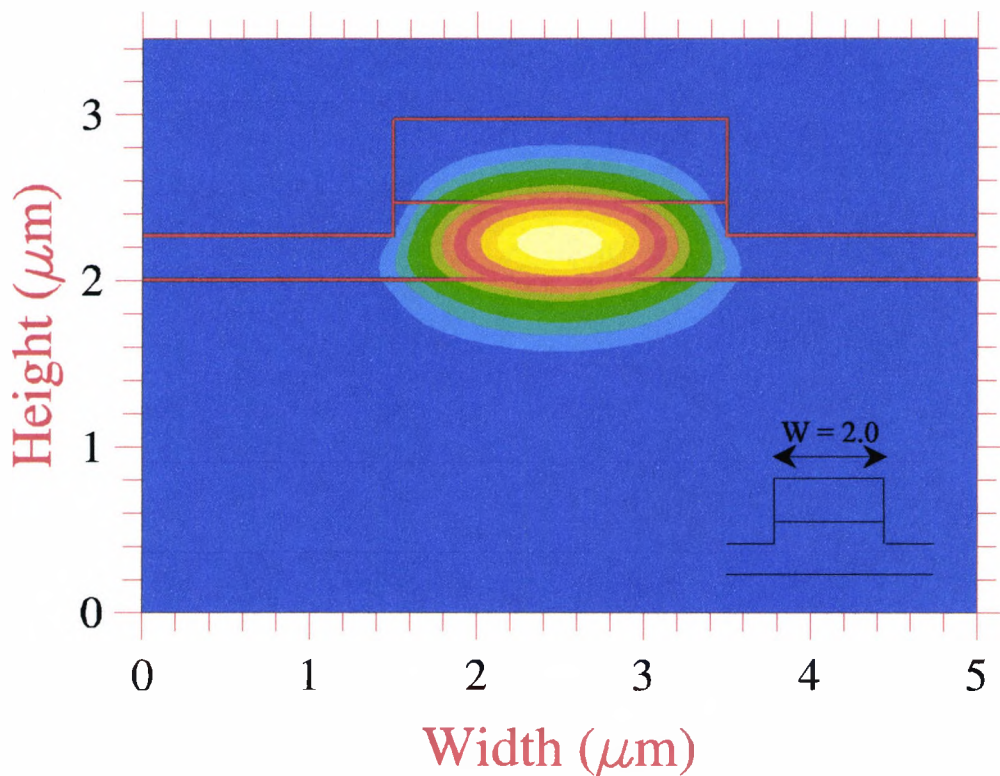
Fig. 5.2 The dominant H_y field component of the quasi-TE mode.
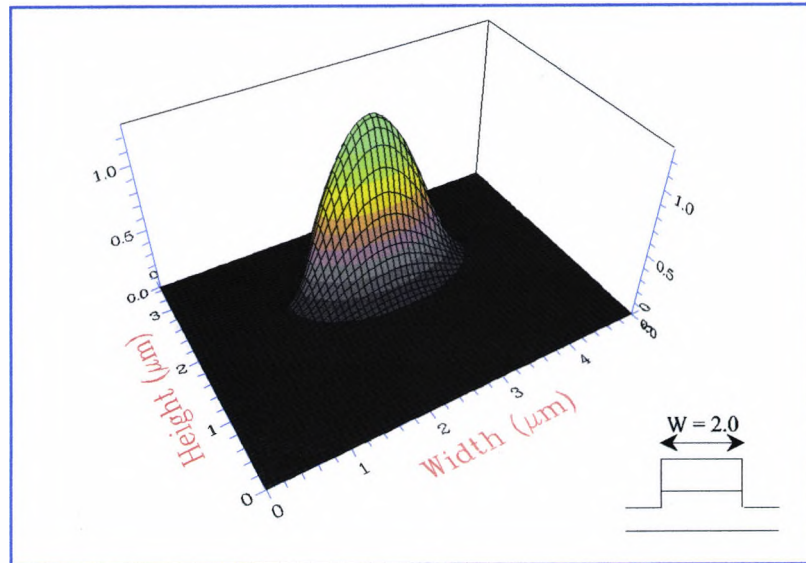
Fig. 5.3 The 3-dimensional view of the dominant H_y field of the H^y_{11} mode.

The non-dominant H_x field component of the H^y_{11} mode is shown in **Fig. 5.4**. This field profile is clearly shown to be anti-symmetric in nature. **Fig. 5.5** shows the 3-dimensional form of the non-dominant H_x field component of the H^y_{11} mode and its maximum magnitude is only ≈ 0.02, normalised to the maximum value of H_y. It should be noted that since all the three components of the **H**-field are continuous across the dielectric interfaces, the H_x contours do not show any singularities at the corners unlike the **E**-field components as was shown by both Van Der Tol *et al.*, and Tzolov and Fontaine (Van Der Tol *et al.*, 1995; Tzolov and Fontaine, 1996).
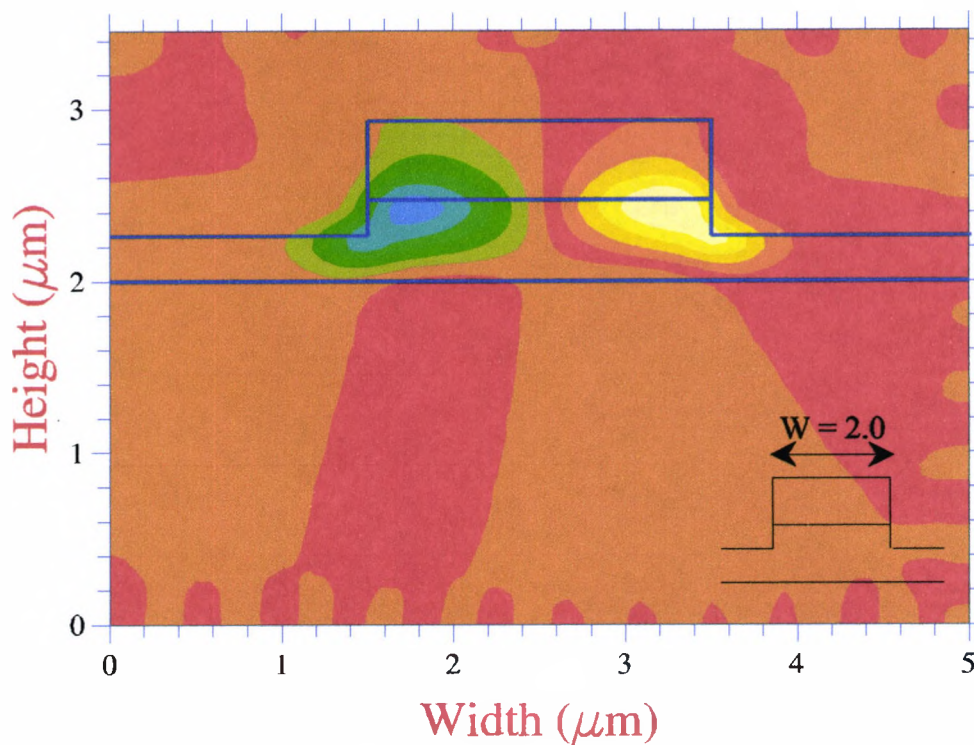
Fig. 5.4 The non-dominant H_x field component of the H^y_{11} mode.
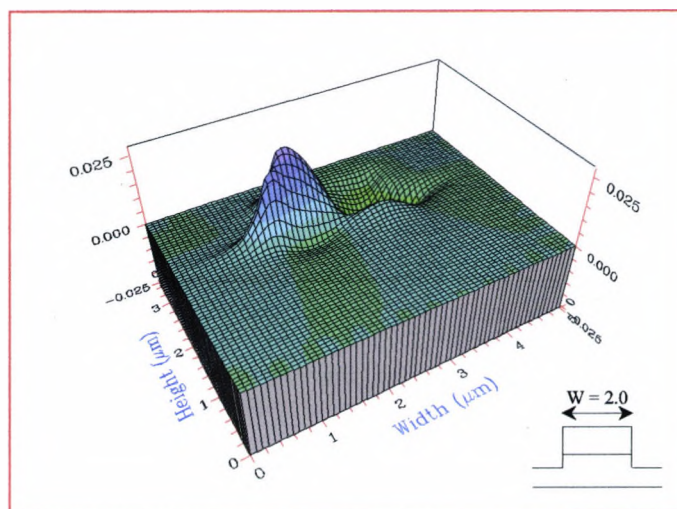
Fig. 5.5 The 3-D view of the non-dominant H_x field of the H^y_{11} mode.

The H_z component of the H^y_{11} mode is shown in **Fig. 5.6**. It can be seen that it has a different contour profile with its maximum values along the two horizontal interfaces.
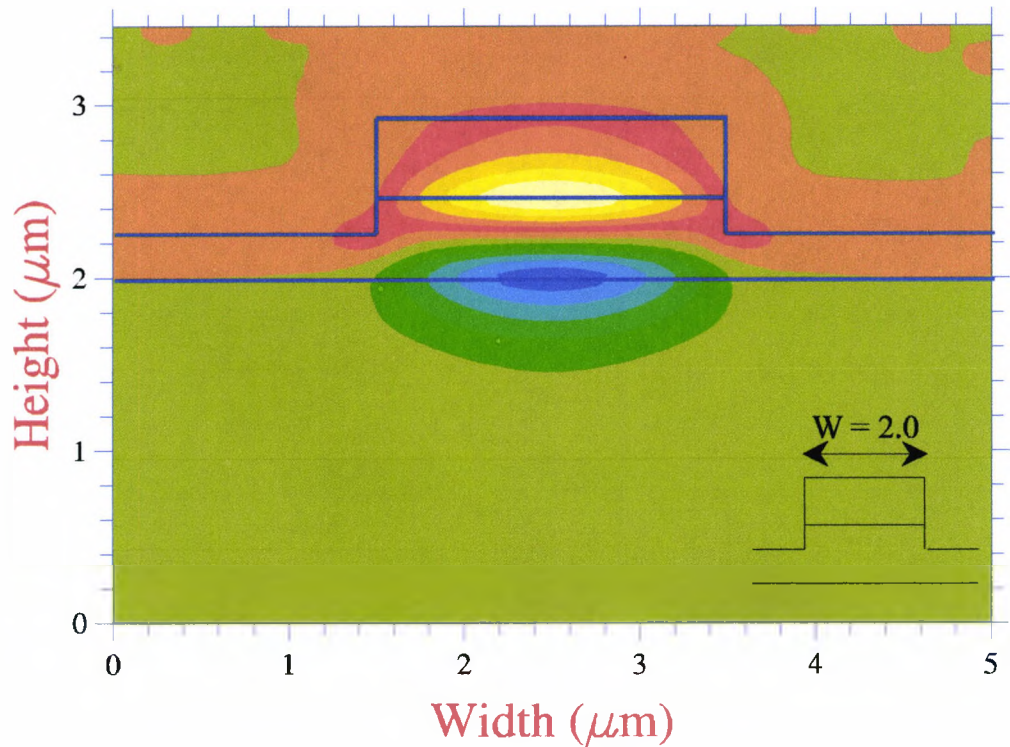
Fig. 5.6 The H_z component of the quasi-TE mode.

The H_x and H_y field profiles of the H^x_{11} mode are shown in **Fig. 5.7** and **Fig. 5.8**, respectively, and these field profiles show a similar behaviour as the H_y and H_x contours of H^y_{11} mode. Therefore the overlap between the non-dominant and dominant field component of both the TE and TM modes is very small, which gives a very low possibility of achieving polarization conversion. The H_z field profile for the quasi-TM mode is shown in **Fig. 5.9** giving a maximum field value along the vertical interface.
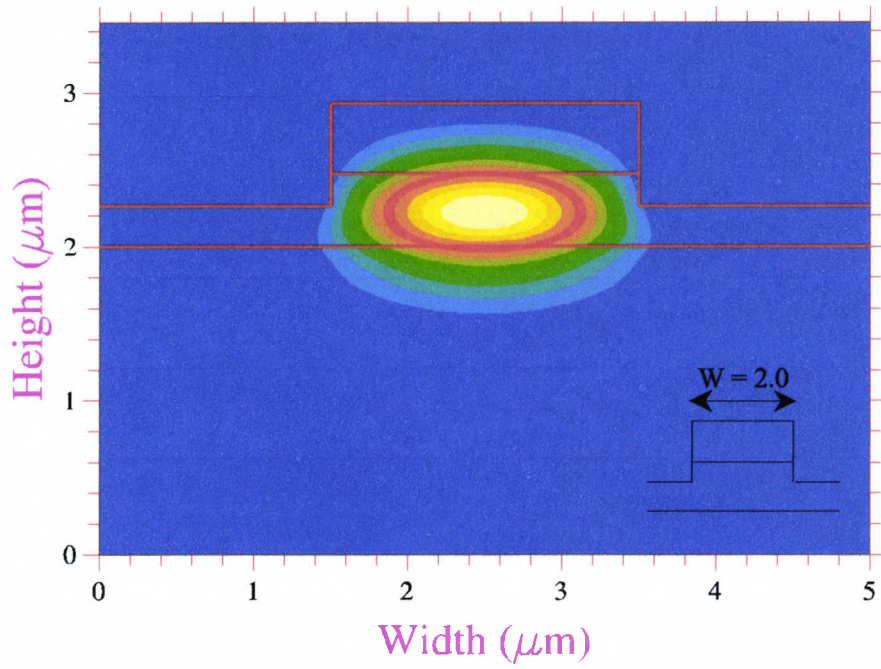
Fig. 5.7 The dominant H_x field profile of the H^x_{11} mode.
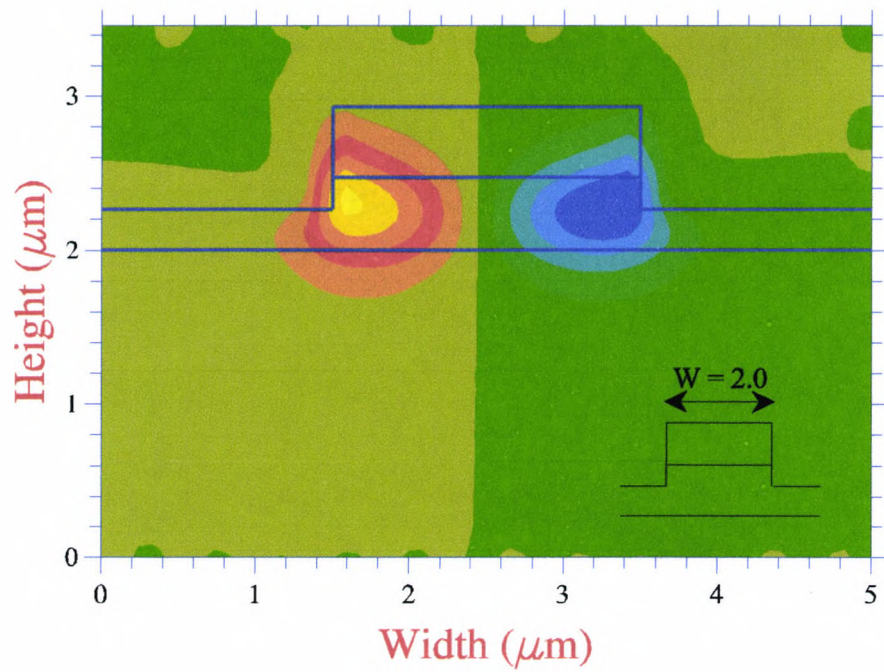
Fig. 5.8 The non-dominant H_y field profile of the H^x_{11} mode.
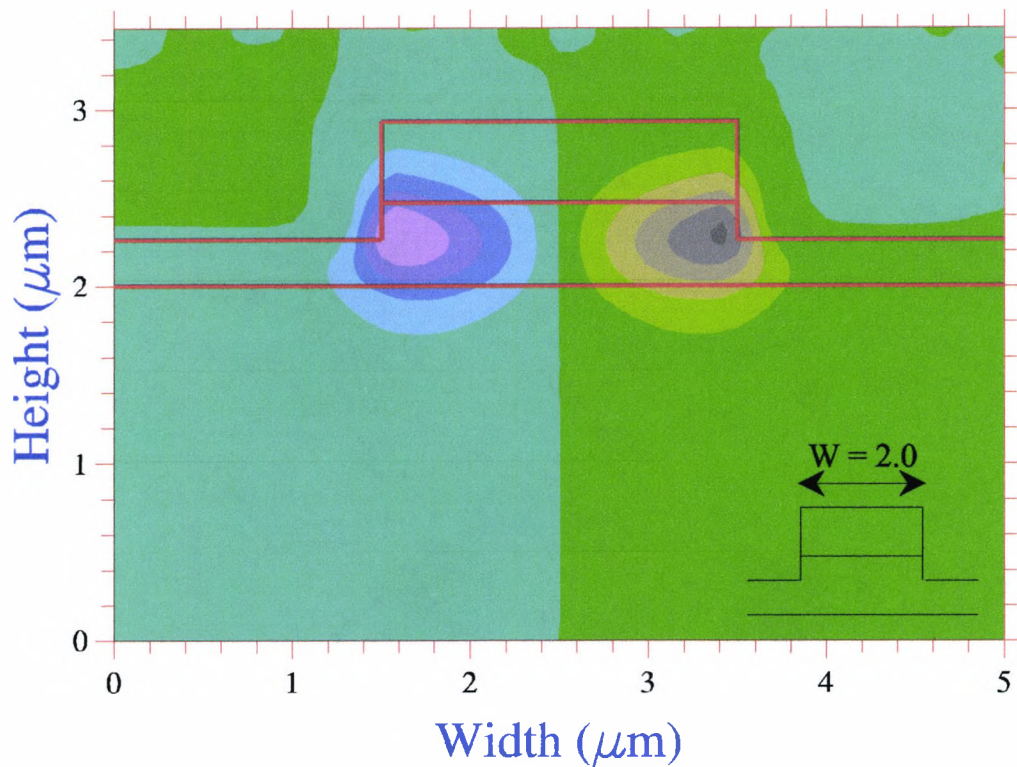
Fig. 5.9 The H_z field profile for the quasi-TM mode.

When fabricating, the sidewalls of a rib waveguide may not be vertical, particularly when wet etching is used. Slanting the sidewalls can affect the polarization coupling. A symmetrical rib waveguide has also been investigated, where both the sidewall angles are taken as 45°. The dominant H_y field of the quasi-TE mode is shown in **Fig. 5.10**, and the non-dominant H_x field is shown in **Fig. 5.11**. In this case, it has been noted that the non-dominant field magnitude increases considerably compared to that in the case of the rib waveguide with vertical sidewalls. However the non-dominant field profile remains anti-symmetric as clearly shown in **Fig. 5.11**.
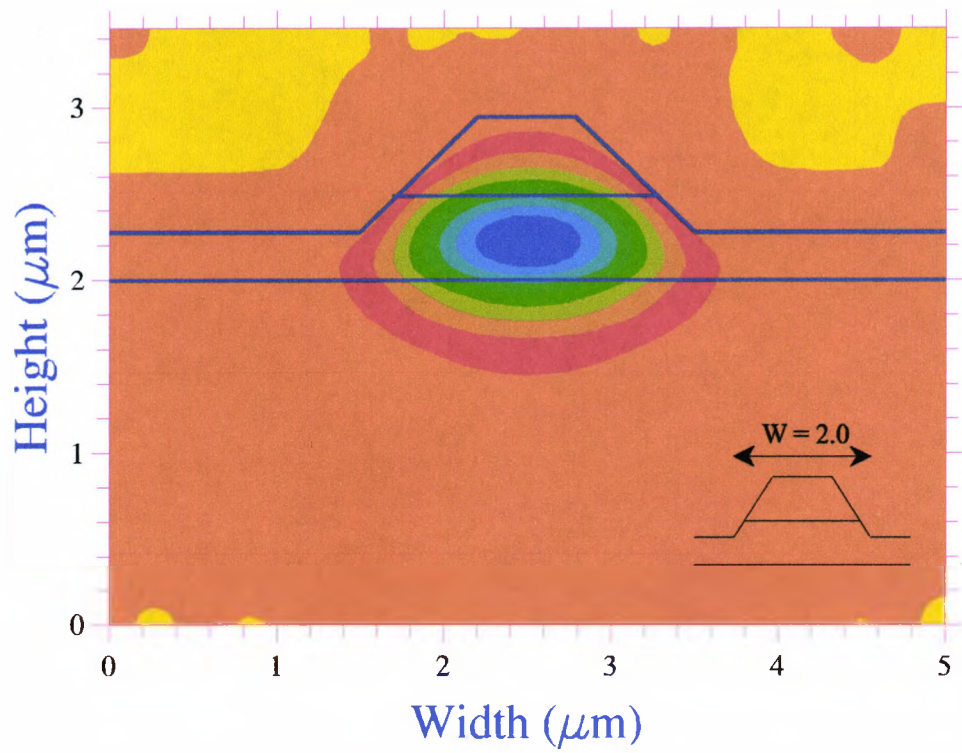
Fig. 5.10 The dominant H_y field of the quasi-TE mode.
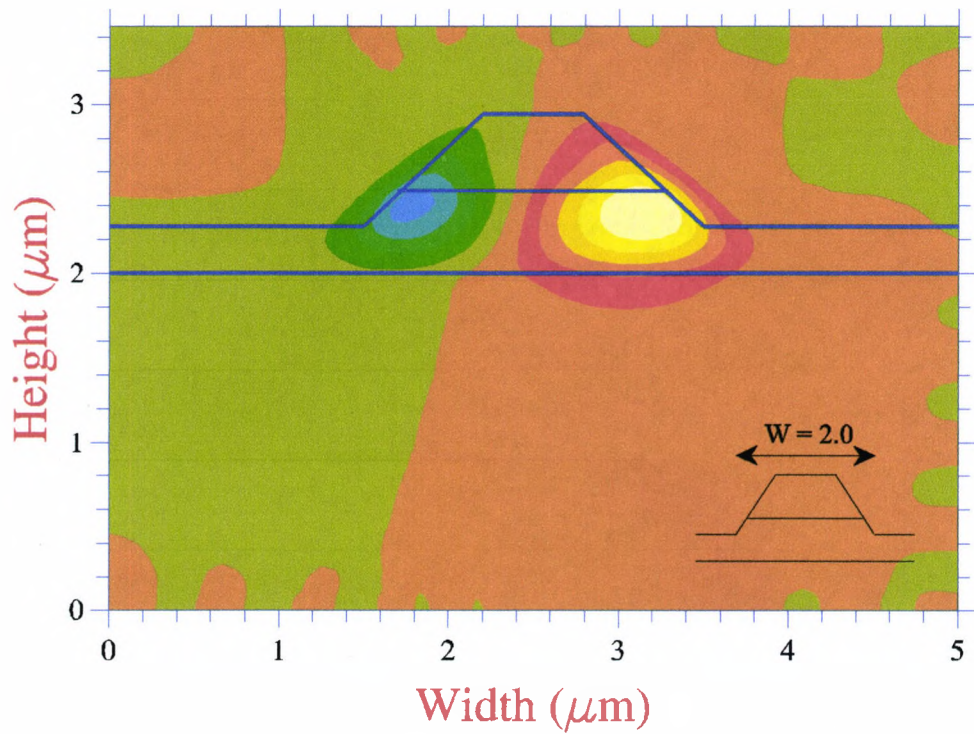
Fig. 5.11 The non-dominant H_x field of the quasi-TE mode.

A similar but non-symmetrical rib waveguide with only one slanted sidewall is considered which could be fabricated by considering both wet and dry etching. The schematic cross section of the slanted sidewall waveguide structure is shown in **Fig. 5.12** and in this case, the angle of the right sidewall is considered to be 45°. The dominant H_y field profile of the H^y_{11} mode is shown in **Fig. 5.13**, and it follows the shape of the slanted rib waveguide core. **Fig. 5.14** shows the non-dominant H_x field profile of the H^y_{11} mode. Here, however, it can be seen that this field profile is very similar to that of the H_y and H_x field of the H^y_{11} and H^x_{11} modes, respectively. For the H^y_{11} mode, the maximum H_x value is 0.1 normalised to the maximum value of H_y component, which is 5 times higher than that of in the case of vertical walled rib waveguide. Apart from the larger magnitude of the non-dominant field, the significantly modified contour profile clearly suggest an enhanced overlap between the vector field components of the quasi-TE and TM modes.
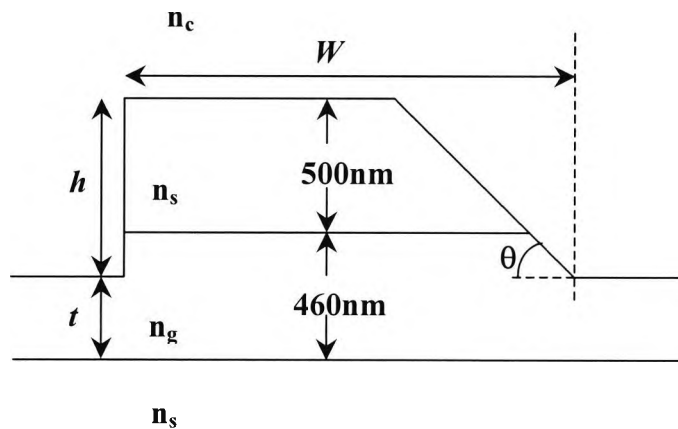
Fig. 5.12 The schematic cross section of the slanted sidewall waveguide structure.
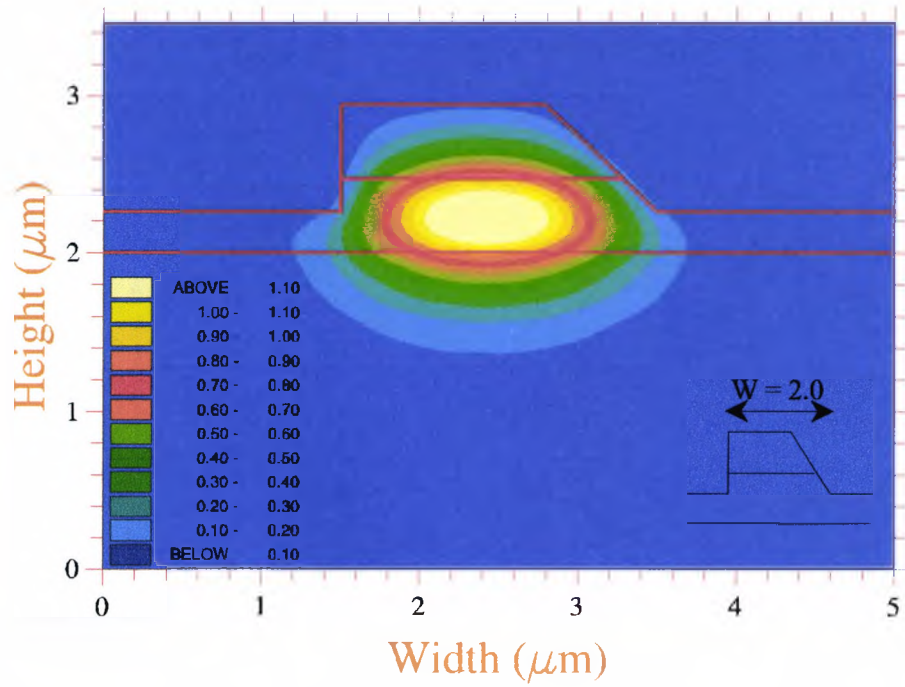
Fig. 5.13 The dominant H_y field profile of the H^y_{11} mode.
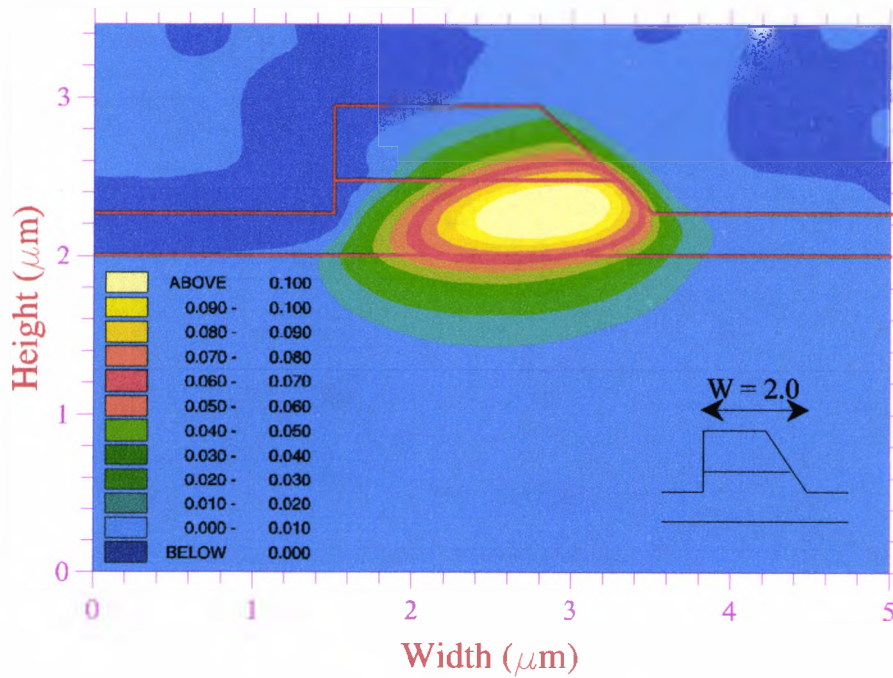
Fig. 5.14 The non-dominant H_x field profile of the H^y_{11} mode.

5.2.2 Analysis of the waveguide characteristics

In the design of a polarization converter, one of the main and most important objectives is to increase the non-dominant field values of the quasi-TE and TM modes. Therefore if the H_x/H_y ratio for the H^y_{11} mode or the H_y/H_x ratio for the H^x_{11} mode is high, there exists a higher possibility of achieving polarization rotation. The variation of the H_x/H_y of the H^y_{11} mode with the waveguide width, W, is shown in **Fig. 5.15**, for different types of waveguide structures. It can be observed that the non-dominant field increases its relative value when the guide width is reduced for all the three cases. However, it can be noted that this ratio is 5 times higher than in the non-symmetric waveguide when compared to the standard rib waveguide with vertical sidewalls. It can also be noted that for the non-symmetric waveguide, the H_x/H_y ratio increases from 0.09 to 0.17 when the rib width, W, is reduced from 2 to 1.5 µm, where as for the case of vertical sidewall rib waveguide, it is only increased from 0.03 to less than 0.04.
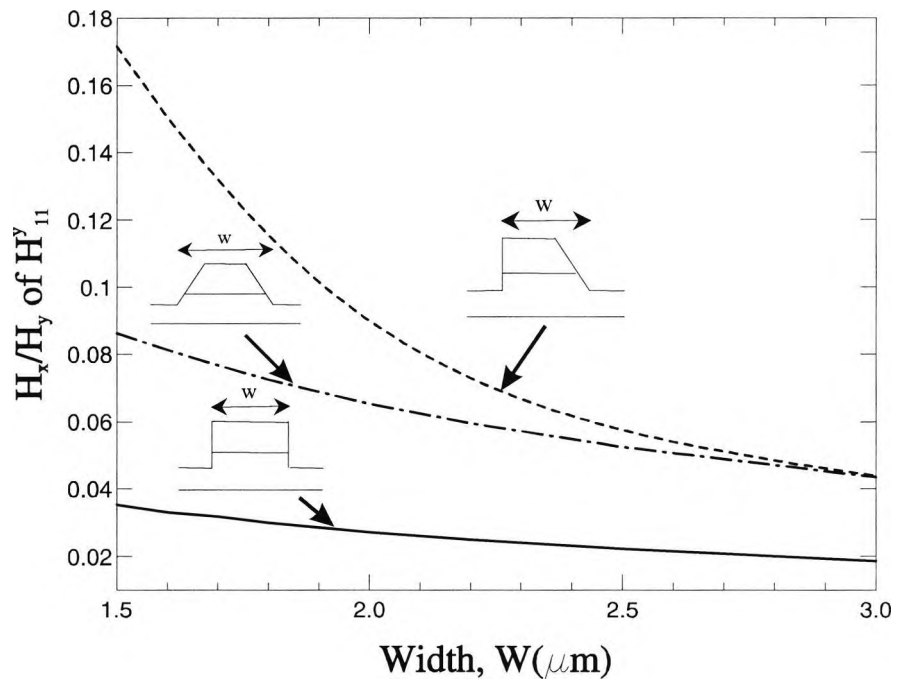
Fig. 5.15 The variation of the H_x/H_y for the H^y_{11} mode with the waveguide width.

Fig. 5.16 shows the variation of H_y/H_x ratio of the H^x_{11} mode with the waveguide width, for all the three cases. It shows a similar behaviour to that of the H^y_{11} mode and the ratio increases from 0.1 to 0.18 when the rib width, W, is reduced from 2 µm to 1.5µm, for the non-symmetric waveguide.
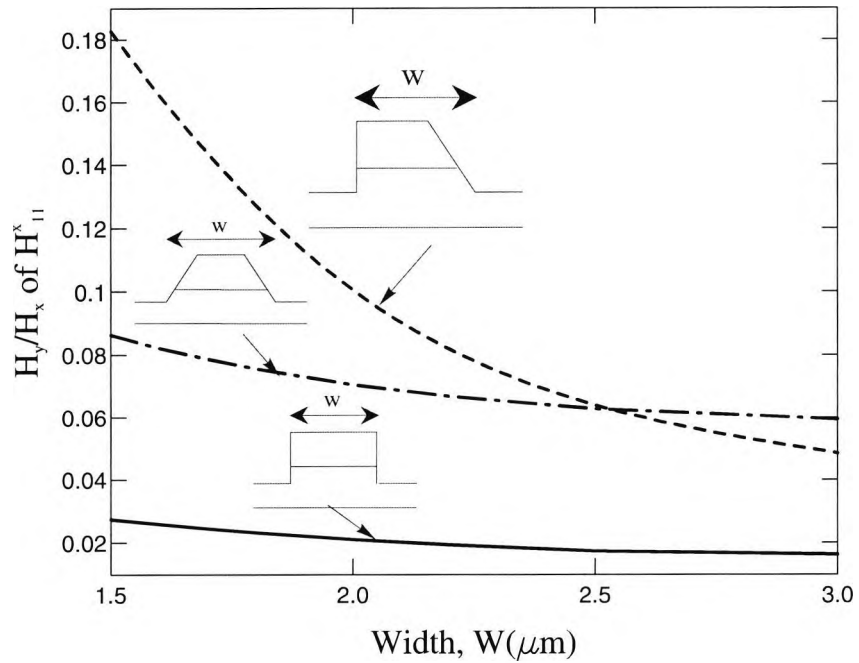
Fig. 5.16 The variation of H_y/H_x ratio of the H^x_{11} mode with the waveguide width.

It has been mentioned earlier that, besides the increment of the non-dominant field values, its overlap integral with the dominant component is also important. In this work, the overlap integral, γ, is defined as,

$$\gamma = \frac{\int H^y_{TE} \cdot H^y_{TM} \, d\Omega}{\int H^y_{TE} \cdot H^x_{TM} \, d\Omega} \qquad \text{for the TE mode} \qquad (5.2)$$

and,

$$\gamma = \frac{\int H^x_{TM} \cdot H^x_{TE} \, d\Omega}{\int H^x_{TM} \cdot H^y_{TE} \, d\Omega} \qquad \text{for the TM mode.} \qquad (5.3)$$

The normalisation has been carried out in terms of the H_y and H_x field components of the quasi-TE and quasi-TM modes, respectively, because these are the dominant components. The variation of the overlap integral with the waveguide width, W, for the quasi-TE mode, is shown in **Fig. 5.17**.
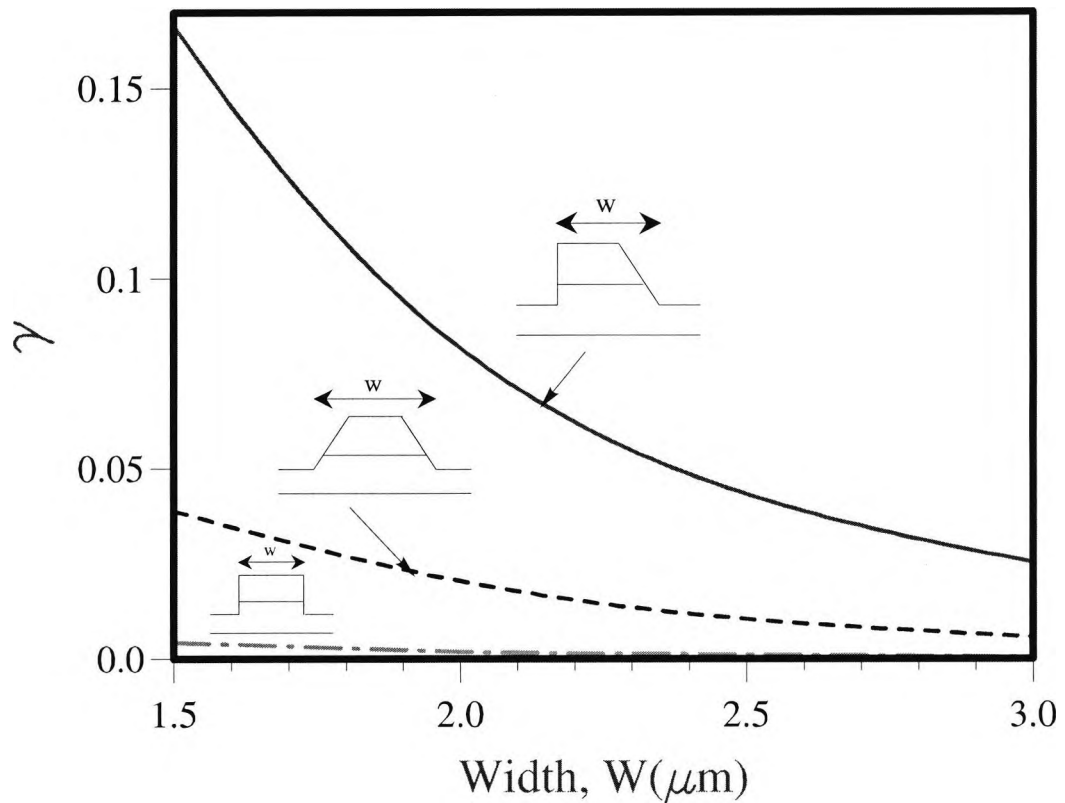
Fig. 5.17 The variation of the overlap integral, γ, with the waveguide width.

As expected, it can be seen that the overlap integral, γ, increases with the reduction of the rib width. It has been particularly observed that the γ value for a non-symmetrical rib waveguide is more than 40 times higher than that of the symmetrical guide at $W = 1.5$ μm, although the field ratio value is only 5 times higher and such a large enhancement was due to the abolition of the symmetry.

Another important parameter in designing a polarization rotator is the accurate calculation of the half-beat length, L_π, as this is necessary to calculate the cascaded waveguide sections precisely. The variations of the half-beat length with the rib width

for all the three cases are shown in **Fig. 5.18**. The half-beat length value of 84 μm for the asymmetric waveguide when W = 2 μm agrees with that from Van Der Tol *et al.*, (Van Der Tol *et al.*, 1995): however it can be noted that for W = 1.5 μm, the half-beat length is even smaller.
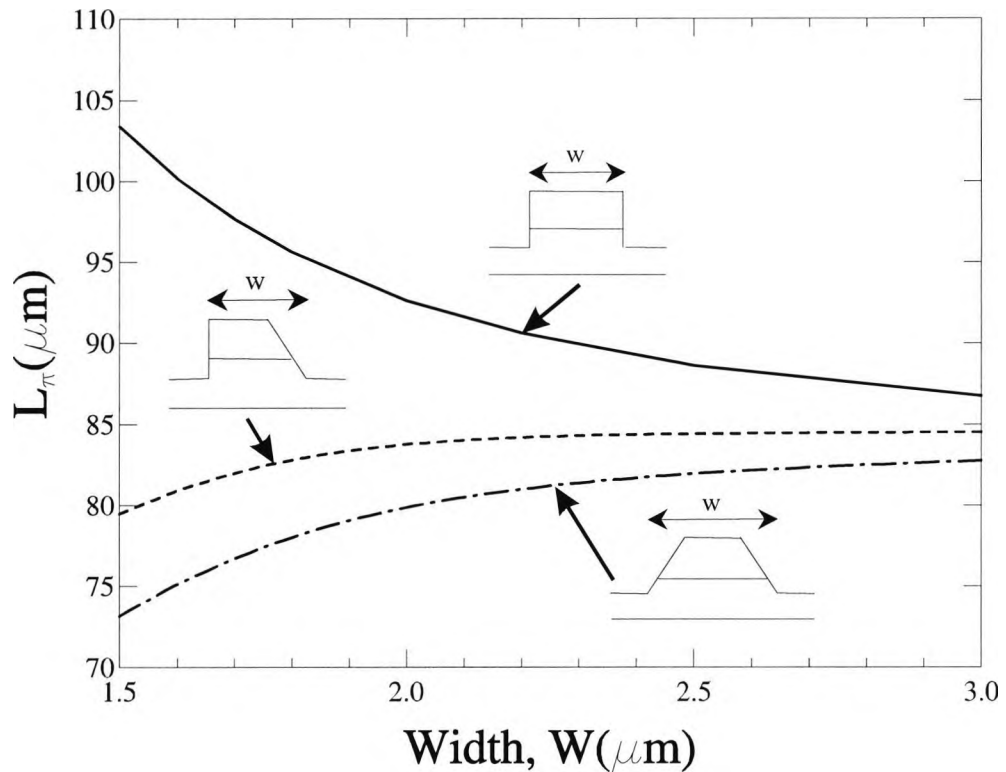
Fig. 5.18 The variations of the half-beat length with the rib width, W.

5.2.3 Simulation results of the power conversion characteristics

A more detailed study of a 1.5 μm wide one side slanted rib waveguide is considered for optimisation of the whole polarization rotator design. In this case, a periodic non-symmetrical offset is introduced to couple uniform sections with opposite angled sides as shown in **Fig. 5.19**.
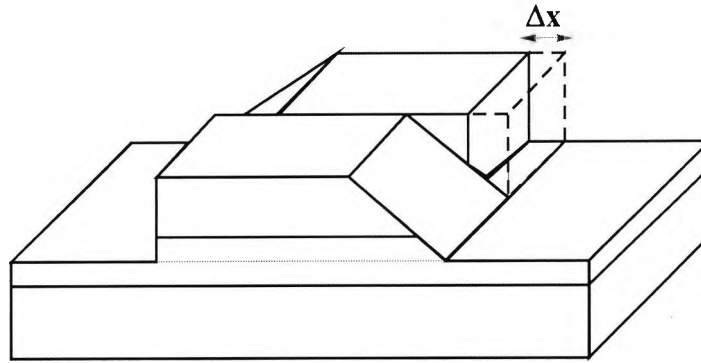
Fig. 5.19 Coupling of the uniform waveguide sections with lateral offset, Δx.

For the junction analysis of the two waveguide sections, the rigorous and more accurate Least Squares Boundary Residual (LSBR) approach (Rahman and Davies, 1988) has been employed. When a TE mode of the first waveguide is incident on the second waveguide, it excites two highly hybrid TE and TM modes. The LSBR method is used to calculate the transmission coefficients, τ_{ee} and τ_{em}, of the excited TE and TM modes respectively. Since the fields in two sections are not symmetric and also not aligned, an additional offset between the guides is necessary to improve the mode conversion and also to reduce the insertion loss. The variation of the transmission coefficients with the lateral offset, Δx, is shown in **Fig. 5.20**, when the TE mode is incident on the junction interface. It can be noted that at $\Delta x = 150$ nm, the TE to TM conversion is maximum. In this case, the maximum τ_{em} value is 0.3 which will rotate the polarization state by $18°$ at each interface according to this particular equation given by (Van Der Tol *et al.,* 1995),

$$P_c = Sin^2 \, (CN) \qquad\qquad\qquad (5.4)$$

N denotes the number of junctions and C is the so-called coupling coefficient. For complete conversion their product must be equal to $\pi/2$. Therefore, when N = 1, $P_c =$ 0.09,

$$0.09 = Sin^2 \, C$$
$$Sin \, C = 0.3$$
$$C \approx 18°$$

Hence, for complete conversion only 5 junctions are required to convert most of the optical power from one polarization state to another. So the overall device length is expected to be less than 400 μm, yielding a much shorter device than earlier reported (Van Der Tol *et al.*, 1995).
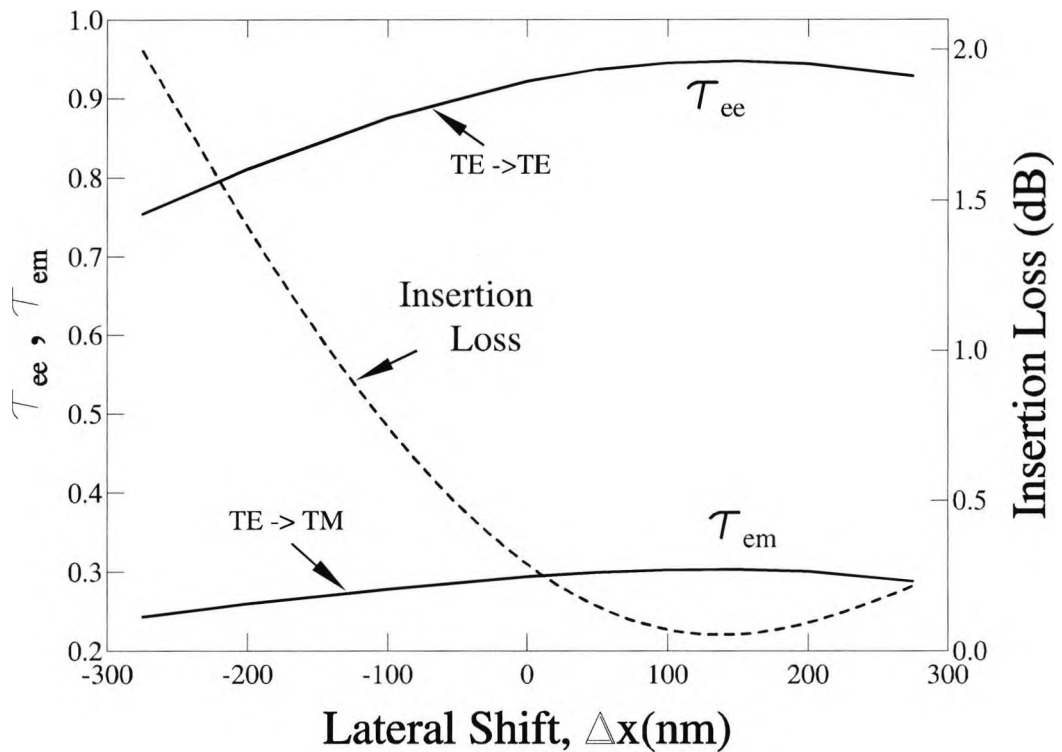
Fig. 5.20 Variation of the excited quasi-TE (τ_{ee}) and TM (τ_{em}) coefficients and insertion loss at each interface with lateral offset between the guides.

The variation of the insertion loss with the lateral offset, Δx, is also shown in **Fig. 5.20**. At $\Delta x = 150$ nm, the optical power loss at each interface is minimum and calculated to be lower than 0.04 dB. So therefore the total insertion loss for all the 5 sections will be less than 0.2 dB. **Fig. 5.21** shows the H_y field profiles of the two waveguides with opposite angled sides. Here the lateral offset is shown, this being used in order to exactly align the field profiles, and it is equal to 150 nm. Hence, at this point, the maximum power conversion could be expected to be as shown in the previous **Fig. 5.20**.
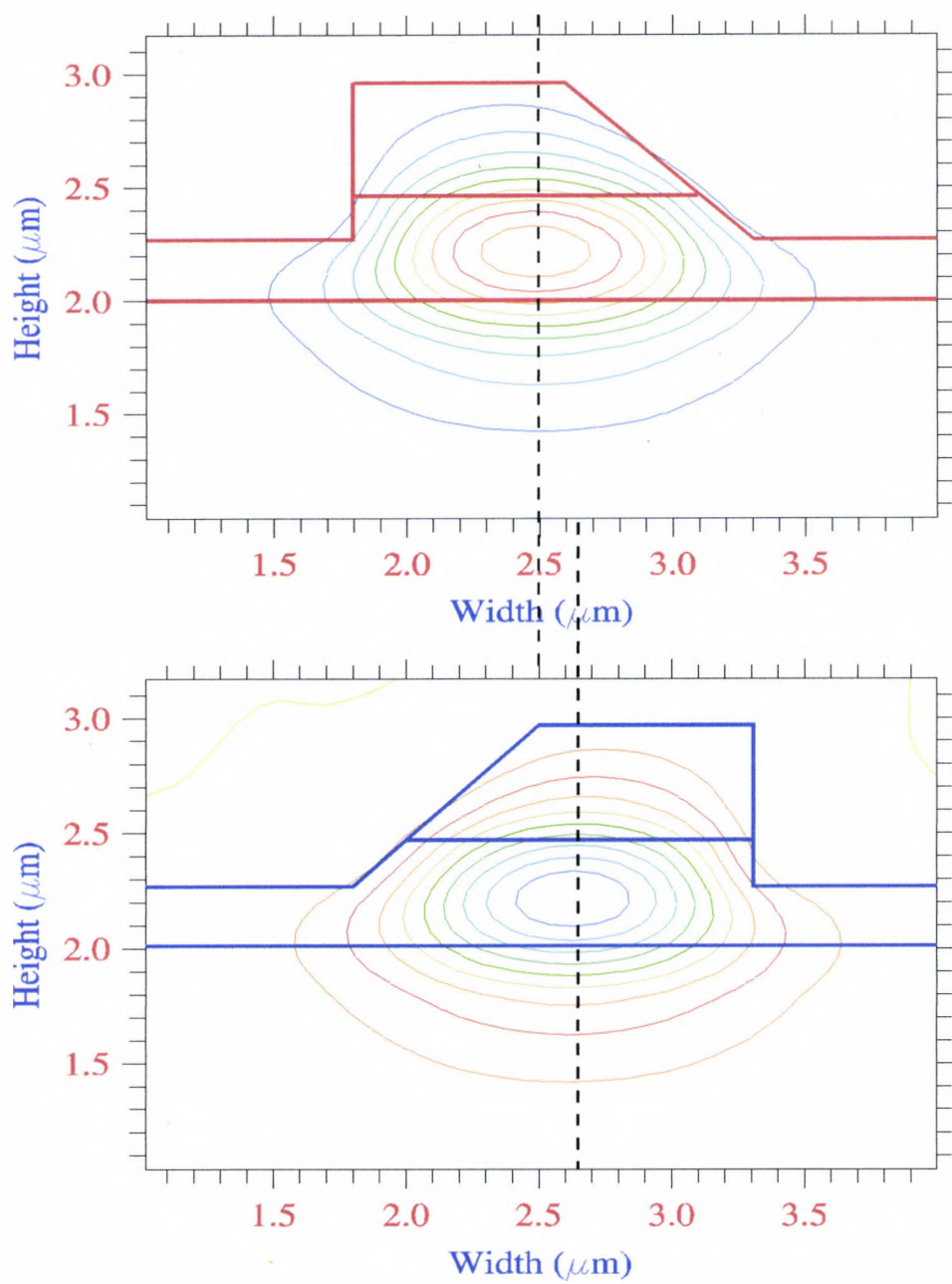
Fig. 5.21 H_y field profiles of the two waveguides with opposite angled sides.

5.3   Single-section passive polarization rotator

Only recently it has been reported that it is possible to achieve polarization rotation in a single-section design (Tzolov and Fontaine, 1996). Huang *et al.* has reported (Huang *et al.*, 2000) the fabrication of a single-section passive polarization converter on GaAs/AlGaAs. In this case, it is important to design a polarization rotating waveguide (PRW) that can support the quasi-TE and quasi-TM modes, which are highly hybrid with nearly equal H_y and H_x field amplitudes and very similar intensity distributions. The degree to which these modes are hybrid (the 'hybridity') is such that the effective polarization angles are 45° from the vertical or horizontal axes for the two polarization states. In such a case, when a nearly pure TE polarized mode is introduced into the longitudinally invariant PRW, from a standard input waveguide (IW) that supports modes with very little degree of hybridisation, and as shown in **Fig. 5.22**, this incident mode only supports the fundamental quasi-TE and TM modes which are excited with almost similar modal amplitudes. However, as the two modes propagate along the PR waveguide, at half-beat length, L_π, they are out of phase and their combined modal fields produce a nearly pure H_x field. At this position, this TM mode requires collection by an output waveguide (OW), which supports a nearly pure TM mode.
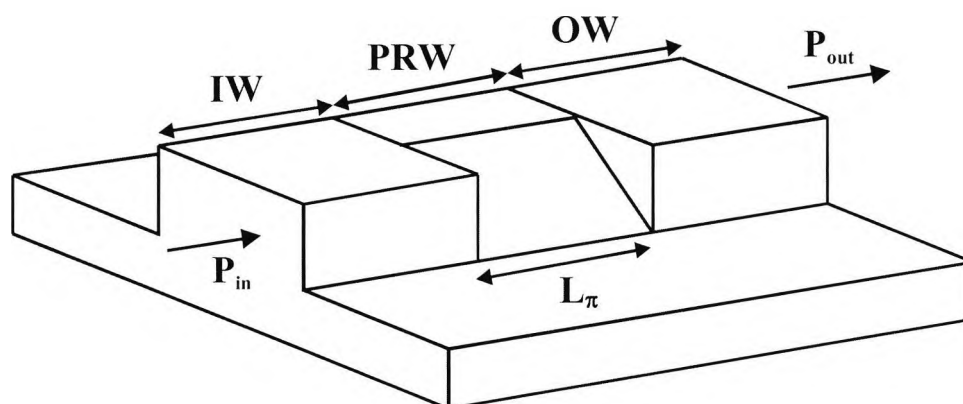
Fig. 5.22 Schematic representation of the single-section polarization rotator.

In this Section 5.3, an improved design of a polarization rotator, based on a single asymmetrical slanted rib waveguide is fully analysed using full vectorial numerical approaches. Since the design of such devices depends on the accurate characterisation

of semiconductor waveguides with truly hybrid modes, a vector rigorous approach is mandatory.

5.3.1 Numerical approaches

Fully vectorial numerical approaches are necessary for the analysis and quantification of polarization rotation. To calculate accurately the vector field profiles, a full vectorial modal solution approach is necessary. Over the last 20 years, various numerical methods have been developed and used to obtain the modal solutions of optical waveguides. The main advantage of the finite-element method (FEM) over the other methods, such as the finite-difference method (FDM), is that a more accurate representation of the waveguide cross-section is possible. A waveguide with a slanted sidewall is often represented in the FDM by a staircase approximation (Weinert and Heidrich, 1993): however, in the case of the FEM, this slanted sidewall can be represented exactly as shown in **Fig. 5.23**. Additionally, since the modes in a semiconductor optical waveguide are hybrid in nature, a full vectorial approach is mandatory (Rahman and Davies, 1984*a*), and more particularly to study the polarization dependence or conversion. For an optical waveguide, all three components of the vector **H**-field are continuous across the dielectric interface, unlike for the alternative **E**-field formulation, where some of the components are discontinuous. It can be noted that for hybrid modes, the non-dominant field components are around the dielectric interfaces, and some of the alternative approaches, such as those based on the **E**-field formulation (Van Der Tol *et al.*, 1995; Tzolov and Fontaine, 1996), could be less than satisfactory to quantify these non-dominant components with sufficient accuracy to provide the basis of an adequate design. To retain the numerical stability, Huang *et al.*, (Huang *et al.*, 2000), had to consider artificial smoothing of the strong semiconductor/air interfaces over a specific length. The finite element method, based on the vector **H**-field formulation (Rahman and Davies, 1984*a*), has been established as one of the most accurate and yet numerically efficient approaches and is widely used to obtain modal fields. Since the polarization dependence arises due to the large index difference at the dielectric interfaces and the slant sidewall enhances this effect, a correct representation of the slanted sidewall and the boundary conditions is expected to be crucial in the analysis of a polarization rotator. This vector FEM (VFEM) modal solution technique can also

be used to calculate the half-beat length between the two polarized modes and give an accurate calculation of this parameter, which is necessary to identify the length of the periodic uniform sections for phase corrections.

Since the PR considered here is composed of three butt-coupled uniform waveguide sections with only two interfaces between them, an alternative junction analysis approach is also considered here. The modal fields of the three uniform sections may be obtained by the use of VFEM. Subsequently the least squares boundary residual (LSBR) method (Rahman and Davies, 1988) is employed to calculate the scattering coefficients of the two hybrid modes at the junction interfaces.

FD mesh   FE mesh
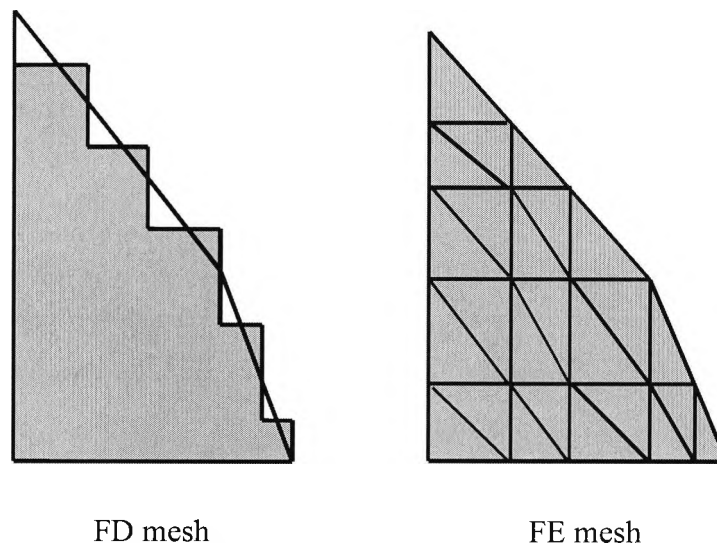
Fig. 5.23 Representation of the slanted sidewall by using the FDM and FEM.

5.3.2 Characteristics of the input-output waveguides

Since the single section polarization rotator considered here consists of semiconductor rib waveguides, two with vertical sidewalls and one with a slanted sidewall, it is necessary to evaluate the hybrid nature of their optical modes in order to obtain an efficient polarization rotator. A schematic structure of the waveguide is shown in **Fig. 5.24**.
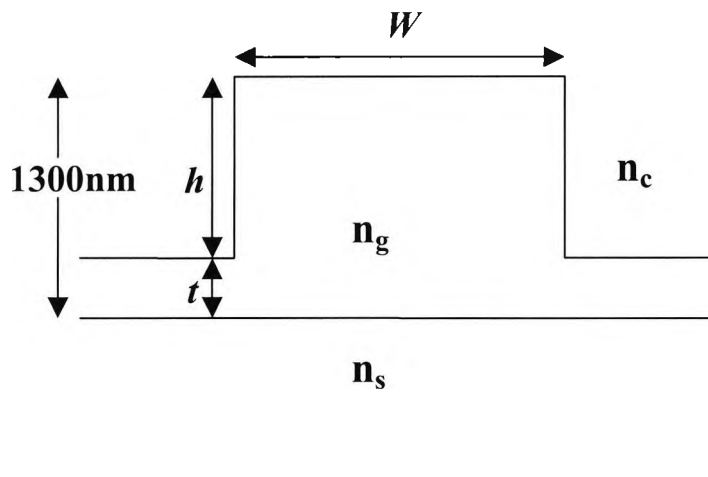
Fig. 5.24 Cross section of the input waveguide.

To fabricate the design presented here, first a 1300 nm thick GaAs epilayer should be formed on $Al_{0.1}Ga_{0.9}As$ substrate. Next lateral confinement could be achieved by etching a ridge (h) of 1200 nm in height. The guide (n_g), substrate (n_s), and cladding (n_c) refractive indices are taken as 3.37, 3.324 and 1, respectively, at the operating wavelength of 1.55 μm.

As mentioned earlier in Section 5.2, the optical modes in the semiconductor waveguides are truly hybrid in nature. The E_x and H_y components are the dominant field components of the quasi-TE (H^y_{11}) mode. The dominant H_y field component of the quasi-TE mode is shown in **Fig. 5.25**, for the case where the width of the waveguide, W, is 2.5 μm. The field profile clearly shows a symmetric behaviour, since the waveguide itself is symmetric along the vertical axis. The non-dominant H_x field component of the H^y_{11} mode is shown 3-dimensionally in **Fig. 5.26**, in order to show clearly the anti-symmetric behaviour. Its maximum magnitude is only 0.007, normalised to the maximum value of H_y.

Mode conversion only takes place at the waveguide discontinuities, but for the waveguides shown above, it is very unlikely that a reasonable polarization rotation would be achieved. This is mainly due to the very dissimilar field amplitudes and the symmetric and anti-symmetric nature of the dominant and non-dominant field profiles

of the polarized modes, thereby giving a very small overlap integral at the discontinuity junctions.
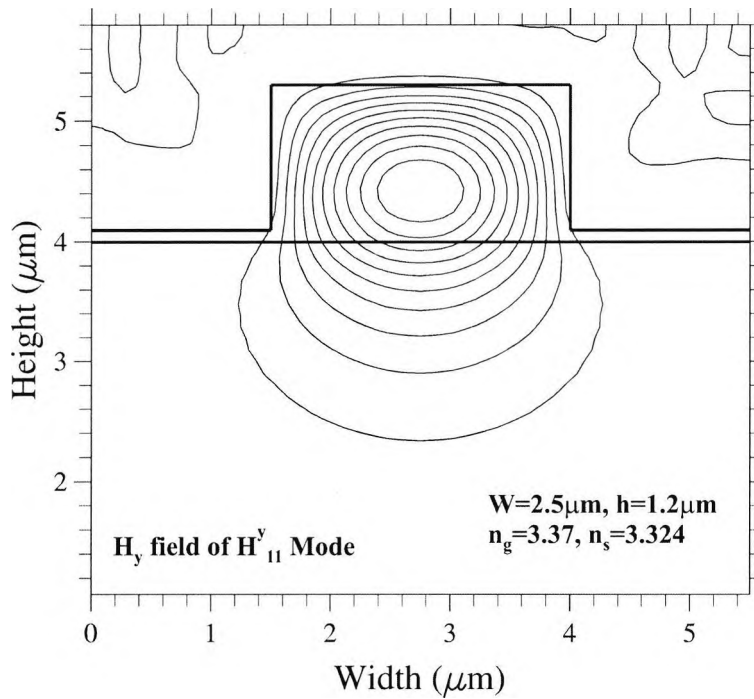
Fig. 5.25 Dominant H_y field component of the quasi-TE mode.
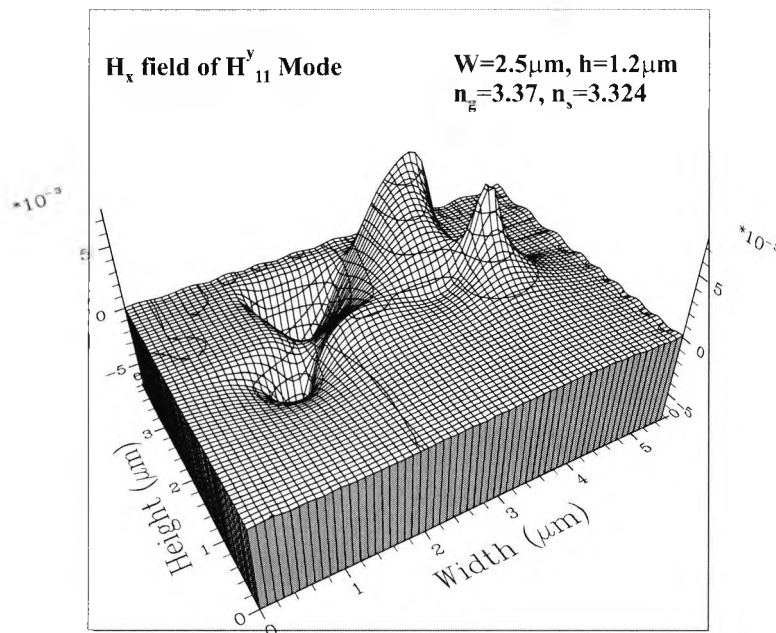
Fig. 5.26 3-D form of the non-dominant H_x field component of the H^y_{11}.

5.3.3 Simulation results of the PRW

Next, the PRW with a slanted sidewall is considered for evaluation. The schematic of the cross section of the waveguide is shown in **Fig. 5.27**, where this could be fabricated by combining the wet and dry etching steps.
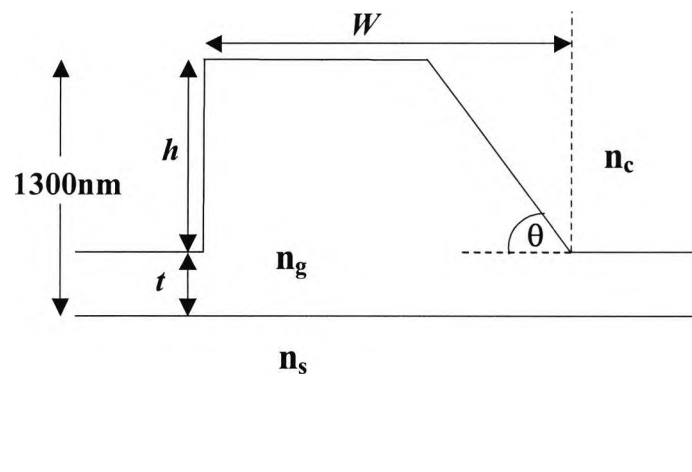
Fig. 5.27 The cross section of the PR waveguide with a slanted sidewall.

In the first example, the angle of the right sidewall with respect to the horizontal axis is considered to be 52°, as this could naturally be formed when wet etching is used. The dominant H_y field profile of the H^y_{11} mode is shown in **Fig. 5.28(a)** and it follows the shape of the slanted rib waveguide core. The non-dominant H_x field profile of the H_y^{11} mode is shown in **Fig. 5.28(b)**. Here, however, the field profile is very similar to that of the dominant H_x and H_y field profiles of the H^x_{11} and H^y_{11} modes respectively. The maximum H_x value is 0.46 (normalised to the maximum value of the dominant H_y component), which is 60 times higher when compared to that of the rib waveguide with vertical sidewalls.

(a)

(b)
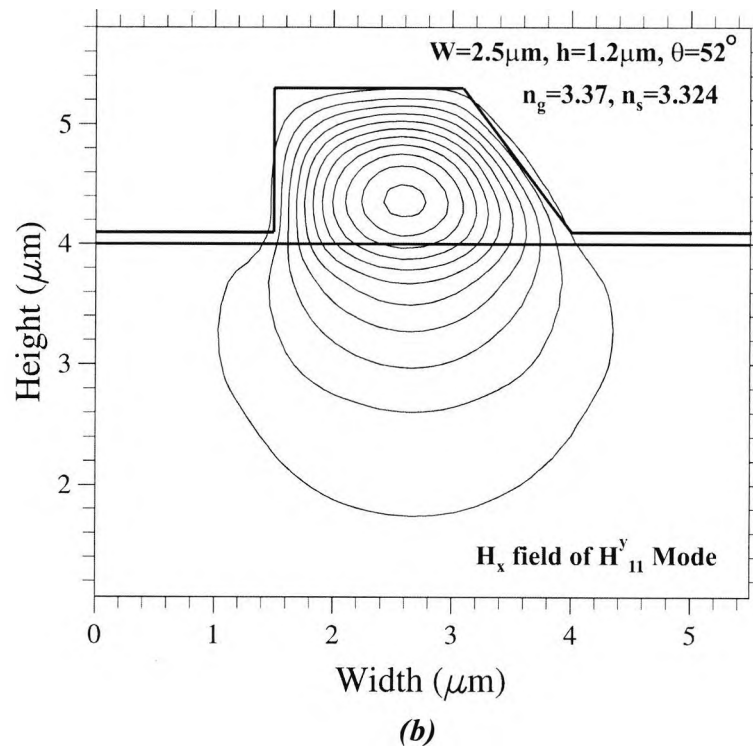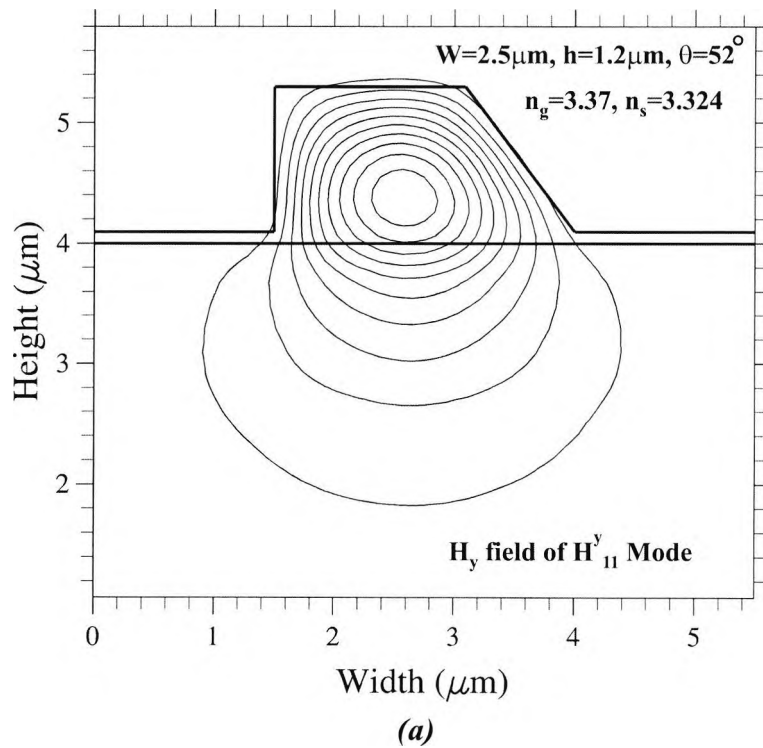
Fig. 5.28 Contour plots of the *(a)* dominant H_y and *(b)* non-dominant H_x field profiles of the H^y_{11} mode.

The variation of the non-dominant/dominant field component ratios (H_x/H_y for H^y_{11} mode and H_y/H_x for the H^x_{11} mode) with the waveguide width, W, is shown in **Fig. 5.29**. From the figure, it can be clearly seen that the hybrid nature is enhanced by reducing the waveguide width, W. When $\theta = 50°$, the H_y/H_x ratio of the H^x_{11} mode increases up to 0.8 as the width, W, is reduced to 2.5 μm. It can be observed that if the width is reduced further, the waveguide cannot support a guided mode. However, for higher slant angles, the degree to which the mode is hybrid can be enhanced further and brought near to unity, by reducing the waveguide width, must be considered. When the slant angle $\theta = 52°$, the H_y and H_x components of the H^x_{11} mode have nearly equal amplitudes as shown by the dashed line, when $W = 2.4$ μm. Another important aspect that was observed is that the hybrid nature of the H^y_{11} mode, shown by a solid line, is slightly lower than that of the H^x_{11} mode.
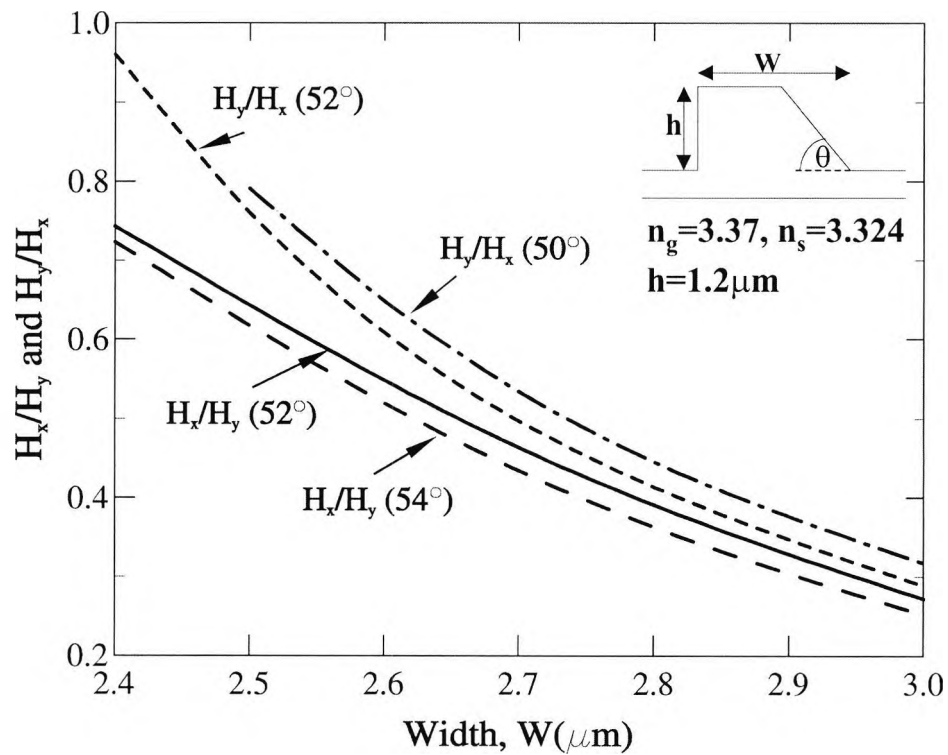
Fig. 5.29 Variation of the non-dominant/dominant field component ratios with the waveguide width.

The variation of the half-beat length, L_π, with the waveguide width is shown in **Fig. 5.30**, as such a length of the hybrid PR waveguide section is needed to reverse the existing polarization state. Three curves are shown for three different slant angles. In **Fig. 5.29**, it was shown that a reduction in waveguide width, *W*, will enhance the polarization rotation: however this figure shows that the device length will be slightly increased. As the slant angle increases, the device length also increases gradually. When $\theta = 54°$, the L_π increases from 661 μm to 772 μm, when *W* is reduced from 3μm to 2.4 μm.
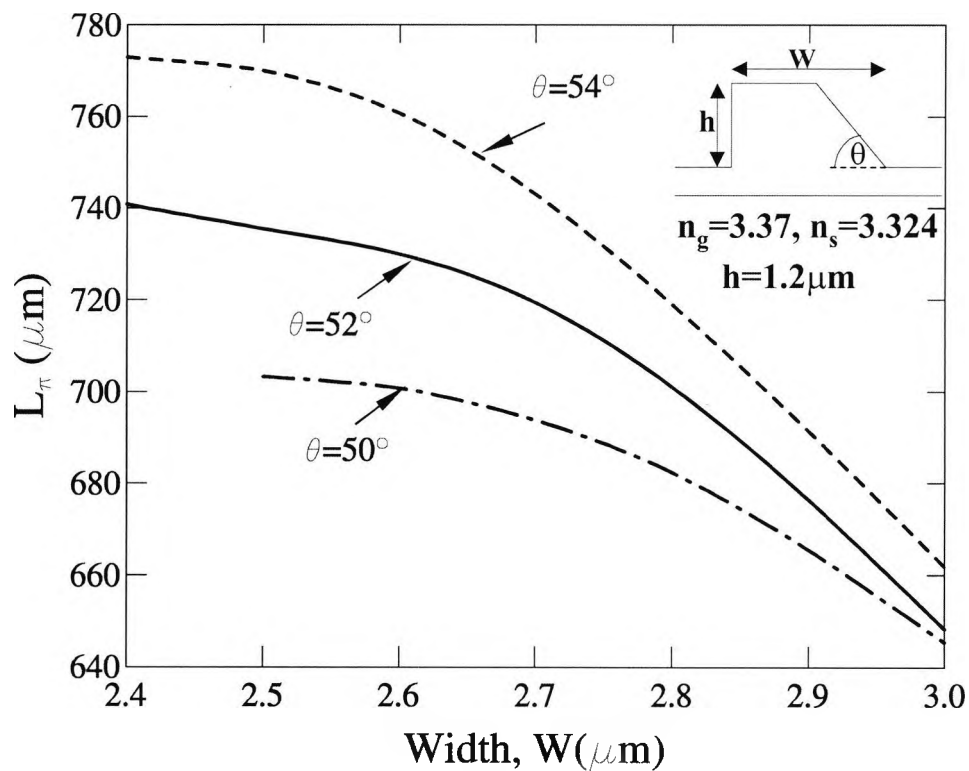
Fig. 5.30 Variation of the half-beat length, L_π, with the waveguide width.

Next, the waveguide width is kept constant at $W = 2.5$ μm, to study the effect of the slant angle, θ, on the hybrid nature and the half-beat length. The variation of the half-beat length, L_π, and the H_x/H_y and H_y/H_x ratios for the $H^y{}_{11}$ and $H^x{}_{11}$ modes, respectively, with the slant angle, θ, are shown in **Fig. 5.31**.
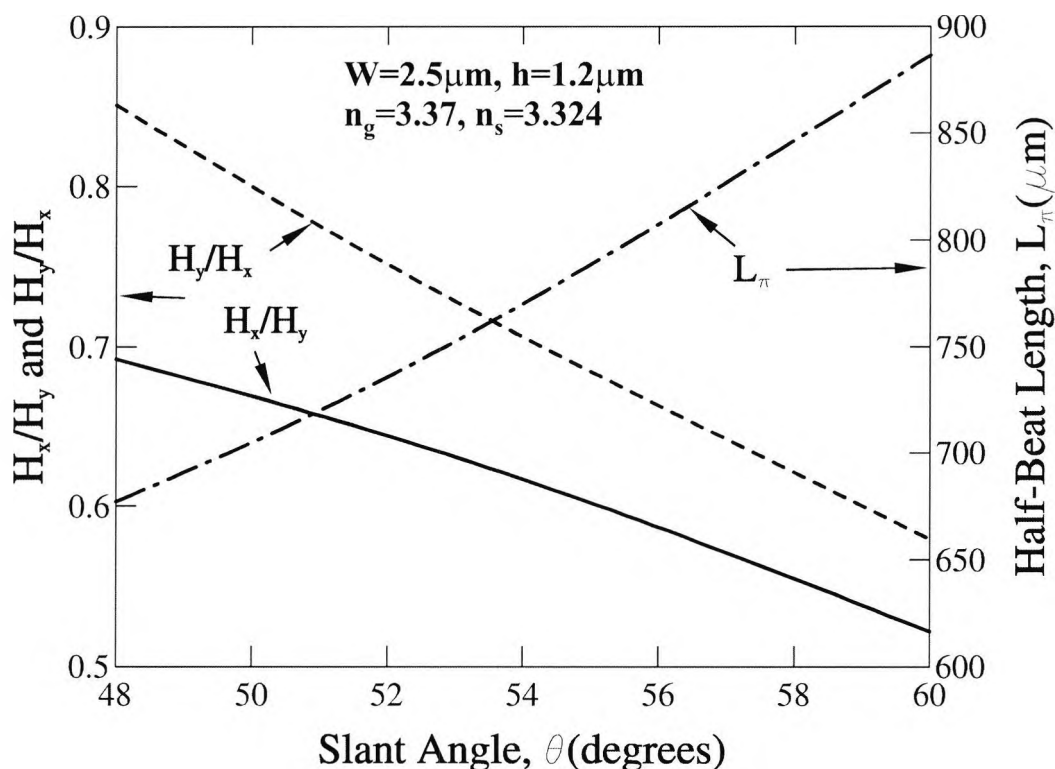
Fig. 5.31 Variation of the field component ratios and half-beat length, with the slant angle, θ.

It can be seen that as the slant angle is reduced from 60° to 48°, the H_x/H_y ratio of the H^y_{11} mode, as shown by a solid line, has increased from 0.52 to 0.69. The ratio of H_y/H_x for the H^x_{11} mode is also shown here by a dashed line and it can be noted clearly that generally the quasi-TM modes are slightly more hybrid than their counterpart quasi-TE modes. It is also shown that the L_π reduces from 887 μm to 680 μm as the slant angle is reduced from 60° to 48°. Overall, when the slant angle is reduced, the polarization conversion is enhanced and also the half-beat length is reduced which are essential for a polarization rotator design, unlike in the case of the reduction of width.

In this study, the effect of index contrast, $\Delta n = n_g - n_s$, has also been investigated. The variation of the H_x/H_y and H_y/H_x field ratios for the H^y_{11} and H^x_{11} modes, respectively, and the half-beat length, L_π, with the index contrast are shown in **Fig. 5.32**. Here, the waveguide width is kept constant at $W = 2.5$ μm and the slant angle, θ is 52°. The guide refractive index, n_g, is also kept constant at $n_g = 3.37$ and only the substrate

refractive index, n_s, is changed. It can be observed from the figure, that the hybrid nature is reduced when Δn is increased, the reason believed to be the fact that the modes are much more confined in the guide core and the fields at the dielectric edges are rather small (for the same waveguide dimensions). However, one important factor that can be observed is the significant reduction of L_π, which can give rise to a better compact polarization rotator design. At $\Delta n = 0.1$, the L_π value decreases to 391 μm.
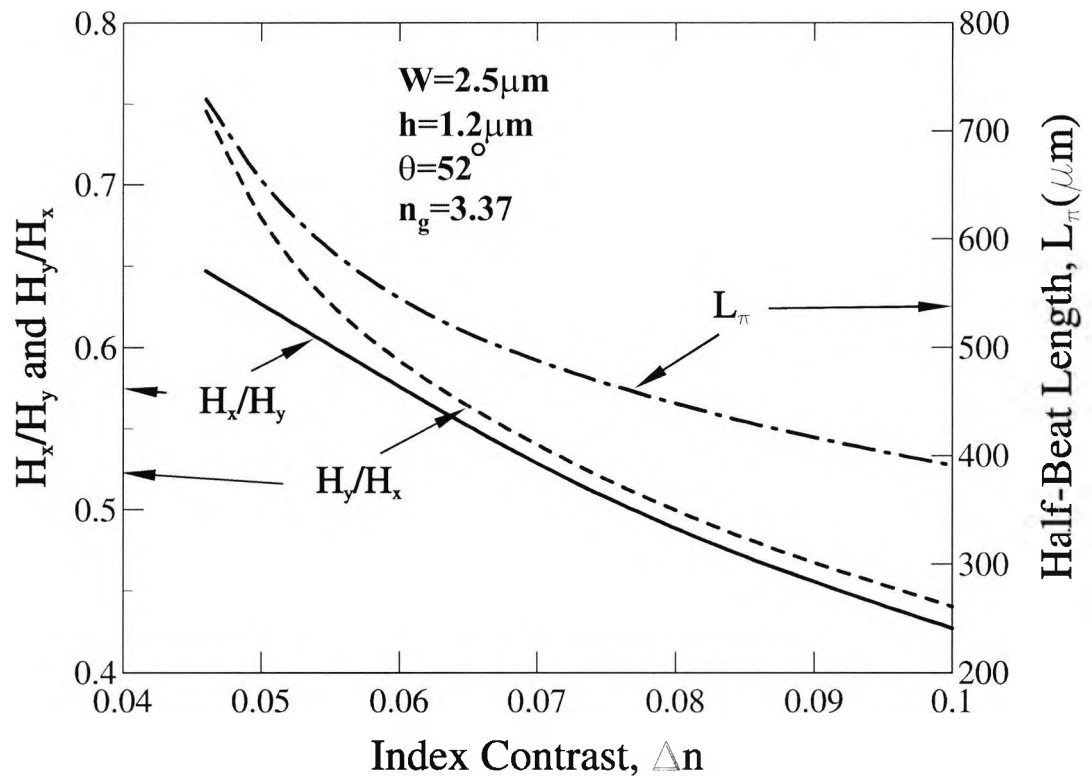
Fig. 5.32 Variation of the field ratios and the half-beat length with the index contrast, Δn.

5.3.4 Evolution of power and insertion loss analysis

Combining all the facts described before, a design has been developed which has a higher index contrast and a reduced waveguide width. The waveguide design parameters are: $W = 2.3$ μm, $\Delta n = 0.1$ ($n_g = 3.37$, $n_s = 3.27$) and $\theta = 48°$.

First, the butt-coupling of the input guide of width 2.3 μm with the PR waveguide section with a slanted sidewall is considered. Here, the waveguides are aligned with no transverse offset as shown in **Fig. 5.33**.
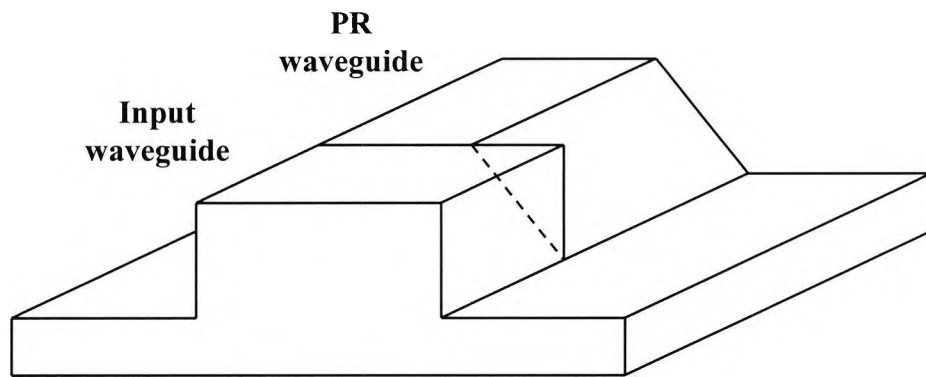
Fig. 5.33 Butt-coupling of the waveguides with no transverse offset.

When a TE mode (without much hybrid) from the input waveguide is incident on the junction, two highly hybrid modes will be excited in the PR waveguide section. The LSBR method (Rahman and Davies, 1988) is employed in order to calculate the modal coefficients of the excited H^y_{11} and H^x_{11} modes. The modal coefficients of the H^y_{11} and the H^x_{11} modes are calculated to be 0.69 and 0.61, respectively. Here, 0.7 dB power is lost at the junction interface, which is converted in to radiation modes.

To obtain a clearer picture of the TE mode converts into the TM mode along the PR waveguide, the field profiles at both ends of the PR waveguide have been investigated. The superposition of the two hybrid modes at the start of the PR section, i.e. at $z = 0^+$, produces a field profile where the H_y component is the dominant. The profile of the H_y field at this position is shown in **Fig. 5.34(a)**. Its relative amplitude is high and the shape is very similar to that of the H_y field profile of the two hybrid modes. However, at $z = 0^+$, the H_x field components of the two hybrid modes almost

cancel out to each other. The residual H_x field profile is shown in **Fig. 5.34*(b)***. Its maximum amplitude is only 0.05, compared to the normalized maximum value of the H_y field. It can also be observed that the maximum amplitude occurs along the slanted sidewall edge of the PR waveguide section. At the start of the PR waveguide, most of the power (P_y), about 99.8%, is carried by the H_y component and only the remaining power of 0.2% (P_x) is carried by the H_x component.

(a)

(b)
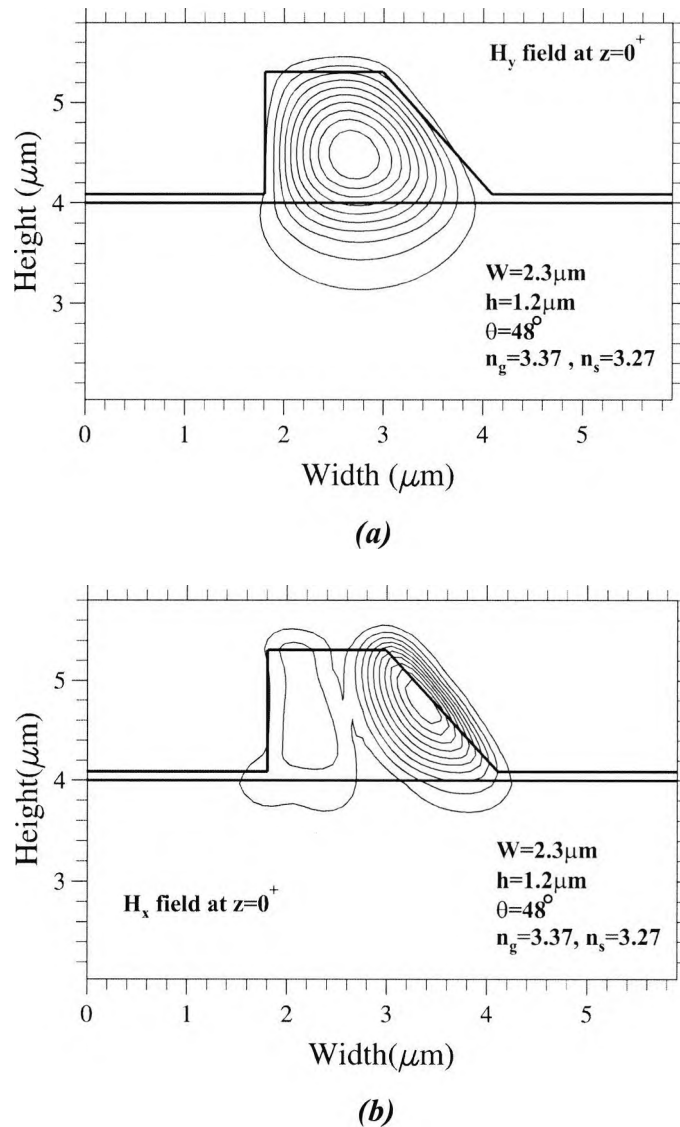
Fig. 5.34 Composite *(a)* H_y and *(b)* H_x field components at $z = 0^+$.

Although two highly hybrid modes with almost equal propagation constants propagate along the PR waveguide, at a distance L_π from the start of the PR waveguide, these two modes become out of phase with each other. Therefore, for the resultant overall field at the end of the PR wavguide section, the H_x field components will add up to

give a nearly pure TM mode, and the H_y components will cancel out. The H_x field at the end of the PR waveguide is shown in **Fig. 5.35(a)**. The H_y field profile is also shown in **Fig. 5.35(b)**, which has a very similar shape as the H_x field, but its maximum amplitude is only 10% of the maximum H_x field. In this case the L_π value is around 320 μm, and at $z = L_\pi$, 98.7% of the input power has been transformed to P_x and only 1.3% has been remained as P_y.

(a)

(b)
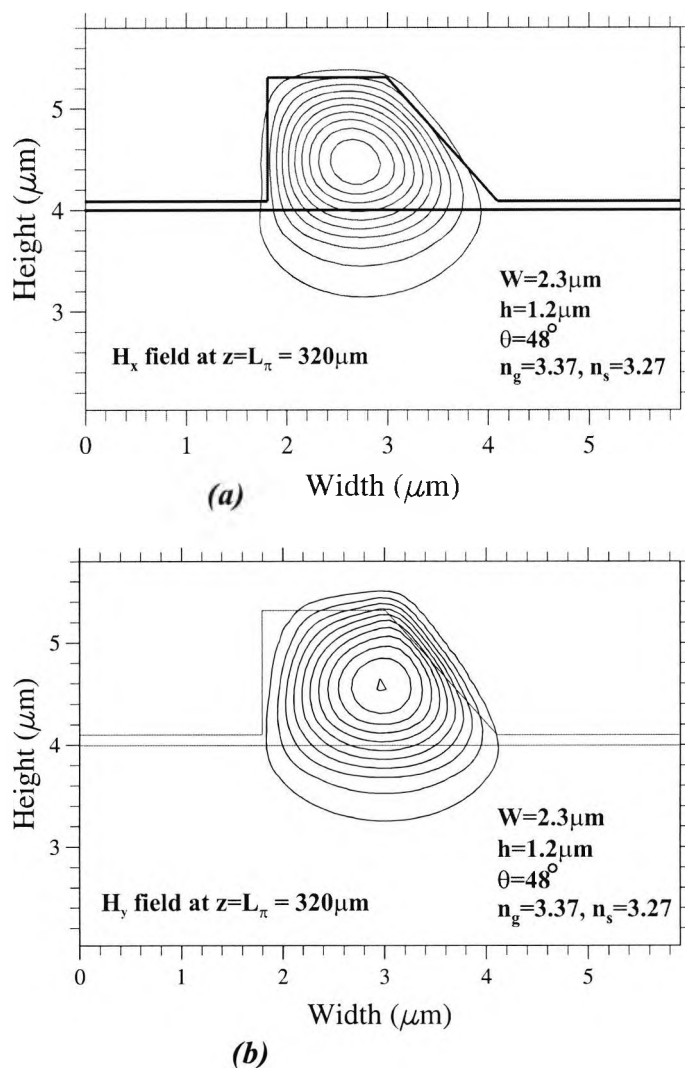
Fig. 5.35 Composite *(a)* H_x and *(b)* H_y field contours at $z = L_\pi$.

Next, the evolution of the H_x and H_y power along the PR waveguide, as obtained from the two hybrid modes, is studied. These power calculations are evaluated from the full vectorial modal field profiles of the modes and their propagation constants which are obtained by using the VFEM and the modal coefficients obtained by the LSBR

method. **Fig. 5.36** shows the evolution of the optical power, P_x, along the PR waveguide when TE mode is incident on the junction interface, for different slant angles.
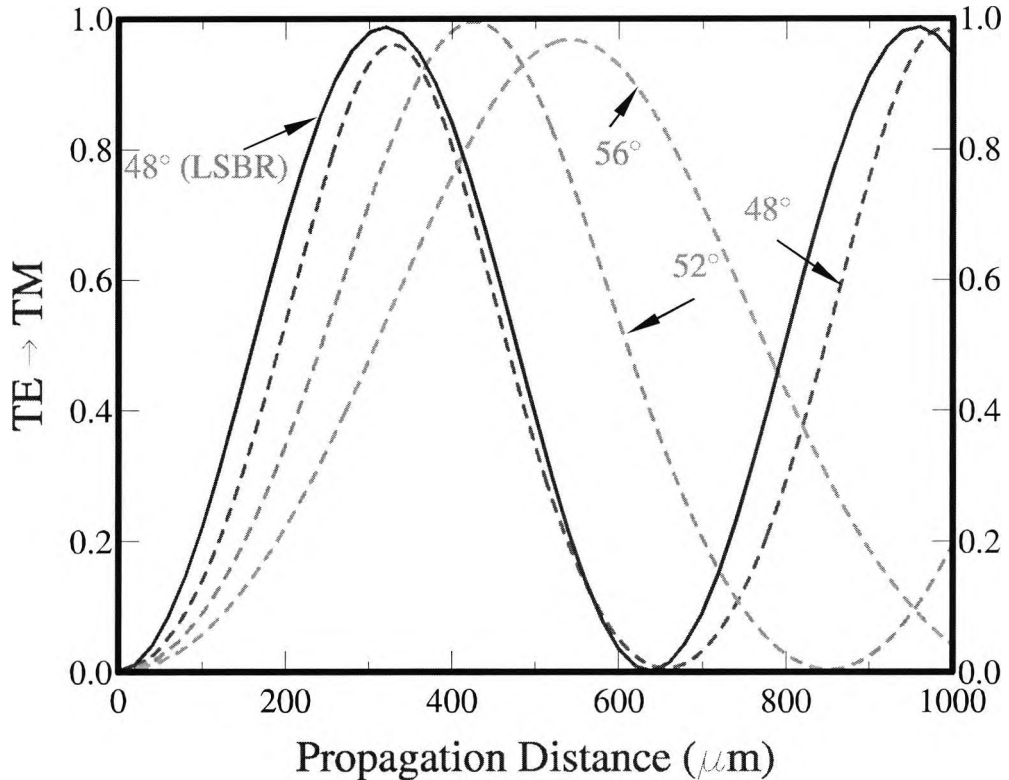
Fig. 5.36 Evolution of the optical power, P_x, along the propagation direction in the PR section.

It can be clearly seen that the P_x values for all the 3 cases reach their maxima at their corresponding half-beat lengths. From the figure, it is clearly visible that the incident TE mode is gradually converted to TM mode along the PR waveguide. For $\theta = 48°$, the maximum conversion occurs at $z = L_\pi = 320$ μm, and if the PR section is not terminated at this point, the power conversion will continue and the P_x power starts reducing further along the waveguide. For $\theta = 52°$ and $\theta = 56°$, the device lengths will be much longer for complete TE to TM power conversion as their corresponding half-beat lengths are higher. If the polarization rotator is terminated at the point where $z = L_\pi$, and butt-coupled to a rib waveguide with vertical sidewalls, which has a very small hybrid nature, most of the converted TM power could be coupled to this output

section. The evolution of the P_y power when the H^x_{11} mode is incident is shown in **Fig. 5.37**.
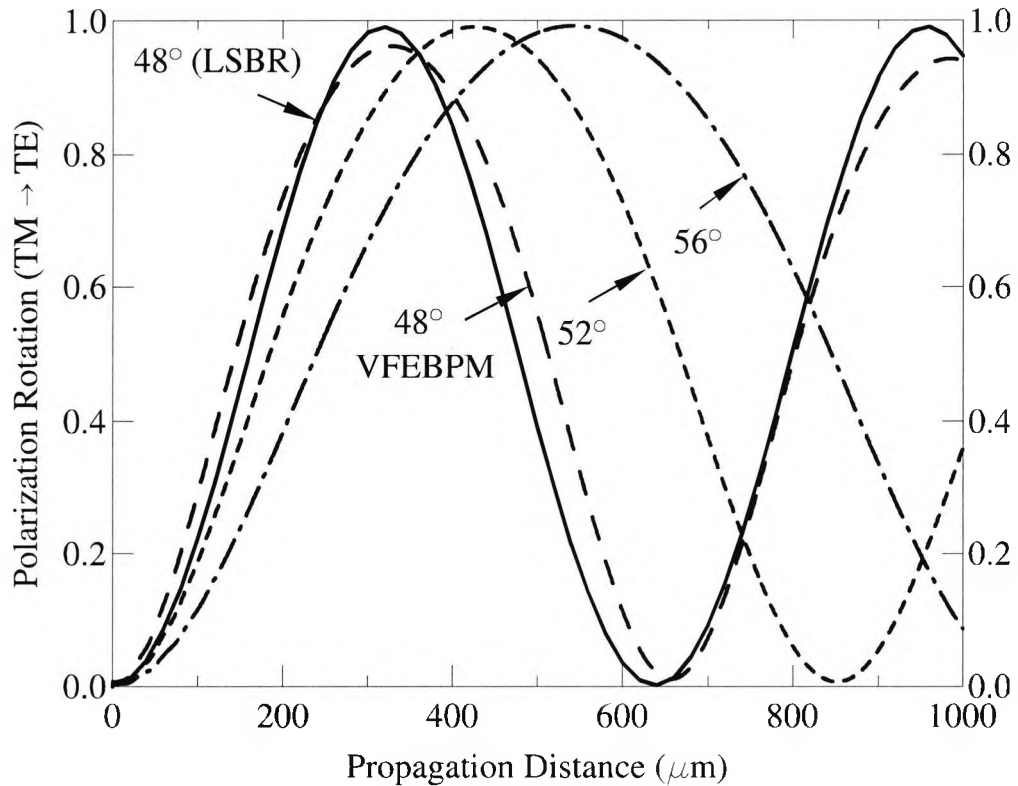
Fig. 5.37 Evolution of the P_y power when the H^x_{11} mode is incident.

A lateral shift between the waveguides is introduced as shown in the diagram in **Fig. 5.38**. Here, the Δx shift for the right hand side ($\rightarrow$) is considered as +ve shifts and similarly, the Δx shift for the left hand side ($\leftarrow$) is considered as −ve. Since the structural shapes of the input waveguide and the PR waveguide are different, their modal profiles are also different. Therefore by introducing the lateral offset, the polarization rotation and more particularly the insertion loss could be improved. To study this effect, the scattering coefficients are obtained by using the LSBR method. For TE mode excitation, the variations of the excited quasi-TE and quasi-TM scattering coefficients, τ_{ee} and τ_{em}, respectively, with the lateral offset, Δx are shown in **Fig. 5.39**. It can be observed that τ_{em} is a maximum when Δx is 250 nm, and in this case, τ_{ee} has also increased to 0.71. Consequently, for the 200 nm offset, the resultant

insertion loss is only 0.27 dB compared to 0.7 dB for a single interface when no offset is considered.
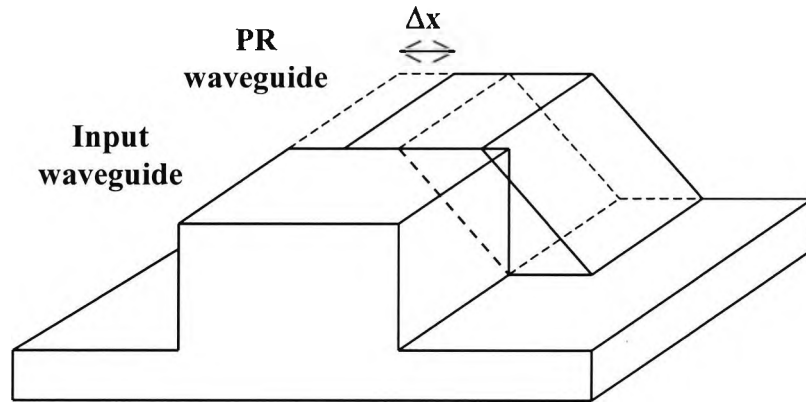
Fig. 5.38 Schematic diagram showing the lateral shift between the waveguides.
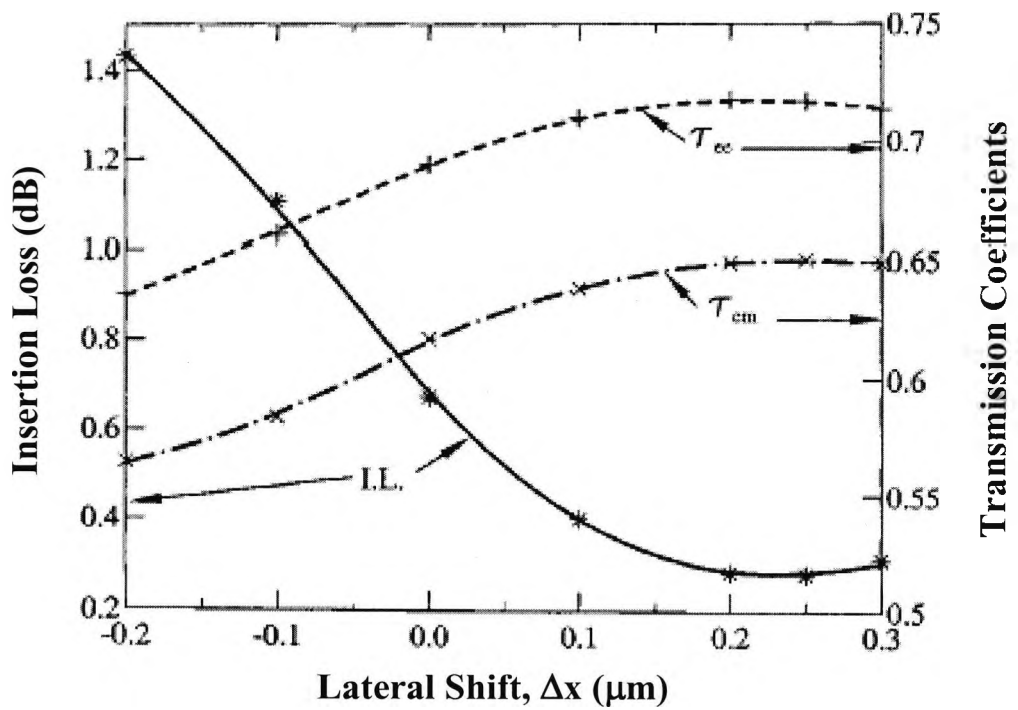
Fig. 5.39 Variations of the excited scattering coefficients, τ_{ee} and τ_{em}, and the insertion loss with the lateral offset, Δx.

So far the operating wavelength, λ, has been kept constant at 1.55 μm for all the cases considered. In this section, the effect of the operating wavelength, λ, on the performance of the polarization rotator was studied. The variations of P_x for three different operating wavelengths are shown in **Fig. 5.40**. It can be observed that for a total range of 80 nm variation of the operating wavelengths around the design wavelength $\lambda = 1.55$ μm, the maximum polarization conversion change is less than 2% and the half-beat length is also remarkably stable.

Summarising all the results, a 320 μm long polarization rotator design having a very low 0.4 dB overall insertion loss, has been achieved. Numerical results also indicate that, overall, more than 99% polarization conversion could be achieved for both TE to TM and TM to TE rotations.
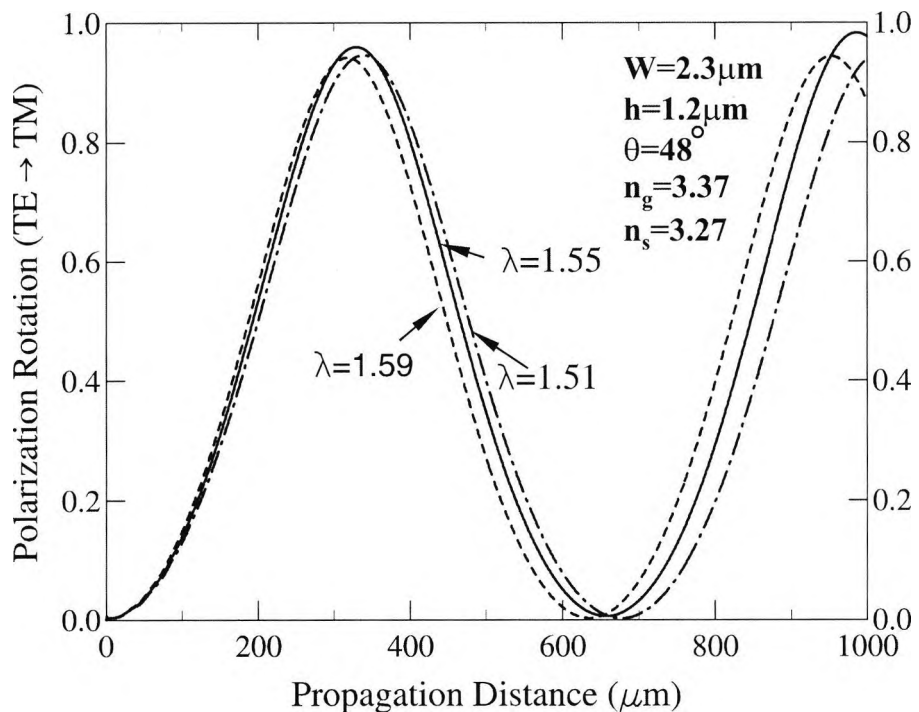
Fig. 5.40 Effect of the operating wavelengths on the polarization conversion efficiency.

5.4   Study of fabrication tolerances

This section is devoted for a detailed study on optimisation of a single-stage slanted waveguide polarization rotator in InP-InGaAsP. The schematic cross-section of the semiconductor PR waveguide is shown in **Fig. 5.41**. The height of the InP cap layer is fixed at 0.5 μm. The height of the InGaAsP (1.08Q) layer grown on InP substrate is 1.3 μm. The refractive indices of InP and InGaAsP are taken as 3.17 and 3.27, respectively, at an operating wavelength of 1.55 μm. All the other parameters used are shown clearly in **Fig. 5.41**.
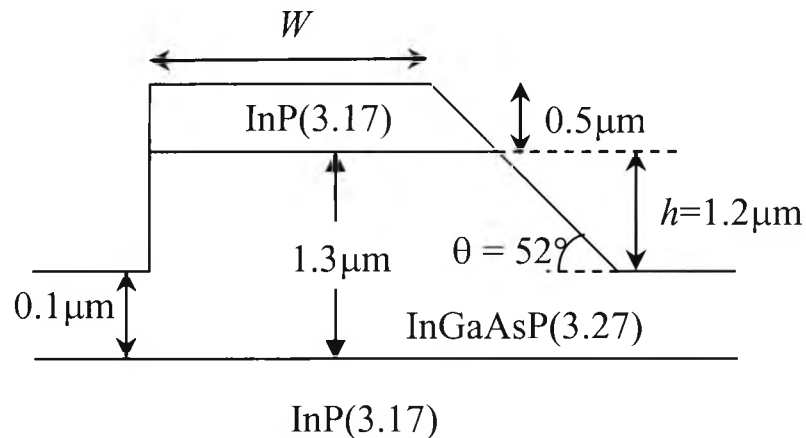
Fig. 5.41 Schematic cross-section of the semiconductor PR waveguide.

Some important characteristics of the single-stage polarization rotator, which consists of the above slanted side walled PR waveguide butt-coupled to another two input-output rib waveguides with vertical side walls, are evaluated. The schematic diagram of the polarization rotator is shown in **Fig. 5.42**. The effects of the rib width of the PR waveguide, slant angle, the index difference, the height of the guide and the operating wavelength on the device length and more particularly, on the conversion ratio and crosstalk have been investigated. Finally, a more important study of the PR waveguide behaviour has been obtained when fabrication tolerances were introduced on each PR waveguide parameter.
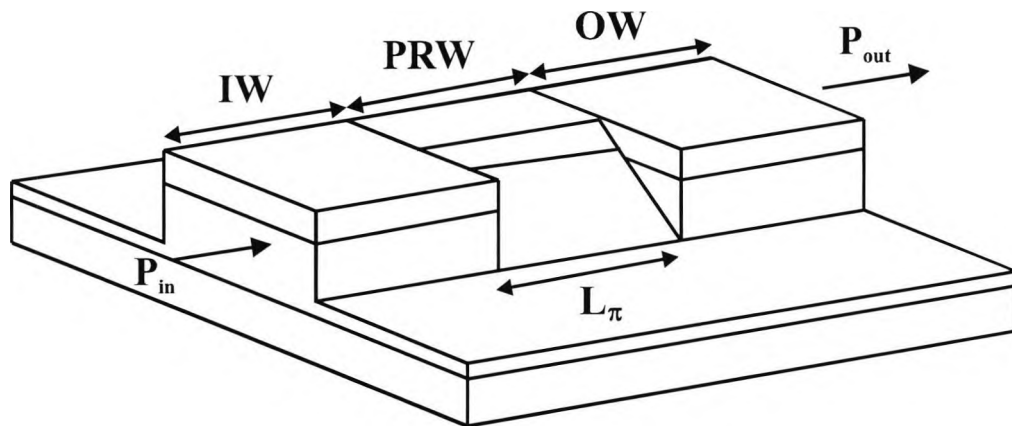
Fig. 5.42 Schematic diagram of the polarization rotator.

5.4.1 Variation of the waveguide width

Simulations were carried out to see the effect of the waveguide width, W, on the modal hybridity, since the width is a key parameter in altering the hybrid nature, as described in previous sections. **Fig. 5.43** shows the variation of the non-dominant/dominant field ratios for both H^y_{11} and H^x_{11} modes, and the half-beat length, L_π, with the waveguide width, W. It can be seen that when W is reduced from 1.5 µm to 1.15 µm, the hybridity of the modes is increased. At a width of exactly 1.15 µm, the hybridity reaches its maximum value of nearly one, which indicates that both of the transverse field components are almost equal. It has also been shown earlier in the Section 5.3, that the hybrid nature of the modes increases with the reduction of the waveguide width. However, it is also shown that hybridity not only can reach unity value but when W is reduced further, in this case, below 1.15 µm, the hybridity reduces. The TM mode also follows a similar behaviour and the maximum hybridity (H_y/H_x) occurs at $W = 1.15$ µm. The hybrid nature of the TM mode is slightly higher than that of the TE mode for a given waveguide width.
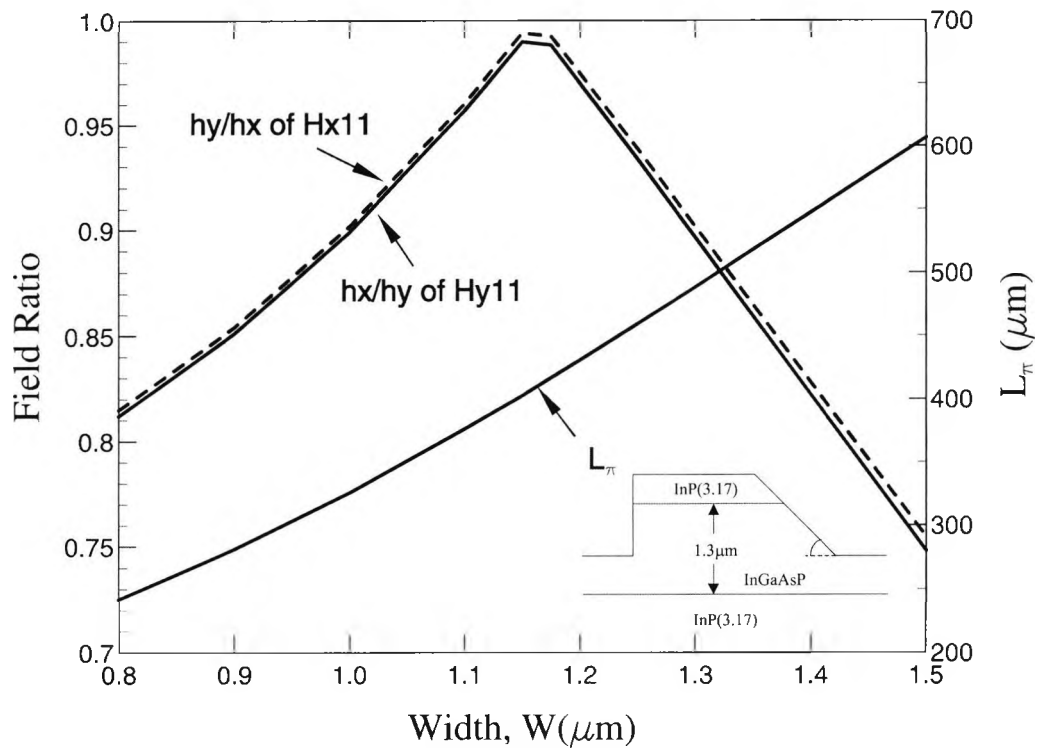
Fig. 5.43 Variation of the non-dominant/dominant field ratios and the half-beat length, L_π with the waveguide width.

When considering the half-beat length variation, it can be seen that, L_π reduces as W reduces, and at the maximum hybrid position, L_π is equal to 403 µm. Therefore, in this whole investigation, the optimum device length for maximum polarization rotation is considered as 403 µm. From the VFEM simulations, it can also be observed that the PR waveguide considered here remains single moded until $W = 1.2$ µm and a waveguide wider than that supports higher order modes.

The butt-coupling of the standard input rib waveguide with vertical side walls, and the PR waveguide was considered as the mode conversion can only be expected to happen at waveguide discontinuities. For the input waveguide, the rib width is taken as the lower width of the slanted PR waveguide and no transverse offset between the guides has been considered. The junction of the waveguides is shown in as an inset in **Fig. 5.44**. When a TE mode from the input guide is incident on the PR waveguide, it excites two highly hybrid modes. τ_{TE} and τ_{TM} are the transmission coefficients of the excited TE and TM polarized modes respectively. The variation of these two

parameters with the PR waveguide rib width, W is shown in **Fig. 5.44**. It can be seen that at $W = 1.5$ μm, τ_{TE} is 0.76 and as W is reduced, it reaches a minimum value of 0.65 at $W = 1.15$ μm. On the other hand, at $W = 1.5$ μm, τ_{TM} is 0.55 and it reaches a maximum value of 0.66 at $W = 1.15$ μm. Around $W = 1.15$ μm, there exist two highly hybrid modes, but the usual definition of quasi-TE and quasi-TM modes are not useful as both of the transverse components are almost equal. At $W = 1.15$ μm, the insertion loss at the junction interface is calculated to be 0.64 dB. If we considered W to be $W \gg 1.5$ μm, then the modal hybridity would be very small and the τ_{TE} would reach 1.0 asymptotically and the τ_{TM} value would be nearly zero.
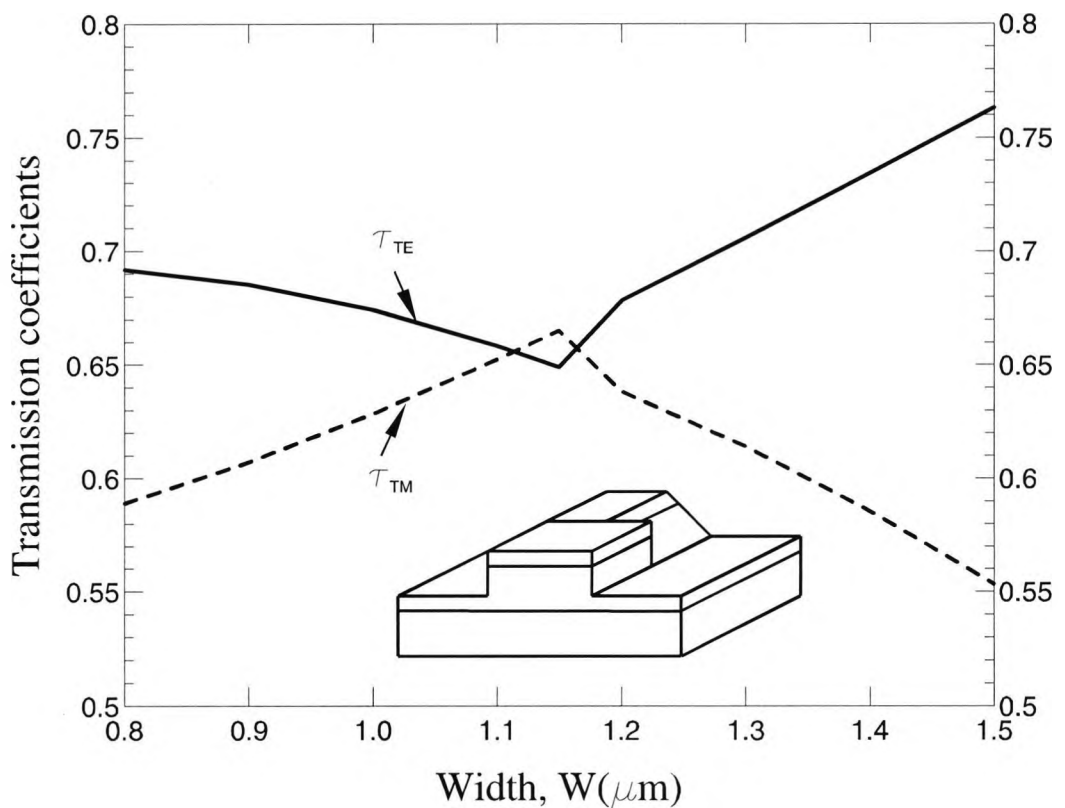
Fig. 5.44 The variation of the excited τ_{TE} and τ_{TM} coefficients with the PR waveguide width, W for input TE polarization.

5.4.1.1   Effect of the waveguide width on polarization conversion

In order to understand how the width of the waveguide affects the TE to TM power conversion, several power calculations along the axial direction of the PR waveguide were obtained for different values of *W*. **Fig. 5.45** shows the evolution of the converted power along the PR waveguide when TE mode is incident.
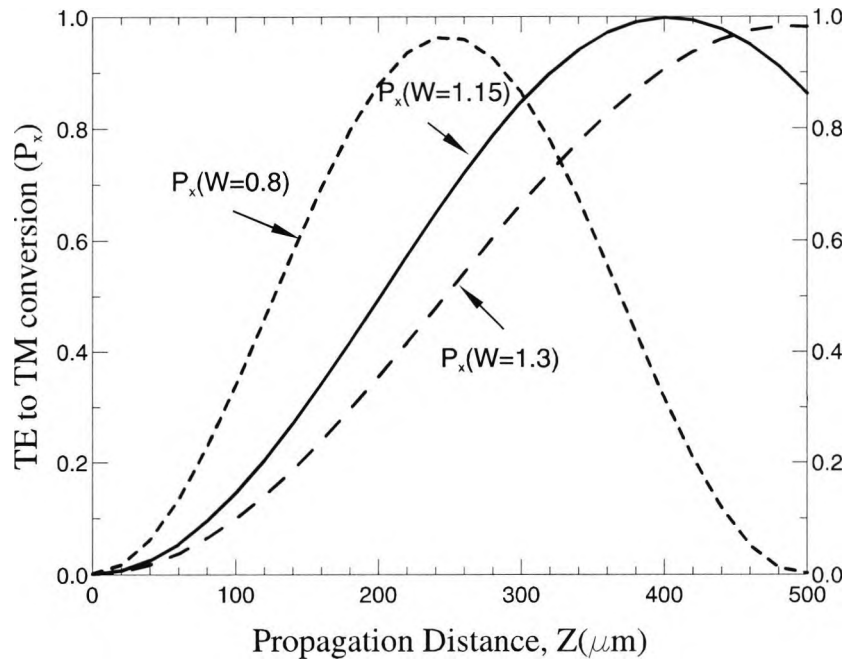
Fig. 5.45 Evolution of the converted power, P_x, along the PR waveguide when TE mode is incident.

Since the input field is nearly pure TE, initially, at the start of the PR waveguide, i.e. z = 0, the H_y polarized power, P_y, is nearly equal to one, and H_x polarized power, P_x is nearly zero. As the excited modes propagate along the PR waveguide section, slowly the two modes become out of phase, P_x increases and P_y decreases, and at a distance L_π, the half-beat length, from the discontinuity along the direction of propagation, z, nearly pure TM polarized power can be collected. It can be clearly seen that, for W = 1.15 µm, the power, P_x, reaches a maximum value of 0.998 at z = 403 µm, which is the corresponding L_π value, and then P_x is gradually reducing as the distance is deviating further away from the L_π. Therefore, in this case, the length of the single-stage polarization converter should be 403 µm. It can be observed from the **Fig. 5.45**, if z = L_π ± 20 µm, then the maximum P_x values at these points will be 0.994 and 0.991, respectively. Therefore, when fabricating the polarization rotator, ± 20 µm

axial tolerance will only results in an additional loss smaller than 0.1 dB. However, when $W = 1.3$ μm, the TM polarized power, P_x reaches to a maximum value 0.983 at a distance $z = 489$ μm from the discontinuity junction. Therefore, when the width of the waveguide is increased to 1.3 μm, not only the power transfer is low (due to a slightly lower hybridity), but also the device length will be much longer. Similarly, for $W = 0.8$ μm, the P_x reaches its maximum value of 0.963 at $z = 242$ μm. This slightly reduced power conversion is a result of the poor hybridity of the modes at shorter widths, as was shown in **Fig. 5.43**. However, it should be noted that, in this case, the device length would be much shorter. It can also be noted that if the device length is fixed at 403 μm and the width of the PR section deviates from the optimum design during the fabrication process, then the converted power will be reduced to 0.910 and 0.301 for $W = 1.3$ μm and 0.8 μm respectively.

5.4.1.2   Fabrication tolerance analysis

A study of how the fabrication tolerances on waveguide width, affect the power conversion and the corresponding crosstalk at specified positions along the propagation direction, z, has been carried out. The numerically simulated results are shown in **Fig. 5.46** for various waveguide widths ranging from 0.8 μm to 1.5 μm.
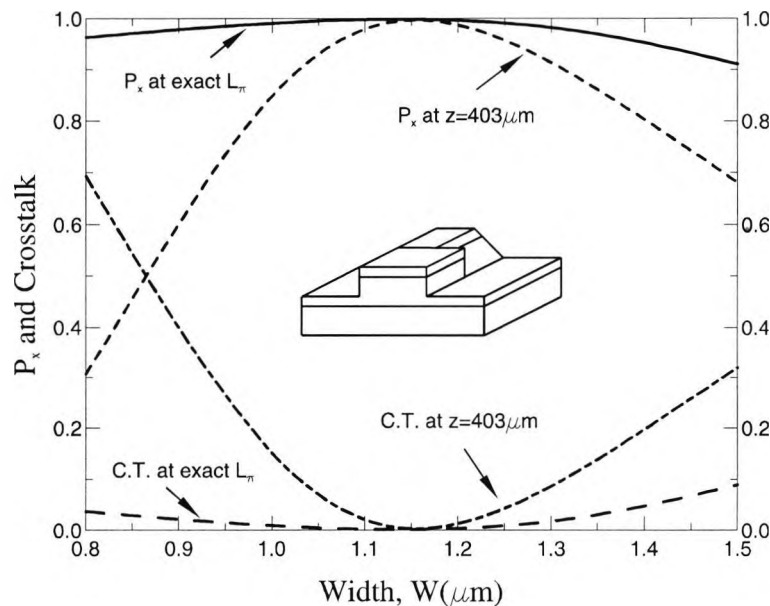
Fig. 5.46 Variation of the converted power, P_x and the crosstalk at $z = L_\pi$ and $z = 403$ μm, with the waveguide width.

Here, the crosstalk can be defined as the unwanted oppositely polarized power, normalised to the total input power, which remains at the end of the PR waveguide section. In this case, when the TE-polarized power P_y is incident, then most of the power will be converted into TM-polarized power P_x at the end of the PR section, although there might be some amount of P_y power remaining. This particular P_y, which is normalised to the total input power, is referred to as the crosstalk. In the numerical simulations, the optimum device length was fixed at 403 µm, because this length corresponds to the ideal design condition to obtain maximum power conversion. The converted TM power, P_x, at their corresponding L_π values, increases from 0.963 to the maximum value of 0.998, when the width increases from 0.8 µm to 1.15 µm and then P_x gradually decreases up to 0.909 with further increase of the width to 1.5 µm. This trend of P_x can be explained by incorporating the variation of hybridity of the modes with the width which was shown in **Fig. 5.43**. Since the hybridity increases with the width up to 1.15 µm and decreases as width increases, a similar sort of trend for the power conversion can be expected, as the hybrid nature is directly related to the polarization rotation. It can be seen that if the device is fabricated with a fixed device length of 403 µm, then as the waveguide width varies, P_x power will be very much lower than that at exact L_π, except at $W = 1.15$ µm. At $W = 1.15$ µm, the L_π matches with the exact fabricated device length, therefore giving highest conversion and also lowest crosstalk of 0.00128, which is equal to -28.9 dB. The crosstalk at the specified device length increases up to 0.698 as W reduces to 0.8 µm and at $W = 1.5$ µm, the crosstalk is about 0.32. At the designed device length of 403 µm, for a width tolerance of 1.15 ± 0.05 µm, the converted TM power will only show an additional loss of less than 0.05 dB and the crosstalk value will deteriorate to –20 dB. However, if during fabrication the width of the uniform sections can be controlled within 1.15 ± 0.1 µm, then the P_x loss would be about 0.3 dB and the crosstalk will deteriorate further at –12 dB.

5.4.2 Fabrication tolerance analysis of the sidewall angle

The variation of the slant angle θ was considered to understand its effect on achieving a better polarization conversion. The non-dominant/dominant field ratios for both TE and TM modes and the half-beat length L_π variation with θ are shown in **Fig. 5.47**.
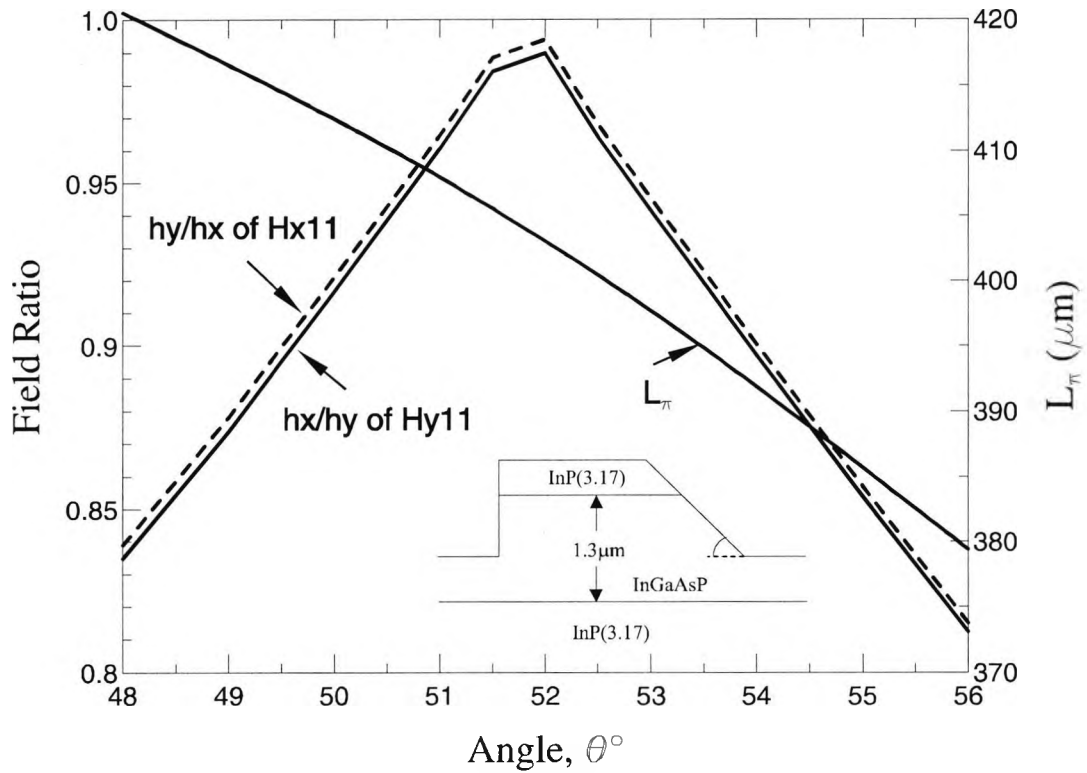
Fig. 5.47 Variation of the field component ratios and the half-beat length L_π with the slant angle, θ.

Here, the width of the waveguide is kept constant at 1.15 μm because that width yielded the maximum hybridity and all the other parameter values are fixed: the index difference between the guide and the substrate, Δn = 0.1, the height, h = 1.2 μm, and the operating wavelength, λ = 1.55 μm. As the facet angle θ increases from 48° to 52°, the hybridity increases and it achieves a maximum value at θ = 52° and further increase in θ will result in a reduction of hybridity. The half-beat length L_π shows a reduction from 420 μm to 379 μm throughout the range of angles considered.

Next, the TE to TM power conversion and the crosstalk have been investigated by varying θ from 48° to 56°. The converted TM power, P_x and crosstalk for both at

exact L_π and at the designed device length 403 μm are shown in **Fig. 5.48**. It can be seen that both P_x curves show a similar kind of trend with having a maximum value of 0.998 at $\theta = 52°$. Because the hybridity is maximum at $\theta = 52°$, as was shown in **Fig. 5.47**, the maximum power conversion should also be expected to happen at 52°. As θ is varied away from 52°, the P_x at $z = 403$ μm is always lower than the P_x at L_π, due to the L_π mismatch. However, here the difference between P_x at exact L_π and the output P_x at $z = 403$ μm, is quite smaller than that of the width variation as shown in **Fig. 5.46**, because both L_π and hybridity were less sensitive with θ. At $\theta = 52°$, the crosstalk is minimum at -28.9 dB. When considering the fabrication of the device, for a tolerance of $\theta = 52 \pm 2°$, the P_x power at the designed length will reduce by 0.05 dB and the crosstalk is expected always to be better than -19 dB.
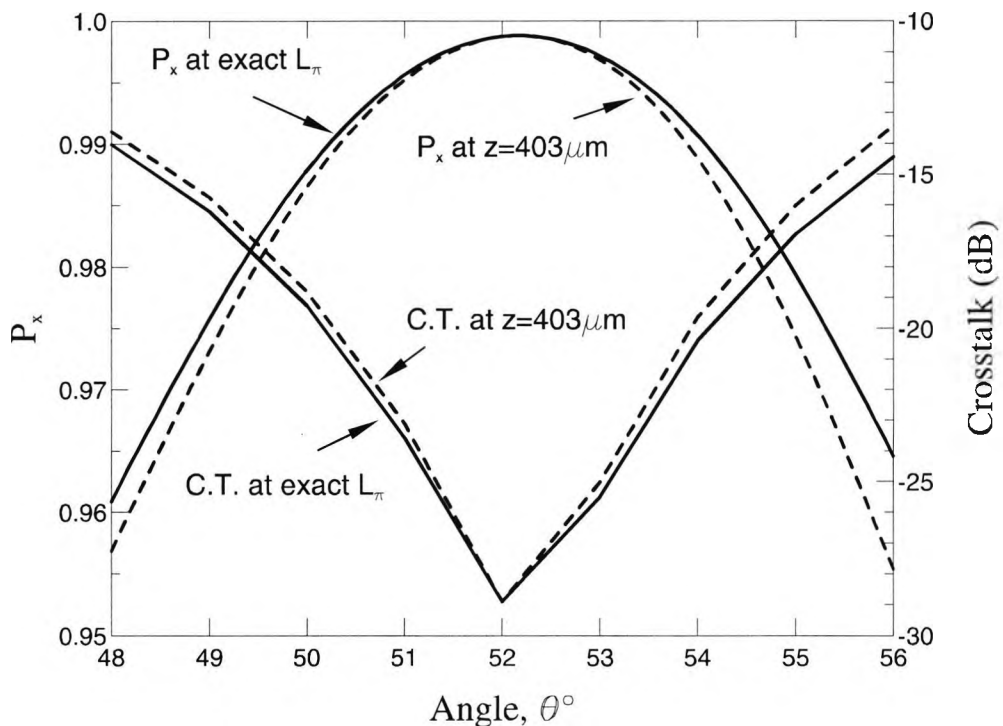
Fig. 5.48 Variation of the converted TM power, P_x and crosstalk at $z = L_\pi$ and $z = 403$ μm, with the slant angle.

5.4.3 Fabrication tolerance analysis of the refractive index difference

The effect of the refractive index difference, Δn, between the guide and the substrate on the hybridity and the device length is shown in **Fig. 5.49**. In the numerical simulation, the other parameters are taken as $W = 1.15$ µm, $\theta = 52°$, $h = 1.2$ µm, and the operating wavelength is kept constant at 1.55 µm. It can be seen that the field ratios increase with Δn up to $\Delta n = 0.1$, and reduce when Δn is increased further. L_π reduces from 411 µm to 393 µm as Δn increases throughout the range of 0.08 to 0.14. At the optimised design value of $\Delta n = 0.1$, it shows the maximum hybridity and here the L_π is 403 µm. It can be noted that the percentage change in L_π and hybridity is much smaller.
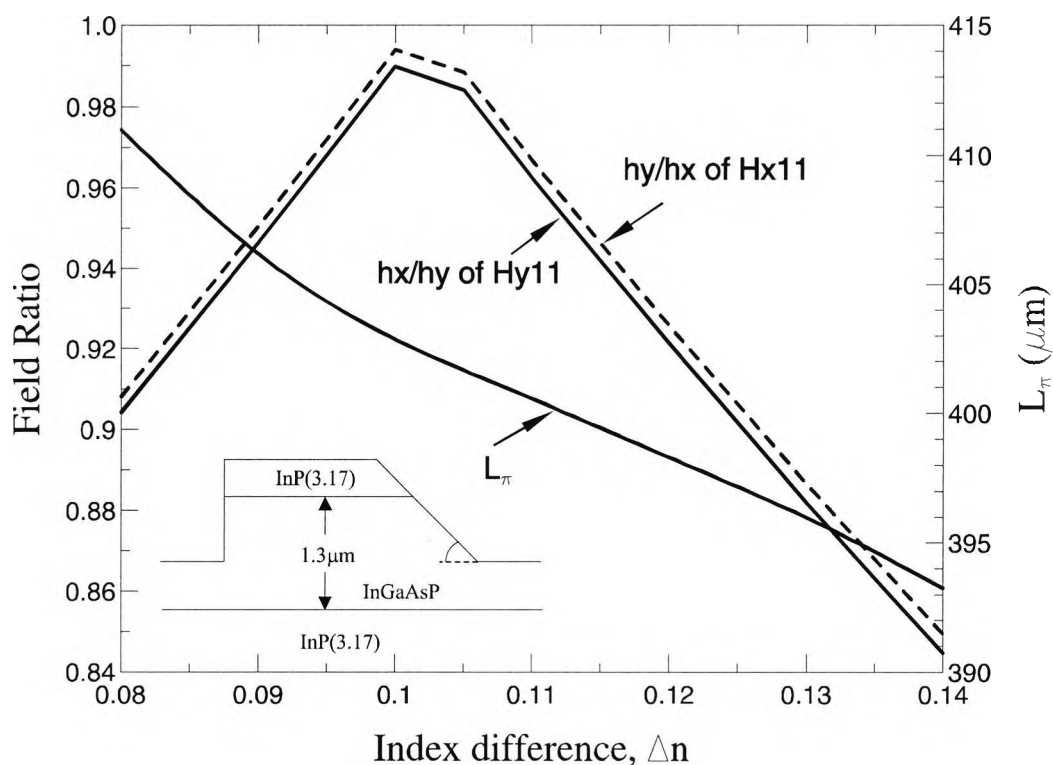
Fig. 5.49 Variation of the field component ratios and the half-beat length with the refractive index difference, Δn.

In order to investigate the tolerance in index difference over the polarization rotation, converted TM power, P_x, when TE is incident, at $z = L_\pi$ and $z = 403$ µm and the crosstalk were obtained within the range of Δn 0.08 to 0.14 as shown in **Fig. 5.50**. The maximum power conversion occurs at $\Delta n = 0.1$ with a low crosstalk of about -28.9

dB. However, the two P_x curves are almost similar and there is hardly any difference between them from $\Delta n = 0.09$ and $\Delta n = 0.13$. This is mostly due to the small difference in L_π values, i.e. only $\pm 2\%$ from the optimised L_π value, 403 μm as shown in **Fig. 5.49**. For a tolerance of $\Delta n = 0.1 \pm 0.01$, the P_x power at designed device length will show less than 0.01 dB additional loss and a crosstalk value better than –26 dB.
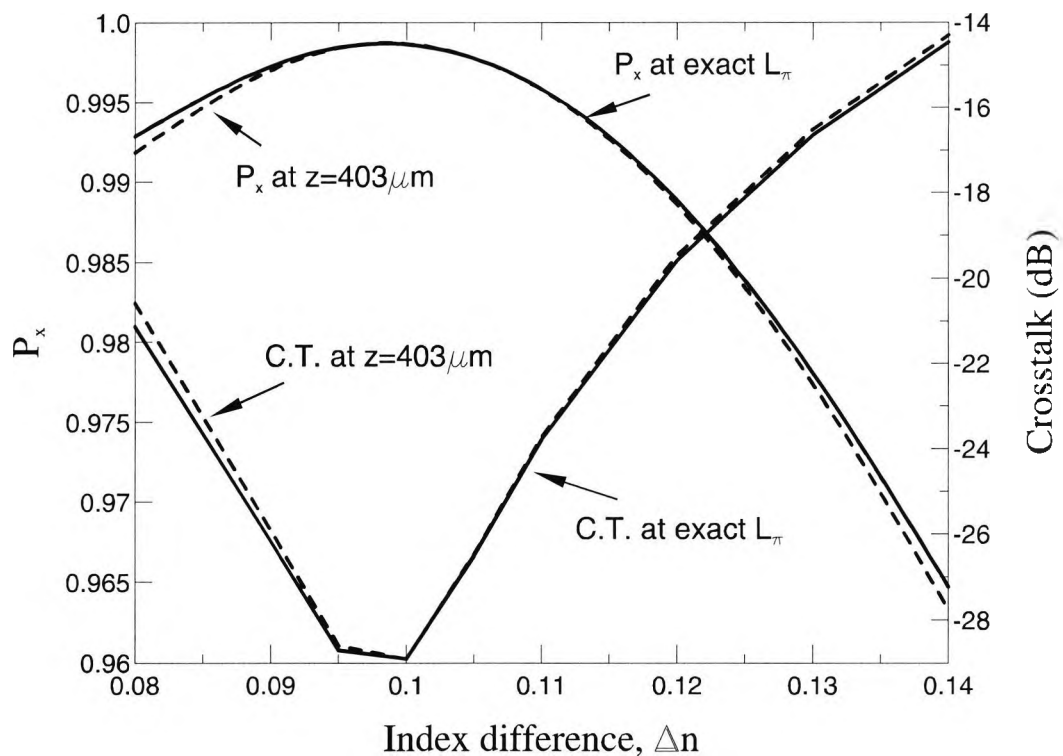
Fig. 5.50   Converted power, P_x and the crosstalk at $z = L_\pi$ and $z = 403$ μm, with the refractive index difference, Δn.

5.4.4 Fabrication tolerance analysis of the height

The behaviour of the hybridity and the device length were studied, when the height of the guiding layer, is varied. As shown in **Fig. 5.51**, the height, h is varied from 0.8μm to 1.25 μm. The hybridity decreases as h decreases and at $h = 0.8$ μm, it becomes lower as 0.72. L_π decreases from 480 μm to 399 μm as h increases. At $h = 0.8$ μm, L_π shows a percentage difference of about 19% from the designed value of 403 μm.

Variations of the converted TM power, P_x, at $z = L_\pi$ and $z = 403$ μm and the crosstalk with the height, h, are shown in **Fig. 5.52**. It can be observed that, since the L_π variation with h is quite large, the converted power P_x at exact L_π and at the designed length, show a very large difference as h reduces to 0.8 μm. At $h = 0.8$ μm, the TM power P_x at exact $L_\pi = 480$ μm is 0.883 and the P_x power at the designed device length is 0.829. Similarly, the crosstalk reaches a higher value of −9.34 dB and −7.67 dB at $z = L_\pi$ and $z = 403$ μm, respectively. During fabrication, when the device length is fixed at 403 μm, a change of $h = 1.2 + 0.05$ μm and $h = 1.2 - 0.1$ μm will show a P_x loss of 0.0005 dB and 0.01 dB, respectively, and crosstalk values of −28.6 dB and −23 dB, respectively.
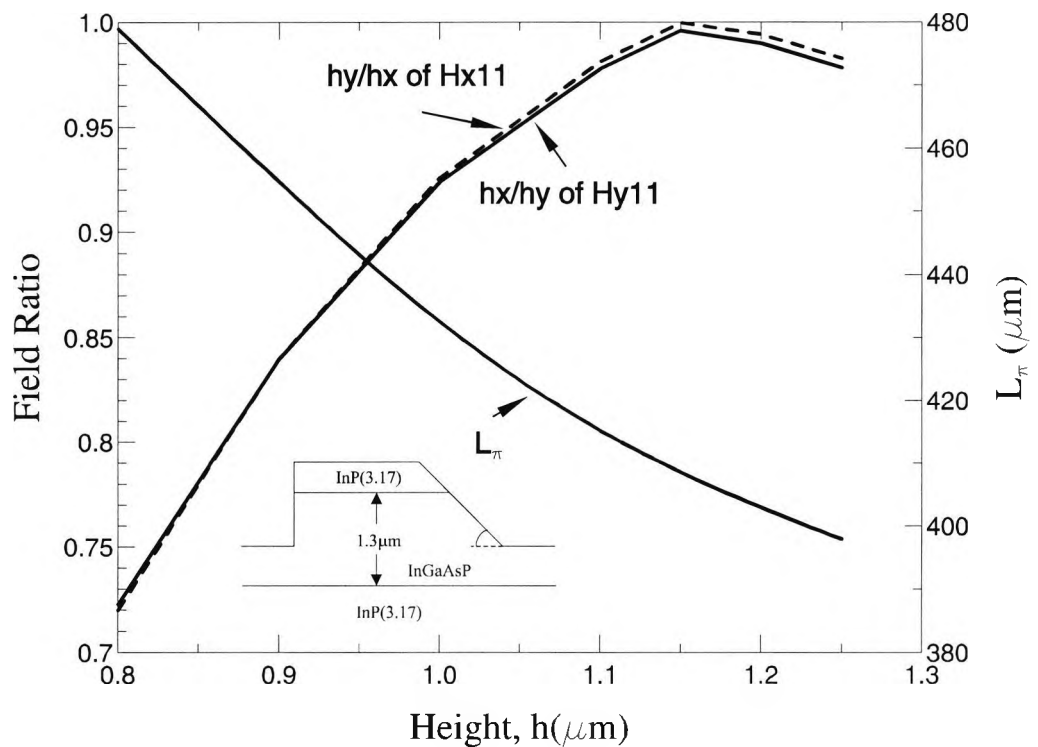
Fig. 5.51 Variation of the field component ratios and the half-beat length with the height, h.
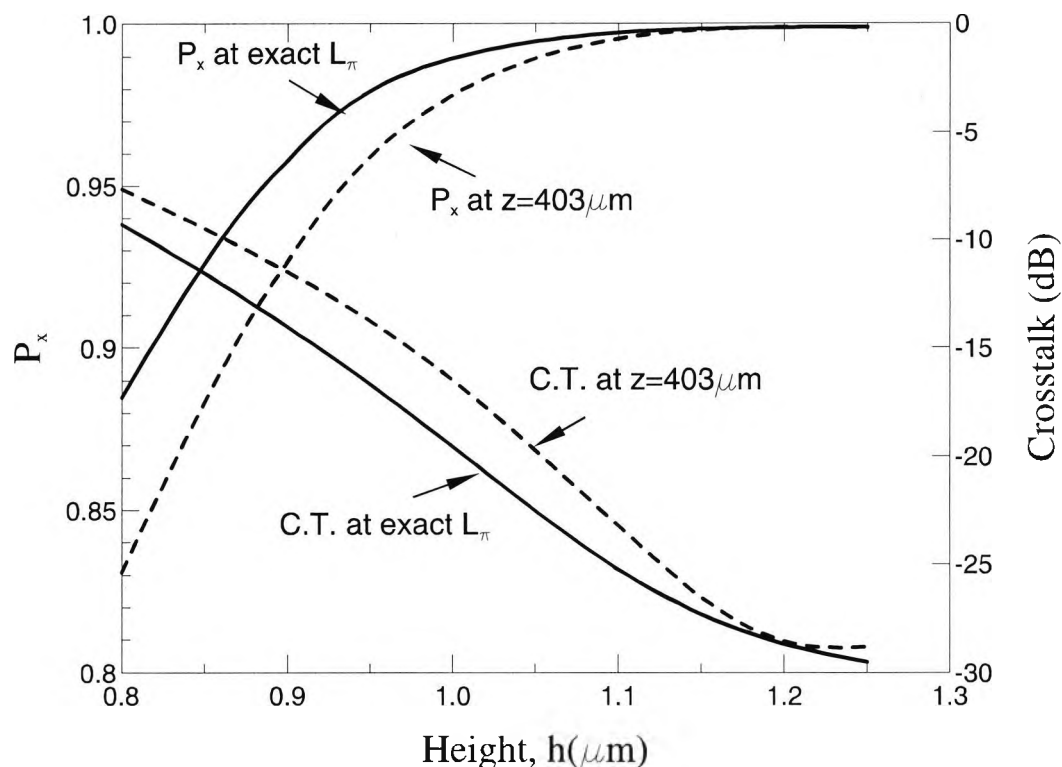
Fig. 5.52 Variations of the converted TM power, P_x, and the crosstalk at $z = L_\pi$ and $z = 403$ μm with the height, h.

5.4.5 Fabrication tolerance analysis of the operating wavelength

In this section, the effect of the operating wavelength on the polarization rotation behaviour is considered and also a study of the fabrication tolerances on the wavelength has been carried out. The operating length, λ, is varied from 1.53 μm to 1.61 μm. When obtaining the modal solutions for different operating wavelength, λ values, refractive index of the guide, i.e. n(InGaAsP), has been modified accordingly to include material dispersion for a given quaternary material at 1.08Q. **Fig. 5.53** shows the variation of the hybridity and L_π with the operating wavelength, λ. It can be seen that the hybridity decreases with the increase in λ. However, the field ratio difference over the range of λ is considerably smaller, giving a value of about 0.07. Half-beat length, L_π also decreases as λ increases giving a minimum L_π of 381.72 μm at $\lambda = 1.61$ μm. Also the value of L_π only shows a change of 30 μm along the whole wavelength range considered.
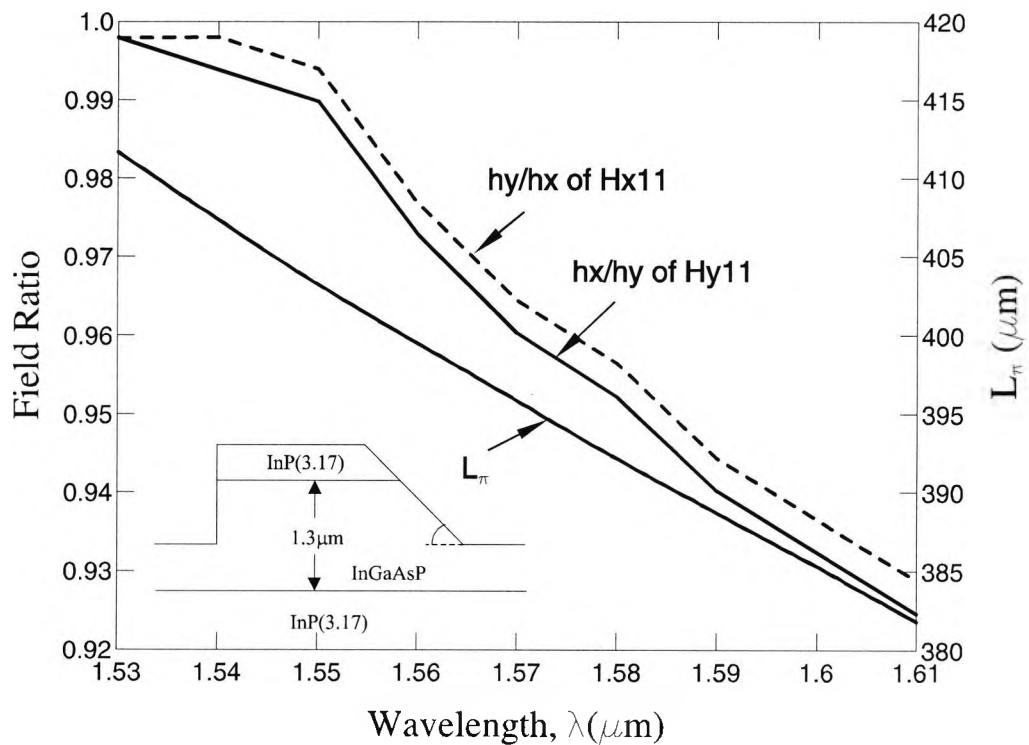
Fig. 5.53 Variation of the hybridity and L_π with the operating wavelength, λ.

The power, P_x, and the crosstalk curves for different wavelengths are shown in **Fig. 5.54**. P_x at exact L_π reduces from 0.998 to 0.995 as λ increases, since the hybridity reduces as shown in **Fig. 5.53**. But this 0.003 difference is hardly affects the behaviour of the polarization rotator. P_x at $z = 403$ μm is also does not show much deviation from the P_x curve at exact L_π, as L_π only shows a little change over the whole wavelength range. At $\lambda = 1.61$ μm the crosstalk for $z = L_\pi$ and $z = 403$μm are – 23.3 dB and –19.2 dB, respectively. For a tolerance of $\lambda = 1.55 \pm 0.02$ μm at the designed length of 403 μm, the P_x loss is about 0.006 dB and the crosstalk is about – 26 dB.
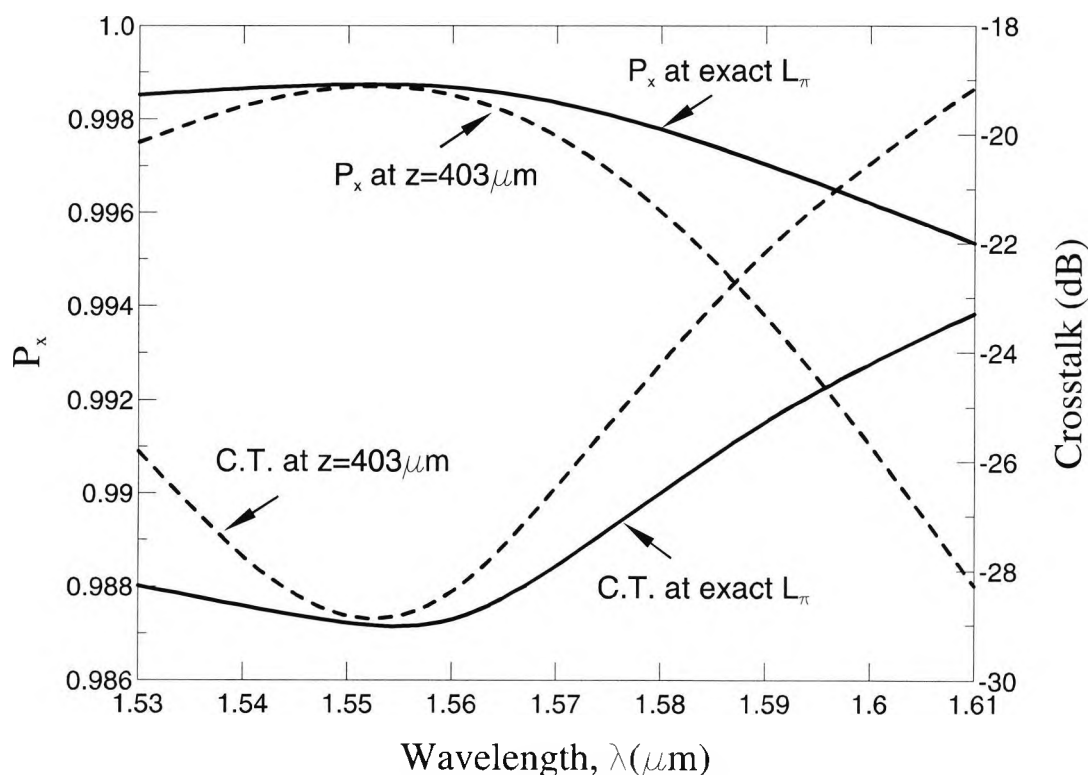
Fig. 5.54 Converted P_x power and the crosstalk at $z = L_\pi$ and $z = 403$ μm with the operating wavelength, λ.

5.5   Novel polarization rotator design in asymmetric shallow-etched waveguides

A schematic diagram of the AlGaAs-GaAs based asymmetric waveguide structure is shown in **Fig. 5.55**. All the waveguide parameters are depicted in this figure. A 0.8μm 25% AlGaAs layer and a 1.3 μm thick GaAs core layer are deposited on a 20% AlGaAs substrate. The left hand side is etched to a depth of d_1 vertically. The right hand side of the waveguide consists of two different angled slanted sidewalls both etched to a depth of d_2. The lower and the upper slant angles are taken as θ_1 and θ_2, and the width of the waveguide, W, is taken as the upper width of the waveguide. The refractive indices of the 25% AlGaAs upper cladding, GaAs core and the 20% AlGaAs substrate at 1.55 μm operating wavelength are taken as 3.24999, 3.37691, and 3.27510, respectively.
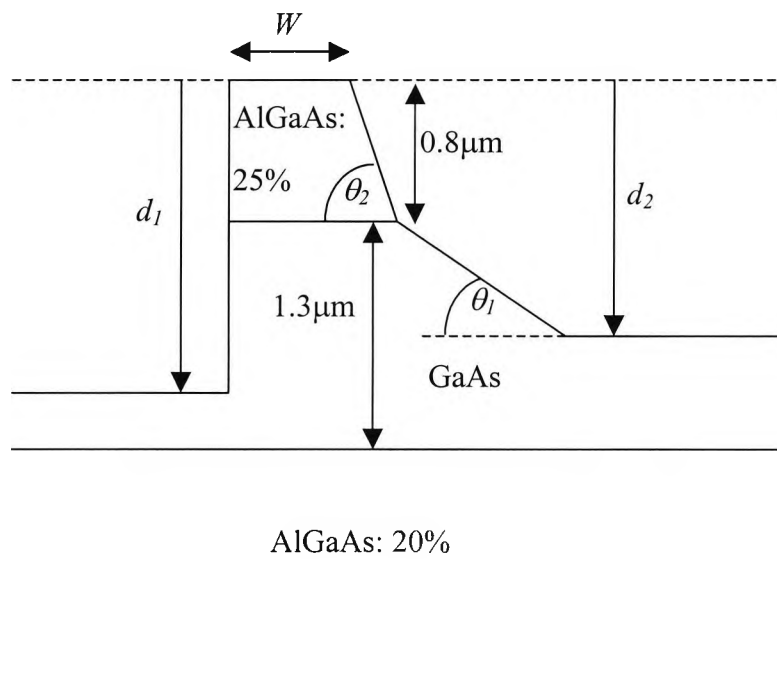
Fig. 5.55 Schematic of the asymmetric polarization rotator structure.

5.5.1 Simulation results

First the field profiles for the quasi-TE (H^y_{11}) mode and the TM (H^x_{11}) mode of the above asymmetric structure are obtained using the Finite Element Method (FEM) based on the vector **H**-field formulation (Rahman and Davies, 1984*a*). Initially, the simulation are carried out for a specific set of waveguide parameters, i.e. when $W =$ 1.0 µm, $d_1 = 2.05$ µm, $d_2 = 1.57$ µm, $\theta_1 = 32°$ and $\theta_2 = 69°$. In this case the lower width of the guide is 2.5 µm. These dimensions and angles have been exactly represented in the numerical discretisation of the waveguide structure. As we already know, the optical modes in semiconductor waveguides are truly hybrid in nature, and the H_y component of the fundamental quasi-TE mode is the dominant field component. The dominant H_y field profile of the H^y_{11} mode is shown in **Fig. 5.56*(a)*** and it follows the shape of the slanted waveguide core. **Fig. 5.56*(b)*** shows the non-dominant H_x field profile of the H^y_{11} mode. It can be seen that the shape of this non-dominant field profile is also very similar to that of the dominant field profile. The amplitudes of the H_y and H_x fields are obtainecd as 0.756, and 0.605 respectively and the propagation constant, β_y is computed to be 13.49707. The contour profiles of the

H_x, and H_y for the quasi-TM mode are not presented here. However, the dominant H_x and the non-dominant H_y field profiles are found to be very similar to those of the TE mode and their corresponding maximum amplitudes are 0.775 and 0.617 respectively. The propagation constant for the TM mode, β_x is computed as 13.48890.
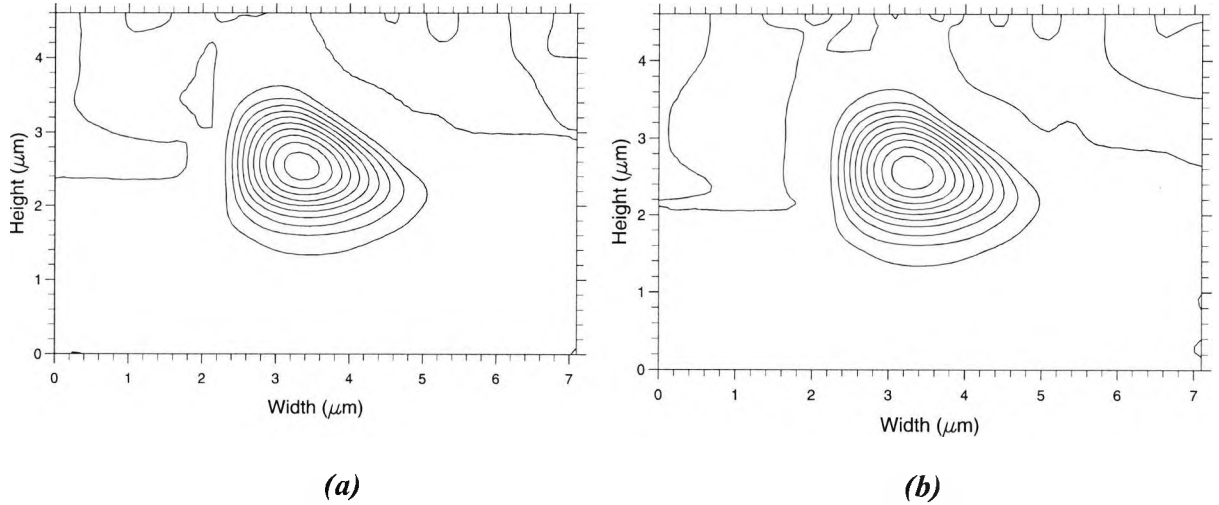
Fig. 5.56 *(a)* H_y field profile and *(b)* H_x field profile of the TE mode, when *W* = 1.0 μm, d_1 = 2.05 μm and d_2 = 1.57 μm.

The width of the waveguide, *W*, is varied to obtain the effect on the modal hybridity. The variation of the H_y and H_x field values of the quasi-TE mode, with the rib width, *W* is shown in **Fig. 5.57**. From the figure, it can be observed that the hybridity is reduced when the width is increased. The significant modal hybridity for waveguides with smaller width suggest that nearly 100% polarization conversion might be possible in a single section polarization design, by employing such an asymmetrical waveguide. When the width, *W* is 2.5 μm, the hybridity is reduced to such an extent that the non-dominant field amplitudes are 0.188 and 0.196 for the TE and TM modes respectively. It can also be noted that when *W* = 2.5 μm, the amplitude of the non-dominant components when compared to their dominant counterparts are reduced to 20%, compared to their 80% values when *W* = 1.0 μm.
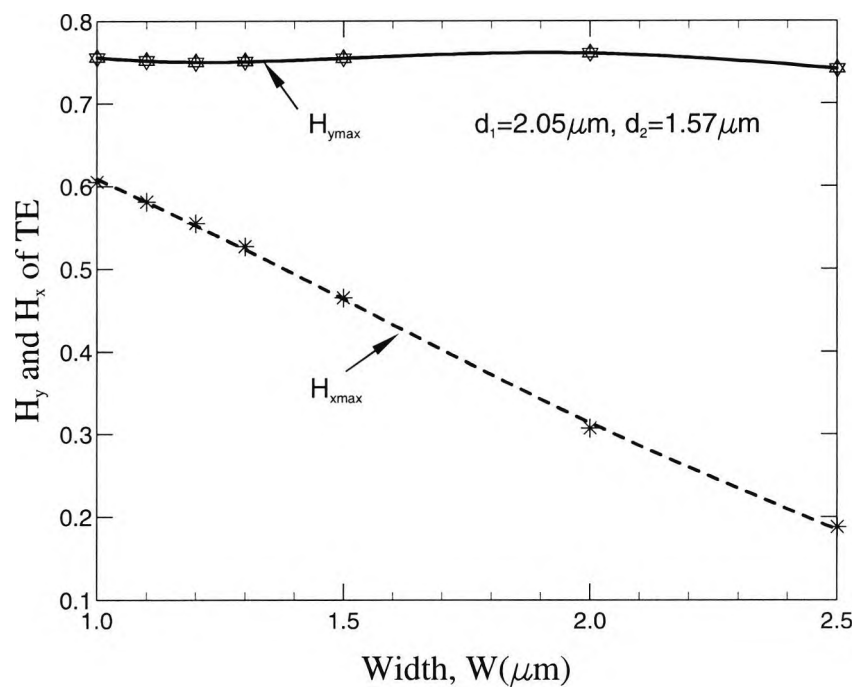
Fig. 5.57 Variation of the maximum H_y and H_x field magnitudes with width, *W*, for the TE mode.

The variation of the half beat length, L_π, with the width, *W* is shown in **Fig. 5.58**. When *W* = 2.5 μm, the half beat length is 924 μm and L_π is decreased as the width is decreased, suggesting a very compact design, below 400 μm, may also be possible.
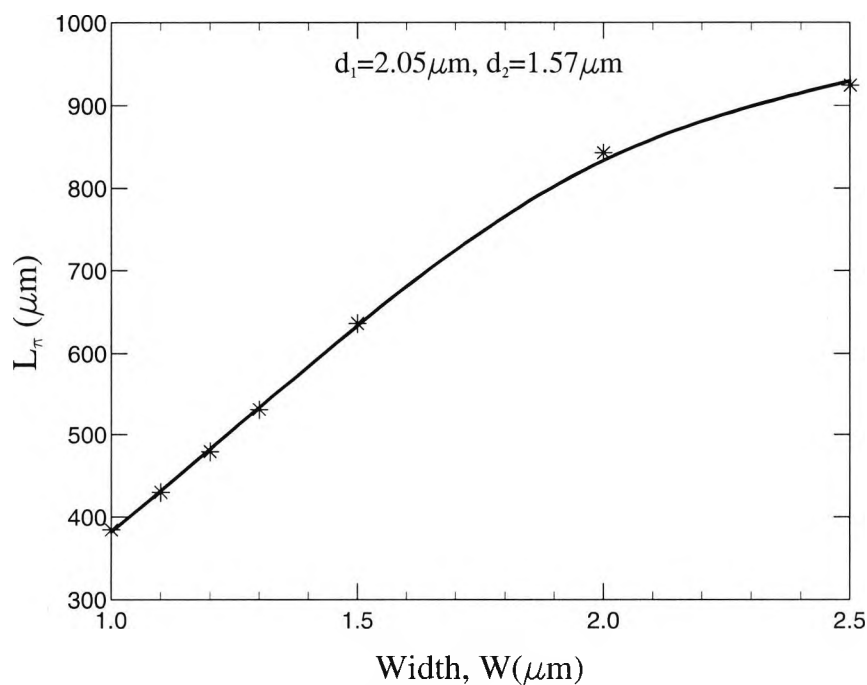
Fig. 5.58 Variation of the half beat length, L_π with width, *W*.

The effects of the etch depths of both sides of the waveguide on the modal hybridity is then studied. The etch depth, d_2 is reduced to 1.2 μm, from its original value 1.57μm. It should be noted that when etch depth, d_2, is reduced, the effective width of the slant section is also reduced from 1.5 μm to 0.9 μm. This reduction also affects the height of etched GaAs layer on the right side of the guide. Here, the slope angles, θ_1 and θ_2 are considered to be same as above. The magnitudes of the dominant and non-dominant field amplitudes for the TE mode are obtained and compared with those of the original structure parameters as shown in **Fig. 5.59**. The non-dominant H_x field amplitude for TE mode is about 66% of that of the previous structure (d_1 = 2.05 μm, d_2 = 1.57 μm), suggesting a significant reduction of their modal hybridity.
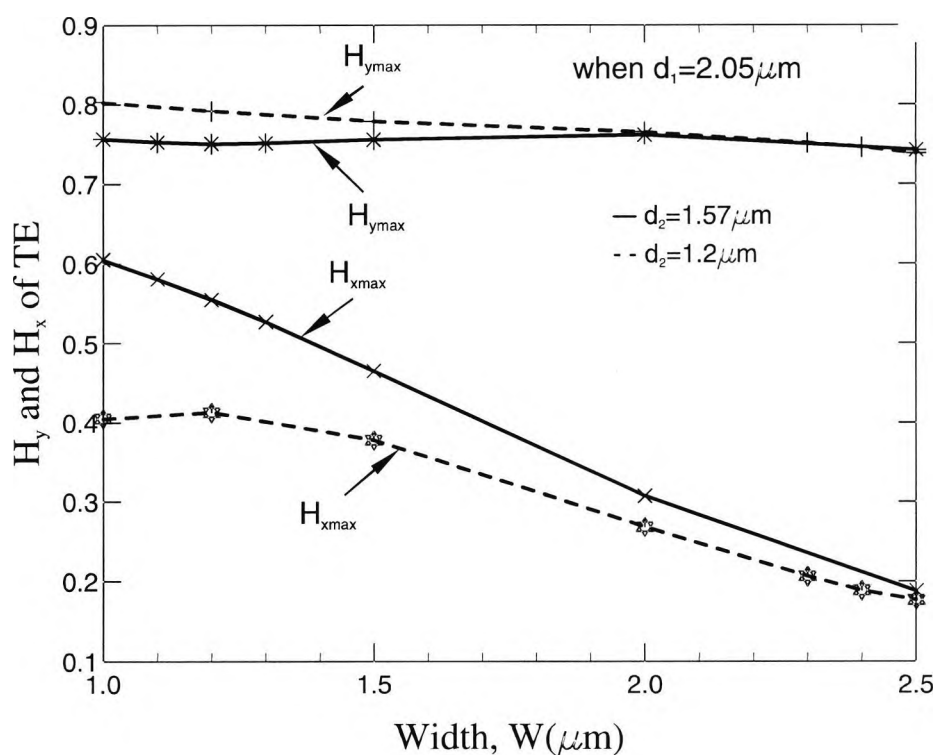
Fig. 5.59 Variation of the maximum H_y and H_x field magnitudes with width, W, for the TE mode (when d_1 = 2.05 μm, d_2 = 1.2 μm).

After that, the dimension d_1 was reduced from 2.05 μm to 1.9 μm and d_2 was kept constant as in the first case equal to 1.57 μm. The variation of H_y and H_x field amplitudes for quasi-TE mode with the width, W is shown in **Fig. 5.60**. As before, the curves for the original structure were also shown for comparison. Here, it can be seen that the hybridity is only slightly reduced than the original structure.
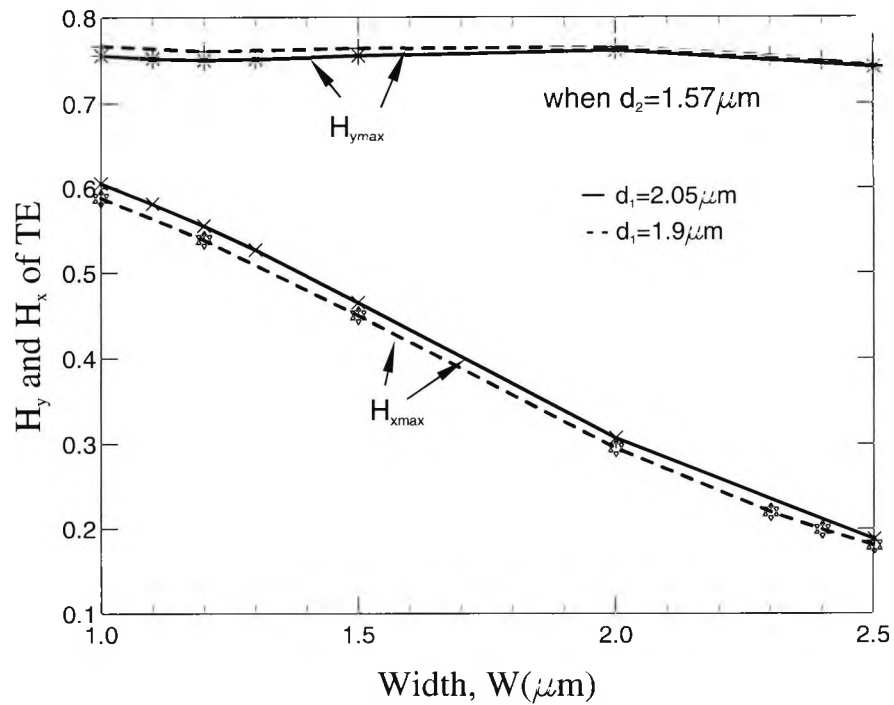
Fig. 5.60 Variation of the maximum H_y and H_x field magnitudes with width, W, for the TE mode (when $d_1 = 1.9$ μm, $d_2 = 1.57$ μm).

For a design of a polarization rotator, it is necessary that the input and output waveguide sections should support nearly pure TE and TM modes. It is known that a waveguide with symmetry along the central vertical axis supports such modes, hence such a structure is considered for its evaluation. Here, a rib waveguide with vertical sidewalls, as shown in **Fig. 5.61** below, is considered to couple the polarization rotator section incorporating the slanted waveguide section.
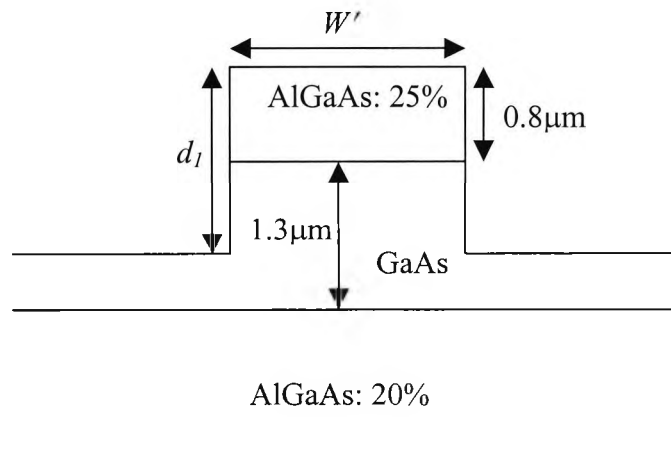
Fig. 5.61 Schematic of the rib waveguide with vertical sidewalls.

The width of the waveguide, W' is considered to be 2.5μm, the same lower width of the slanted waveguide section, as considered earlier. The dominant H_y field component of the quasi-TE mode is found to be symmetric, whereas the non-dominant H_x field profile is clearly anti-symmetric, with its maximum amplitude of only 0.007. H_x and H_y field profiles of the H^x_{11} mode are also similar to the contour profiles of H_y and H_x of H^y_{11} mode, respectively.

The straight rib waveguide is then used as the input section to butt-couple the slanted semiconductor waveguide. The very efficient and accurate Least Squares Boundary Residual (LSBR) method is used to obtain the transmission coefficients at the discontinuity interface. When TE mode of the straight rib waveguide is incident on the interface, the transmission coefficients, τ_{ee} and τ_{em} are obtained as 0.70826 and 0.61461, respectively. Here, τ_{ee} and τ_{em} are the transmission coefficients of the excited TE and TM modes in the PR section, when TE polarized light is incident. For this design the overall insertion loss is 0.558 dB at the butt-coupling junction. At first, no offset between the two guides has been considered and it is assumed that their left side vertical walls are aligned. The field profiles at the beginning of the slanted wave-guide (i.e. at $z = 0$) are shown in **Figs. 5.62** and **5.63**. At $z = 0$, the maximum field magnitudes of H_y and H_x are nearly 0.9 and 0.044, respectively. Here the TE power (P_y) and the TM power (P_x) were computed as 0.99862 and 0.00138 respectively.
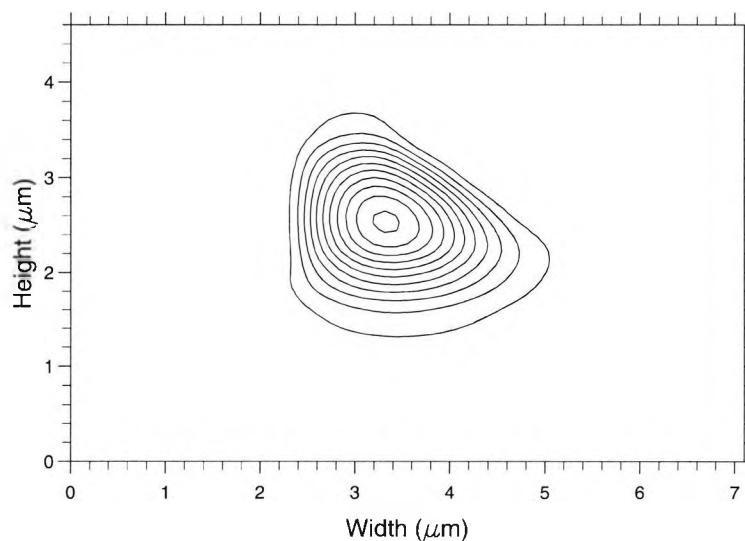
Fig. 5.62 H_y field profile at $z = 0$ when TE input is incident.
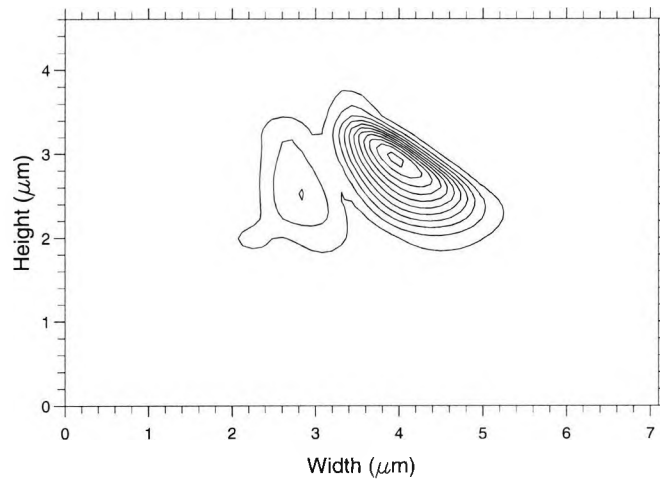
Fig. 5.63 H_x field profile at $z = 0$ when TE input is incident.

At $z = L_\pi$ (≈ 400 μm), most of the power has been transferred to TM, giving H_x and H_y field amplitudes to be nearly 0.88 and 0.115 respectively and P_x, P_y to be 0.9804 and 0.01959, respectively. The resultant H_y and H_x field profiles at the end of the PR section are shown in **Figs. 5.64** and **5.65**, respectively.
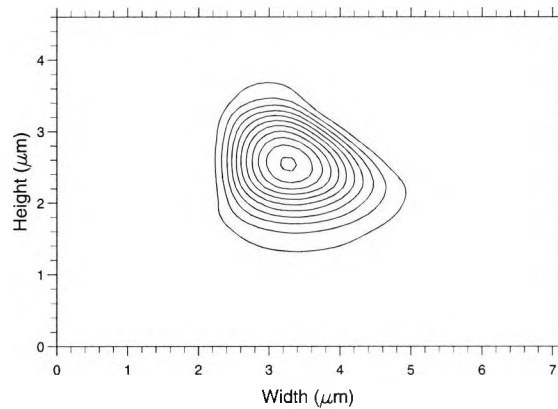
Fig. 5.64 H_x field profile $z = L_\pi$ when TE input is incident.
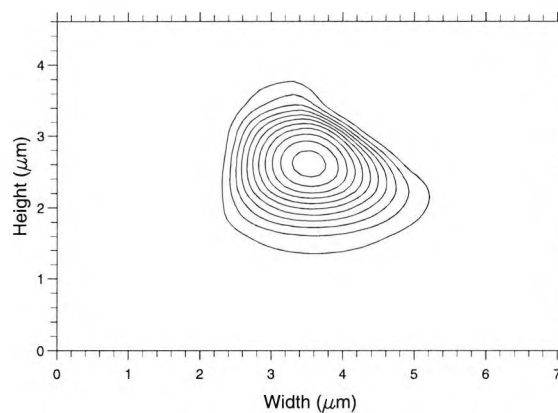
Fig. 5.65 H_y field profile $z = L_\pi$ when TE input is incident.

Since the modal field profiles of the straight and the slanted rib wave-guides are not aligned properly, next an offset was considered between the guides in order to improve the conversion and to reduce the insertion loss. By observing the modal field profiles of the input and slanted sections, 0.2 μm lateral shift between the centres was identified. Next the lateral offset, Δx, of 0.2 μm is considered for its rigorous evaluation. In this case, τ_{ee} and τ_{em} values were changed to 0.72061 and 0.63313 respectively with a much reduced insertion loss of 0.36 dB. The H_y and H_x field amplitudes at $z = 0$, are computed as 0.93 and 0.043, respectively and the P_y and P_x powers are calculated to be 0.99867 and 0.00132 respectively. At $z = L_\pi$, the maximum H_x magnitude has risen up to 0.91 and H_y maximum magnitude was 0.11 giving the power P_x and P_y of 0.98188 and 0.01812 respectively. The appropriate H_x field profile is shown in **Fig. 5.66**. The evolution of polarization power along the polarization rotator is shown in **Fig. 5.67**. It can be observed that if it is terminated at $z = L_\pi = 390$ μm and butt-coupled to a waveguide similar to the input waveguide, nearly pure TM (98.2%) polarized light can be obtained from the output.
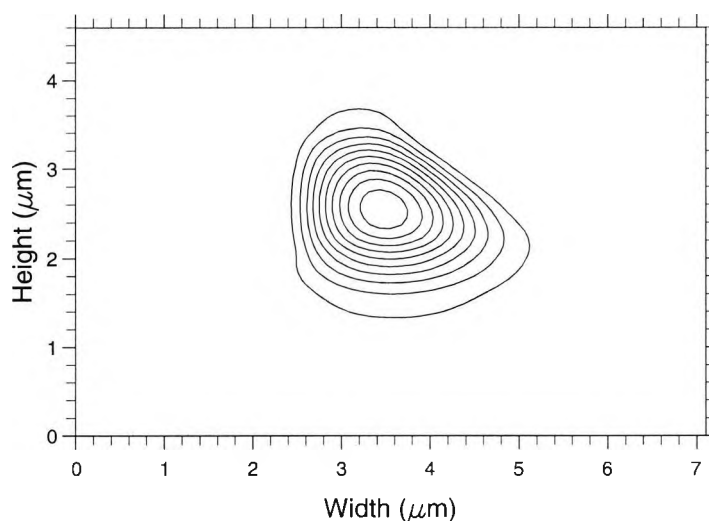
Fig. 5.66 H_x field profiles at $z = L_\pi$ when the offset, $\Delta x = 0.2$ μm, for the TE input.
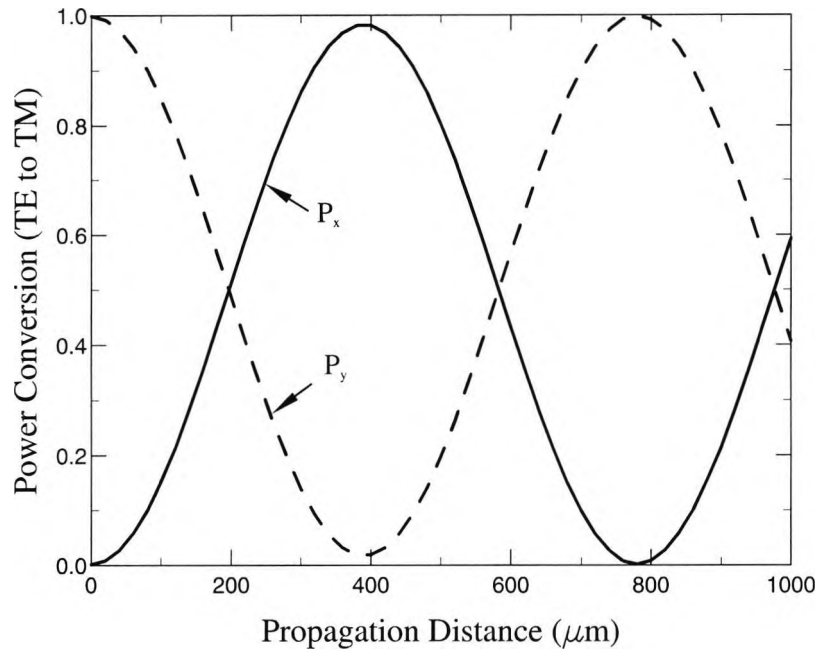
Fig. 5.67 Power conversion efficiency versus the propagation distance, z (μm) for TE input.

5.6   Updated design incorporating new features

The modelling that has been performed so far in the previous section has optimised W, d_1, d_2 and the lateral offset, Δx of the junction with the feed waveguide. The optimised parameters were W = 1.0 μm, d_1 = 2.05 μm, d_2 = 1.57 μm and the lateral offset is 0.2 μm, θ_1 and θ_2 are 32° and 69° respectively.

The effect of processing variations and wavelength on the performance of the structure has been studied next. Since the dimensions W and d_2 have a critical effect on the hybridity of the modes, further thorough investigation of these parameters should be concerned. Another parameter so far not considered is the verticality of the dry etch on the left hand side waveguide wall. In order to investigate this feature, an updated design for the polarization rotator with new features which are introduced by processing constraints is shown below in **Fig. 5.68**.
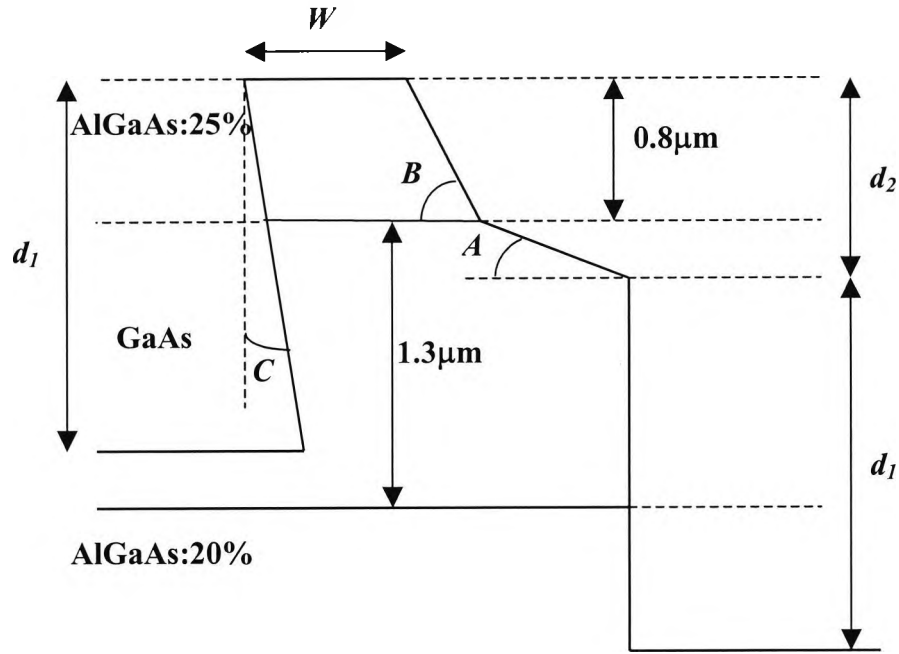
Fig. 5.68 Schematic of the new design for the polarization rotator.

The dry etch is now performed on both sides of the rotator. The undercut angle, C, has only been included in the left hand side of the waveguide, and it is assumed that this small undercut would have an insignificant effect on the right hand side wall and therefore considered as a vertical sidewall. The refractive indices of the GaAs, 20% AlGaAs and 25% AlGaAs at 1.55 µm wavelength, are taken as 3.37691, 3.27510 and 3.24999 respectively. Here d_1 is the etch depth of the left hand slanted sidewall and the right hand side vertical wall. d_2 is the etch depth of the right hand side slanted side wall. W is the upper width of the waveguide and A, B are the slant angles of the right hand sidewall.

The modal solution for the design with optimised parameters was obtained using the Finite Element Method (FEM) based on the vector **H**-field formulation (Rahman and Davies, 1984*a*). The optimised parameter values are;

$C = 0°$, $W = 1.0$ µm, $A = 32°$, $B = 69°$, $d_1 = 2.05$ µm, $d_2 = 1.57$ µm, $\lambda = 1.55$ µm.

For this case the propagation constant β_y of the H^y_{11} mode is computed as 13.49682. The field profiles of the three components, H_y and H_x for the quasi-TE (H^y_{11}) mode

are shown in **Fig. 5.69(a)** and **(b)**. **Fig. 5.69(a)** clearly shows the dominant H_y field of the fundamental quasi-TE mode, follows the shape of the slanted waveguide core and the maximum magnitude of the H_y field is 0.751964. **Fig. 5.69(b)** shows the non-dominant H_x field and the shape of the field contours is almost similar to the dominant field component. The amplitude of this field is 0.624376, showing a much improved hybridity of the optical modes. Similarly, the propagation constant, β_x of the H^x_{11} mode is computed as 13.48901. As a result the new value of the half-beat length, L_π is calculated as, 402.25 μm. This value is slightly different from the reported value of the previous structure in which there was no vertical sidewall in the right hand side.
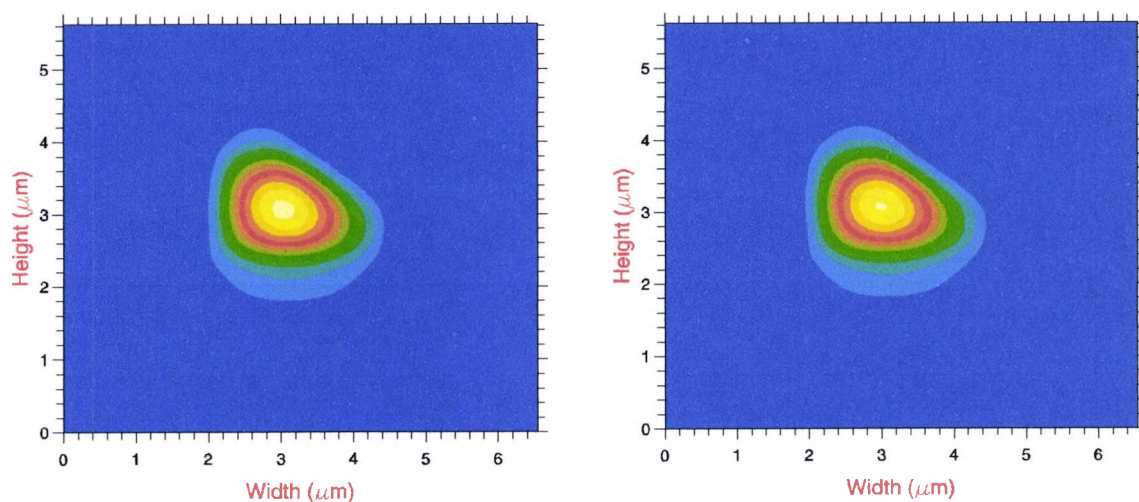
Fig. 5.69(a) H_y and **(b)** H_x field profiles for the quasi-TE (H^y_{11}) mode.

The parameters are varied within the regions as shown in **Table 5.1**, and simulations are carried out to investigate the effect of each parameter on the hybridity of the modes and the overall TE to TM power conversion.

Parameter	Range
C	0.0° - 2.0° step 0.5°
W	0.8 – 1.2 step 0.1μm
A	30° - 34° step 1°
B	65° - 73° step 2°
d_2	1.51 – 1.63 step 0.03μm
λ	1.53 – 1.61 step 0.02μm

Table 5.1 Parameter regions used for simulations.

The dimension d_l is kept constant at 2.05 µm and the width of the feed waveguide is also kept constant at 2.5 µm. The power calculation at the junction was obtained using the Least Squares Boundary Residual (LSBR) Method (Rahman and Davies, 1988) without considering any lateral offset between the waveguides.

5.6.1 Effect of the undercut angle, *C*

The undercut angle, *C* is varied from 0° to 2.0°, and the variation of the non-dominant field/dominant field ratio for both TE and TM modes are shown in **Fig. 5.70**. It is clearly visible that the hybridity of the TM (H^x_{11}) mode is slightly greater than that of the TE (H^y_{11}) mode. The hybridity is reduced with the increase of the undercut angle *C*, giving a percentage variation of about 3.4% for *C*=2°, with respect to the corresponding value for the optimised parameter *C* (i.e. *C*=0°).
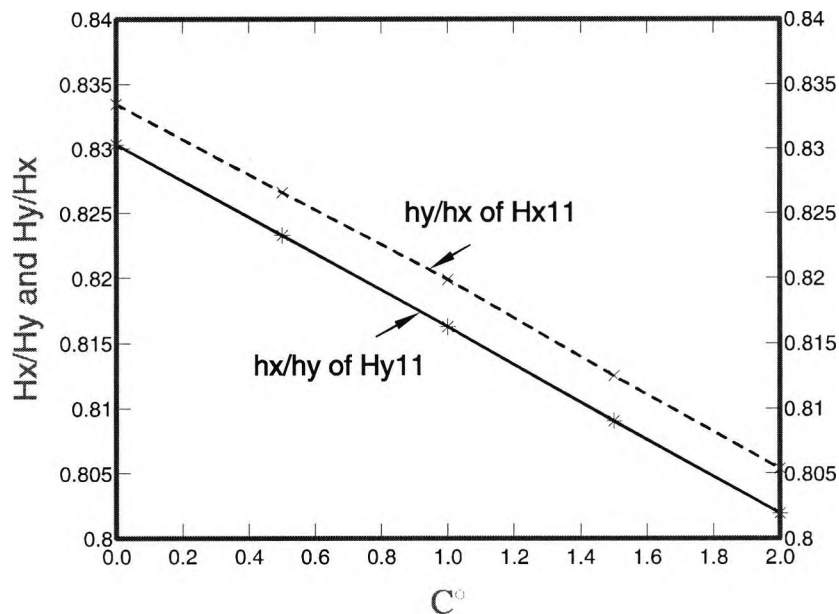
Fig. 5.70 Variation of the non-dominant field/dominant field ratio for TE and TM modes with the undercut angle, *C*.

Fig. 5.71 shows the variation of the half-beat length, L_π, with the undercut angle, *C*. At 0°, the L_π is 402.25 µm, and the value is reducing with the increase of *C*. The percentage variation of L_π over the range is about 10%. **Fig. 5.72** shows the variation of TM power at the output waveguide when TE power is launched from the feed waveguide. The solid line shows the power conversion at the designed half-beat

length, L_π = 402.25 μm for optimised structure and the dashed line implies the power conversion at exact L_π positions for different values of C. Here we can see that the P_x power at z = 402.25 μm is deviating from the corresponding value of power at exact L_π, as C increases. The reason for this is that the difference between the exact L_π position and 402.25 μm is increasing with the angle C. Therefore the power conversion at 402.25 μm is always lower than at exact L_π, as the maximum power occurs only at exact L_π position. As a result of the reduced hybridity with C, the power conversion is reduced with the value of C for both cases. The percentage variation of P_x at 402.25 μm is about 6% over the complete range of C. The insertion loss is 0.916 dB for the optimised design, i.e. when C = 0°. The calculation of the insertion loss is given later, in Section 5.6.7 and also a table of tabulated results of transferred power, P_x and crosstalk for each parameter variation is shown in **Table 5.3**.
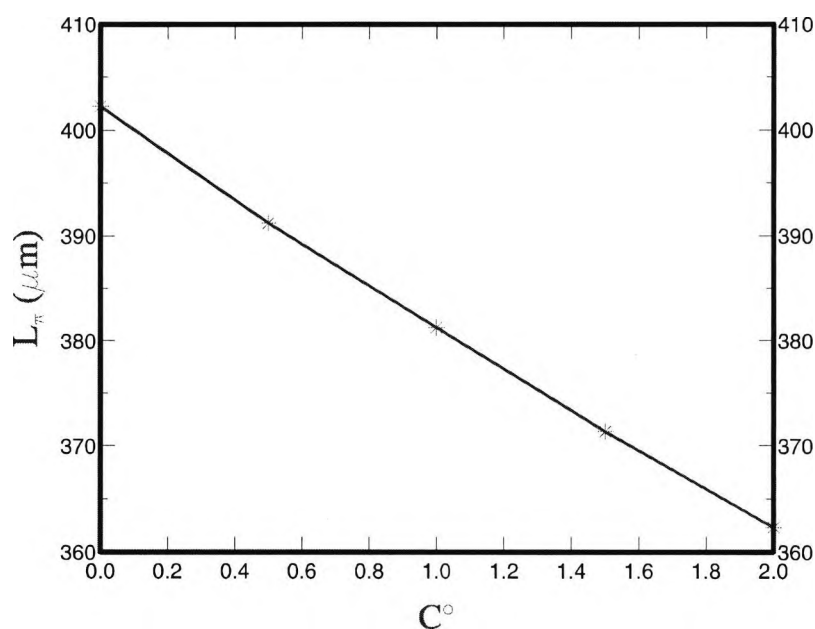
Fig. 5.71 Variation of the half-beat length, L_π, with the undercut angle, C.
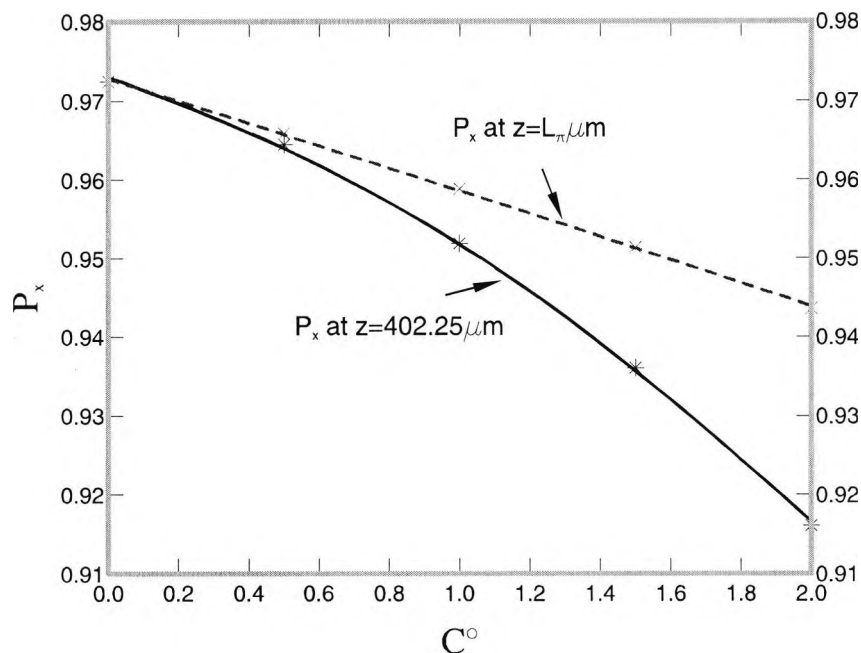
Fig. 5.72 Variation of TE to TM power conversion with the undercut angle, *C*, at different positions along the propagation direction.

5.6.2 Effect of the waveguide width, *W*

The dimension *W*, was varied from 0.8 μm to 1.2 μm and the simulations have been carried out to see the effect on modal hybridity and TE to TM power conversion. **Fig. 5.73** shows the variation of non-dominant/dominant field ratios for H^y_{11} and H^x_{11} modes. It is clearly seen that the hybridity is maximum at *W* = 0.8 μm and reduced as the width, *W* is increased. The variation is about +7.6% or –10% with respect to the corresponding field ratio value for the centre *W* value (i.e. *W* = 1.0 μm). The half-beat length, L_π variation is shown in **Fig. 5.74** and it can be seen that it drastically increases with the increase of *W*. The variation is about +23% or –20% from the L_π value for *W* = 1.0 μm. Therefore at *W* = 0.8μm, we can predict a better power conversion within a smaller length as a result of much improved hybridity and shorter L_π.
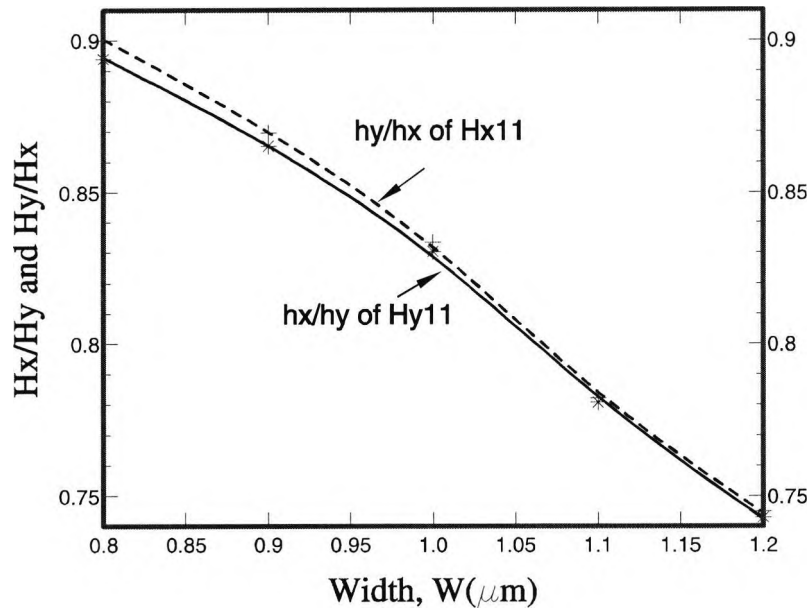
Fig. 5.73 Variation of the hybridity of the modes with width, *W*.
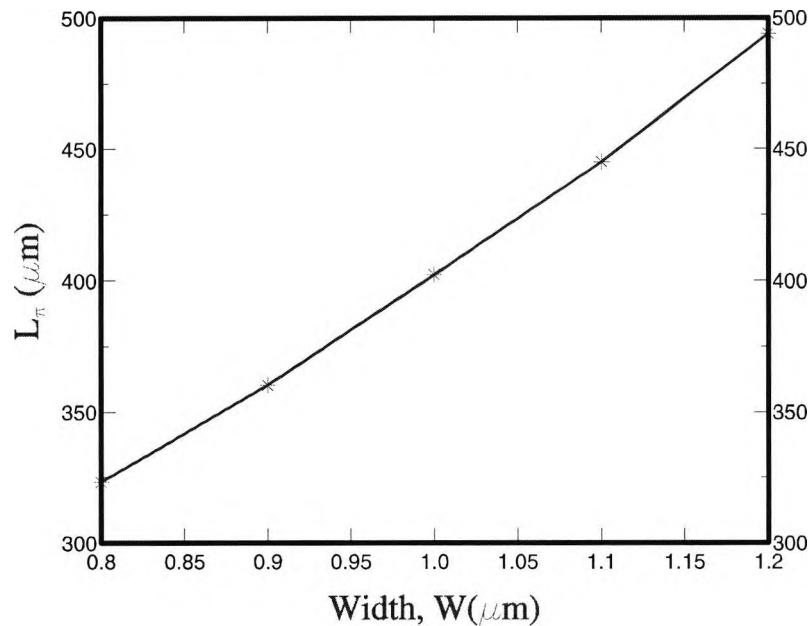
Fig. 5.74 Variation of the half beat length, L_π , with width, *W*.

The TE to TM power conversion curves are shown in **Fig. 5.75** for both at 402.25 μm and exactly at L_π for each *W* value. The P_x power at $z = 402.25$ μm is maximum at $W = 1.0$ μm, as the length matches with the exact L_π value and decreases as *W* deviates from 1.0 μm. The change is about 20% with respect to the value at 1.0 μm. The P_x power at $z = L_\pi$ μm, is maximum when $W = 0.8$ μm due to the increase in

hybridity. Power conversion at $W = 0.8$ μm is higher than that of at $W = 1.2$ μm, i.e. $\Delta W = +0.4$ μm, since in the former case, enhanced hybridity yields higher polarization conversion. **Fig. 5.76** shows the crosstalk variation for both cases at $z = 402.25$ μm and $z = L_\pi$ μm, with width, W. The minimum cross-talk of -15.6dB at $z = 402.25$ μm occurs at $W = 1.0$ μm and it increases accordingly as the power conversion is reduced. At exact L_π the cross-talk reduces up to -25.7 dB at $W = 0.8$ μm which is the width corresponds to the maximum power conversion.
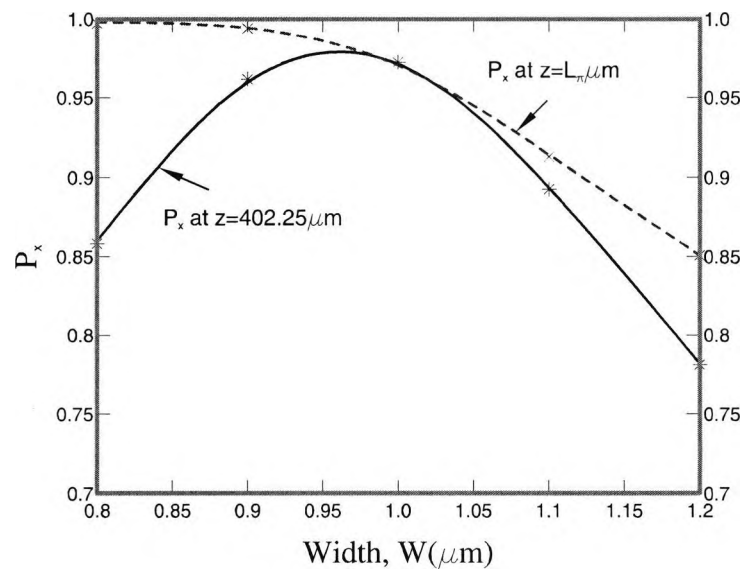
Fig. 5.75 Variation of TE to TM power conversion with the width, W, at different positions along the propagation direction.
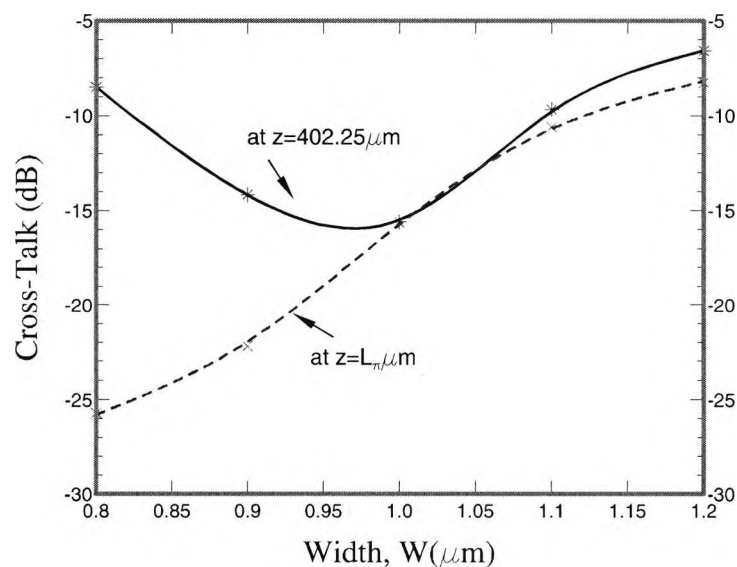
Fig. 5.76 Variation of the crosstalk with the width, W, at different positions along the propagation direction.

5.6.3 Effect of the sidewall angle, A

The variation of the non-dominant/dominant field ratios for TE and TM modes with the angle, A is shown in **Fig. 5.77**. It is visible that the hybridity for both the TE and TM modes are nearly the same and increases as the angle A increases. The variation with respect to the value at the optimised parameter, $A = 32°$, is about $\pm 11\%$. **Fig. 5.78** shows the L_π variation with the angle A and the L_π values over the range of $30°$-$34°$ is nearly the same and the magnified curve clearly shows a maximum around $A = 32°$. The variation of the L_π value is only 0.5%. Therefore the TE to TM power conversion is very much similar and undistinguishable at both $z = 402.25$ μm and at exact L_π as shown in **Fig. 5.79**. However, the transmitted TM power is considerably increased with the angle, A as a result of the improved modal hybridity. Power variation is about -9.5% or +3% with respect to the value at $A = 32°$.
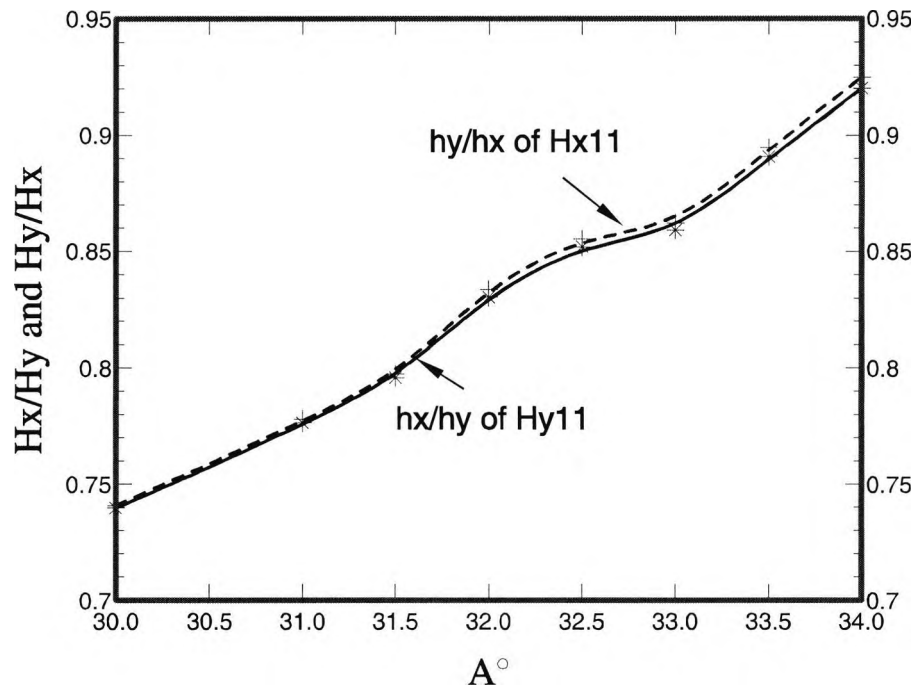
Fig. 5.77 Variation of the hybridity of the modes with the angle, A.
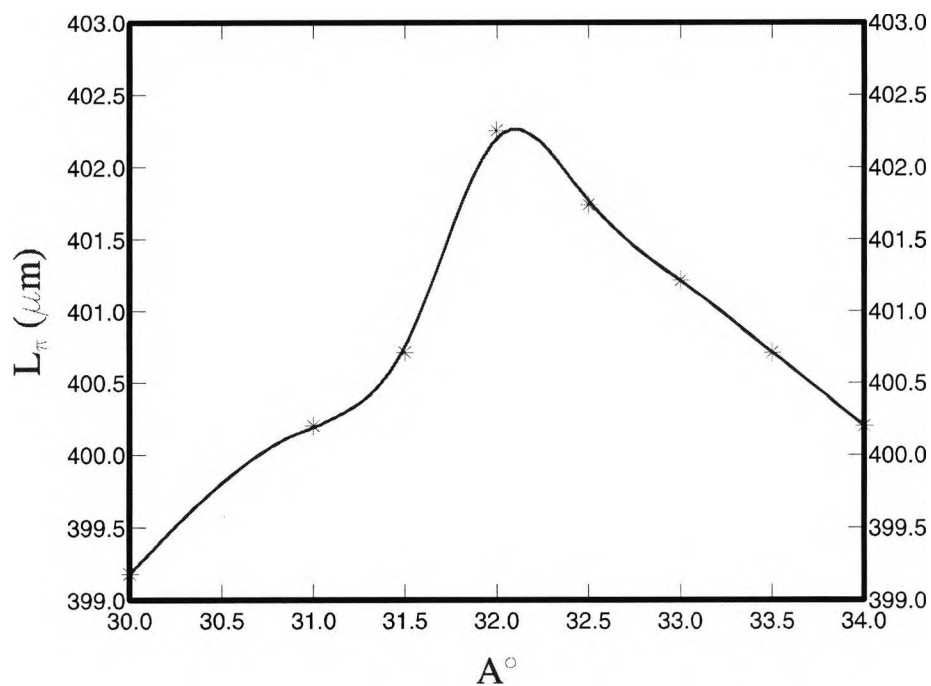
Fig. 5.78 Variation of the half beat length, L_π , with the angle, A.
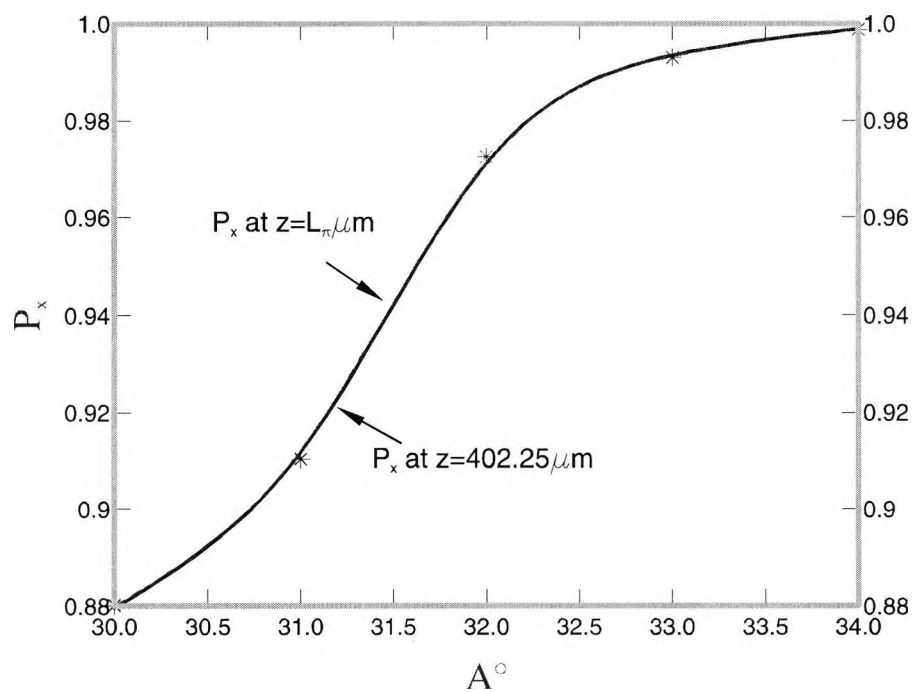
Fig. 5.79 Variation of the TE to TM power conversion with the angle, A, at different positions along the propagation direction.

5.6.4 Effect of the sidewall angle, *B*

The effect of the angle *B* on the hybridity of the modes is shown in **Fig. 5.80**. The field ratios are increased as the angle *B* is increased from 65° to 73°. The variation is about −5% or +2.4% with respect to the optimised value at *B* = 69°. The half-beat length, L_π decreases with the value of angle *B* and the L_π variation is about +5.4% or − 5.7% as shown in **Fig. 5.81**.
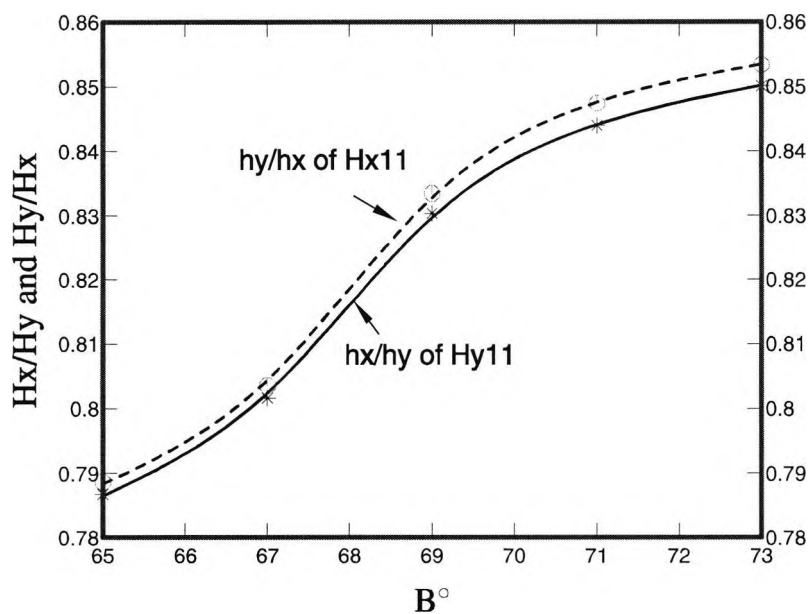
Fig. 5.80 Variation of the hybridity of the modes with the angle, *B*.
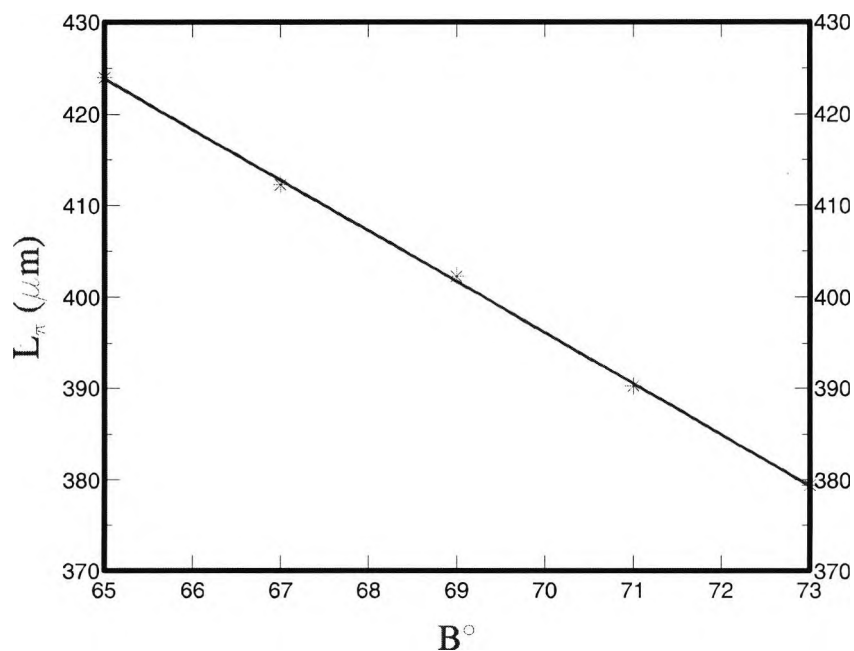
Fig. 5.81 Variation of the half beat length, L_π , with the angle, *B*.

The TM power curve is shown in **Fig. 5.82**. According to the figure, the TM power at $z = 402.25$ μm and at $z = L_\pi$ μm is almost similar for the region from $B = 67°$ to $B = 69°$, and in the other regions the power at $z = 402.25$ μm is slightly less than that at $z = L_\pi$ μm. However, the P_x power is increased with B, in both cases as a result of the increased hybridity and the variation is about –6% or +1% over the whole range of B.
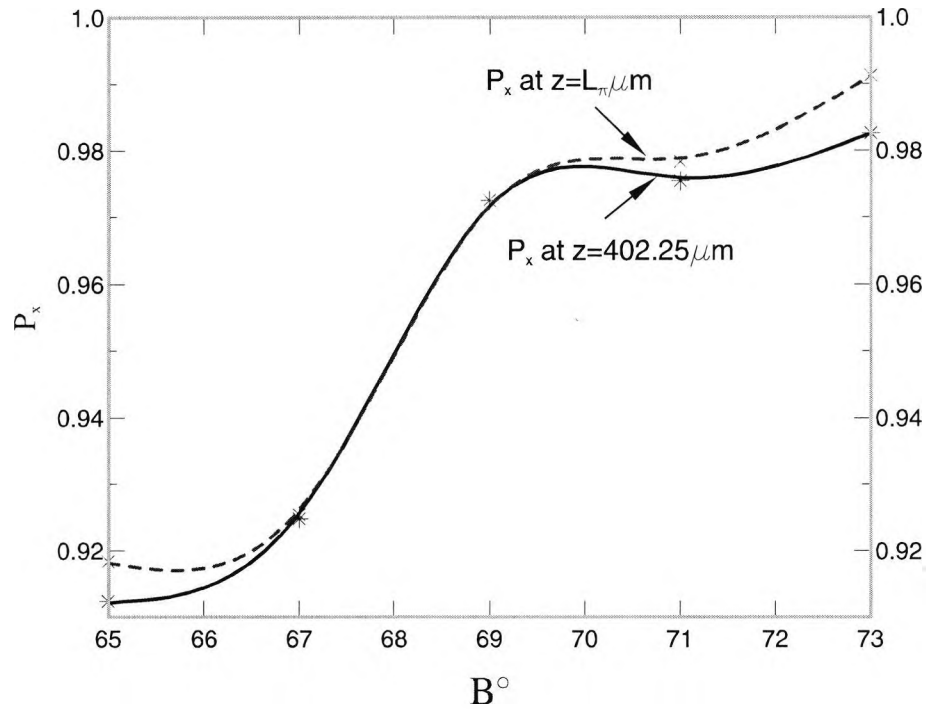
Fig. 5.82 Variation of the TE to TM power conversion with the angle, B, at different positions along the propagation direction.

5.6.5 Effect of the slanted etch depth, d_2

Fig. 5.83 shows the effect of d_2, on the hybridity of the modes. It can be seen that the non-dominant/dominant field ratios are decreased as the dimension d_2 is increased from 1.51 μm to 1.63 μm. The percentage variation is about +5% or –4% from the optimised value at $d_2 = 1.57$ μm. According to **Fig. 5.84**, the L_π reduces as the dimension d_2 increases, the variation being ±3% from the value at $d_2 = 1.57$ μm.

Fig. 5.85 shows the TE to TM power conversion variation curve for different values of d_2 ranging from 1.51 μm to 1.63 μm. The TM powers at $z = 402.25$ μm and $z = L_\pi$

µm are almost similar over the range of d_2 considered. P_x power is reduced as the value of d_2 increases due to the decrease in modal hybridity. The variation of the power is +2% or –5% over the region of consideration.
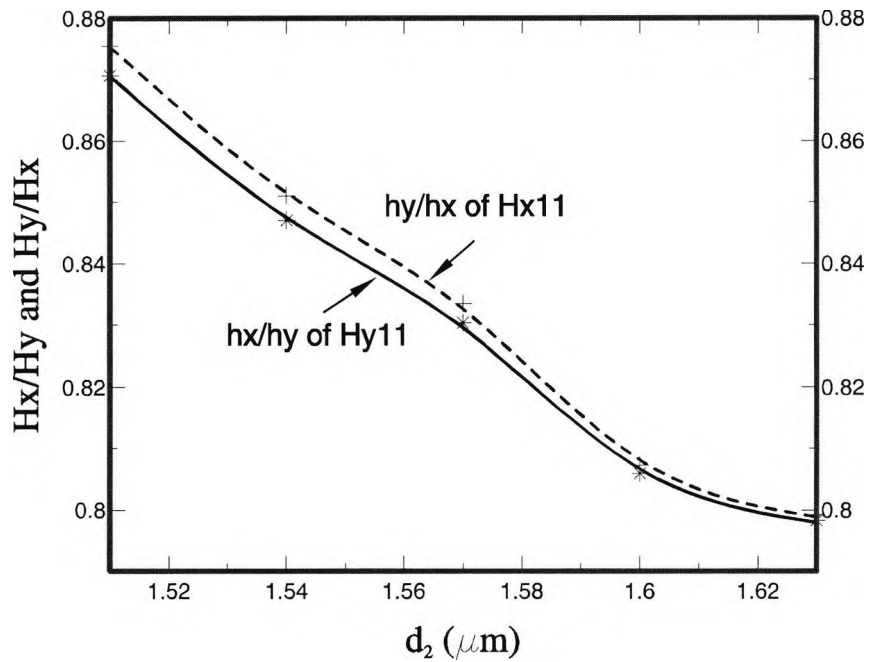
Fig. 5.83 Variation of the hybridity of the modes with the slanted etch depth, d_2.
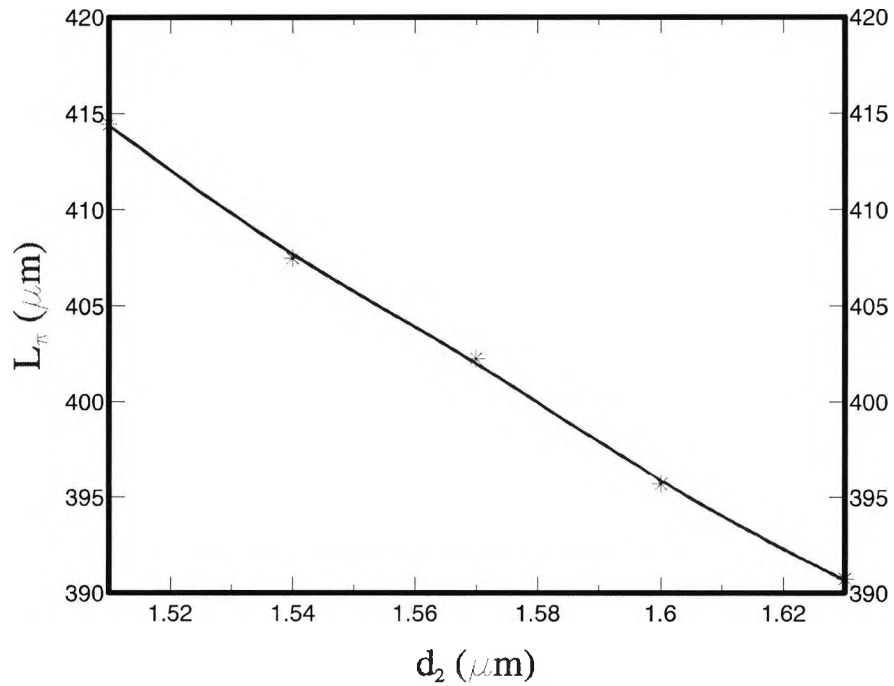
Fig. 5.84 Variation of the half beat length, L_π, with the slanted etch depth, d_2.
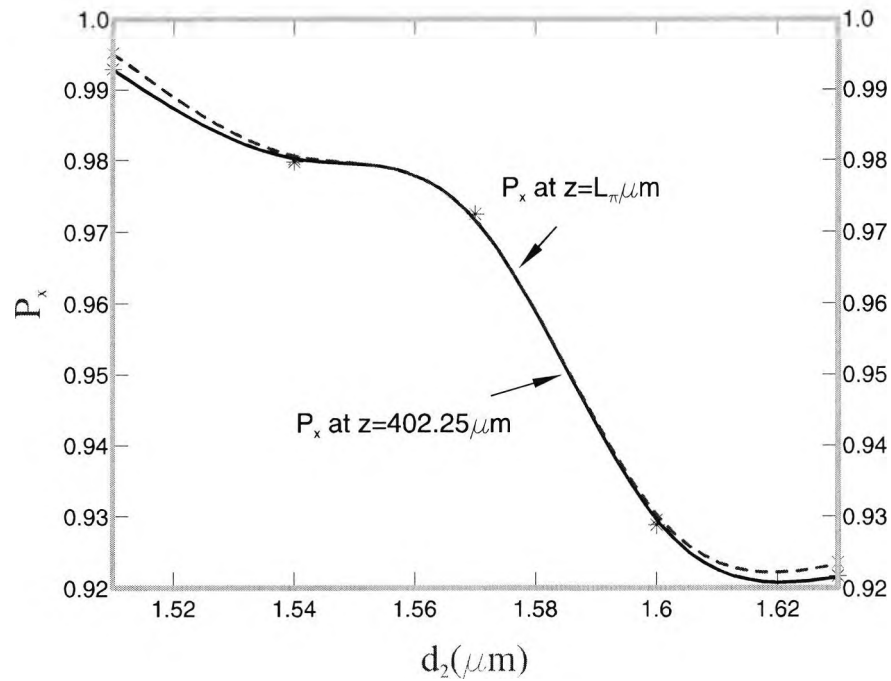
Fig. 5.85 Variation of the TE to TM power conversion with the slanted etch depth, d_2, at different positions along the propagation direction.

5.6.6 Effect of the wavelength, λ

Fig. 5.86 shows the variation of the non-dominant/dominant field ratios for both TE and TM modes with the wavelength, λ. The hybridity is clearly increased as the wavelength is increased from 1.53 µm to 1.61 µm, giving a percentage variation of about −1% or +3% with respect to the ratio value at the optimum position $\lambda = 1.55$ µm. This is anticipated, since increased wavelength is equivalent to the reduction in waveguide dimensions compared to the wavelength. The variation of L_π with λ is shown in **Fig. 5.87** and it shows that the L_π value decreases with the increase in λ. The percentage change is around +1.7% or -5%.

Then the TE to TM power conversion is obtained and the variation is shown in **Fig. 5.88**. The P_x power at $z = 402.25$ µm is always lower than the value at $z = L_\pi$ µm except at $\lambda = 1.55$ µm at which the power is the same for both cases as the length 402.25 µm itself is the exact L_π.

However, the power conversion is maximum at $\lambda = 1.61$ μm as the hybridity is maximum at that point. The percentage power change at $z = 402.25$ μm is about -0.5% or 0.4%.
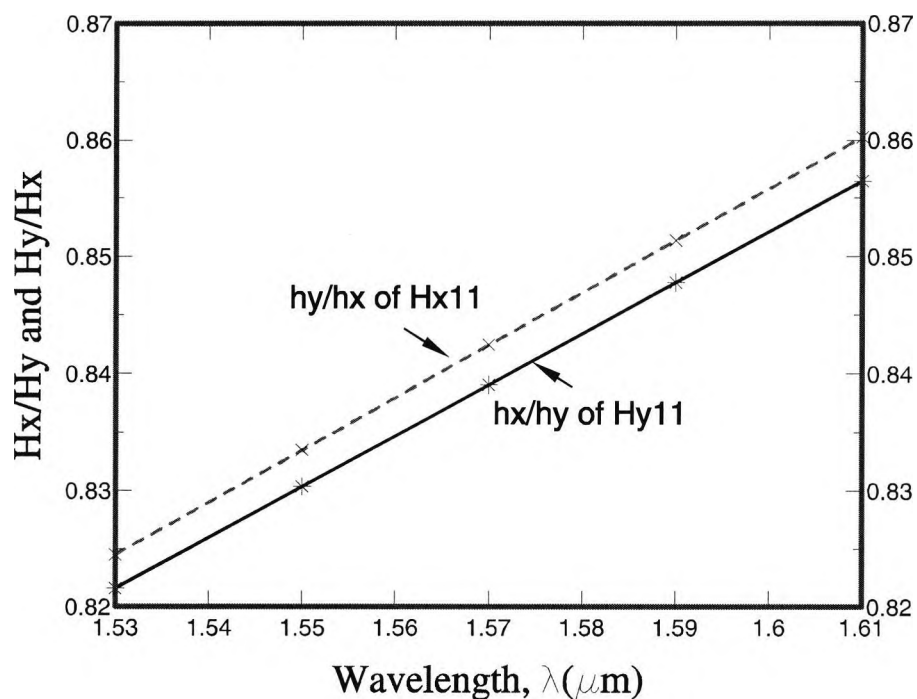
Fig. 5.86 Variation of the hybridity of the modes with the wavelength.
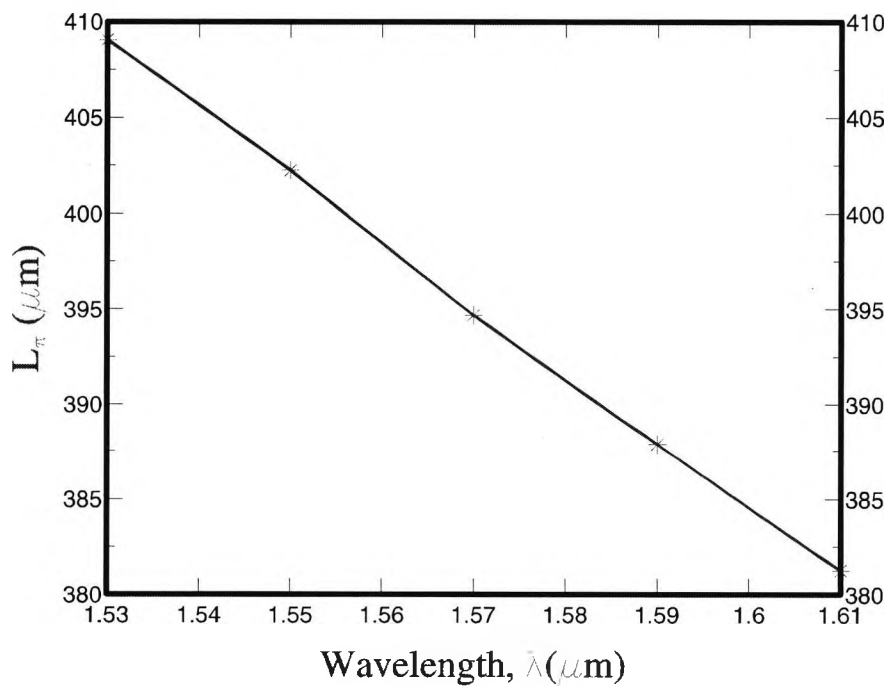
Fig. 5.87 Variation of the half beat length, L_π, with the wavelength.
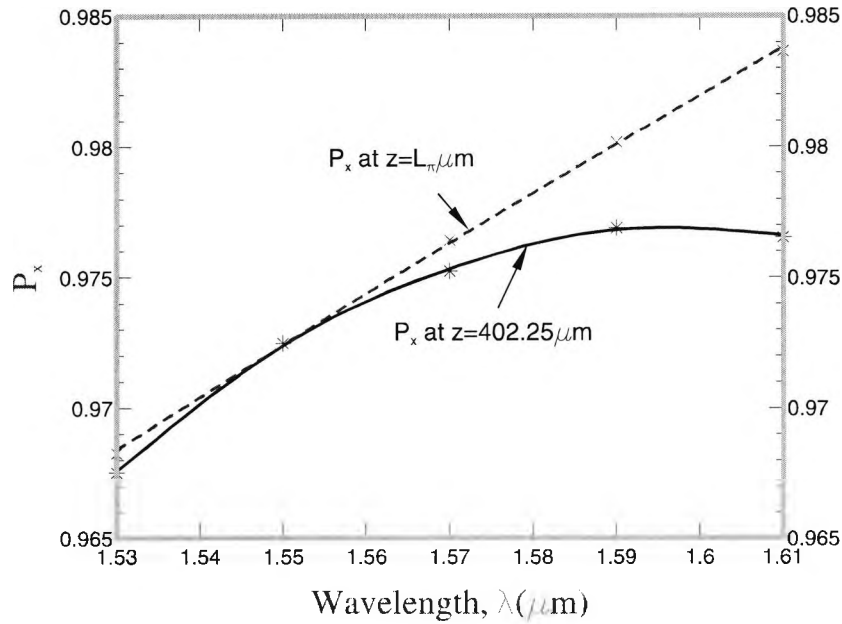
Fig. 5.88 Variation of the TE to TM power conversion with the wavelength, at different positions along the propagation direction.

5.6.7 Insertion loss and summary of the simulation results

The **Table 5.2** is given to show the percentage change of each polarization-based parameters such as, hybridity, L_π and converted TM power over the regions considered with respect to those of the optimised structure dimensions. It can be clearly observed, the width of the waveguide, W, is the key and the most sensitive parameter when designing the polarization rotator, and the power conversion is less sensitive to the other waveguide parameters and the wavelength.

Parameter	Percentage change		
	H_x/H_y of H^y_{11}	$L_\pi(\mu m)$	P_x power at $z = 402.25\mu m$
C^o	-3.4%	-10%	-6%
$W\ (\mu m)$	+7.6% or −10%	+23% or −20%	-20%
A^o	±11%	-0.5%	-9.5% or +3%
B^o	-5% or +2.4%	+5.4% or −5.7%	-6% or +1%
$d_2\ (\mu m)$	+5% or −4%	±3%	+2% or −5%
$\lambda\ (\mu m)$	-1% or +3%	+1.7% or −5%	-0.5% or +0.4%

Table 5.2 Percentage changes of the performance over each parameter regions with respect to the optimum.

Tabulated results of the insertion loss, the converted power, P_x, and crosstalk for each waveguide parameter and the wavelength are shown in **Table 5.3**. When unit power is incident on the junction, it excites two highly hybrid modes and the excited transmission coefficients of the modes are given by τ_{TE} and τ_{TM}. Therefore the total power transferred is computed as $(\tau_{TE}^2 + \tau_{TM}^2)$ and hence the insertion loss is given by $1 - (\tau_{TE}^2 + \tau_{TM}^2)$. Insertion loss calculated in dB scale is given below.

Parameter	P_x		Cross-Talk (dB)		Insertion Loss (dB)
	at $z=402.25\mu m$	at exact $L_\pi \mu m$	at $z=402.25\mu m$	at exact $L_\pi \mu m$	
C^o					
0	0.972487	0.972487	-15.6048	-15.6048	-0.91559
0.5	0.964480	0.965898	-14.4953	-14.6723	-0.91847
1.0	0.951854	0.958833	-13.1744	-13.8546	-0.92143
1.5	0.936068	0.951336	-11.9429	-13.1280	-0.92478
2.0	0.916090	0.943585	-10.7618	-12.4861	-0.92830
$W(\mu m)$					
0.8	0.858247	0.997308	-8.4847	-25.6992	-0.94759
0.9	0.961722	0.993977	-14.1705	-22.2019	-0.72956
1.0	0.972487	0.972487	-15.6048	-15.6048	-0.91559
1.1	0.892314	0.912801	-9.6784	-10.5949	-0.38762
1.2	0.780996	0.850594	-6.5955	-8.2563	-0.27438
A^o					
30	0.880066	0.880197	-9.2106	-9.2153	-0.46940
31	0.910398	0.910539	-10.4768	-10.4837	-0.49810
32	0.972487	0.972487	-15.6048	-15.6048	-0.91559
33	0.993028	0.993000	-21.5664	-21.5496	-0.58417
34	0.998783	0.998867	-29.1471	-29.4615	-0.62098
B^o					
65	0.912370	0.918408	-10.5735	-10.8835	-0.43364
67	0.924798	0.925364	-11.2377	-11.2706	-0.47964
69	0.972487	0.972487	-15.6048	-15.6048	-0.91559
71	0.975380	0.978337	-16.0871	-16.6428	-0.92941
73	0.982621	0.991242	-17.6000	-20.5764	-0.65661
$d_2\,(\mu m)$					
1.51	0.992866	0.995126	-21.4673	-23.1211	-0.56867
1.54	0.979762	0.980172	-16.9383	-17.0272	-0.85063
1.57	0.972487	0.972487	-15.6048	-15.6048	-0.91559
1.60	0.928813	0.929507	-11.4760	-11.5186	-0.52383
1.63	0.921739	0.923549	-11.0645	-11.1661	-0.52009
$\lambda\,(\mu m)$					
1.53	0.967521	0.968262	-14.8840	-14.9842	-0.91643
1.55	0.972487	0.972487	-15.6048	-15.6048	-0.91559

1.57	0.975246	0.976438	-16.0635	-16.2779	-0.91486
1.59	0.976895	0.980184	-16.3629	-17.0298	-0.91418
1.61	0.976543	0.983642	-16.2974	-17.8627	-0.91376

Table 5.3 Tabulated results of polarization conversion and insertion loss.

5.7 Summary

In Chapter 5, various designs of passive polarization rotators have been investigated. Numerical simulations have been obtained using the rigorous full vectorial based Finite Element Method. Initially, it was demonstrated that the semiconductor optical waveguides without symmetry are particularly suitable to increase the hybrid nature of the fundamental modes, thereby increasing the overlap between the polarization states. By using the versatile VFEM approach, the slant angles of the waveguide were represented exactly. The LSBR method has also been employed to analyse the waveguide junction interface.

A design of a compact 400 μm long passive polarization rotator with cascaded asymmetrical waveguide sections, with a very low insertion loss of 0.2 dB, has been presented. However, another important approach of a polarization rotator design has also been investigated, incorporating a single-section rib waveguide with a slanted sidewall. The effects of the waveguide width, index contrast, slant angle and the lateral offset between the sections, on the polarization rotation behaviour and the device length, were thoroughly investigated.

A detailed study of the fabrication tolerances of a compact passive, single-stage polarization rotator has been presented, by using rigorous numerical tools based on the VFEM method and the LSBR method. The length of the optimised PR is 403 μm and it is expected to have a low insertion loss of 0.6 dB. A 99.8% polarization rotation can be achieved with a very low crosstalk value of -29 dB. Fabrication tolerances were introduced for each waveguide parameter and also for the operating wavelength. When fabricating the device, the most crucial parameter to consider is the waveguide width, W. The simulated results clearly show that the variation of the slant angle, the

index difference, and the height hardly have any effect on the polarization behaviour. The device performance is reasonably stable with the variation of the operating wavelength. Finally, a novel polarization rotator design in asymmetric shallow-etched waveguides was introduced and its performance was analysed. Consequently, the design has been updated with new features, such as the use of an undercut angle in the left side wall and the performing of the dry etch on both sides of the rotator according to the processing constraints. A detailed polarization conversion study was undertaken to investigate the effect of each waveguide parameter.

Chapter 6

Polarization Crosstalk Studies in Silica Waveguides

6.1 Introduction

The next generation of systems for the "*all optical*" network will require higher performance components with dramatically lower costs per function. One approach to achieve significantly lower costs per function is to employ Planar Lightwave Circuits (PLC) to integrate multiple optical functions on a single substrate leading to a single package. The PLC technology (Kawachi, 1996) is mainly based on the low loss, integrated silica waveguides on silicon. The most prominent feature of silica waveguides is their simple and well-defined waveguide structure. The recent progress in PLC technology allows photonics component manufacturers to develop various complex integrated optic components, such as, 8×8 optical matrix switches (Okuno *et al.*, 1994) and arrayed waveguide grating (AWG) multiplexers and demultiplexers (Takahashi *et al.*, 1990; Takada *et al.*, 1996; Schauwecker *et al.*, 2000). The successful construction of these types of circuits strictly depends upon the low propagation loss of the silica-based waveguides. However, polarization crosstalk may also be an important issue to consider when fabricating such silica-based waveguides.

Modes in optical waveguides with two-dimensional confinement are not strictly transverse electric (TE) or transverse magnetic (TM), but hybrid in nature, which means all the six components of the magnetic and electric fields are present. The H_y component is the dominant component for the quasi-TE (H^y_{11}) mode and H_x component is the non-dominant field, which is usually very small. Similarly, for the fundamental quasi-TM (H^x_{11}) mode, the H_x is the dominant field component and the H_y component is the non-dominant one. Pure TE or TM modes with only H_y or H_x components, without the other transverse component of the magnetic field, would not exchange power between themselves. Polarization conversion can take place due to the interaction of the dominant and non-dominant components of the quasi-TE and TM modes, respectively or vice versa. The modal hybridity is defined as the ratio of the non-dominant to the dominant field components of the fundamental modes, as stated in the previous chapters, and it is an important parameter when considering polarization crosstalk studies. Generally the modal hybridity is higher in semiconductor waveguides compared to silica waveguides, due to their higher refractive index contrast between the core and the substrate, Δn. It has been reported in the earlier chapters of this thesis that for waveguides with structural asymmetry, they are capable of enhancing the hybridity and this effect has been exploited to design various types of polarization rotators. For example, passive polarization rotators have been designed incorporating semiconductor waveguide bends (Obayya *et al.*, 2001) and using semiconductor waveguides with slanted sidewalls (Tzolov and Fontaine, 1996; Rahman *et al.*, 2001; Somasiri *et al.*, 2002).

The hybridity of the optical modes in silica waveguides with low index contrast (Δn) is considerably smaller. Such low Δn waveguides are also superior to the high Δn waveguides in terms of fibre-coupling losses and are preferred for the fabrication of simple PLCs. Although polarization mode dispersion (PMD) has been clearly identified as a major problem for high data rate long distance optical data transmission using low loss silica fibres, however, polarization crosstalk in a few centimetres long planar silica waveguide has not yet been regarded as a serious problem. Only recently, Takada and Mitachi (Takada and Mitachi, 1998) have reported more than −21 dB polarization crosstalk in a 10 m long coil-like silica waveguide with 0.4% index contrast, which they attribute due to the presence of the curved corners. However,

recently some optical component manufacturers are developing plans to use waveguides with even higher index contrast to reduce waveguide bending radius, which in turn may reduce the chip size (Schauwecker *et al.*, 2000) or this can be used to increase the functionality of the chip. For examples, Inoue and Hida (Inoue and Hida, 2001) reported that by using *only* 1.5% Δn, a 400 channel AWG can be fabricated on a 15 cm wafer and a 512 channel AWG multi/demultiplexer fabrication on a 10 cm wafer has also been reported (Takada *et al.*, 2001). In this particular chapter, the results of our investigation on the possible polarization crosstalk in high Δn silica waveguides and its dependence on the sidewall slant angle are reported.

6.2   Planar silica waveguides

In the design of photonic devices and systems, mostly square shaped waveguides are considered because of their nearly circular mode shapes. In this investigation, a high Δn square shaped silica waveguide in the silicon-oxynitride (Si-O-N) material system is considered. The height, H is taken as 6 μm and the width, W is varied in order to understand its effect on the modal hybridity and the field profiles. However, in this case the two polarized modes also are degenerate when the height, H and the width, W of the waveguide are exactly equal. The square shaped waveguide cross section is shown in **Fig. 6.1**. As can be seen from the schematic figure, the core is completely surrounded by the cladding material. The core refractive index, n_g is assumed as 1.5 and the cladding refractive index, n_s is varied to control the index difference, Δn. The operating wavelength is considered to be 1.55 μm. In the initial investigation, the sidewalls of the waveguide are assumed to be perfectly vertical.

To study the polarization dependence, use of full vectorial numerical approaches is mandatory. First of all, to study the modal hybridity and to calculate the vector modal fields accurately, a full vectorial **H**-field based vector finite element formulation (VFEM) (Rahman and Davies, 1984*a*) is used. For an optical waveguide, all the three components of the modal magnetic field are continuous across the dielectric interfaces, unlike its dual **E**-field, whose normal component is not continuous across the dielectric interfaces.
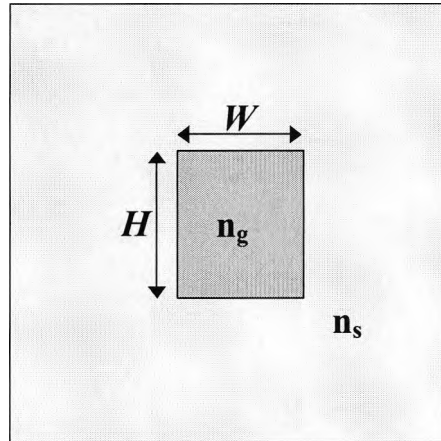
Fig. 6.1 Cross section of the silica waveguide with vertical sidewalls.

Next, the slanted sidewalls with slant angle, θ, are introduced in order to investigate its effect on the polarization conversion. The cross section of the silica waveguide with slanted sidewalls is shown in **Fig. 6.2**.
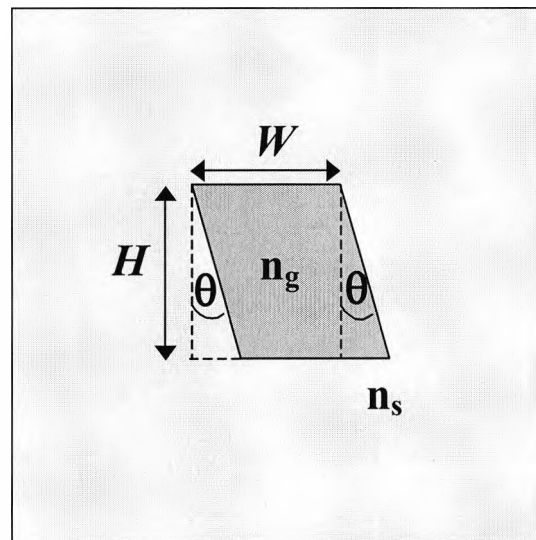
Fig. 6.2 Cross section of the silica waveguide with slanted sidewalls.

To study the effect of the sidewall slant angle on the polarization crosstalk, it is essential to represent the waveguide cross section accurately. A waveguide with a slanted sidewall can also be represented by a staircase approximation when using the finite difference method, but may need many steps to represent the sidewall slant dequately. However, in the VFEM method, the sidewall slant can be represented exactly using a smaller number of triangular elements.

6.2.1 Modal field analysis of the silica waveguides

To study the effect of the waveguide width, W on the modal degeneration, first a 3 μm wide rectangular waveguide with $\theta = 0°$, is considered. Here the index difference, Δn is considered as 1.5% giving $n_g = 1.5$ and $n_s = 1.4775$. **Fig. 6.3** shows the contour of the dominant H_x component for the quasi-TM (H^x_{11}) mode and it can be clearly seen that the field profile is symmetric along both the x and y axes of the waveguide. The field profile for the non-dominant H_y component of the quasi-TM mode is shown in **Fig. 6.4** and the field is clearly asymmetric along both the x and y axes of the waveguide, showing some field singularities at the four corners of the waveguide. The H_z field component of the H^x_{11} mode is also shown in **Fig. 6.5**. The field amplitude ratio of the non-dominant H_y field to the dominant H_x field for the quasi-TM mode is very small at 0.0028. There are two positive and two negative peaks at the four corners of the waveguide in such a way that the overall field profile is asymmetric along both the x- and y-axes and therefore the overlap integral of the vector modal fields of the two polarized modes is expected to be smaller. As a result, the power conversion between the two modes would be negligible at the waveguide irregularities.
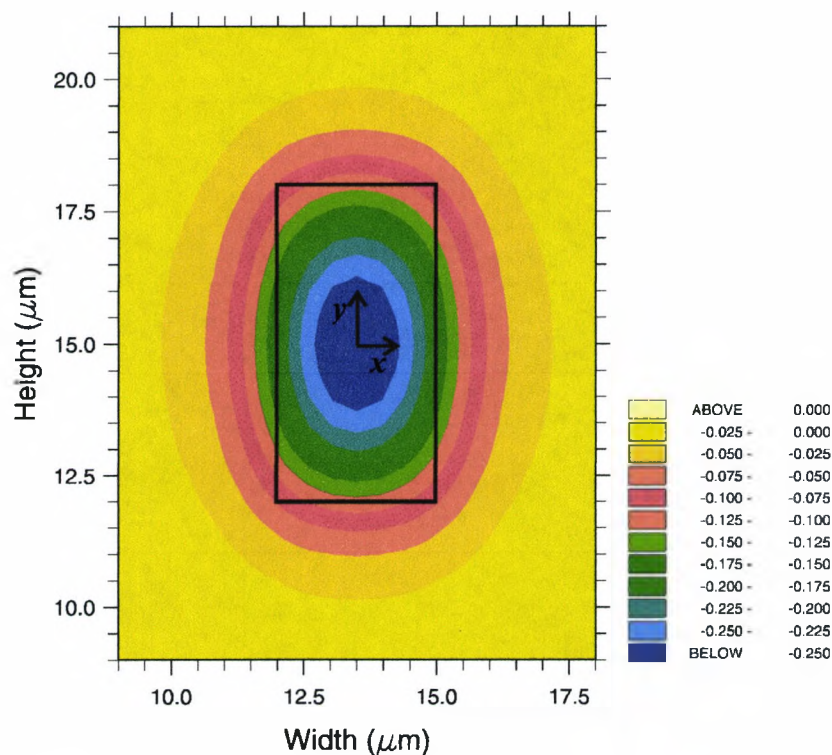
Fig. 6.3 The dominant H_x component for the quasi-TM (H^x_{11}) mode.
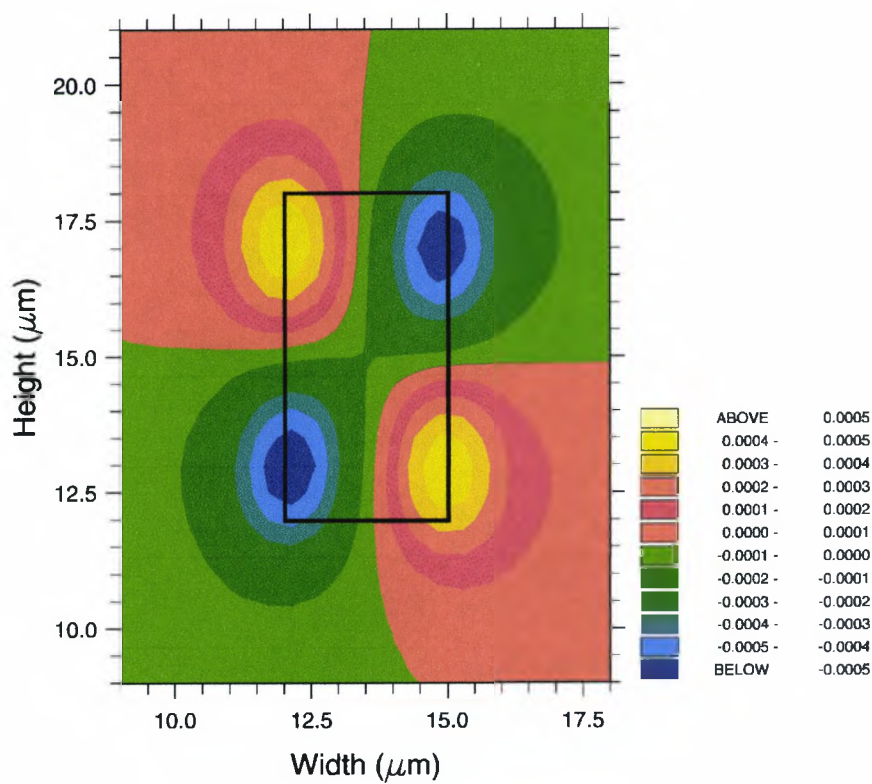
Fig. 6.4 The non-dominant H_y component for the quasi-TM (H^x_{11}) mode.
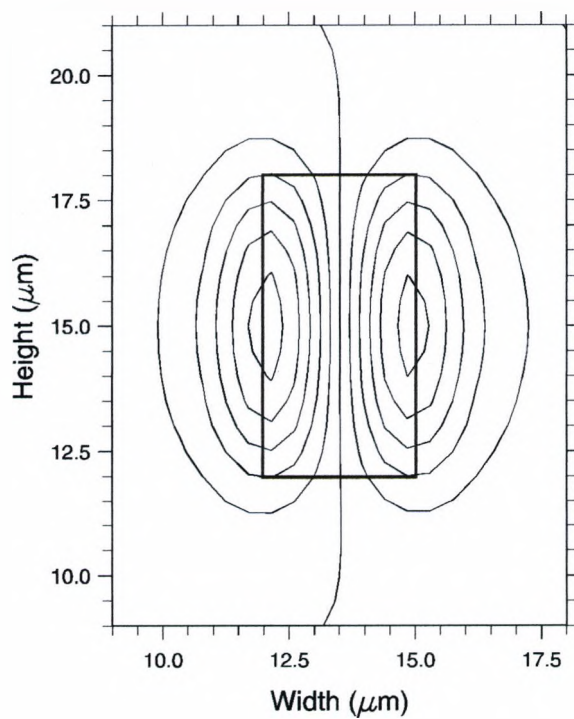
Fig. 6.5 H_z field component of the H^x_{11} mode.

Similarly the dominant H_y field of the quasi-TE (H^y_{11}) mode has two-fold symmetry and the non-dominant H_x field is asymmetric along the x and y-axes as shown in **Figs. 6.6** and **6.7**, respectively.
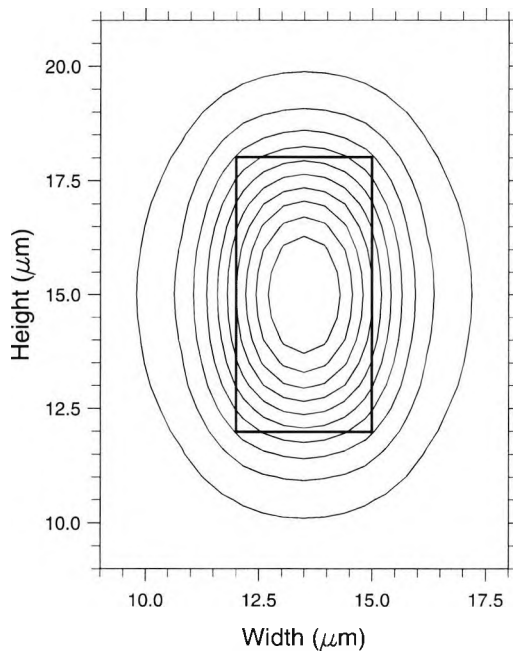
Fig. 6.6 The dominant H_y field of the quasi-TE (H^y_{11}) mode.
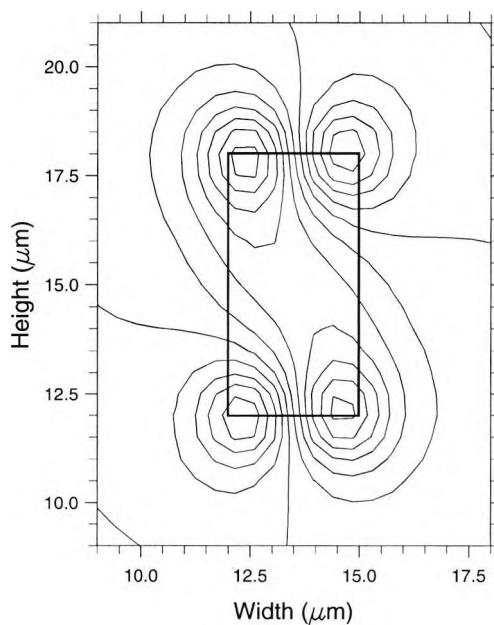
Fig. 6.7 The non-dominant H_x field of the quasi-TE (H^y_{11}) mode.

For this case, when $W = 3$ μm ($W < 6$ μm), the propagation constant, β_x of the quasi-TM mode is higher than that of the quasi-TE mode. If the waveguide width is increased, the propagation constants of both the quasi-TE and quasi-TM modes are increased. **Figs. 6.8** and **6.9** show the dominant H_x and the non-dominant H_y field components of the quasi-TM mode when $W = 5$ μm and $\theta = 0°$.
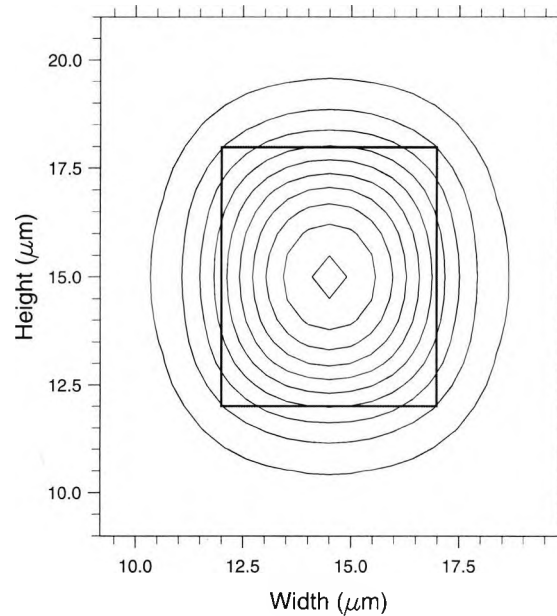
Fig. 6.8 The dominant H_x field component of the quasi-TM mode, when $W = 5$ μm.
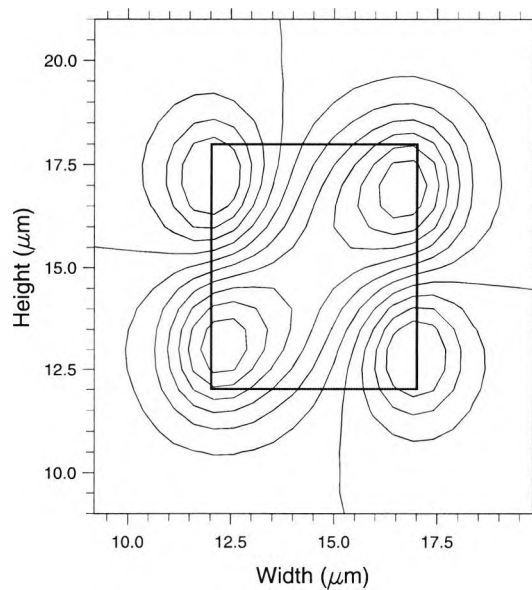
Fig. 6.9 The non-dominant H_y field component of the quasi-TM mode, when $W = 5$ μm.

As *W* is increased from 3 μm to 5 μm, the dominant field profile remains symmetric: however, it can be clearly observed that the shape of the non-dominant field profile is modified. When the width, *W* is exactly equal to the height, *H*, i.e. in this case, *W* = *H* = 6 μm, the two propagation constants of the quasi-TM and quasi-TE modes are equal and the two modes degenerate. When the two fundamental modes degenerate, both of their transverse H_x and H_y field components are symmetric in shape and also have equal amplitudes. However, this modal degeneration only occurs when the width, *W*, is equal or very close to its height. The dominant H_y and the non-dominant H_x field profiles for the H^y_{11} mode are shown in **Figs. 6.10** and **6.11**, respectively, when *W* = 6 μm and θ = 0°., i.e. at the instant of modal degeneration. From the field profiles at different widths, it can be clearly understood that the symmetric nature of the field profile changes as the polarized modes approach the modal degeneration. When the waveguide width, *W* is wider than 6 μm, the propagation constant, β_y of the quasi-TE mode is higher than that of the quasi-TM mode.
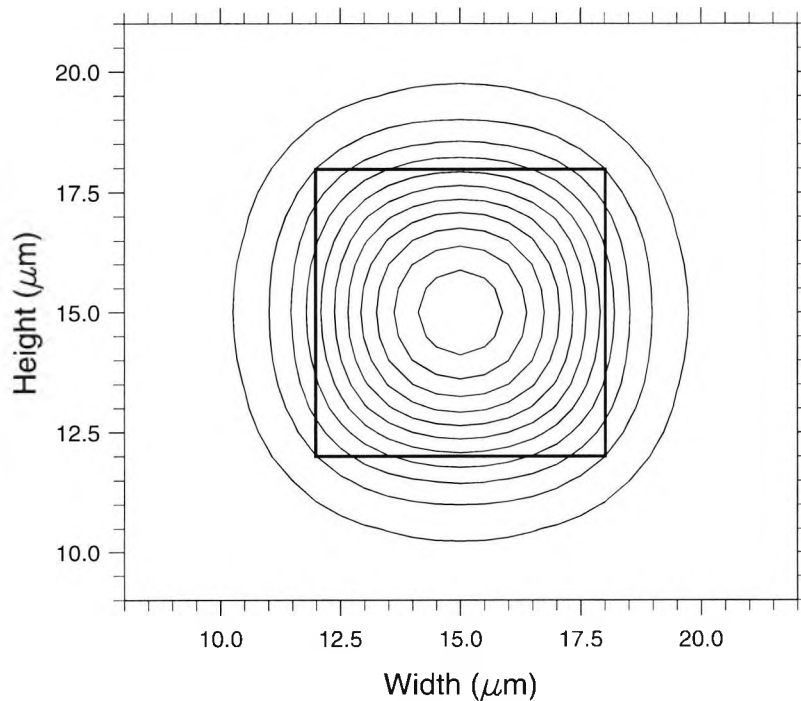
Fig. 6.10 The dominant H_y field profile for the H^y_{11} mode, when *W* = 6 μm and θ = 0°.
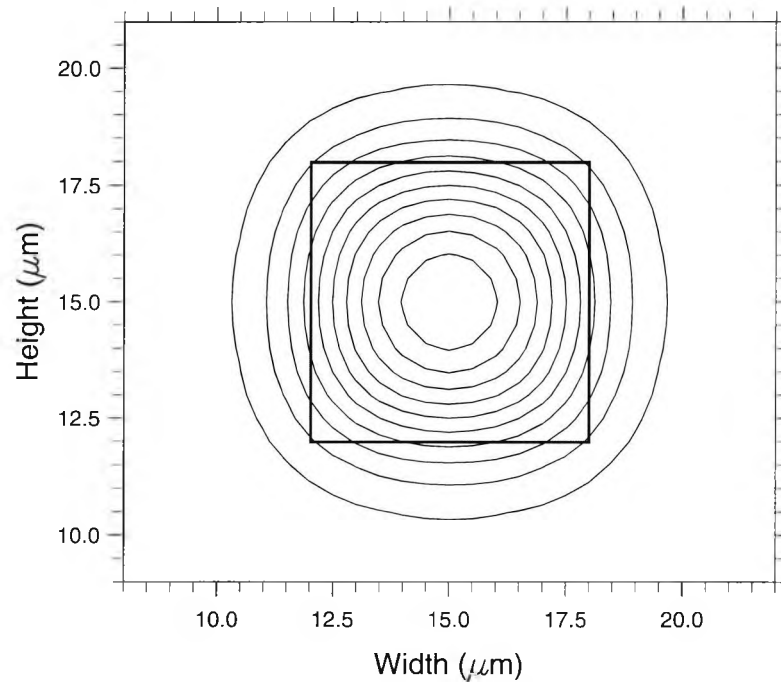
Fig. 6.11 The non-dominant H_x field profile for the H^y_{11} mode, when
$W = 6$ μm and $\theta = 0°$.

The modal hybridity can also be enhanced when the structural asymmetry (Rahman *et. al.*, 2001) is introduced. It may also be possible that during the fabrication process, the structure sidewall may not be exactly vertical and the effect of this deviation is studied next. The slant angle, θ is changed form $0°$ to $1°$. **Figs. 6.12** and **6.13** show the dominant H_x and the non-dominant H_y field components, respectively, for the H^x_{11} mode, when $W = 5$ μm and $\theta = 1°$. Here, the shape of the non-dominant field profile modifies dramatically and is clearly similar to the shape of the dominant field profile. The hybridity is increased to 0.051 as a result of the slight change in the slant angles of the sidewalls. Therefore it is expected that for such waveguides, there would be a significant overlap between the vector field profiles of the two polarized modes and a significant power conversion may take place between them.
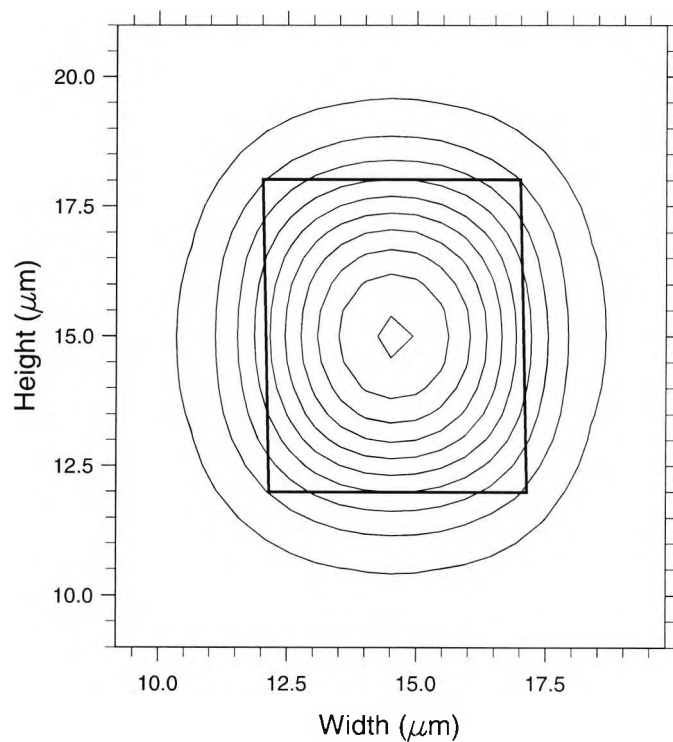
Fig. 6.12 The dominant H_x field component for the H^x_{11} mode, when $W = 5\mu$m and $\theta = 1°$.
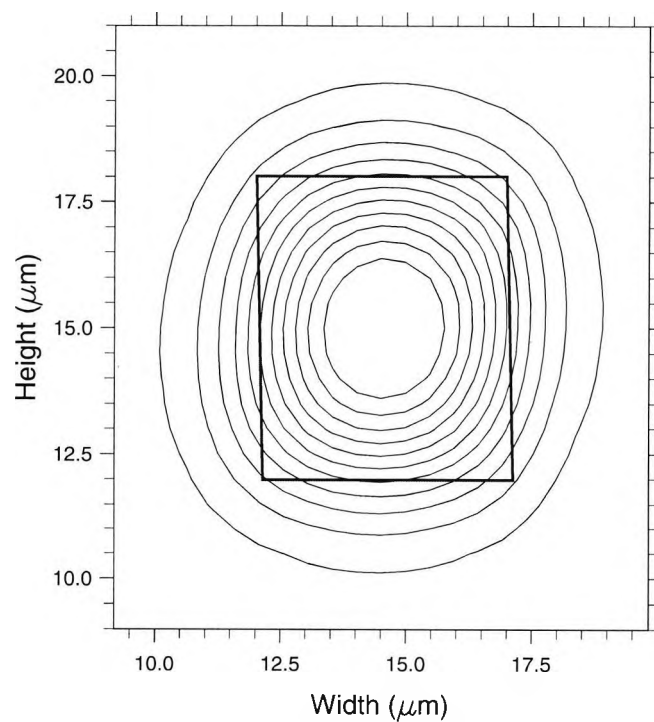
Figs 6.13 The non-dominant H_y field component for the H^x_{11} mode, when $W = 5$ μm and $\theta = 1°$.

6.3   Waveguide simulation results

In this section, the hybridity and the half-beat length, which are the two key parameters involved when considering polarization conversion are analysed thoroughly. Variations of the modal hybridity with the waveguide width for different slant angles are shown in **Fig. 6.14** for $\Delta n = 1.5\%$ and the H is kept constant at 6 µm. For slant angle 0°, the hybridity is maximum at $W = 6$ µm and reduces as W deviates from 6 µm. However, for other slant angles, maximum hybridity occurs at slightly lower widths. It can be clearly observed that the hybridity is a strong function of the slant angle, θ. When θ increases, the hybridity also increases accordingly. For $\theta=1°$ slant angle, the hybridity reduces to 50% of the maximum value when W deviates only ± 70 nm from being a perfectly square waveguide and for $\theta=5°$, the hybridity value reduces to 50% when W deviates about ± 0.3 µm from 6 µm. In this case, the modal hybridity does not strongly depend on the index contrast. There is a slight asymmetry of the variation of the modal hybridity with the waveguide width and it can be observed that for a wider waveguide of $W = 7$ µm, the hybridity is lower than that of $W = 5$ µm due to stronger confinement of the modes. Nearly 100% power conversion from one polarization state to another is only possible when their hybridity value is close to unity. For such strongly hybrid modes the usual understanding of the TE or TM mode may no longer be valid. However, to identify these modes, they have been classified as the TE or TM types, whenever $H_y > H_x$ or $H_x > H_y$, respectively.

Variation of the half-beat length, L_π, of the two polarized modes with the waveguide width, W, for $\Delta n = 1.5\%$ is shown in **Fig. 6.15**. Here, the half-beat length, L_π is defined as $\pi/(\beta_x-\beta_y)$, where β_x and β_y are the propagation constants of the two orthogonally polarized fundamental modes. At a distance equal to L_π along the waveguide, maximum polarization conversion can take place. This maximum conversion, P_{max}, can be nearly 100% only if the hybridity is close to unity. On the other hand, when hybridity is smaller than 1, although the polarization conversion (P_c) cannot be 100%, however, by cascading several sections of L_π length, the maximum conversion can be enhanced. However, in the design of periodic polarization rotators, a number of waveguide sections with reversed structural asymmetry would be needed to introduce the necessary phase reversal, as the maximum conversion for each L_π

section is very smaller. According to **Fig. 6.15**, it can be noted that the L_π values are highest at $W = 6$ μm for all the slant angles considered here. The L_π value reduces as the width moves away from 6 μm. For $\theta = 1°$, the maximum L_π is about 60 cm and for $\theta = 2°$, the maximum L_π value drops to 30 cm. However, when θ increases to 5°, the maximum L_π drops further to 12 cm. This shows that both the L_π and the modal hybridity strongly depend on the slant angle, θ, and any slight deformity of the waveguide cross section will have a significant effect on the polarization conversion in silica waveguides. The L_π variation along the range of waveguide widths, is not strictly symmetrical, and it can be noted that L_π at a wider width of 7 μm is greater than that of $W = 5$ μm.
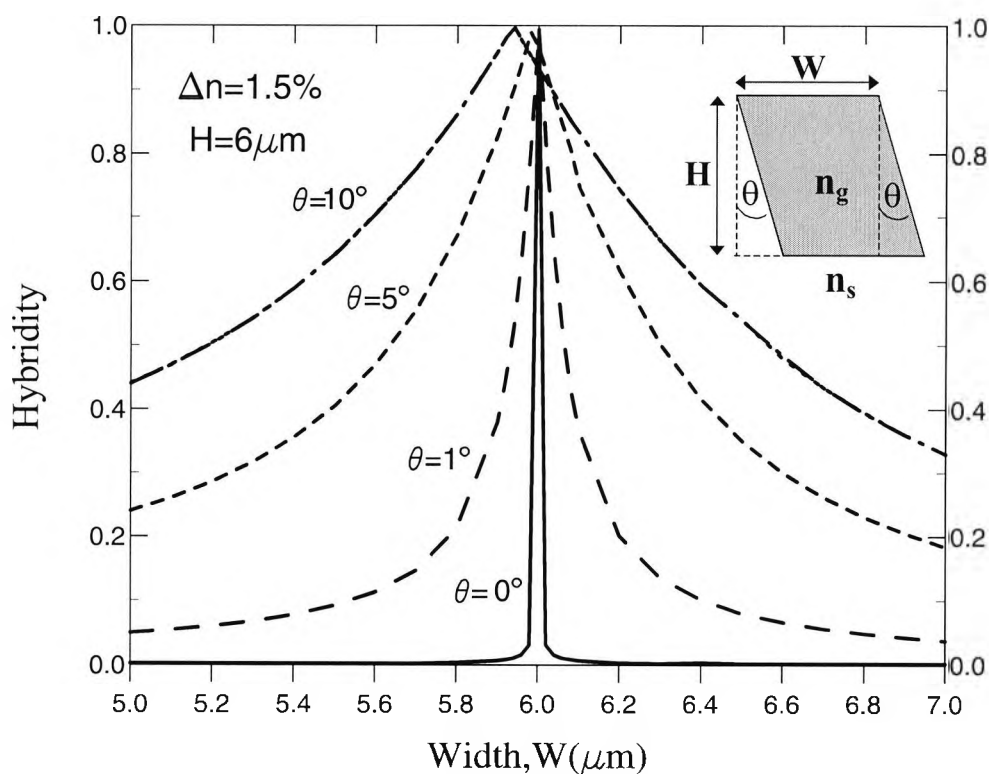
Fig. 6.14 Variation of the hybridity with the waveguide width, *W*.
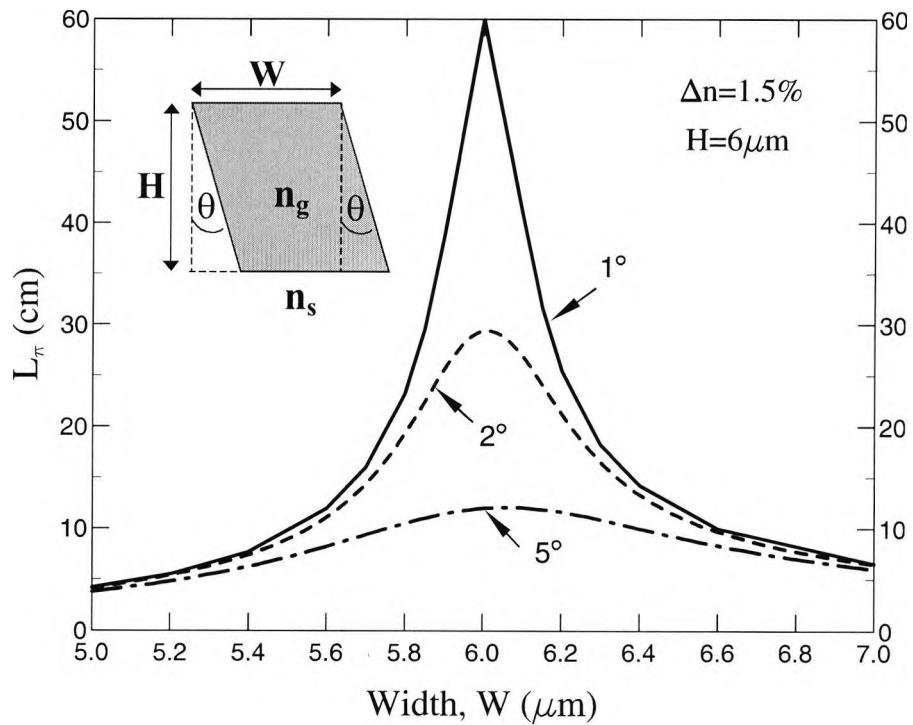
Fig. 6.15 Variation of the half-beat length, L_π, with the waveguide width, *W*.

6.4   Results of the junction analysis

This section is devoted for the analysis of the power transfer and the resulting crosstalk calculations. To calculate the power conversion between the two orthogonally polarized modes, when a pure TE or TM mode is incident from the input waveguide, a rigorous and full vectorial approach is mandatory to obtain the scattering coefficients. In this respect, the simple overlap integral approach (Van Der Tol *et al.*, 1995; Tzolov and Fontaine, 1996) may be inadequate and in this study, a rigorously convergent fully vectorial least squares boundary residual (LSBR) method (Rahman and Davies, 1988) is employed, which is an accurate and versatile numerical tool. The LSBR method uses the propagation constants and the field values generated by the finite element method and it is used to calculate the modal coefficients of the two hybrid modes at the junction interface.

6.4.1 Variation of the modal coefficients

It is shown that, when the sidewalls of the silica waveguide are not vertical ($\theta \neq 0°$), then the modes are not purely TE or TM, but hybrid in nature and in that case there is the possibility of polarization conversion in such waveguides due to the irregularities in their cross sections. If a pure TE or a TM mode is incident in such a waveguide, it will excite both the hybrid modes in the waveguide. To understand this phenomenon, the butt-coupling of the input silica waveguide which consists of vertical sidewalls, i.e. when $\theta = 0°$, and the slanted sidewall silica waveguide is considered for evaluation.

The excited modal coefficients, τ_e and τ_m of the two quasi-TE and TM modes, respectively, are found by using the LSBR method, when a pure TE mode is incident. The variation of τ_e with the width is shown in **Fig. 6.16**. It can be noted that when the waveguide has nearly vertical sidewalls, i.e. $\theta = 1°$, and because the hybridity is smaller at $W = 7$ μm or 5 μm, the τ_e is nearly equal to 1. Since the hybridity is equal to 1 at $W = 6$ μm, the τ_m is generated and therefore τ_e becomes smaller reducing to a value of $1/\sqrt{2}$. At this stage, both the modes carry 50% of the total input optical power. When the slant angle, θ increases then the τ_e value reduces. However, τ_e rapidly increases when the width of the waveguide is not exactly equal to its height, *H*, for waveguides with nearly perfect vertical sidewalls (i.e. $\theta = 1°$).

Fig. 6.17 shows the variation of the modal coefficient, τ_m, with the width, when TE is incident from the straight input waveguide. When *W* deviates from 6 μm, the τ_m value becomes very smaller, and at $W = 5$ μm or $W = 7$ μm its value becomes nearly zero (since hybridity is low and τ_e is dominant which nearly equals 1). On the other hand, τ_m value reaches $1/\sqrt{2}$ exactly at $W = 6$ μm due to the highly hybrid modes. As θ increases, not only the τ_m increases but also decreases slowly with the change in the width, *W*. When hybridity is maximum i.e. nearly 1, both TE and TM carry equal power since $\tau_e = \tau_m = 1/\sqrt{2}$.
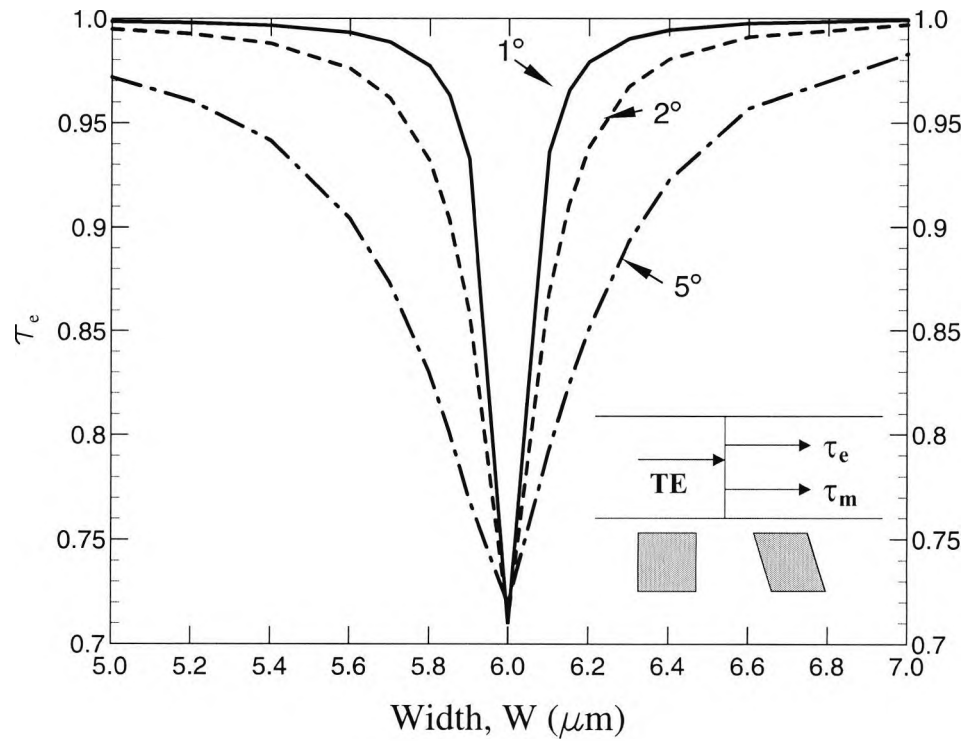
Fig. 6.16 Variation of the modal coefficient, τ_e, with the waveguide width, W, when TE mode is incident.
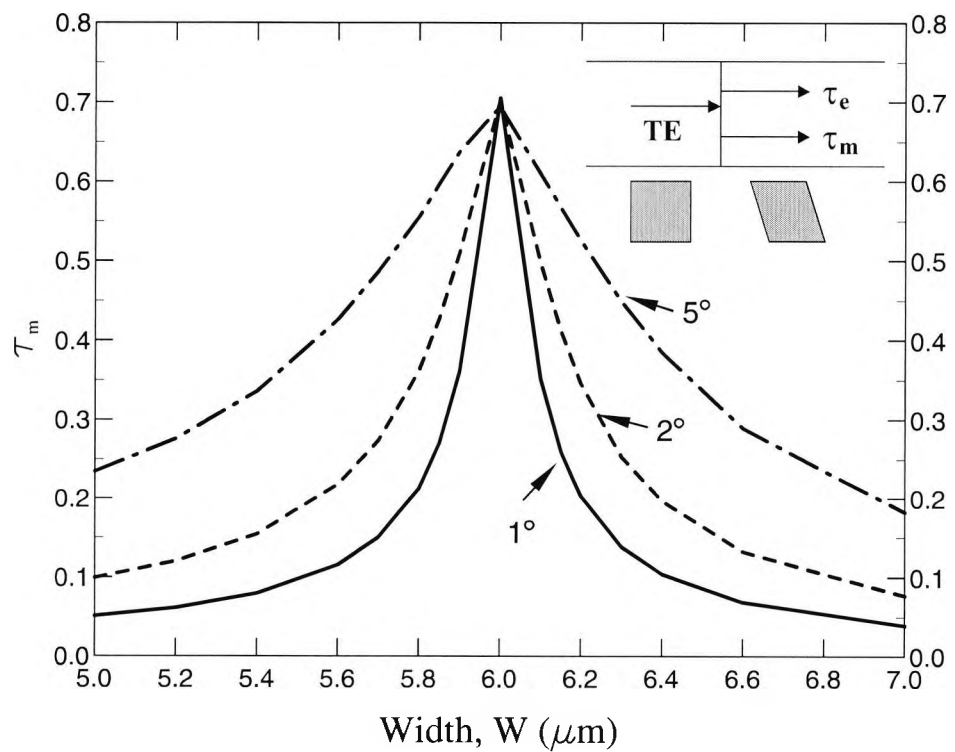
Fig. 6.17 Variation of the modal coefficient, τ_m with the waveguide width, W, when TE mode is incident.

6.4.2 Polarization conversion analysis

To analyse the undesirable polarization conversion process along the silica waveguide the power conversion from TE to TM is computed, by the use of the modal coefficients and the modal fields. It has been shown earlier, that when $W = 6$ μm, the hybridity is equal to 1 and $\tau_e = \tau_m = 1/\sqrt{2}$. When a pure TE mode is incident on to a waveguide with slanted sidewalls, it decomposes into two highly hybrid TE and TM modes, both carrying equal power. Their combined field is similar to the incident pure TE field and the TE polarized power, P_{TE} at the start (i.e. $z = 0$) is equal to 1. However, at a distance L_π along the axial direction of the waveguide, these two modes become out of phase and their combination will yield pure TM, thereby giving TE polarized power, $P_{TE} = 0$ and TM polarized power, $P_{TM} = 1$. **Fig. 6.18** indicates an approximate graphical implementation of the above mentioned power conversion phenomenon.
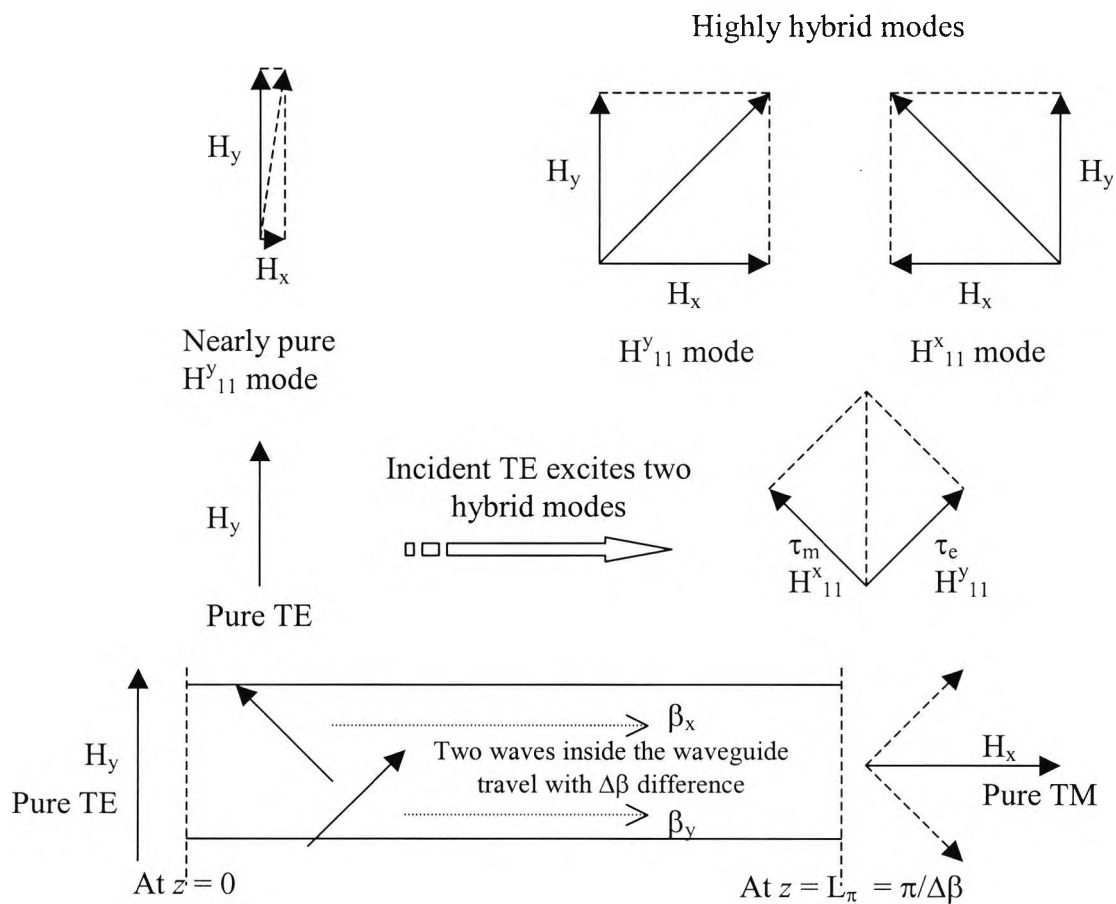
Fig. 6.18 Graphical implementation of polarization conversion.

The evolution of polarization powers along the axial direction, z, of the waveguide are shown in **Fig. 6.19** for different widths when $\theta = 5°$. When $W = 6$ μm, almost 100% of the TE power is converted into TM power at $z = 12$ cm, and if the waveguide length continues further, then the power conversion will be reversed. When $W = 5.8$ μm, since $\tau_e > \tau_m$, the maximum power conversion is only 85% and it takes place at $z = 10.5$ cm. For $W = 5.6$ μm, the maximum conversion drops to 60% at $z = 8$ cm. For $W = 5.4$ μm, the maximum conversion drops further to 40% at a shorter distance of $z = 6.2$ cm. It can also be noted that, when the guide width is smaller than 6 μm, the maximum power conversion is lower: however, the initial rate of polarization conversion is slightly higher than that for $W = 6$ μm.
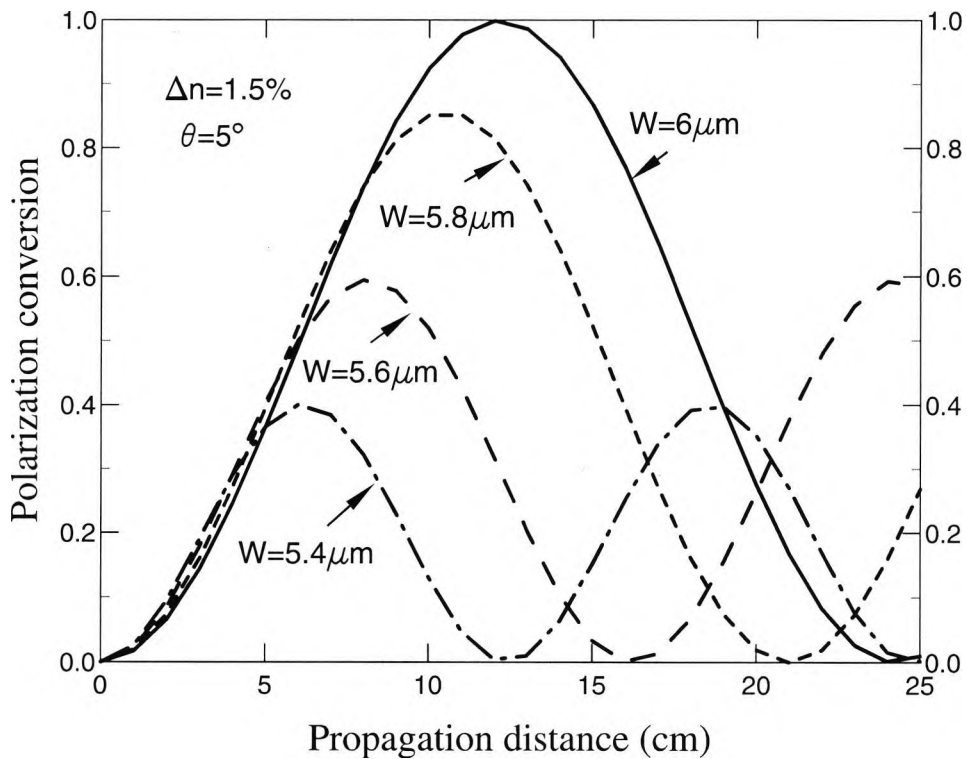
Fig. 6.19 Evolution of the TM polarized power along the axial direction, z, for different widths, when TE mode is incident.

The effect of the slant angle on the polarization conversion process is then studied at the highest hybrid position, i.e. when W = 6 μm. The evolution of polarization conversion powers from TE to TM, for different slant angles are shown in **Fig. 6.20**, when W = 6 μm and Δn = 1.5%. It can be clearly seen that when θ = 1°, the maximum power conversion is 100% at 60 cm. Also for θ = 2°, the maximum conversion value is also 100%, but since the L_π is smaller, the maximum conversion takes place at z = 30 cm. Similarly when θ = 5°, the maximum power conversion happens at z = 12 cm. If z exactly matches the L_π, then all the optical power could be converted from one polarization state to another. In this particular study, the design objective was not to obtain 100% polarization conversion, but to get a more clear idea about this undesirable polarization conversion process. It can be also noted that for higher angles, the polarization conversion rate is much higher since the L_π values are smaller.
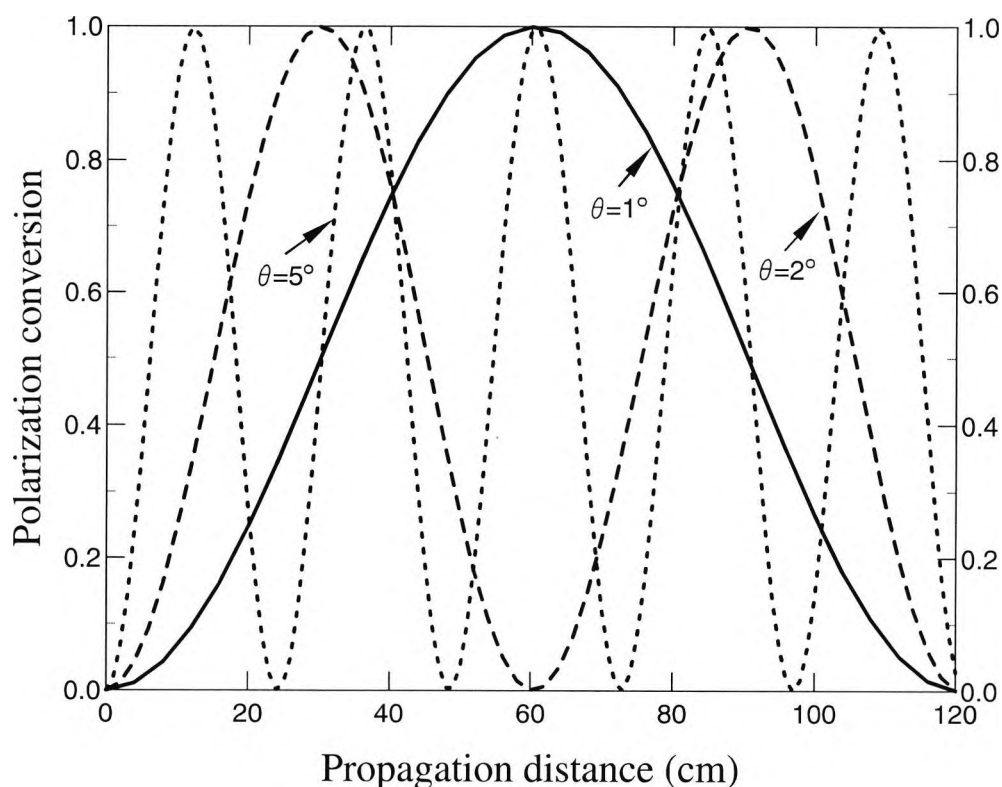
Fig. 6.20 Evolution of the TM polarized power along the axial direction, z, for different slant angles, when TE mode is incident.

It is also useful to investigate the effect of waveguide width and the slant angle on the maximum polarization conversion. The variation of the maximum polarization conversion with the width is shown in **Fig. 6.21** for different slant angles. It can be noted that at $W = 6$ μm, the possible maximum conversion can always be 100% for all the three cases, since the modal hybridity can also be the maximum, equal to 1. However, to achieve this 100% conversion, the device length has to be also longer since L_π is also maximum at $W = 6$ μm. When W is not exactly 6 μm, the hybridity reduces and therefore the magnitude of the excited TM mode, τ_m reduces. As a result the maximum power conversion also reduces as can be seen in **Fig. 6.21**. Although the maximum power conversion drops rapidly as the width deviates from 6 μm value, and the associated L_π length is reduced, however, some significant polarization crosstalk may still exist. When the slant angle of the sidewalls increases, then the maximum power conversion value increases rapidly since the hybridity is considerably higher for larger slant angles. A waveguide with $W = 5.5$ μm and $\theta = 5°$, nearly 50% TE power can be converted to TM power if the waveguide length is equal to L_π, which in this case, is only 7 cm.
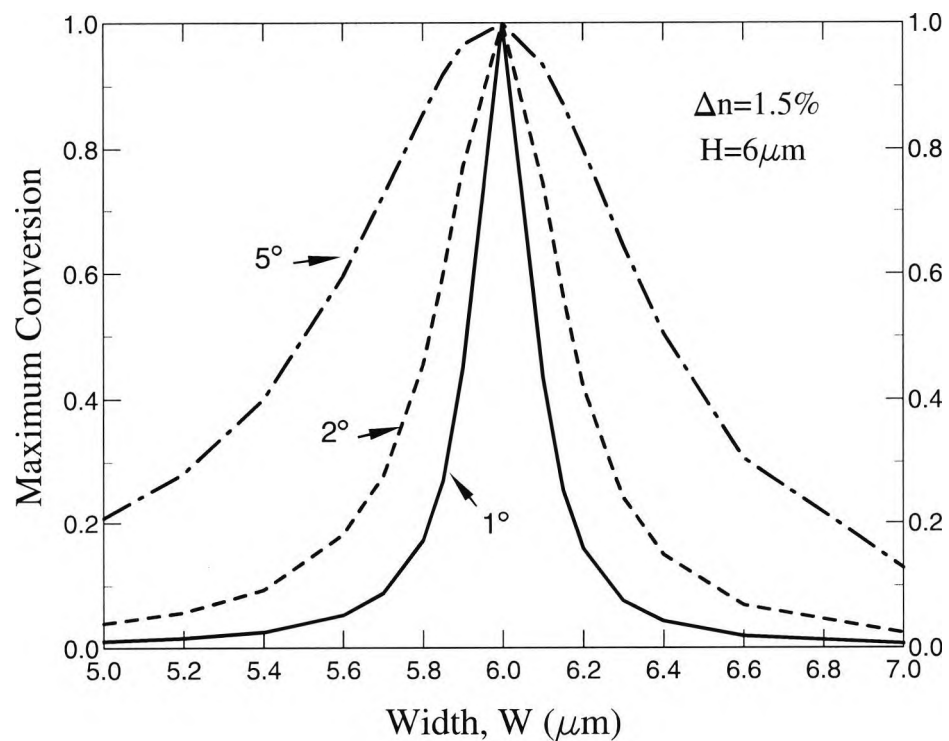
Fig. 6.21 Variation of the maximum polarization conversion with the waveguide width, W.

6.4.3 Polarization crosstalk

A planar silica waveguide may be significantly long, such as in an AWG chip, and polarization conversion may be a serious challenge for such systems. The variation of the crosstalk for fixed length sections of the waveguide is studied next. Polarization crosstalk for a moderately long, 1 cm silica waveguide is shown in **Fig. 6.22** for different slant angles when $\Delta n = 1.5\%$. It can be seen that for a waveguide with $W = 5$ μm, $\theta = 1°$, the polarization crosstalk is about -28 dB, and this value gets smaller when the waveguide width is larger. For $W = 7$ μm, $\theta = 1°$, the crosstalk is much better at -34 dB. However, for $\theta = 2°$, the crosstalk range is higher and for $\theta = 5°$ it is increased further up to a value of -15 dB when $W = 5$ μm. Next, the length of the waveguide, L, is increased to 5 cm in order to study the effect of polarization crosstalk on a longer guide.
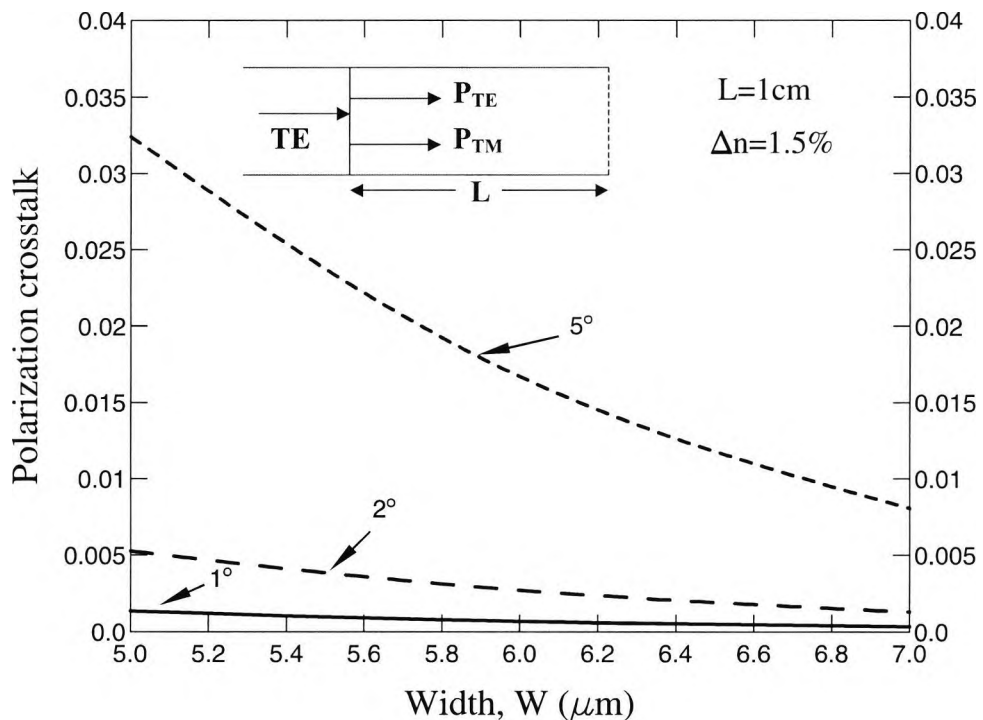
Fig. 6.22 Variation of the polarization crosstalk with the waveguide width, W, in a 1 cm long silica guide.

Fig. 6.23 shows the variation of the crosstalk with the width, for different slant angles. It can be clearly noted that the crosstalk increases substantially when the waveguide length, L increases. The maximum crosstalk for $\theta = 1°$, is nearly -17 dB when $W = 5.8$ μm. However, the crosstalk for $\theta = 5°$ is significantly higher, and the maximum crosstalk of -4 dB occurs when $W = 5.6$ μm. Since the value of the L_π (i.e. 8 cm) for $W = 5.6$ μm, $\theta = 5°$, is closer to the 5 cm long guide considered here, the crosstalk is much higher in this case. Next, the variation of the polarization crosstalk is considered when the length, L of the waveguide is increased further up to 10 cm. **Fig. 6.24** shows the variation of the possible polarization crosstalk with the waveguide width, W, for different slant angles. The maximum crosstalk for slant angle, $\theta = 5°$, is considerably higher at -0.34 dB and it occurs when $W = 6$ μm. Since the hybridity is maximum for $W = 6$ μm, and also for $\theta = 5°$ the L_π (i.e. 12 cm) value is very close to the waveguide length considered here, 10 cm, a large amount of polarization crosstalk could be expected.
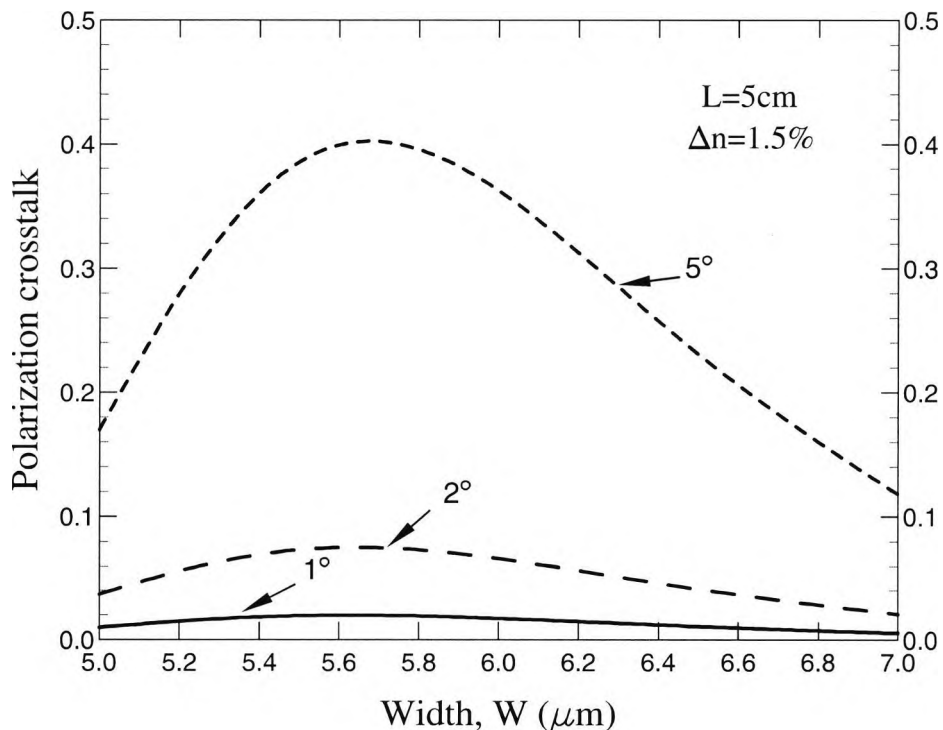
Fig. 6.23 Variation of the polarization crosstalk with the waveguide width, W, in a 5 cm long silica guide.
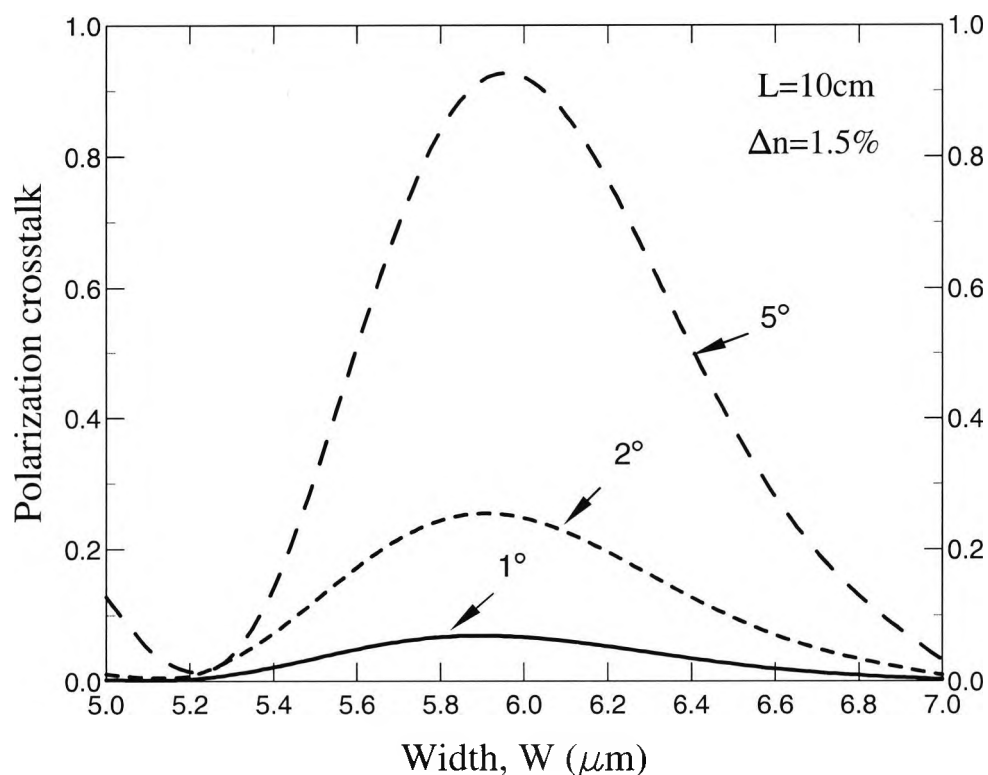
Fig. 6.24 Variation of the polarization crosstalk with the waveguide width, *W*, in a 10 cm long silica guide.

6.5   Summary

This chapter focused mainly the origin of the polarization crosstalk in silica waveguides and it is clearly shown that a significant polarization conversion can take place in a long silica waveguides with high Δn, but this may not be critical for a relatively short (in the order of 1cm) waveguide with nearly perfect vertical sidewalls. However, if its sidewalls are not perfectly vertical then polarization crosstalk may be significant for many silica-based components. It is also shown that for a 10 cm long silica waveguide with a sidewall slant of 5°, the crosstalk could be as high as −0.34 dB. It is also known that the curvature in waveguide also enhances the polarization conversion (Takada and Mitachi, 1998; Obayya *et al.*, 2001), and hence the effect of long curved waveguides, such as inside an AWG chip or input output bend sections, also requires further investigation to avoid undesirable polarization crosstalk in the systems. In silica waveguides, induced stress during the fabrication process also affects their polarization characteristics, and the FEM-based modal

solution approach (Liu *et al.*, 1995) could be used to study polarization issues in such waveguides.   200

Summarising all the simulation results, it can be clearly understood that the polarization crosstalk in planar silica waveguides increases with the increase of the refractive index contrast, the waveguide sidewall slant angle and the waveguide length.

Chapter 7

Polarization Controller

7.1 Introduction

The control of optical polarization is an important factor in determining the overall system performance in both coherent optical fibre transmission systems and interferometric optical fibre sensor devices. Since the state of polarization (SOP) of the transported signal in long single-mode fibre fluctuates randomly as a result of changes in the temperature, stress, and humidity of the fibre, a fading of the output signal occurs. Therefore, in an optical heterodyne (or homodyne) receiver, or when an optical integrated circuit is used in the receiver, a polarization state control scheme is indispensable (Okoshi, 1985). Also in fibre optical sensors, polarization matching between the two superposed waves must be achieved by some appropriate means.

Several techniques have been proposed to overcome this problem. The complete and the simplest possible solution is the use of a polarization-maintaining fibre over the entire length of the communication channel (Okoshi, 1981). However the polarization-maintaining fibre may have problems which arise from fibre attenuation and splicing, and also cannot be used in practical communication networks at a reasonable cost. Other alternative means are using a polarization diversity receiver in which the

orthogonal polarization components of the received signal are detected separately and added later after an appropriate phase compensation (Okoshi *et al.*, 1983) and various SOP control schemes at the receiving end which matches the local oscillator (LO) polarization state with that of the signal. From these techniques, the SOP control schemes using a polarization controller yields the best receiver sensitivity. These SOP controllers have been realised using fibre squeezers (Creaner *et al.*, 1988), electro-optic crystals (Kubota *et al.*, 1980), fibre cranks which can be rotated (Okoshi *et al.*, 1985), polarization preserving fibres wound on to piezoelectric cylinders (Walker and Walker, 1988), rotatable fibre coils (Matsumoto and Kano, 1986) and Faraday rotators.

A polarization-state control device should be able to convert an arbitrary, time variant state of polarization into a TE or TM polarization. The most important conditions in a SOP control scheme are low insertion loss, endless control capability and fast control speeds. Since the SOP at the end of a long conventional single-mode fibre is subject to slow but potentially large changes, the tracking range of the polarization control system should be "endless" in order to ensure reliable communication without interruptions. All-fibre devices have the advantage of low-loss characteristics, and effectively unlimited transformation ranges have been demonstrated with polarization controllers using for example, cascaded electro-magnetic squeezers, endlessly rotatable optical retardation plates and liquid crystal polarization rotators. However all the mechanical schemes have poor temporal response as compared with the electro-optic and Faraday devices and are inherently slow and therefore not suitable for practical applications. On the other hand, much faster control speeds can be obtained with integrated-optic polarization controllers which are of particular interest for future production because of their low drive voltages, and compact sizes which in turn keep the receiver small and low coupling losses to single-mode fibres (Alferness and Buhl, 1985). Such integrated-optic polarization controllers, involving no mechanical deformation, are expected to be potentially more reliable in their long term performance.

In order to meet the increasing demands for bandwidth due to the accelerated growth of Internet data traffic, a line rate growth to 40 Gb/s and beyond is inevitable. At such high data rates, various issues, particularly the maintaining of the correct polarization,

are critical since high-speed data transmissions are very sensitive to light polarization. Future optical transmission systems will also exhibit an increased polarization mode dispersion (PMD) vulnerability and will require new tests and compensation systems. Hence, polarization controllers are considered as key elements for use in polarization mode dispersion compensation, which maintains a specific polarization of light as a signal travels across a single-mode fibre in high-speed 10 and 40 Gb/s optical networks. In high-speed/long-distance optical fibre transmission systems, PMD is one of the most serious degradation factors limiting the bit rate and the transmission distance (Poole and Wagner, 1986; Kikuchi, 2001). In general, the PMD is caused by the different transmission speeds of the two states of polarization of the signal (SOPs) thereby introducing a time delay between them as they propagate along the fibre. Polarization control devices for PMD compensation must be electronically controlled and must be able to react fast to track the PMD variations. Therefore integrated optic based polarization controllers are much preferred and so far most of the designs have been realised as isolated components in Lithium niobate (LiNbO$_3$) materials giving endless polarization control (Walker *et al.*, 1988; Heismann *et al.*, 1990; Heismann and Whalen, 1991).

However, a semiconductor-based polarization controller would be a more promising alternative to the classical LiNbO$_3$ integrated components since the advantage of monolithic integration with other functionalities, such as the laser and the detector on the same substrate can be taken into account. Recently a considerable interest has been shown in designing high-speed AlGaAs-GaAs polarization controllers (Rahmatian *et al.*, 1998). Recently, Grossard *et al.*, (Grossard *et al.*, 2001) reported a design of polarization rotator in a shallow-etched 19 mm long GaAs/AlGaAs with Y-Z crystal orientation to reduce the modal birefringence. They have reported a maximum of 90% conversion by successfully achieving phase matching with the use of an electro-optic phase matching control electrode with a 40V polarization conversion voltage. In this chapter, a novel design of a compact twin electrode polarization controller with symmetrically applied phase matching voltage and asymmetrically applied voltage to control the polarization state of the output optical signal is reported and characteristically optimised by using a rigorous vectorial approach, based on the finite element method.

7.2   Design concept

All the optical waveguides considered in the previous chapters are composed of normal optical waveguide materials with a constant refractive indices, i.e. an isotropic material. However, the optical properties of certain materials can be altered by an externally applied electric field. When an electric field is applied across an optical medium, the distribution of electrons within it is distorted so that the polarizability and hence the refractive index of the medium changes anisotropically. The concept of this electro-optic effect accounts for the operation of most electro-optic devices. In this study, the result of this so-called electro-optic effect is used to realise a compact polarization controller by making a naturally isotropic crystal e.g. gallium arsenide (GaAs) anisotropic.

Consider a voltage, V_1, is applied to a semiconductor rib waveguide via a metal electrode as shown in **Fig. 7.1**. Hence a modulating **E**-field consisting of E_y and E_x field components will be generated.
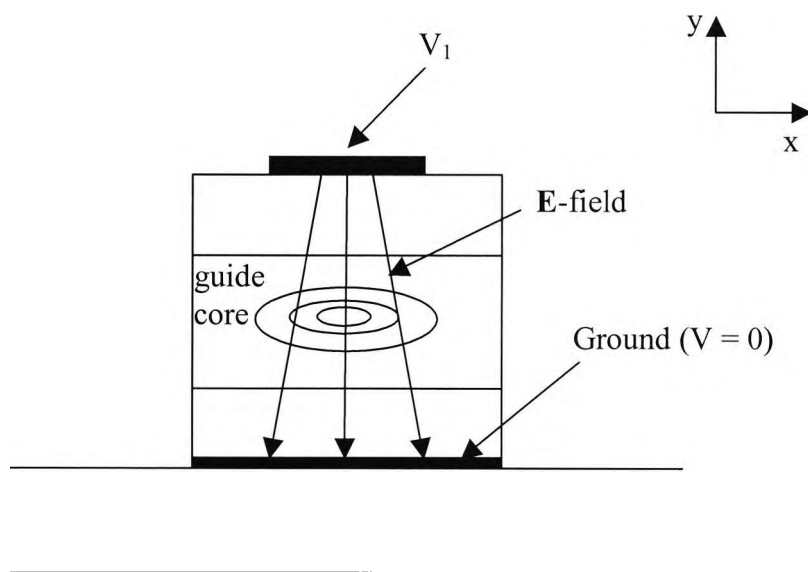
Fig. 7.1 Electro-optic rib waveguide structure.

If $V_1 = 0$, then there is no modulating field and a zero electro-optic effect exists. For such an isotropic waveguide, the refractive index distribution can be written as;

$$\hat{n} = \begin{bmatrix} n_{xx} & n_{xy} & n_{xz} \\ n_{yx} & n_{yy} & n_{yz} \\ n_{zx} & n_{zy} & n_{zz} \end{bmatrix} \tag{7.1}$$

Here, $n_{xx} = n_{yy} = n_{zz} = n$ are the only non-zero elements.

If $V_1 \neq 0$, there exists a modulating field with components E_y and E_x. The E_y field component is the major component spreading vertically over the core area since the applied overall **E**-field is itself nearly vertical. The E_x field is smaller in the core and hence is the minor field component. As a result of the induced electro-optic effect, the refractive index changes and for semiconductor waveguide materials, this refractive index distribution becomes a 3×3 tensor in the form;

$$\hat{n} = \begin{bmatrix} n + \Delta n_{xx} & \Delta n_{xy} & 0 \\ \Delta n_{yx} & n + \Delta n_{yy} & 0 \\ 0 & 0 & n + \Delta n_{zz} \end{bmatrix} \tag{7.2}$$

where n is the refractive index distribution of the waveguide structure when no modulating field is applied. Δn_{xx}, Δn_{xy}, Δn_{yx}, Δn_{yy}, and Δn_{zz} are the perturbations in the refractive index due to the electro-optic effect.

These changes of the refractive index are proportional to the applied modulating **E**-field. The proportional constant is known as the electro-optic coefficient, r. For semiconductor materials, such as InP and GaAs, the electro-optic coefficient is r_{41}, which is taken as equal to $1.4 * 10^{-6}$ μm/V for GaAs (Yariv and Yeh, 1984). In general, the E_y component causes the changes in diagonal elements in the matrix equation (7.2) and these changes Δn_{xx}, Δn_{yy} and Δn_{zz} can be calculated by,

$$\Delta n_{xx} = -\Delta n_{zz} = \frac{1}{2} n^3 r_{41} E_y \tag{7.3}$$

$$\Delta n_{yy} \;=\; 0 \tag{7.4}$$

The off diagonal elements, Δn_{xy} and Δn_{yx} are related to the E_x field component by;

$$\Delta n_{xy} \;=\; \Delta n_{yx} \;=\; \frac{1}{2}\, n^3\, r_{41}\, E_x \tag{7.5}$$

The important fact to consider when realising polarization controllers is the possibility of TE and TM mode coupling. The mode coupling is possible via the off diagonal Δn_{xy} elements. As derived in the earlier Chapters 5 and 6, the polarization conversion in semiconductor optical waveguides is only achieved by introducing an asymmetry in the waveguide geometry. Hence the design focus here is to achieve polarization conversion by another form of asymmetry introduced by a non-symmetric applied voltage.

During simulation, it is necessary to employ numerical approaches, which should be able to handle the material anisotrophy achieved as a result of the electro-optic effect. In this study rigorous numerical tools based on the vector **H**-field finite element method (Rahman and Davies, 1984*a*) have been used. In order to account for the electro-optic effect, a finite element based solution of the Laplace equation (Young, 1988; Koshiba *et al.*, 1999) has been used. The calculation of the transverse modulating field components $E_x(x,y)$ and $E_y(x,y)$ by utilising Laplace's equation is briefly discussed in **Appendix 2**. For the analysis of the overall performance of the device, the TE to TM power conversion characteristics have been obtained with the use of LSBR method (Rahman and Davies, 1988), which is a rigorously convergent junction analysis approach.

7.3   Simulation results

The cross section of the deep etched polarization controller waveguide structure, based on AlGaAs-GaAs in the [011] direction of propagation, is depicted in **Fig. 7.2.** The dimensions of the epitaxial layers, which are grown on a (100) GaAs substrate, are clearly shown in the figure. In this design, the widths of the electrodes, W_e, on top of the cap layer are taken as 1 μm and the separation between them, s, is 3 μm (4 μm centre to centre). The material descriptions of the layers and their appropriate refractive indices at an operating wavelength of 1.55 μm are given in the following **Table 7.1** starting from the top layer.
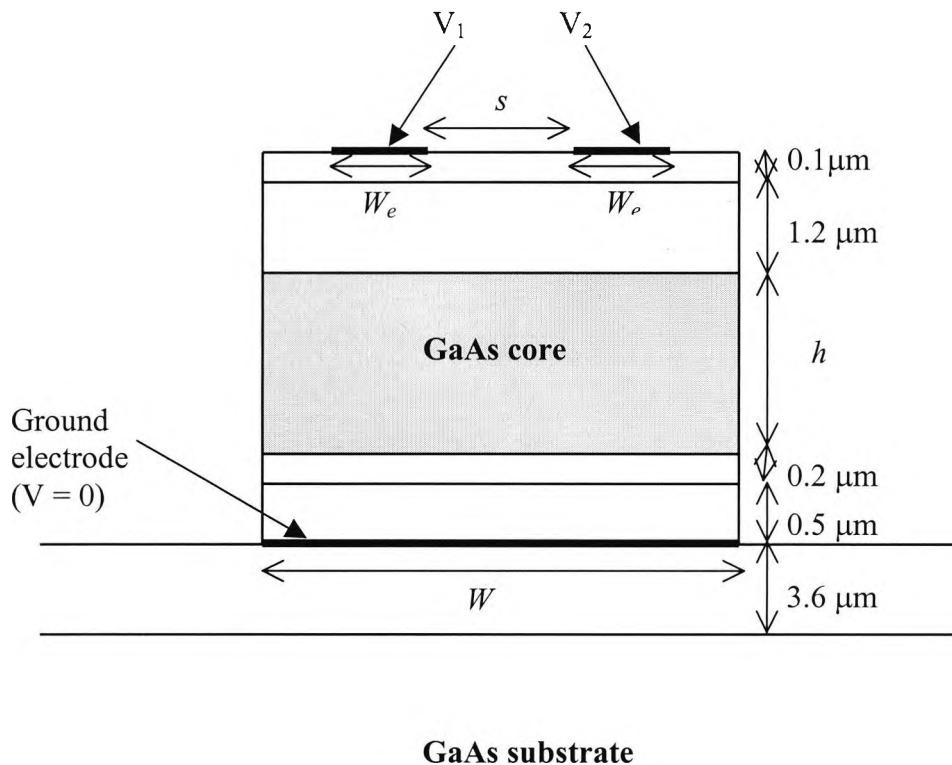
Fig. 7.2   Schematic of the active AlGaAs-GaAs based polarization controller waveguide.

Layer	Al concentration	Refractive index	Thickness (μm)
GaAs cap	0	3.37694563	0.1
AlGaAs upper cladding	20%	3.28117240	1.2
GaAs core	0	3.37694563	Varied
AlGaAs lower cladding	20%	3.28117240	0.2
AlGaAs lower cladding	30%	3.23251960	0.5
AlGaAs lower cladding	6%	3.34618124	3.6

Table 7.1 AlGaAs-GaAs waveguide layer description.

7.3.1 Simulation of the passive waveguide

Initially the simulations were carried out without including the electrodes ($V_1 = V_2 = 0V$). The variations of $\Delta\beta$ with the waveguide width, W, are shown in **Fig. 7.3** for passive waveguides with different core heights, h. The modal birefringence is an important parmater in the design of polarization controllers. Here $\Delta\beta$ is the difference between the propagation constants, β_y and β_x, of the two fundamental TE and TM polarized waves, respectively. It can be clearly seen that for both the cases when $h = 2.5$ μm and $h = 3$ μm, as the width of the waveguide, W is reduced: initially, $\Delta\beta$ is reduced slowly but below a particular width, this value is reduced quite rapidly. It has also been observed that for a lower waveguide width, the TE and TM mode could have the same propagation constant value and in this case they would be phase matched without any applied voltage. For example, when $h = 3$ μm, the phase matching between the TE and TM modes occurs around $W = 2.15$ μm. Below this value the propagation constant, β_x is higher than the β_y value. It can be noted that for $h = 2.5$ μm, this $\Delta\beta$ value is higher and the corresponding phase matching width would be even smaller. It is clearly demonstrated here that an optical waveguide can be designed to have identical phase velocities for the two orthogonal polarizations, or in other words, they would be degenerative without any applied voltage. Such a passive structure is relatively easy to fabricate, but the polarization converter would be very

long and the polarization conversion would not be controllable. Further, the device performance is expected to be very sensitive to the fabrication processes.

The design aim undertaken here is to bring the phase matching by using an applied voltage and to control the polarization rotation by breaking up the symmetry by the use of the twin electrodes. A narrower waveguide will have a low $\Delta\beta$ value, but may not be suitable for the design approach considered here with twin electrodes, as a reasonable separation between them has to be maintained.
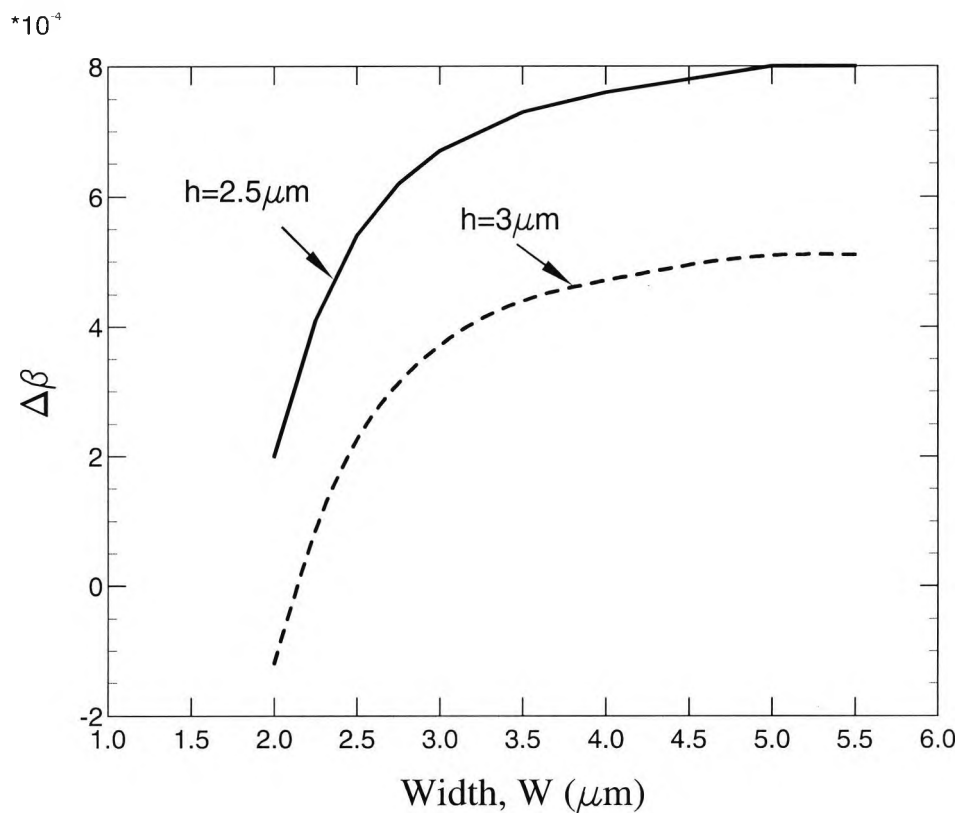
Fig. 7.3 Variations of $\Delta\beta$ with the waveguide width, W.

Since the $\Delta\beta$ value is considerably larger for $h = 2.5$ μm, it is also anticipated that a larger phase matching voltage would be required. It can also be noticed that when the waveguide core height is increased, the $\Delta\beta$ value is significantly reduced as shown in **Fig. 7.3**. In this case, as the core height is increased, it is expected that W would also need to be wider to achieve a similar aspect ratio, necessary for phase matching.

7.3.2 Simulation of the active waveguide

A voltage is applied via the twin electrodes and the effect of this applied voltage to achieve phase matching is studied. Here, V_1 and V_2 are applied in the left and right upper electrodes respectively, and a highly doped lower electrode is used as the ground electrode. **Figs. 7.4(a)** and **(b)** show the contour plots of the vertical E_y and horizontal E_x modulating electric field components when the applied voltages are symmetrical, i.e., $V_1 = V_2$. It can be noted that the E_y component is symmetric but the E_x field component is asymmetric and nearly zero in the waveguide core region. As can be seen from equation (7.3), the E_y field changes the n_{xx} (the x-component of the diagonal refractive index), which in turn affects the propagation constants of the TE polarized modes. On the other hand, the refractive index in the y-direction, n_{yy} is not changed (i.e $\Delta n_{yy} = 0$), so the propagation constants of the TM polarized modes are unchanged. However, the effect of Δn_{xy} (the off diagonal element which causes mode coupling) is negligible since the applied E_x field is perfectly asymmetric and the overall contribution is zero. Hence the polarization conversion would hardly be possible.

The variations of the propagation constants with the voltages V_1 and V_2 are shown in **Fig. 7.5**. In this case, the waveguide width, W, is taken as 5.5 μm, and the electrode width, W_e, and the separation between the electrodes are taken as 1 μm and 3 μm, respectively. It can be noted that for the crystal arrangement, the propagation constant for the TM mode, β_x, does not change with the applied voltage, but the propagation constant for the TE mode, β_y is linearly reduced with the applied reverse bias. The left-hand side scale is used for the case where $h = 3$ μm. The right-hand side scale is used for the case when $h = 2.5$ μm and it can be observed that when $V_1 = V_2 = -40.95$V, the modes have the same propagation constants and therefore degenerate. On the other hand, for the case when $h = 3$ μm, the phase matching voltage is only -28.33 V, which is a significant reduction. To the best of our knowledge this is the lowest phase matching voltage reported for a semiconductor based polarization controller. Consequently, by optimising the design parameters this phase matching voltage can be reduced even further.
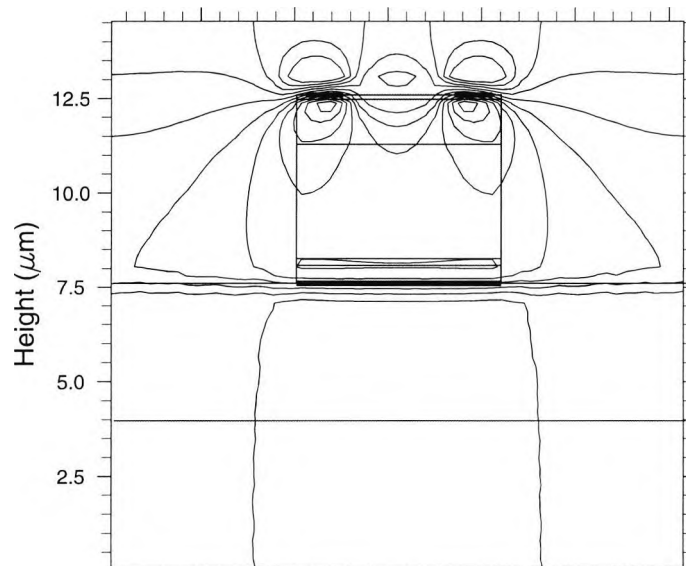
(a)
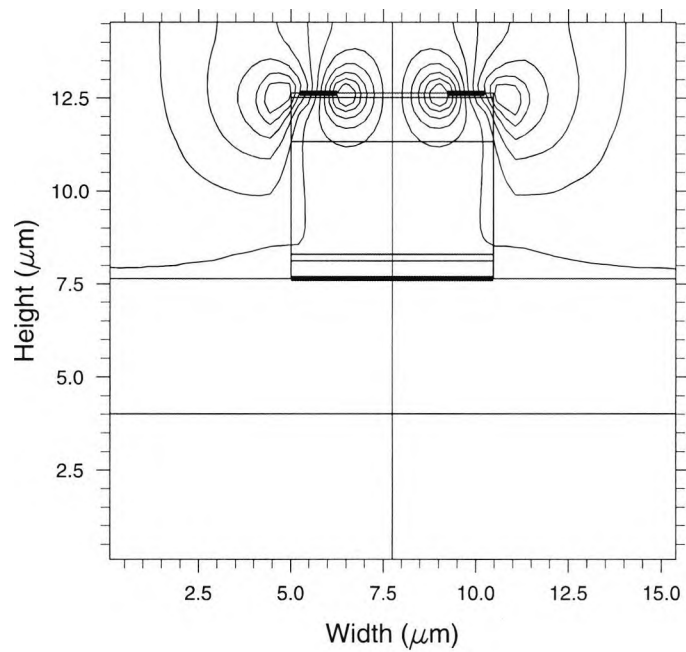
(b)

Fig. 7.4 Field profiles of the applied voltage ($V_1 = V_2 = -28.33$ V, $h = 3$ μm). *(a)* the E_y field *(b)* the E_x field.
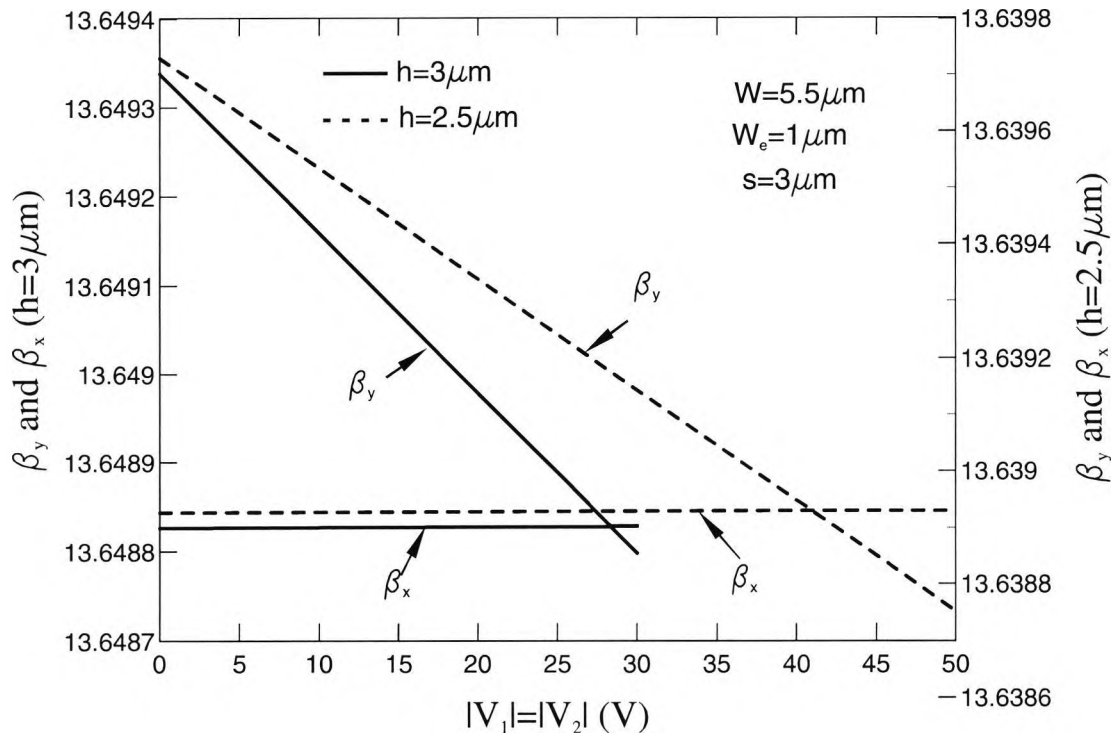
Fig. 7.5 Variations of the propagation constants with the voltages V_1 and V_2.

With the applied voltage, when the modes are phase matched, they are degenerative and also hybrid in nature. The variation of the modal hybridity with the applied voltage is shown in **Fig. 7.6**. Here the modal hybridity is defined as the ratio of the non-dominant to the dominant field components for a given polarization. It can be observed that for $h = 2.5$ μm, when $V_1 = V_2 = -40.95$ V, the H_x and H_y coefficients are almost equal. On the other hand, the hybridity is maximum for $h = 3$ μm at $V_1 = V_2 = -28.33$ V, as expected. However, in this case when $h = 3$ μm, the hybridity curve is not as sharp as that of $h = 2.5$ μm, which indicates a stronger interaction between the polarized modes. It can also be noted that the modal hybridity reduces rapidly as V_1 and V_2 deviate from the phase matching values.
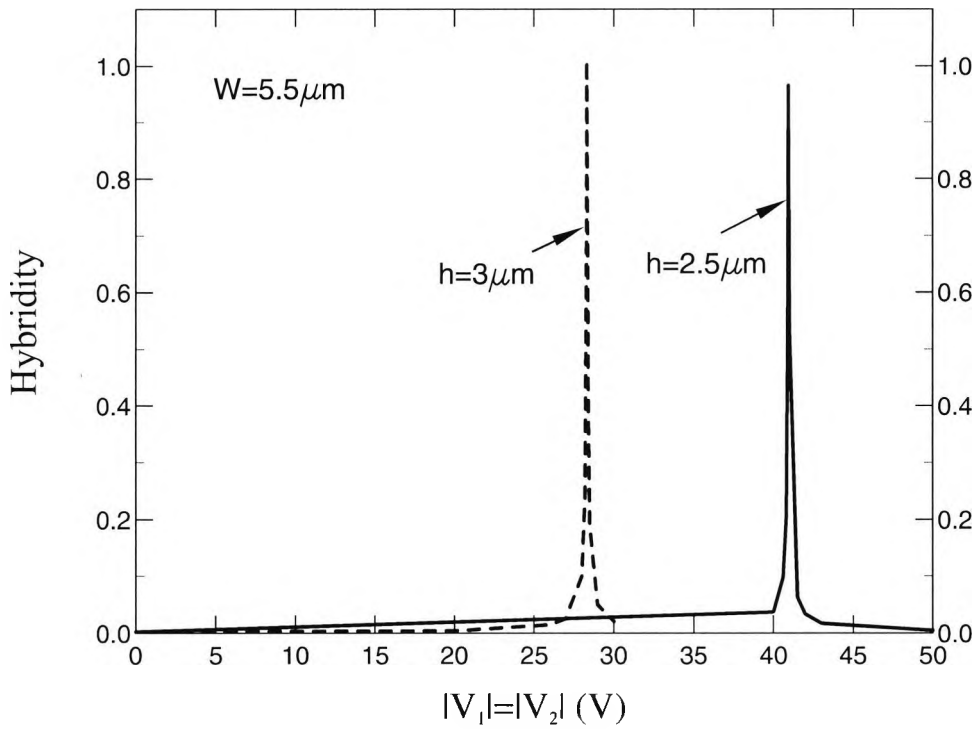
Fig. 7.6 Variation of the modal hybridity with the applied symmetrical voltages.

In order to analyse the effect of asymmetry of the structure on the polarization conversion, a non-symmetry is introduced to the modulating field. Hence the resultant E-field distribution becomes non-symmetric as is clearly shown in **Fig. 7.7**, when the applied voltages, V_1 and V_2 are -33.33 V and -23.33 V, respectively, giving a voltage difference of $\delta = 10V$. The E_x field component is especially affected, as shown in **Fig. 7.7(a)**. The non-symmetrical nature of the field profile is clearly visible, introducing higher strength on the left-side of the waveguide, hence causing a change in the off-diagonal entries of the refractive index matrix, i.e. Δn_{xy} becomes non zero. Consequently these affected off-diagonal index entries enhance the hybridity and produce mode coupling between the two orthogonal TE and TM modes giving a significant polarization conversion between them. The resultant E_y field profile is shown in **Fig. 7.7(b)**, and this is also non-symmetrical, but its overall effect on the reduction of β_x remains the same.
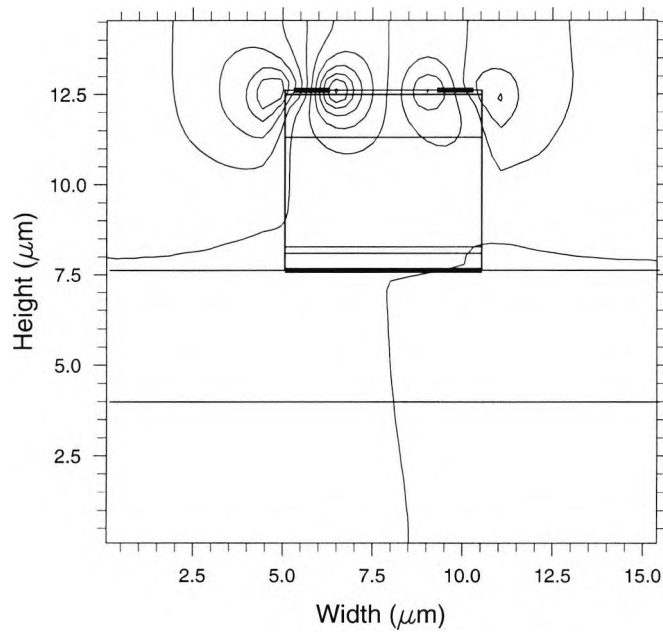
(a)
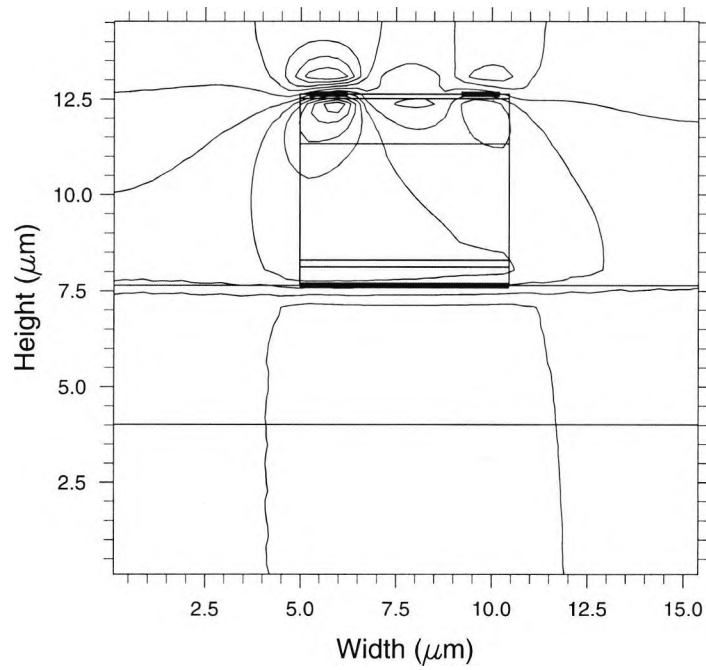
(b)

Fig. 7.7 *(a)* The resultant E_x field profile   *(b)* The resultant E_y field profile, when V_1 and V_2 are asymmetrical ($V_1 = -33.33$ V, $V_2 = -23.33$ V, $h = 3$ μm).

The refractive index change distributions, Δn_{xx} and Δn_{xy} are shown in **Fig. 7.8 (a)** and **(b)** when the applied voltages are symmetrical at $V_1 = V_2 = -28.33$ V. It can be clearly seen that Δn_{xx} is symmetrical and Δn_{xy} is asymmetrical. Since the changes of these diagonal and off-diagonal refractive indices are calculated by multiplying the values of E_y and E_x, respectively, with the electro-optic coefficient r_{41}, the distributions look similar to the corresponding **E**-field components. **Fig. 7.9 (a)** and **(b)** show the refractive index change distributions, Δn_{xx} and Δn_{xy} when asymmetrical voltages ($V_1 = -33.33$ V and $V_2 = -23.33$ V) are employed with a voltage difference of 10 V. Here, the index distributions clearly show an asymmetry, compared to the refractive index difference distributions with symmetrical voltages.

(a)   *(b)*
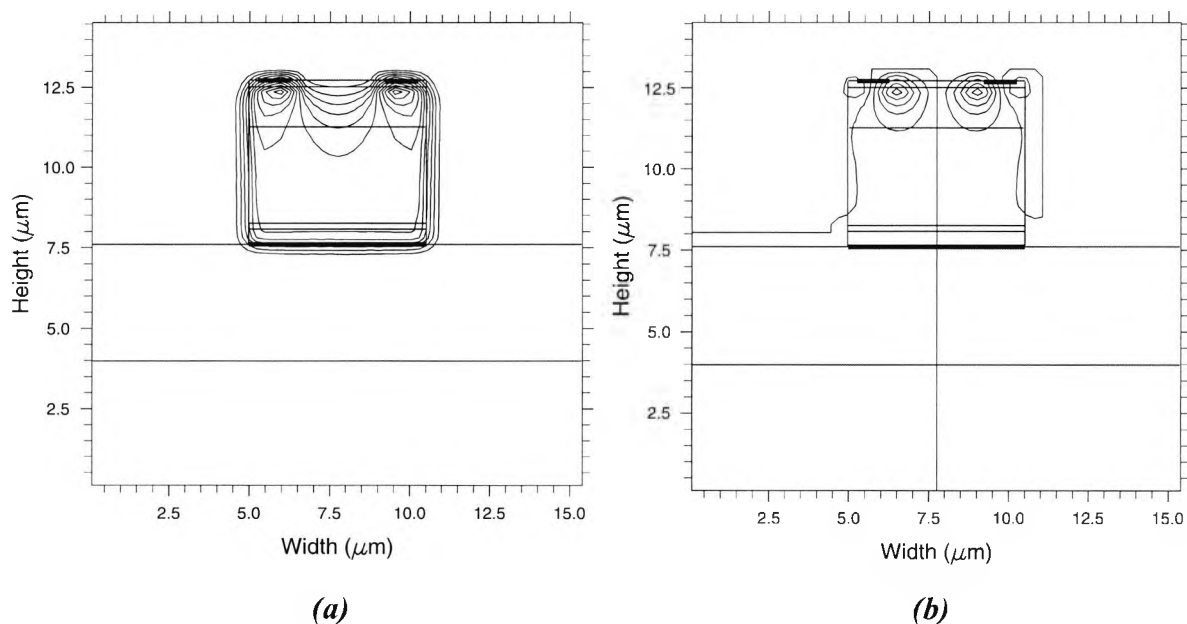
Fig. 7.8 Changes of the refractive index elements for symmetrical voltages ($V_1 = V_2 = -28.33$ V) *(a)* Δn_{xx} and *(b)* Δn_{xy}.
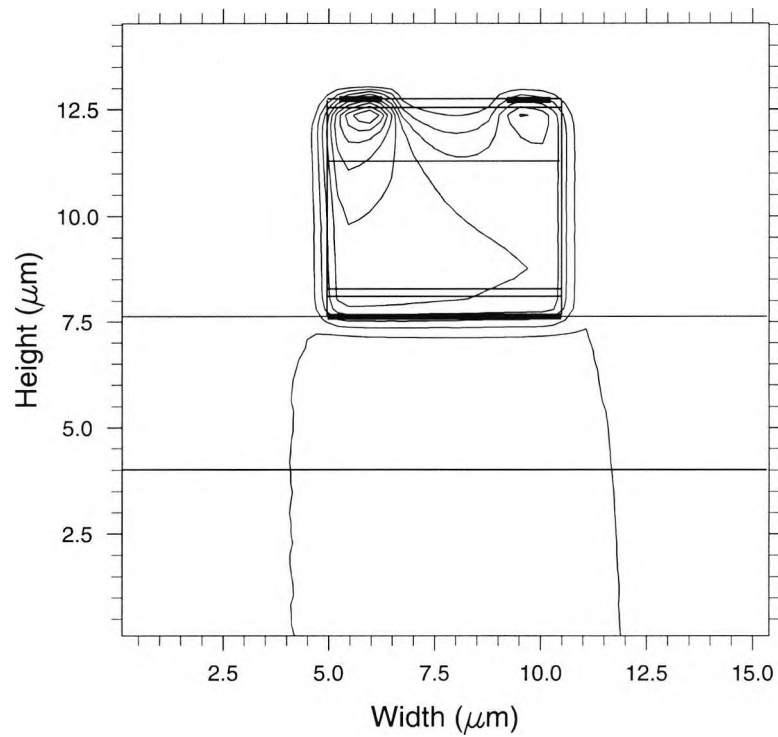
(a)
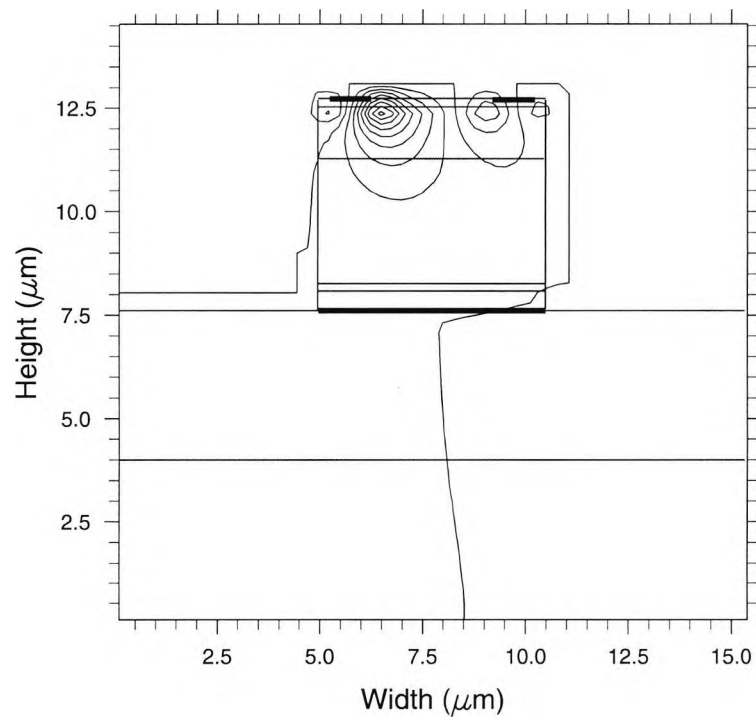
(b)

Fig. 7.9 Changes of the refractive index elements for asymmetrical voltages (V_1 = -33.33 V, V_2 = -23.33 V) *(a)* Δn_{xx} and *(b)* Δn_{xy}.

It has been noted that when the applied voltages are equal, the half beat length, L_π, is very large. Therefore the device length would be very long and would also be very sensitive with the applied voltage. Here the half-beat length is defined as;

$$L_\pi = \pi / |\beta_y - \beta_x| \qquad\qquad (7.6)$$

By introducing a non-symmetrical voltage, the half-beat length can be reduced drastically. Variations of the half-beat lengths with the voltage difference, δ, are shown in **Fig. 7.10**, for the two different core heights. Here, for $h = 3$ µm and $h = 2.5$ µm, the average voltage $V_{av} = (V_1 + V_2)/2$, is kept fixed at -28.33 V, and -40.95 V, respectively. δ is the difference between the voltages V_1 and V_2. It can be observed that when δ is 0 V, the half-beat length is more than several metres. However, by introducing a small non-symmetry this L_π value can be reduced significantly. It can also be observed that for a lower core height, the L_π value is slightly smaller. When $\delta = 5$ V, the L_π values are 56 mm and 51 mm for core heights of 3 µm and 2.5 µm, respectively. However, when δ is 10 V, this value reduces to 28 mm and 26 mm for $h = 3$ µm and $h = 2.5$ µm, respectively. When a non-symmetrical voltage is applied, the total voltage needed for the phase matching, $(V_1 + V_2)$ remains the same as the total voltage needed to establish the phase matching in the symmetrical case.
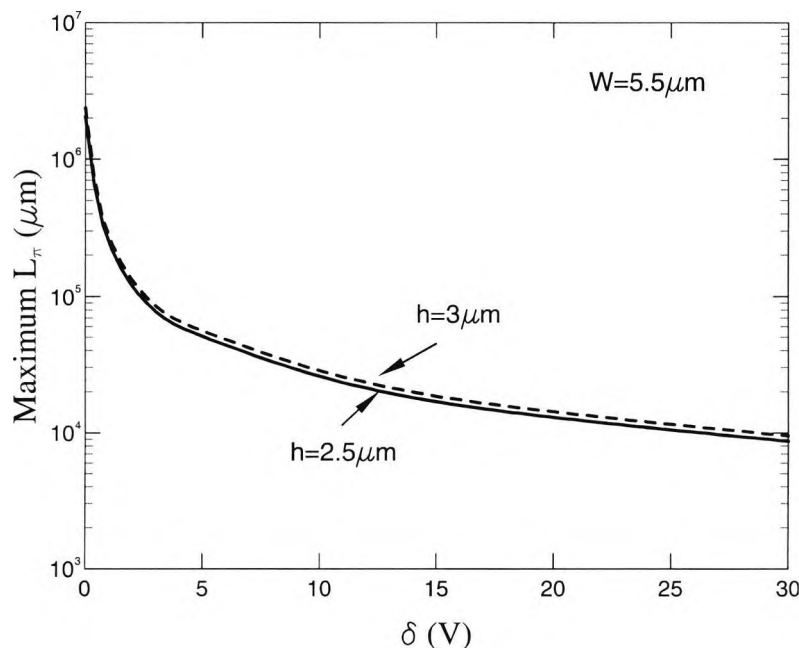
Fig. 7.10 Variations of the half-beat lengths with the voltage difference, δ.

Fig. 7.11 shows the variation of the product, $L_\pi.\delta$ with the voltage difference, δ. The product, $L_\pi.\delta$ remains constant around 26 Vcm and 28 Vcm for δ larger than 5V, when $h = 2.5$ μm and $h = 3$ μm, respectively. When the voltage difference is reduced to lower than 5 V, the $L_\pi.\delta$ reduces drastically and it shows that around this region the corresponding L_π does not increase to that amount so as to maintain the $L_\pi.\delta$ value.
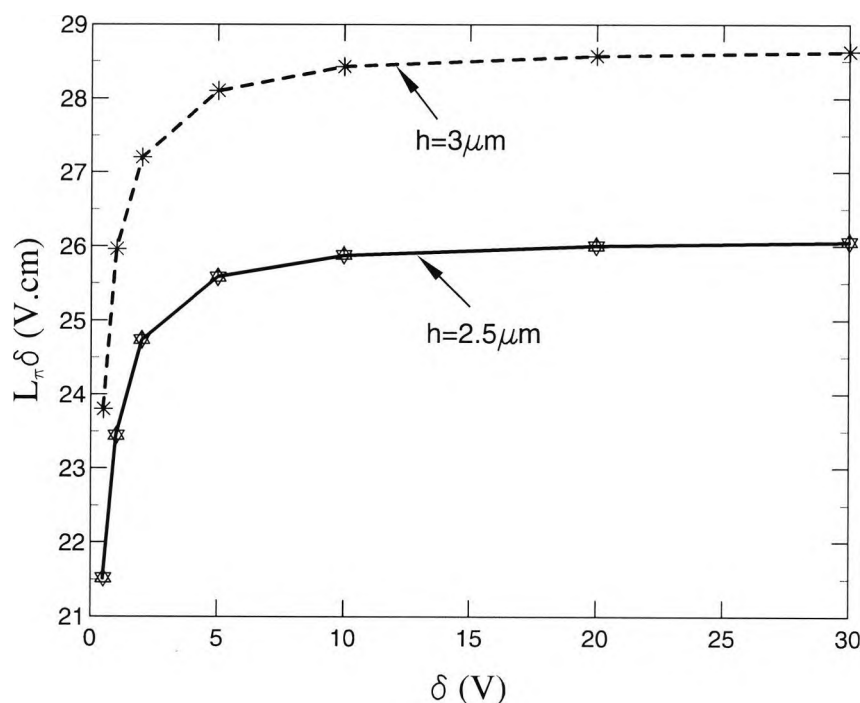
Fig. 7.11 Variation of $L_\pi\delta$ with the voltage difference δ.

It was observed from **Fig. 7.6** that modal hybridity was very sensitive to the phase matching voltage, when $V_1 = V_2$. This is not only suggests the creation of an unreasonably long device but it also would make its operation very sensitive to the applied voltage. The variation of the modal hybridity is expected to be less sensitive when the structural symmetry is broken (Somasiri *et al.*, 2002). The variation of the modal hybridity with the applied average voltage when the voltage difference is maintained is shown in **Fig. 7.12**. It can be noted that even when the average voltage has drifted by 1 V, the modal hybridity remains reasonably high for both cases of $h = 3$ μm and $h = 2.5$ μm. Also the modal hybridity is less sensitive to the voltage

variations. By comparison, it can be seen that for $h = 3$ μm, the required average voltage for phase matching is smaller and the L_π value is slightly larger. However, for the case of $h = 2.5$ μm, the phase matching voltage is larger and the L_π value is slightly smaller. Therefore when designing such a device, a suitable compromise between the phase matching voltage and the device length has to be considered. When the voltage asymmetry, δ, is reduced, the device length is slightly longer and the modal hybridity varies faster as the voltage changes. Therefore, the higher the voltage difference, the more controllable the polarization conversion, and also the device length is shorter.

Next, the behaviour of the polarization controller in terms of the power conversion between the TE and TM modes was studied. Since the asymmetrical voltage applied to the two electrodes achieves the controlling of the polarization state, here the performance of the polarization controller with such asymmetrical voltages only has been considered. The input waveguide considered here is a general passive rib waveguide with the same waveguide dimensions as shown in **Fig. 7.2**. The waveguide width, W is 5.5 μm. However in order to account for the polarization conversion phenomenon, a full vectorial junction analysis approach is needed, and here the most powerful LSBR method has been employed. **Fig. 7.13** shows the evolution of TM power conversion along the propagation direction of the active polarization controller waveguide when TE polarized light is incident from the passive input waveguide. The voltage difference, δ, is kept constant at 10 V and the power curves are obtained for core heights, $h = 2.5$ μm and 3 μm. The average voltages have been maintained at the phase matching voltages for the two cases, i.e. at −28.33 V and at −40.95 V for $h = 3$ μm and $h = 2.5$ μm, respectively. It can be clearly seen that for $h = 2.5$ μm, the maximum power conversion occurs at a slightly lower device length (≈ 26 mm) than that of for $h = 3$ μm (≈ 28 mm), since the corresponding L_π value is slightly lower. In both the cases, nearly 100% TE to TM power conversion was obtained, as the phase matching conditions have been achieved. Therefore it can be emphasised that 100% conversion efficiency can be obtained if the difference between the propagation constants β_x and β_y is 0, i.e. when the modes are phase matched. These results indicate that by adjusting the phase matching and the symmetry, δ, the polarization state of an incoming optical signal can be controlled.
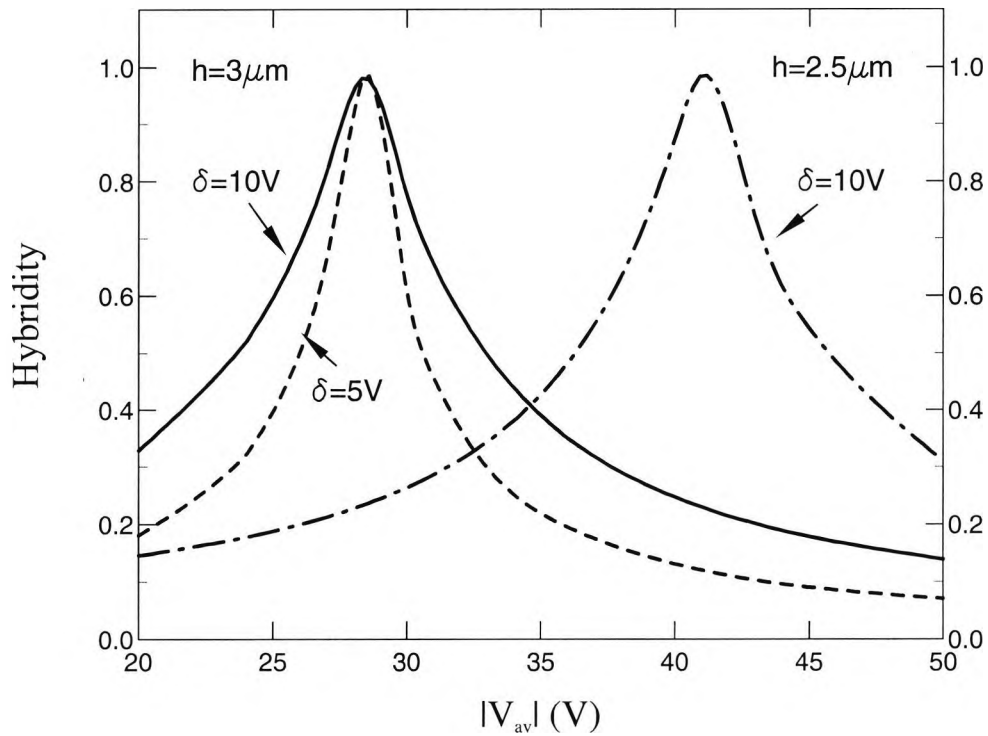
Fig. 7.12 Variation of the modal hybridity with the applied average voltage when voltage difference is maintained.
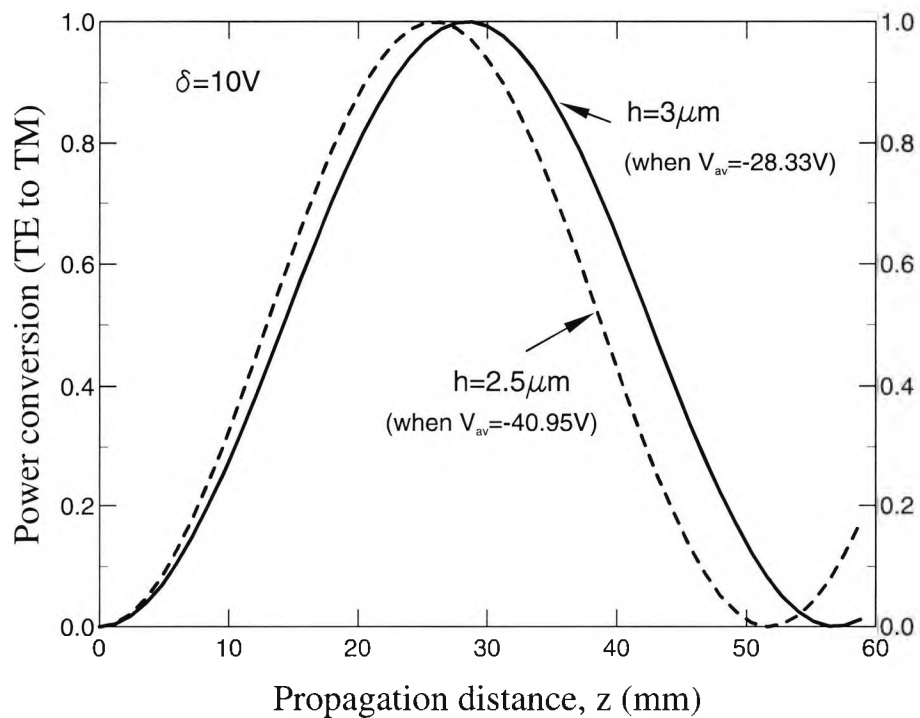
Fig. 7.13 Evolution of TM powers along the propagation direction for different core heights.

In order to understand the effect of the average applied voltage on the controller characteristics, several power curves along the propagation direction, z, for a waveguide core height, $h = 3$ μm, and with a voltage difference maintained at $\delta = 10V$, are shown in **Fig. 7.14**. According to the figure, it has been clearly shown that the maximum (100%) power conversion occurs at $V_{av} = -28.33$ V, as expected. However, for other cases, the power conversion efficiencies are less. On the other hand, the lengths at which the maximum power conversion occurs also vary for different V_{av} values, according to the corresponding half-beat lengths.
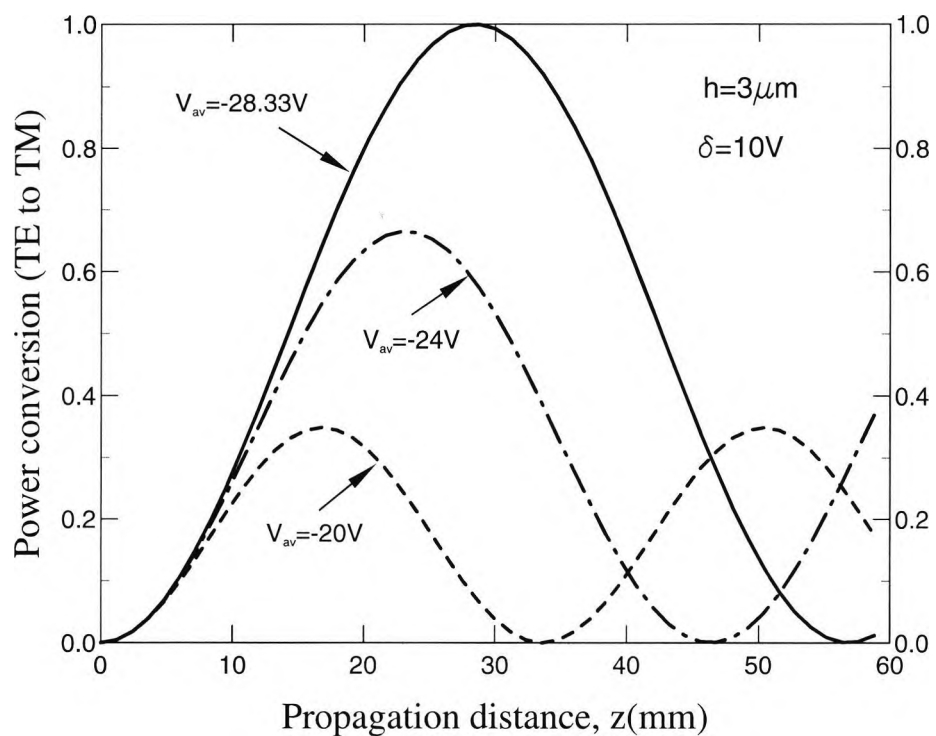
Fig. 7.14 TE to TM power conversion along the propagation direction, z, for different average voltages.

7.4   Summary

In this chapter, a novel design aspect of an active polarization controller based on AlGaAs-GaAs has been demonstrated. A rigorous full vectorial approach based on the versatile finite element method has been used to achieve accurate numerical simulations, which can consider the full permittivity tensor, which may arise due to the electro-optic effect. Initially, the propagation characteristics of the passive waveguide structure have been discussed and the phase matching has been achieved at a very much lower value of width. However, because of the long device length and the high performance sensitivity with the fabrication processes, the novel idea of incorporating a non-symmetrical modulating electric field was considered. The phase matching was achieved by variation of the applied voltage and consequently the polarization rotation was controlled by breaking the voltage symmetry. Hybridity and half-beat length variations were achieved for different waveguide core heights and for various differential voltages. Nearly 100% TE to TM polarization mode conversion was obtained by applying an average voltage of -28.33 V. It can also be noted that the δ voltage can be controlled to match the L_π to be exactly the same as the device length. However, optimising the waveguide geometrical parameters and the electrode dimensions further may give rise to a better performance in terms of polarization controllability, with low total and differential voltages.

Chapter 8

Conclusions and Future Directions

8.1   General conclusions

The primary objective of this research work has been to investigate polarization issues in opto-electronic systems by designing and characterising new compact integrated optical devices. The objectives set out at the beginning of the study have been successfully achieved with a detailed analysis of results during the course of the entire work. In this work, a numerical method based on the vectorial finite element formulation and the rigorously convergent least squares boundary residual (LSBR) method have been extensively used in order to accurately characterise various types of 3-dimensional optical waveguides and to study their polarization effects. This thesis considers a series of polarization-related waveguide components such as, passive polarization rotators, splitters and polarization controllers.

Many integrated optical subsystems incorporate guided-wave photonic devices and connecting optical waveguides with two-dimensional confinement and a high index contrast between the core and claddings. The modes in such waveguides and devices are highly hybrid in nature, with all the six components of the electric and magnetic fields being present the overall system will be polarization dependent. In present day

opto-electronic systems, this polarization issue is a key issue to be tackled for further improvement of their performance. Even though there are many available techniques for the study of optical waveguide problems, the finite element method has emerged as the most powerful, versatile and accurate method in analysing polarization properties in such systems. This method can handle a wide range of optical waveguide problems with arbitrary cross section, arbitrary index profile, anisotropy and non-linearity thus enabling the development of efficient and flexible computer programs. In this work, the emphasis was also placed on developing the finite element-based techniques for further use in design and analysis of novel practical waveguides such as, rib waveguides, ridge waveguides and silica-based planar waveguides, all with slanted side walls, deeply etched waveguides and electro-optic waveguides.

The previous chapters have dealt with the basic principles and theory of the numerical methods, and the characteristic simulations of novel polarization based integrated optical devices, by employing vector **H**-field finite element method along with the LSBR technique.

Chapter 2 was devoted to the mathematical background for the finite element method. The vector **H**-field variational formulation has been implemented. In this formulation, the magnetic field vector **H** is naturally continuous across the dielectric interfaces and also the associated natural boundary condition is that of an electric wall, which is very convenient to implement in many practical waveguide problems. The primary concepts such as the discretisation of the domain, the shape functions and the element matrices were also explained in detail. Since the shape functions provide only an approximate representation of the true fields, it is necessary to increase the number of elements to reduce the resulting error. By doing this, the numerical model comes closer to the real physical problem. However with this **H**-field formulation, the appearance of the spurious modes along with the physical modes is a main drawback. The penalty function method was introduced in order to eliminate these spurious modes by imposing the constraint $\nabla \cdot \mathbf{H} = 0$. The finite element method has been proved to be a very powerful method of finding the field profiles and the propagation characteristics of the guided modes of most of the optical guided-wave devices. On the other hand, it can also be used to determine the initial field distribution data for the

simulation analysis of the waveguide discontinuities by using the LSBR method or the beam propagation method.

In an optoelectronic system, when the modes are hybrid, polarization conversion can take place either unintentionally or deliberately at waveguide junctions. It is also necessary to analyse the butt-junction accurately in order to obtain the scattering coefficients. In this work the least squares boundary residual approach, where the continuity of the tangential fields is enforced in the useful least-square sense over the discontinuity interface has been widely used to analyse such waveguide discontinuity. Chapter 3 was dealt with the mathematical theory underlying the LSBR method. The LSBR method is an alternative to the point matching method and is rigorously convergent. The method was used to obtain both the transmission and the reflection coefficients of all the polarized modes by considering both the guided and radiation modes of the structures. It has also been used extensively to calculate the power transfer from one polarization to another along the axial direction of the waveguide considered.

In Chapter 4, the realisation of a polarization splitter based on a multimode interference (MMI) coupler, comprising of deeply etched semiconductor waveguide has been presented. Polarization splitter separates the input light into two waveguide outputs; one for each orthogonal polarization. Guided-wave optical TE/TM mode splitters are essential devices when the polarization state identification plays an important role in optical signal transmission. Although the optical devices based on MMI effects are generally considered to be polarization insensitive, the numerical simulations carried out using the rigorous vectorial finite element method, indicate a significant level of polarization dependence of MMI-based semiconductor waveguides. In this chapter, the design consideration of the MMI-based device has been discussed in terms of the self-imaging phenomenon. Beating between the modes in the multimode waveguide leads to this so-called self-imaging principle, whereby an input optical field is reproduced in the form of multiple copies. MMI waveguide characteristics were analysed in terms of coupling lengths of both the TE and TM polarizations and the L_π(TE)/ L_π(TM) ratios. It has been shown that the coupling length for the TE polarization is smaller than that of the TM polarization. Device

performance has been achieved by considering two interference mechanisms, called the restricted interference and the general interference mechanisms. An analysis of the quadrature error calculations was undertaken, which in turn are used to account for the field deterioration of the images along the MMI waveguide. Here, the junction between the input guide and the wider MMI waveguide was analysed by the use of the LSBR method, which ultimately gives all the modal transmission coefficients. A detailed investigation of the imaging properties of both the general and restricted interference mechanisms has been performed. The performance of the whole device was simulated for different MMI guide widths and for different input/output waveguide widths. The polarization dependence has been exploited extensively in the design of a compact, single-section polarization splitter by using a deeply etched semiconductor waveguide.

One of the key components in opto-electronic integrated circuits for coherent optical system applications is a polarization rotator, which can be used to control the polarization states. They can also be used for polarization division multiplexing or in polarization diversity heterodyne receivers, to provide 45° operation. In Chapter 5, the focus has been to design and optimise some novel polarization rotators using full vectorial numerical approaches. In the simulation, the vector finite element method has been used to find the modal solutions followed by the LSBR method to investigate the junction analysis. The first polarization rotator configuration presented was the cascaded-section polarization rotator by using waveguides with slanted sidewalls. To study the effect of the slanted side wall slope angle, it is essential to represent this feature exactly. By using the finite element method, the arbitrary slant angles were represented exactly with a considerable number of elements. The design concept of the polarization rotator was that if each section length matches half the beat length between the fundamental TE and TM modes of that section, a constructive interference between the two polarization modes occurs, leading to the build up of polarization conversion during propagation. In this chapter it has been shown that the degree to which the two polarization modes, TE and TM are hybrid i.e. the hybridity in each waveguide section, can be enhanced by breaking up the waveguide symmetry in both the vertical and horizontal directions through slanting one of the side walls. In normal waveguides with purely vertical side walls, due to the symmetry of the

structure in both transverse directions, the overlap integral between the minor and the major field components of both the TE and TM modes is very small, which gives a very low possibility of achieving polarization conversion. These concepts have been extensively shown with the aid of dominant and non-dominant field profiles of both TE and TM modes and the variation of the overlap integral for different waveguide structures. Another important characteristic was that the overlap integral increases with the reduction of the guide width and also the half beat length reduces considerably for the asymmetrical guide with the reduction of the width of the waveguide giving excellent design considerations for a short and efficient passive polarization rotator. An additional lateral offset has also been introduced between the guides to improve the mode conversion and to reduce the insertion loss at the junction interface. Consequently, a design of a compact 400 μm long passive polarization converter with less than 0.2 dB total insertion loss was proposed.

The second polarization rotator configuration considered was based on the use of a single-section asymmetrical optical waveguide butt-coupled between two standard input/output rib waveguides. Here it was important to design a polarization rotator waveguide that can support TE and TM modes, which are highly hybrid in such a way that the effective polarization angles are about 45° from the vertical or horizontal axes. When a purely TE mode of the input standard waveguide that supports modes with very little degree of hybridity is incident on such a polarization rotator waveguide, it was shown that two hybrid TE and TM polarized modes of similar modal amplitudes were excited. However at an exact half beat length, along the polarization rotator waveguide, the two modes become out of phase, which gives rise to a nearly pure TM mode. At this length, the converted power could be coupled to a standard output waveguide. Firstly the characteristics of the input-output waveguides were investigated to show their unlikeliness to achieve a reasonable polarization rotation. Next, an extensive study of the polarization rotator waveguide was carried out to see the effects of the waveguide width, index contrast and the slant angle on the polarization rotator performance in terms of hybridity, efficiency and the half beat lengths. The evolution of power along the polarization rotator waveguide and the insertion loss analysis were carried out once the butt-junction of the input and the polarization rotator waveguide has been analysed by the rigorous LSBR method. The

composite field profiles at the junction and at the end of the polarization rotator waveguide showed an excellent polarization conversion from TE to TM and TM to TE power. Here, the results of the evolution of optical power from TE to TM and vice versa, along the polarization rotator waveguide have been extensively compared with the results using the vector finite element beam propagation method. The results from both the independent approaches have shown a quite good agreement. A lateral shift between the waveguides was introduced for the sake of improving the polarization rotation and more particularly the insertion loss. Hence, a device of overall length of 320 μm and a very low insertion loss of 0.4 dB, with a capability of high polarization conversion was presented. The results obtained have demonstrated a stable polarization rotator performance within a range of the operating wavelength variation.

The next section in Chapter 5 was devoted to an investigation of the expected performance of a compact low-loss polarization rotator. Here an optimisation of a single-section asymmetric optical waveguide polarization rotator was achieved numerically by varying the waveguide parameters and also a study of fabrication tolerances has been performed. Initially, the variation of the hybridity for both TE and TM modes, and the half beat length with the waveguide width was considered. Numerical results showed that when the width is reduced the hybridity of the modes is increased to reach a maximum value of unity at a specific value of the width, which indicates that both of the transverse field components are almost equal. However by reducing the width further, the modal hybridity is reduced from its maximum value, and this particular feature was reported for the first time in our work. Another important feature was that the modal hybridity for the TM mode is slightly higher than that of the TE mode for any given waveguide width. The half beat length at the maximum hybridity position was considered as the optimum device length when analysing the fabrication tolerance study. The effect of the waveguide width on the TE to TM conversion was investigated by using power transfer curves for several different values of widths. The effect of the fabrication tolerances of the waveguide parameters (width, slant angle, index difference, height) on the polarization rotator performance in terms of the power conversion and the corresponding crosstalk at specified longitudinal positions have then been considered. The simulated results obtained demonstrate that there is hardly any effect on the polarization rotator

behaviour with the variation of the slant angle, index difference and the height. The most crucial parameter to consider when fabricating the device is the waveguide width. It has been shown that for a guide width tolerance of $1.15 \pm 0.1 \mu m$, the converted power was reduced by 0.3 dB from the optimum value, and the crosstalk was increased up to −12 dB. It has also been shown that the device performance is reasonably stable with the variation of the operating wavelength.

A novel design concept of a polarization rotator in shallow-etched semiconductor waveguides with the right hand side consisting of two different slanted side walls is also considered for its rigorous evaluation. By varying the various waveguide parameters, the polarization conversion properties were thoroughly analysed and a 400 μm long polarization rotator device was obtained with 98% TE to TM polarized power conversion. By introducing a lateral offset of 0.2 μm between the input and the PR waveguide, a lower insertion loss of 0.36 dB has been achieved. The tolerances to the fabrication processing variations and to the operating wavelength were considered next, by utilising an updated version of the original PR waveguide with new waveguide features which have been introduced by particular processing constraints. The effect of the verticality of the dry-etch was also analysed accordingly. Effects of each waveguide parameter on the hybridity, polarization conversion and the polarization crosstalk were investigated. Once again, it can be clearly noticed that the width of the waveguide plays a key role and is the most sensitive parameter when fabricating such polarization rotator waveguides.

The rapid progress of the Internet has led to an urgent need for flexible networks with a much larger capacity than at present. Large-scale and narrow-channel spacing arrayed-waveguide grating (AWG) multi/demultiplexers are very attractive components for such applications with a view to realising ultra-high density wavelength division multiplexing (WDM) systems. The construction depends on the successful fabrication of silica-based waveguides with a low propagation loss, and polarization crosstalk in such systems is an important criterion for characterising these waveguides. To achieve a larger scale AWG, the length of the silica slab waveguides has to be longer thereby increasing the bending radius, which in turn increases the chip size. By employing high index contrast (Δn), the chip size could be greatly

reduced as smaller radius (bend) can be achieved. Hence, in Chapter 6, the origin of polarization crosstalk in such high Δn planar silica waveguides and the possible effect of their non-ideal slanted side walls have been investigated. Initially, the modal analysis was carried out in order to obtain important **H**-field profile characteristics of the planar silica waveguides with both vertical and slanted side walls. It has been clearly seen that when the width and the height of the waveguide are equal, the modal degeneration occurs for the waveguides with vertical side walls. It was also shown that when the width is lower than the height of the waveguide, the longitudinal propagation constant of the quasi-TM mode is higher than that of the quasi-TE mode, and the propagation constants for both the modes increase with further increase in the guide width, and become equal at the modal degeneration. Variations of the modal hybridity and the half-beat lengths have been investigated for different side wall slant angles. Next, the waveguide junction between the standard planar waveguide with vertical side walls and the waveguide with slanted side walls was analysed, by using the LSBR method. The variations of the transmission coefficients have been obtained followed by the TE to TM power conversion for different side wall slant angles and waveguide widths. A thorough investigation of the polarization crosstalk at different longitudinal positions was also considered. Hence, it was clearly shown that a significant polarization crosstalk could take place in a long silica waveguide with high refractive index difference, but this may not be a critical issue for waveguide lengths around 1 cm with perfectly vertical side walls. The simulation results obtained have shown that the non-ideal side walls could be regarded as the main cause of increasing the polarization crosstalk for many silica-based optoelectronic systems.

In standard single mode fibres the state of polarization usually fluctuates randomly due to variations in the physical environment of the fibre. Polarization sensitive receivers in fibre optical communication systems therefore require polarization controllers to transform the fluctuating output state of polarization of the fibre into the desired input state of the polarization of the receiver. Hence the polarization manipulation can be regarded as an important issue for all optical, high data speed systems. Polarization mode dispersion (PMD) is also an important issue in the quest to build high speed (10 Gb/s, 40 Gb/s and higher) communication networks. Polarization controller is an essential element in PMD compensation schemes. Therefore in

Chapter 7, the emphasis has been given to a novel design of a polarization controller making use of the III-V semiconductor materials as an alternative to the typical lithium niobate integrated polarization controllers. The electro-optic effect was achieved by introducing two electrodes, which were placed on the top of the semiconductor waveguide with a considerable separation between them. A brief explanation underlying the design was given initially and the simulations of the passive waveguide were presented next. The width of the waveguide was varied in order to obtain the phase matching condition. However the corresponding waveguide width where the propagation constant difference of the TE and TM modes is nearly zero is considerably shorter, and also the half-beat length was quite larger making the device length enormously longer. The phase matching was achieved for a waveguide with reasonable width, by applying symmetrical voltages via the electrodes. It was clearly shown that by optimising waveguide parameters, the phase matching could be altered extensively. Here, the effect of waveguide core height was only investigated and as the core height was increased to 3 µm, the phase matching voltage dropped to -28.33 V. As the half-beat lengths are very larger when the voltages are symmetrical, non-symmetrical voltages were introduced to drastically decrease the device lengths. The refractive index profiles of the changes in diagonal and off diagonal elements in the refractive index matrix were also shown. The hybridity of the modes was analysed for different applied average voltages and it was clearly shown that the hybridity is reasonably high for a range of average applied voltages considered. When the voltage difference was increased, the modal hybridity varies slowly with the average voltages applied. The study of power conversion between the TE and TM modes proved nearly 100% mode conversion from TE to TM is possible and it was also shown that by changing the waveguide geometry, a much compact polarization controller with low total and differential voltages could be obtained.

8.2   Future directions

At 40 Gbit/s, which is in the next generation of transmission rates, various issues particularly the manipulation of the state of polarization (SOP) is expected to play a key role. Polarization Mode Dispersion (PMD) is one of the most crucial problems related to polarization manipulation and it can impose significant limitations on the distance over which transmission is possible. Therefore, a further study could involve an anlysis and optimisation of optoelectronic subsystems required to perform polarization control irrespective of the incoming SOP.

Polarization modulation and scrambling are amongst the other topics related to polarization manipulation, which need further attention. Polarization division multiplexing (PDM) can be used to enhance the speed further for next generation optical modulators by doubling the effective data rate. Moreover the PDM technique could be used to double the bit-rate capacity of ultra-long distance soliton transmission systems (Evangelides Jr. *et al.*, 1992) and it has also been used to reduce the soliton-soliton interaction for two 20Gb/s signals multiplexed to 40Gb/s line rate by interleaving polarization states over more than 10000 km distance (Morita *et al.*, 1999). Polarization scrambling has become important to avoid polarization hole burning in long haul transmission lines with cascaded EDFAs. Consequently, the anticipated subsystem could be consisted of novel designs of the key components, such as fast polarization controllers, modulators, switches and scramblers with low polarization crosstalk all in semiconductor based integrated optic format. The effect of fabrication tolerances for each component and the complete subsystem could be carried out.

To compensate the polarization-dependant delays, counter compensating isolated delay lines could be evaluated. By utilising compact bends, a few cm long spiral waveguides could be designed and using several switched sections with unequal lengths, a variable differential group delay (DGD) section could also be implemented.

Calculation of the Element Matrices

From equation (2.55);

$$[A]_e = \varepsilon^{-1} \int_\Delta [Q]^* [Q] \, d\Omega$$

$$= \varepsilon^{-1} \int_\Delta \begin{bmatrix} -\beta^2 [N]^T [N] + \dfrac{\partial [N]^T}{\partial y} \dfrac{\partial [N]}{\partial y} & -\dfrac{\partial [N]^T}{\partial y} \dfrac{\partial [N]}{\partial x} & j\beta [N]^T \dfrac{\partial [N]}{\partial x} \\[2ex] -\dfrac{\partial [N]^T}{\partial x} \dfrac{\partial [N]}{\partial y} & -\beta^2 [N]^T [N] + \dfrac{\partial [N]^T}{\partial x} \dfrac{\partial [N]}{\partial x} & j\beta [N]^T \dfrac{\partial [N]}{\partial y} \\[2ex] j\beta \dfrac{\partial [N]^T}{\partial x} [N] & j\beta \dfrac{\partial [N]^T}{\partial y} [N] & \dfrac{\partial [N]^T}{\partial y} \dfrac{\partial [N]}{\partial y} + \dfrac{\partial [N]^T}{\partial x} \dfrac{\partial [N]}{\partial x} \end{bmatrix} d\Omega$$

$$\text{(A1.1)}$$

From equation (2.56);

$$[B]_e = \mu \int_\Delta [\mathbf{N}]^T [\mathbf{N}] \, d\Omega$$

$$= \mu \int_\Delta \begin{bmatrix} [N]^T [N] & [0]^T [0] & [0]^T [0] \\ [0]^T [0] & [N]^T [N] & [0]^T [0] \\ [0]^T [0] & [0]^T [0] & [N]^T [N] \end{bmatrix} d\Omega \qquad \text{(A1.2)}$$

The integrations of the shape functions in equations (A1.1) and (A1.2) can be evaluated by using the following relation for a triangular element;

$$\int_\Delta N_1^i N_2^j N_3^k \, d\Omega = \frac{i! \, j! \, k! \, 2!}{(i + j + k + 2)!} A_e \qquad \text{(A1.3)}$$

where A_e is the area of the triangular element.

Hence the following integrals can be achieved;

$$\int_{\Delta} N_1^2 \, d\Omega = \int_{\Delta} N_2^2 \, d\Omega = \int_{\Delta} N_3^2 \, d\Omega = \frac{A_e}{6} \tag{A1.4}$$

$$\int_{\Delta} N_1 N_2 \, d\Omega = \int_{\Delta} N_2 N_3 \, d\Omega = \int_{\Delta} N_1 N_3 \, d\Omega = \frac{A_e}{12} \tag{A1.5}$$

$$\int_{\Delta} d\Omega = A_e \tag{A1.6}$$

Therefore from equation (A1.1), some of the elements of the 9×9 $[A]_e$ matrix can be calculated as;

$$[A]_{e(1,1)} = \frac{1}{\varepsilon} \int_{\Delta} -\beta^2 N_1^2 + \left(\frac{\partial N_1}{\partial y}\right)^2 \, d\Omega = \frac{1}{\varepsilon}\left[\frac{-\beta^2 A_e}{6} + c_1^2 A_e\right] \tag{A1.7}$$

$$[A]_{e(1,2)} = \frac{1}{\varepsilon} \int_{\Delta} -\beta^2 N_1 N_2 + \frac{\partial N_1}{\partial y}\frac{\partial N_2}{\partial y} \, d\Omega = \frac{1}{\varepsilon}\left[\frac{-\beta^2 A_e}{12} + c_1 c_2 A_e\right] \tag{A1.8}$$

$$[A]_{e(1,4)} = \frac{1}{\varepsilon} \int_{\Delta} \frac{-\partial N_1}{\partial y}\frac{\partial N_1}{\partial x} \, d\Omega = -\frac{1}{\varepsilon} c_1 b_1 A_e \tag{A1.9}$$

Matrix $[B]_e$ is also a 9×9 matrix and some of the elements are calculated as;

$$[B]_{e(1,1)} = \mu \int_{\Delta} N_1^2 \, d\Omega = \mu \frac{A_e}{6} \tag{A1.10}$$

$$[B]_{e(1,2)} = \mu \int_{\Delta} N_1 N_2 \, d\Omega = \mu \frac{A_e}{12} \tag{A1.11}$$

$$[B]_{e(1,4)} = 0 \tag{A1.12}$$

Appendix 2

Calculation of the transverse modulating field components

The potential distribution, $\phi(x,y)$ is governed by the following Laplace's equation;

$$\nabla \cdot \phi = 0 \tag{A2.1}$$

From Laplace's equation, the following two dimensional functional can be obtained,

$$L(\phi) = \iint \left[\varepsilon_{xx} \left(\frac{\partial \phi}{\partial x} \right)^2 + \varepsilon_{yy} \left(\frac{\partial \phi}{\partial y} \right)^2 \right] dx\, dy \tag{A2.2}$$

where ε_{xx} and ε_{yy} are the dielectric constants along the x and y directions, respectively.

By using the FEM, this expression can be minimised with respect to each nodal potential value with the applied electrode voltages as constraints and a system of linear algebraic equation is generated which is given by;

$$\mathbf{S}\,\phi = \mathbf{b} \tag{A2.3}$$

where ϕ is the nodal electrostatic potential vector and the vector $\mathbf{b}$ originates from the imposed voltages. Consequently the potential distribution $\phi(x,y)$ can be used to determine the two transverse components of the modulating electric fields, $E_x(x,y)$ and $E_y(x,y)$, according to the equation given below;

$$\mathbf{E} = -\nabla \phi(x,y) \tag{A2.4}$$

Subsequently, these $E_x(x,y)$ and $E_y(x,y)$ field components can be used to calculate the electrooptic contribution to the tensor refractive indices, as depicted in equations (7.3)-(7.5).

List of Publications by the author

1) Rahman, B.M.A., **Somasiri, N.,** and Rajarajan, M., "Compact passive polarization converter using slanted semiconductor rib waveguides," *OSA Conference on Integrated Photonics Research (IPR),* Quebec City, Canada, July, 12-15, 2000. *IPR Technical Digest,* pp. 60-62, 2000.

2) Rahman, B.M.A., Wongchareon, T., Obayya, S.S.A, Rajarajan, M., Themistos, C., **Somasiri, N.,** Anwar, N., El-Mikati, H.A., and Grattan, K.T.V., "Rigorous analysis of photonic devices by using the finite element method," *8th IEEE International Symposium on High Performance Electron Devices for Microwave and Optoelectronic Applications (EDMO),* pp. 173-178, Glasgow, Scotland, 2000.

3) Rahman, B.M.A., Obayya, S.S.A., **Somasiri, N.,** Rajarajan, M., Grattan, K.T.V., and El-Mikati, H.A., "Design and characterisation of compact single-section passive polarization rotator," *J. Lightwave Technol.,* vol. 19, no. 4, pp. 512-519, 2001.

4) Rahman, B.M.A, Obayya, S.S.A., **Somasiri, N.,** and Grattan, K.T.V., "Design of compact passive polarization converter in semiconductor waveguides," *10th European Conference on Integrated Optics (ECIO'01),* pp. ThPo4, Paderbom, Germany, April 04-06, 2001.

5) Rahman, B.M.A., Themistos, C., **Somasiri, N.,** and Grattan, K.T.V., "Optical polarizer in deeply-etched MMI Waveguides," *10th European Conference on*

Integrated Optics (ECIO'01), pp. ThB2.3, Paderborn, Germany, April 04-06, 2001.

6) Rahman, B.M.A., Obayya, S.S.A., **Somasiri, N.,** and Grattan, K.T.V., "Design of ultra-compact polarization rotators using slanted side walls," *Int. Optoelectronic & Communications Conf., OECC/IOOC 2001,* pp. 585-586, Sydney, Australia, July 2001.

7) Rahman, B.M.A., **Somasiri, N.,** Themistos, C., and Grattan, K.T.V., "Design of optical polarization splitters in a single-section deeply-etched MMI waveguide," *Appl. Phys. B-Lasers Opt.,* vol. 73, no.5-6, pp. 613-618, Oct. 2001.

8) **Somasiri, N.,** Rahman, B.M.A., and Obayya, S.S.A., "Fabrication tolerance study of a compact passive polarization rotator," *J. Lightwave Technol.,* vol. 20, no. 4, pp. 751-757, 2002.

9) Rahman, B.M.A., Obayya, S.S.A., **Somasiri, N.,** Rajarajan, M., Abdelmalek, F., and Grattan, K.T.V., "Polarization issues in optical guided-wave devices and systems," *10th International Workshop on Optical Waveguide Theory and Numerical Modelling,* Nottingham, UK, April 2002.

10) Rahman, B.M.A., **Somasiri, N.,** and Windmann, M., "Increased polarization crosstalk in planar silica waveguides with high index contrast and non-vertical sidewalls," *OSA Conference on Integrated Photonics Research (IPR),* pp. IThA2-1-IThA2-3, Vancouver, Canada, July 2002.

11) Rahman, B.M.A, **Somasiri, N.,** and Windmann, M., "Polarization crosstalk in high index contrast planar silica waveguides," *IEEE Photon. Technol. Lett.,* pp. 1109-1111, 2002.

12) **Somasiri, N.,** Rahman, B.M.A., and Obayya, S.S.A., "Design of compact passive polarization rotator," *International Conference on Numerical Simulation*

of Semiconductor Optoelectronic Devices (NUSOD-02), pp. 78-79, Zurich, Switzerland, Sept. 25-27, 2002.

13) Rahman, B.M.A., Obayya, S.S.A., **Somasiri, N.**, Rajarajan, M., "Polarization issues in optoelectronic subsystems," *Photonics India 2002*, Bombay, Dec. 2002.

14) Rahman, B.M.A., Obayya, S.S.A., **Somasiri, N.**, "Polarization issues in optoelectronic devices and systems," *Conference on Physics and Simulation of Optoelectronic Devices XI*, San Jose, California, Jan. 27-31, 2003. *Proceedings of the Society of Photo-optical Instrumentation Engineers (SPIE)*, pp. 363-374, 2003.

15) **Somasiri, N.**, and Rahman, B.M.A., "Polarization crosstalk in high index contrast planar silica waveguides with slanted sidewalls," *J. Lightwave Technol.*, vol. 21, no. 1, pp. 54-60, 2003.

16) Obayya, S.S.A., **Somasiri, N.**, Rahman, B.M.A., and Grattan, K.T.V., "Full vectorial finite element modelling of novel polarization rotators," *Opt. Quant. Electron.*, vol. 35, no. 4, pp. 297-312, 2003.

17) Rajarajan, M., Rahman, B.M.A., Wongcharoen, T., Themistos, C., **Somasiri, N.**, Haxha, S., and Grattan, K.T.V., "Review of finite-element characterisation of photonic devices," *J. Mod. Optic.*, vol. 50, no. 12, pp. 1835-1848, 2003.

18) Rahman, B.M.A., Obayya, S.S.A., **Somasiri, N.**, Rajarajan, M., Themistos, C., Grattan, K.T.V., "Polarization issues in optoelectronic systems," *Conference on Active and Passive Optical Components for WDM Communications III*, Orlando, Florida, Sep 08-11, 2003. *Proceedings of the Society of Photo-optical Instrumentation Engineers (SPIE)*, pp. 235-249, 2003.

References

- Ahmed, S. and Daly, P., "Finite element method for inhomogeneous waveguides," *Proc. IEE*, vol. 116, pp. 1661-1664, 1969.

- Albrecht, P., Hamacher, M., Heidrich, H., Hoffmann, D., Nolting, H. P., and Wienert, C. M.,"TE/TM mode splitters on InGaAsP/InP," *IEEE Photon. Technol. Lett.*, vol. 2, no. 2, pp. 114-115, 1990.

- Alferness, R. C. and Buhl, L. L., "High-speed waveguide electro-optic polarization modulator," *Opt. Lett.*, vol. 7, no. 10, pp. 500-502, 1982.

- Alferness, R. C. and Buhl, L. L., "Low loss, wavelength tunable, waveguide electro-optic polarization controller for $\lambda = 1.32$ μm," *Appl. Phys. Lett.*, vol. 47, no. 11, pp. 1137-1139, 1985.

- Angkaew, T., Matsuhara, M., and Kumagai, N., "Finite element analysis of waveguide modes: A novel approach that eliminates spurious modes," *IEEE Trans. Microwave Theory Tech.*, vol. MTT-35, no. 2, pp. 117-123, 1987.

- Balland, G., Paski, R. M., and Baker, R. A., "TAT-12/13 integration development tests – interim results," in *Proc. International Conf. Optical Fibre Submarine Telecom.*, Paper 3.6, March 1993.

- Bathe, K., *Finite element procedure in engineering analysis*, Englewood Cliffs, NJ; Prentice-Hall, 1982.

- Berk, A. D., "Variational principles for electromagnetic resonators and waveguides," *IRE Trans. Antennas Propagat.*, vol. AP-4, pp. 104-111, 1956.

- Bierwirth, K., Schulz, N., and Arndt, F., "Finite difference analysis of rectangular dielectric waveguide structures," *IEEE Trans. Microwave Theory Tech.*, vol. MTT-34, no. 11, pp. 1104-1114, 1986.

- Bissessur, H., PagnodRossiaux, P., Mestric, R., and Martin, B., "Extremely small polarization independent phased-array demultiplexers on InP," *IEEE Photon. Technol. Lett.*, vol. 8, no. 4, pp. 554-556, 1996.

- Bossavit, A., and Mayergoyz, I., "Edge-elements for scattering problems," *IEEE Trans. Magnetics*, vol. 25, no. 4, pp. 2816-3821, 1989.

- Brooke, G. H. and Kharadly, M. M. Z., "Step discontinuities on dielectric waveguides," *Electron. Lett.*, vol. 12, no. 18, pp. 473-475, 1976.

- Burke, S. V., "Spectral index method applied to coupled rib waveguides," *Electron. Lett.*, vol. 25, no. 9, pp. 605-606, 1989.

- Burke, S. V., "Spectral index method applied to two nonidentical closely separated rib waveguides," *IEE Proc. Pt. J*, vol. 137, no. 5, pp. 289-292, 1990.

- Burke, S. V., "Planar waveguide analysis by the spectral index method: II. Multiple layers, optical gain and loss," *Opt. Quantum Electron.*, vol. 26, no. 2, pp. 63-77, 1994.

- Chiang, K. S., "Analysis of optical fibres by the effective-index method," *Appl. Opt.*, vol. 25, no. 3, pp. 348-354, 1986*a*.

- Chiang, K. S., "Dual effective index method for the analysis of rectangular dielectric waveguides," *Appl. Opt.*, vol. 25, no. 13, pp. 2169-2174, 1986*b*.

- Chiang, K. S., "Review of numerical and approximate methods for the modal analysis of general optical dielectric waveguides," *Opt. Quantum Electron.*, vol. 26, no. 3, pp. S113-S134, 1994.

- Chiang, K. S., Lo, K. M., and Kwok, K. S., "Effective-index method with built-in perturbation correction for integrated optical waveguides," *J. Lightwave Technol.*, vol.14, no. 2, pp. 223-228, 1996.

- Chung, Y., Dagli, N., and Thylen, L., "Explicit finite difference vectorial beam propagation method," *Electron. Lett.*, vol. 37, no. 23, pp 2119-2121, 1991.

- Clarricoats, P. J. B. and Sharpe, A. B., "Modal matching applied to a discontinuity in a planar surface waveguide," *Electron. Lett.*, vol. 8, no. 2, pp. 28-29, 1972.

- Creaner, M. J., Steele, R. C., Walker, G. R., and Walker, N. G., "565 Mbit/s Optical PSK transmission system with endless polarization control," *Electron. Lett.*, vol. 24, no. 5, pp. 270-271, 1988.

- Csendes, Z. J. and Silvester, P., "Numerical solution of dielectric loaded waveguides: I – Finite-element analysis," *IEEE Trans. Microwave Theory Tech.*, vol. MTT-18, no. 12, pp. 1124-1131, 1970.

- Cullen, A. L., Ozkan, O., and Jackson, L. A., "Point-matching technique for rectangular-cross-section dielectric rod," *Electron. Lett.*, vol. 7, no. 17, pp. 497-499, 1971.

- Cullen, A. L. and Yeo, S. P., "Using the least-squares boundary residual method to model the summetrical five-port waveguide junction," *IEE Proc. Pt. H*, vol. 134, no. 2, pp. 116-124, 1987.

- Dagli, N. and Fonstad, C. G., "Microwave equivalent circuit representation of rectangular dielectric waveguides," *Appl. Phys. Lett.*, vol. 49, no. 6, pp. 308-310, 1986.

- Davies, J. B. and Muilwyk, C. A., "Numerical solution of uniform hollow waveguides with boundaries of arbitrary shape," *Proc. IEE*, vol. 113, no. 2, pp. 277-284, 1966.

- Davies, J. B., "Review of methods for numerical solution of the hollow-waveguide problem," *Proc. IEE*, vol. 119, no. 1, pp. 33-37, 1972.

- Davies, J. B., "A least-squares boundary residual method for the numerical solution of scattering problems," *IEEE Trans. Microwave Theory Tech.*, vol. MTT-21, no. 2, pp. 99-104, 1973.

- Davies, J. B., Fernandez, F. A., and Philippou, G. Y., "Finite element analysis of all modes in cavities with circular symmetry," *IEEE Trans. Microwave Theory Tech.*, vol. MTT-30, no. 11, pp. 1975-1980, 1982.

- Davies, J. B., *The finite element method*, in *Numerical techniques for microwave and millimeter-wave passive structures*, Edited by T. Itoh, New York: Wiley, pp. 33-132, 1989.

- Davies, J. B., "Finite element analysis of waveguides and cavities – a review," *IEEE Trans. Magnetics*, vol. 29, no. 2, pp. 1578-1583, 1993.

- Desai, C. S., *Elementary finite element method*, Prentice-Hall Inc., New Jersey, 1979.

- English, W. J. and Young, F. J., "An E vector variational formulation of the Maxwell equations for cylindrical waveguide problems," *IEEE Trans. Microwave Theory Tech.*, vol. MTT-19, no. 1, pp. 40-46, 1971.

- Evangelides Jr., S. G., Mollenauer, L. F., Gordon, J. P., and Bergano, N. S., "Polarization multiplexing with solitons," *J. Lightwave Technol.*, vol.10, no. 1, pp. 28-35, 1992.

- Feit, M. D. and Fleck, Jr., J. A., "Computation of mode properties in optical fibre waveguides by a propagating beam method," *Appl. Opt.*, vol. 19, no. 7, pp.1154-1164, 1980.

- Fernandez, F. A. and Davies, J. B., "Least-squares boundary residuals solution of microstrip step discontinuities," *Electron. Lett.*, vol. 24, no. 10, pp. 640-641, 1988.

- Garner, S. M., Chuyanov, V., Lee, S. S., Chen, A., Steier, W. H., and Dalton, L. R., "Vertically integrated waveguide polarization splitters using polymers," *IEEE Photon. Technol. Lett.*, vol. 11, no. 7, pp. 842-844, 1999.

- Goell, J. E., "A circular-harmonic computer analysis of rectangular dielectric waveguides," *Bell Syst. Tech. J.*, vol. 48, pp. 2133-2160, 1969.

- Gordon, J. P. and Mollenauer, L. F., "Effects of fiber nonlinearities and amplifier spacing on ultra-long distance transmission," *J. Lightwave Technol.*, vol. 9, no. 2, pp. 170-173, 1991.

- Goto, N. and Yip, G. L., "A TE-TM mode splitter in LiNbO$_3$ proton exchange and Ti diffusion," *J. Lightwave Technol.*, vol. 7, no. 10, pp. 1567-1574, 1989.

- Grossard, N., Porte, H., Vilcot, J. P., Beche, B., and Goedgebuer, J. P., "AlGaAs-GaAs polarization converter with electrooptic phase mismatch control," *IEEE Photon. Technol. Lett.*, vol. 13, no. 8, pp. 830-832, 2001.

- Habara, K., "LiNbO$_3$ directional coupler polarization splitter," *Electron. Lett.*, vol. 23, no. 12, pp. 614-616, 1987.

- Hano, M., "Finite-element analysis of dielectric-loaded waveguides," *IEEE Trans. Microwave Theory Tech.*, vol. MTT-32, no. 10, pp. 1275-1279, 1984.

- Hayashi, M., Tanaka, H., and Suzuki, M., "40 Gb/s demonstration of wide range of PMD compensation using a polarizer," in *Proc. OECC/IOOC,* Sydney, Australia, pp. 48-49, July 2001.

- Hayata, K., Koshiba, M., Eguchi, M., and Suzuki, M., "Novel finite-element formulation without any spurious solutions for dielectric waveguides," *Electron. Lett.*, vol. 22, no. 6, pp. 295-296, 1986.

- Heaton, J. M., Jenkins, R. M., Wight, D. R., Parker, J. T., Birbeck, J. C. H., and Hilton, K. P., "Novel 1-to-N way integrated optical beam splitters using symmetric mode mixing in GaAs/AlGaAs multimode waveguides," *Appl. Phys. Lett.*, vol. 61, no. 15, pp. 1754-1756, 1992.

- Heismann, F., Divino, M. D., and Buhl, L. L.,"Integrated-optic polarization controller with unlimited transformation range," *Appl. Phys. Lett.,* vol. 57, no. 9, pp. 855-857, 1990.

- Heismann, F. and Whalen, M. S., "Broadband reset-free automatic polarization controller," *Electron. Lett.,* vol. 27, no. 4, pp. 377-379, 1991.

- Heismann, F. and Smith, R. W., "High-speed polarization scrambler with adjustable phase chirp," *IEEE J. Select. Topics Quantum Electron.,* vol. 2, no. 2, pp. 311-318, 1996.

- Hempelmann, U., Herrmann, H., Mrozynski, G., Reimann, V., and Sohler, W., "Integrated optical proton exchanged TM-pass polarizers in LiNbO3: modelling and experimental performance," *J. Lightwave Technol.,* vol. 13, no. 8, pp. 1750-1759, 1995.

- Hirayama, K. and Koshiba, M., "Analysis of discontinuities in an open dielectric slab waveguide by combination of finite and boundary elements," *IEEE Trans. Microwave Theory Tech.,* vol. MTT-37, no. 4, pp. 761-767, 1989.

- Hockham, G. A. and Sharpe, A. B., "Dielectric – waveguide discontinuities," *Electron. Lett.,* vol. 8, no. 9, pp. 230-231, 1972.

- Huang, W. P., Xu, C. L., and Chaudhuri, S. K., "A finite difference vector beam propagation method for three-dimensional waveguide structures," *IEEE Photon. Technol. Lett.,* vol. 4, no. 2, pp. 148-151, 1992.

- Huang, W. P. and Xu, C. L., "A wide-angle vector beam propagation method," *IEEE Photon. Technol. Lett.,* vol. 4, no. 10, pp. 1118-1120, 1992.

- Huang, J. Z., Scarmozzino, R., Nagy, G., Steel, M. J., and Osgood Jr., R. M., "Realization of a compact and single-mode optical polarization converter," *IEEE Photon. Technol. Lett.,* vol. 12, no. 3, pp. 317-319, 2000.

- Ikeuchi, M., Sawami, H., and Niki, H., "Analysis of open-type dielectric waveguides by the finite-element iterative method," *IEEE Trans. Microwave Theory Tech.,* vol. MTT-29, no. 3, pp. 234-239, 1981.

- Imoto, N., Kawana, A., Machida, S., and Tsuchiya, H., "Characteristics of dispersion free single mode fibre in the 1.5-μm wavelength region," *J. Quantum Elect.,* vol. 16, pp.1052-1058, 1980.

- Inoue, Y. and Hida, Y., "Large-scale arrayed-waveguide gratings," *Proc. OECC/IOOC,* pp. 29-32, 2001.

- Kagami, S. and Fukai, I., "Application of boundary-element method to electromagnetic field problems," *IEEE Trans. Microwave Theory Tech.*, vol. MTT-32, no. 4, pp. 455-461, 1984.

- Kao, K. C. and Hockham, G. H., "Dielectric fibre surface waveguides for optical frequencies," *Proc. IEE*, vol. 113, no. 7, pp. 1151-1158, 1966.

- Kapron, F. P., Keck, D. B., and Maurer, R. D., "Radiation losses in glass optical waveguides," *Appl. Phys. Lett.*, vol. 17, pp. 423-425, 1970.

- Kawachi, M., "Recent progress in silica-based planar lightwave circuits on silicon," *IEE Proc.-Optoelectron.*, vol. 143, no. 5, pp. 257-262, 1996.

- Kendall, P. C., McIlroy, P. W. A., and Stern, M. S., "Spectral index method for rib waveguide analysis," *Electron. Lett.*, vol. 25, no. 2, pp. 107-108, 1989.

- Kikuchi, N., "Analysis of signal degree of polarization degradation used as control signal for optical polaristaion mode dispersion compensation," *J. Lightwave Technol.*, vol. 19, no. 4, pp. 480-486, 2001.

- Knox, R. M. and Toulios, P. P., "Integrated circuits for the millimeter through optical frequency range," in *Proceedings, Symposium on Submillimeter Waves.* Brooklyn: Polytechnic Press, pp. 497-516, 1970.

- Kogelnik, H., *Theory of optical waveguides in: Guided-wave optoelectronics*, Ed. By T. Tamir, Heidelberg, Springer-Verlag, 1990.

- Konrad, A., "Vector variational formulation of electromagnetic fields in anisotropic media," *IEEE Trans. Microwave Theory Tech.*, vol. MTT-24, no. 9, pp. 553-559, 1976.

- Konrad, A., "High-order triangular finite elements for electromagnetic waves in anisotropic media," *IEEE Trans. Microwave Theory Tech.*, vol. MTT-25, no. 5, pp. 353-360, 1977.

- Koshiba, M., Hayata, K., and Suzuki, M., "Approximate scalar finite-element analysis of anisotropic optical waveguides," *Electron. Lett.*, vol. 18, no. 10, pp. 411-413, 1982.

- Koshiba, M., Hayata, K., and Suzuki, M., "Vectorial finite-element method without spurious solutions for dielectric waveguide problems," *Electron. Lett.*, vol. 20, no. 10, pp. 409-410, 1984.

- Koshiba, M. and Suzuki, M., "Vectorial wave analysis of optical waveguides with rectangular cross-section using equivalent network approach," *Electron. Lett.*, vol. 21, no. 22, pp. 1026-1028, 1985.

- Koshiba, M., Hayata, K., and Suzuki, M., "Finite element formulation in terms of the electric-field vector for electromagnetic waveguide problems," *IEEE Trans. Microwave Theory Tech.*, vol. MTT-33, no. 10, pp. 900-905, 1985a.

- Koshiba, M., Hayata, K., and Suzuki, M., "Improved finite-element formulation in terms of the magnetic-field vector for dielectric waveguides," *IEEE Trans. Microwave Theory Tech.*, vol. MTT-33, no. 3, pp. 227-233, 1985b.

- Koshiba, M. and Suzuki, M., "Boundary-element analysis of dielectric slab waveguide discontinuities," *Appl. Opt.*, vol. 25, no. 6, pp. 828-829, 1986a.

- Koshiba, M., and Suzuki, M., "Vectorial wave analysis of dielectric waveguides for optical integrated circuits using equivalent network approach," *J. Lightwave Technol.*, vol. 4, no. 6, pp. 656-664, 1986b.

- Koshiba, M., Hayata, K., and Suzuki, M., "Vector-E field finite element analysis of dielectric optical waveguides," *Appl. Opt.*, vol. 25, no. 1, pp. 10-11, 1986.

- Koshiba, M., *Optical waveguide analysis*, McGraw-Hill, Inc., 1992.

- Koshiba, M., and Inoue, K., "Simple and efficient finite-element analysis of microwave and optical waveguides," *IEEE Trans. Microwave Theory Tech.*, vol. MTT-40, no. 2, pp. 371-377, 1992.

- Koshiba, M., Tsuji, Y., and Nishio, M., "Finite-element modeling of broad-band traveling-wave optical modulators," *IEEE Trans. Microwave Theory Tech.*, vol. MTT-47, no. 9, pp. 1627-1633, 1999.

- Kubota, M., Oohara, T., Furuya, K., and Suematsu, Y., "Electrooptical polarization control on single-mode optical fibres," *Electron. Lett.*, vol. 16, no. 15, pp. 573, 1980.

- Lee, S. S., Garner, S., Chen, A., Chuyanov, V., Steier,W. H., Ahn, S. W., and Shin, S. Y., "TM-pass polarizer based on a photobleching-induced waveguide in polymers," *IEEE Photon. Technol. Lett.*, vol. 10, no. 6, pp. 836-838, 1998.

- Lin, C., Kobrinski, H., Frenkel, A., and Brackett, C. A., "Wavelength-tunable 16 optical channel transmission experiment at 2 Gbit/s and 600 Mbit/s for broadband subscriber distribution," *Electron. Lett.*, vol. 24, no. 19, pp. 1215-1216, 1988.

- Liu, Y., Rahman, B. M. A., and Grattan, K. T. V., "Analysis of the birefringence properties of optical fibres made by a perform deformation technique," *J. Lightwave Technol.*, vol. 13, no. 2, pp. 142-147, 1995.

- Mabaya, N., Lagasse, P. E., and Vandenbulcke, P., "Finite element analysis of optical waveguides," *IEEE Trans. Microwave Theory Tech.*, vol. MTT-29, no. 6, pp. 600-605, 1981.

- Mahmoud, S. F., and Beal, J. C., "Scattering of surface waves at a dielectric discontinuity on a planar waveguide," *IEEE Trans. Microwave Theory Tech.*, vol. MTT-23, no. 2, pp. 193-198, 1975.

- Maiman, T. H., "Stimulated optical radiation in ruby," *Nature*, vol. 187, pp. 493-494, 1960.

- Marcatili, E. A. J., "Dielectric rectangular waveguide and directional coupler for integrated optics," *Bell Syst. Tech. J.*, vol. 48, pp. 2071-2102, 1969.

- Matsumoto, M., Tsutsumi, M., and Kumagai, N., "Bragg reflection characteristics of millimeter waves in a periodically plasma-induced semiconductor waveguide," *IEEE Trans. Microwave Theory Tech.*, vol. MTT-34, no. 4, pp. 406-411, 1986.

- Matsumoto, T. and Kano, H., "Endlessly rotatable fractional-wave devices for single-mode-fibre optics," *Electron. Lett.*, vol. 22, no. 2, pp. 78-79, 1986.

- Mears, R. J., Reekie, L., Jauncey, L., and Payne, D. N., "High-gain, rare-earth-doped fibre amplifier at 1.54 μm," in *Proc. Conf. Optical Fibre Communication (OFC)*, Paper W12, 1987.

- Mikami, O., "LiNbO$_3$ coupled-waveguide TE/TM mode splitter," *Appl. Phys. Lett.*, vol. 36, no. 7, pp. 491-493, 1980.

- Miller, S. E., "Integrated optics: An introduction," *Bell Syst. Tech. J.*, vol. 48, no. 7, pp. 2059-2069, 1969.

- Mollenauer, L. F., Lichtman, E., Neubelt, M. J., and Harvey, G. T., "Demonstration using sliding-frequency guiding filters, of error-free soliton transmission over more than 20 Mm at 10 Gbit/s single channel, and over more than 13 Mm at 20 Gbit/s in a two-channel WDM," *Electron. Lett.*, vol. 29, no. 10, pp. 910-911, 1993.

- Morishita, K. and Kumagai, N., "Unified approach to the derivation of variational expression for electromagnetic fields," *IEEE Trans. Microwave Theory Tech.*, vol. MTT-25, no. 1, pp. 34-40, 1977.

- Morishita, K., Inagaki, S., and Kumagai, N., "Analysis of discontinuities in dielectric waveguides by means of the least squares boundary residual method," *IEEE Trans. Microwave Theory Tech.*, vol. MTT-27, no. 4, pp. 310-315, 1979.

- Morita, I., Tanka, K., Edagawa, N., and Suzuki, M., "40 Gb/s single-channel soliton transmission over transoceanic distances by reducing Gordon-Haus timing jitter and soliton-soliton interaction," *J. Lightwave Technol.*, vol. 17, no. 12, pp. 2506-2511, 1999.

- Nakazawa, M., Suzuki, K., Yamada, E., Kubota, H., Kimura, Y., and Takaya, M., "Experimental demonstration of soliton data transmission over unlimited distances with soliton control in time and frequency domains," *Electron. Lett.*, vol. 29, no. 9, pp. 729-730, 1993.

- Ng, F. L., "Tabulation of methods for the numerical solution of the hollow waveguide problem," *IEEE Trans. Microwave Theory Tech.*, vol. 22, no. 3, pp. 322-329, 1974.

- Obayya, S. S. A., Rahman, B. M. A., and El-Mikati, H. A., "New full-vectorial numerically efficient propagation algorithm based on the finite element method," *J. Lightwave Technol.*, vol. 18, no. 3, pp. 409-415, 2000.

- Obayya, S. S. A., Rahman, B. M. A., Grattan, K. T. V., and El-Mikathi, H. A., "Beam propagation modelling of polarization rotation in deeply etched semiconductor bent waveguides," *IEEE Photon. Technol. Lett.*, vol. 13, no. 7, pp. 681-683, 2001.

- Ohtaka, M., Matsuhara, M., and Kumagai, N., "Analysis of the guided modes in slab-coupled waveguides using a variational method," *IEEE J. Quantum Electron.*, vol. QE-12, pp. 378-382, 1976.

- Okoshi, T., "Single polarization single-mode optical fibres," *IEEE J. Quantum Electron.*, vol. QE-17, no. 6, pp. 879-884, 1981.

- Okoshi, T., Ryu, S., and Kikuchi, K., "Polarization diversity receiver for heterodyne/coherent optical fiber communications," in *Proc. IOOC/OFC'83*, Paper 30C3-2, 1983.

- Okoshi, T., "Polarization-state control schemes for heterodyne or homodyne optical fibre communications," *J. Lightwave Technol.*, vol. 3, no. 6, pp. 1232-1237, 1985.

- Okoshi, T., Fukaya, N., and Kikuchi, K., "New polarization-state control device: Rotatable fibre cranks," *Electron. Lett.*, vol. 21, no. 20, pp. 895-896, 1985.

- Okuno, M., Kato, K., Ohmori, Y., and Matsunaga, T., "Improved 8×8 integrated optic matrix switch using silica-based planar lightwave circuits," *J. Lightwave Technol.*, vol. 12, no. 9, pp. 1597-1606, 1994.

- Peng, S. T., and Oliner, A. A., "Guidance and leakage properties of a call of open dielectric waveguides: Part I – Mathematical formulations," *IEEE Trans. Microwave Theory Tech.*, vol. MTT-29, no. 9, pp. 843-855, 1981.

- Pola, J. R. P., Biehlig, W., and Lederer, F., "A generalization of the spectral index method toward multiple rib waveguides," *J. Lightwave Technol.*, vol. 14, no. 3, pp. 454-461, 1996.

- Poole, C. D. and Wagner, R. E., "Phenomenological approach to polarization dispersion in long single-mode fibres," *Electron. Lett.*, vol. 22, no. 19, pp. 1029-1030, 1986.

- Qiao, L. and Wang, J., "A modified ray-optic method for arbitrary dielectric waveguides," *IEEE J. Quantum Elect.*, vol. 28, no. 12, pp. 2721-2727, 1992.

- Rahman, B. M. A. and Davies, J. B., "Finite-element solution of integrated optical waveguides," *J. Lightwave Technol.*, vol. 2, no. 5, pp. 682-688, 1984a.

- Rahman, B. M. A. and Davies, J. B., "Finite-element analysis of optical and microwave waveguide problems," *IEEE Trans. Microwave Theory Tech.*, vol. MTT-32, no. 1, pp. 20-28, 1984b.

- Rahman, B. M. A. and Davies, J. B., "Penalty function improvement of waveguide solution by finite elements," *IEEE Trans. Microwave Theory Tech.*, vol. MTT-32, no. 8, pp. 922-928, 1984c.

- Rahman, B. M. A. and Davies, J. B., "Analysis of optical waveguide discontinuities," *J. Lightwave Technol.*, vol. 6, no. 1, pp. 52-57, 1988.

- Rahman, B. M. A., Obayya, S. S. A., Somasiri, N., Rajarajan, M., Grattan, K. T. V., and El-Mikathi, H. A., "Design and characterization of compact single-section passive polarization rotator," *J. Lightwave Technol.*, vol. 19, no. 4, pp. 512-519, 2001.

- Rahmatian, F., Jaeger, N. A. F., James, R., and Berelo, E., "An ultrahigh-speed AlGaAs-GaAs polarization converter using slow-wave coplanar electrodes," *IEEE Photon. Technol. Lett.*, vol. 10, no. 5, pp. 675-677, 1998.

- Rajarajan, M., Themistos, C., Rahman, B. M. A., and Grattan, K. T. V., "Characterization of metal-clad TE/TM mode splitters using the finite element method," *J. Lightwave Technol.*, vol. 15, no. 12, pp. 2264-2269, 1997.

- Reddy, J. N., *An introduction to the finite element method*, McGraw-Hill Inc., New York, 1984.

- Rein, H. M., Hauenschild, J., Moller, M., McFarland, W., Pettengill, D., and Doernberg, J., "30 Gbit/s multiplexer and demultiplexer ICs in silicon bipolar technology," *Electron. Lett.*, vol. 28, no. 1, pp. 97-99, 1992.

- Runge, P. K., "Impact of fibre optics on undersea communication," in *Proc. Conf. Optical Fibre Communication (OFC)*, Invited paper ThH2, 1992.

- Saad, M. S., "Review of numerical methods for the analysis of arbitrarily-shaped microwave and optical dielectric waveguides," *IEEE Trans. Microwave Theory Tech.*, vol. 33, no. 10, pp. 894-899, 1985.

- Schauwecker, B., Przyrembel, G., Kuhlow, B., and Radehaus, C., "Small-size silicon-oxynitride AWG demultiplexer operating around 725 nm," *IEEE Photon. Technol. Lett.*, vol. 12, no. 12, pp. 1645-1646, 2000.

- Schlak, M., Weinert, C. M., Albrecht, P., and Nolting, H. P., "Tunable TE/TM-mode converter on (001)-InP-substrate," *IEEE Photon. Technol. Lett.*, vol. 3, no. 1, pp. 15-16, 1991.

- Shani, Y., Alferness, R., Koch, T., Koren, U., Oron, M., Miller, B. I., and Young, M. G., "Polarization rotation in asymmetric periodic loaded rib waveguides," *Appl. Phys. Lett.*, vol. 59, no. 11, pp. 1278-1280, 1991.

- Shigesawa, H., and Tsuji, M., "Mode propagation through a step discontinuity in dielectric planar waveguide," *IEEE Trans. Microwave Theory Tech.*, vol. MTT-34, no. 2, pp. 205-212, 1986.

- Soldano, L. B., de Vreede, A. H., Smit, M. K., Verbeek, B. H., Metaal, E. G., and Groen, F. H., "Mach-Zehnder Interferometer Polarization Splitter in InGaAsP/ InP," *IEEE Photon. Technol. Lett.*, vol. 6, no. 3, pp. 402-405, 1994.

- Soldano, L. B. and Pennings, E. C. M., "Optical multi-mode interference devices based on self-imaging: Principles and applications," *J. Lightwave Technol.*, vol. 13, no. 4, pp. 615-627, 1995.

- Somasiri, N., Rahman, B. M. A., and Obayya, S. S. A., "Fabrication tolerance study of a compact passive polarization rotator," *J. Lightwave Technol.,* vol. 20, no. 4, pp. 751-757, 2002.

- Srivastava, R., Kao, C. K., and Ramaswamy, R. V., "WKB analysis of planar surface waveguides with truncated index profiles," *J. Lightwave Technol.*, vol. 5, no. 11, pp. 1605-1609, 1987.

- Stauffer, J. R., "FT3C-a lightwave system for metropolitan and intercity applications," *J. Selected Areas Communication*, vol. SAC-1, pp. 413-419, 1983.

- Stern, M. S., Kendall, P. C., and McIlroy, P. W. A., "Analysis of the spectral index method for vector modes of rib waveguides," *IEE Proc. Pt. J*, vol. 137, no. 1, pp. 21-26, 1990.

- Suzuki, Y., Iwamura, H., Miyazawa, T., and Mikami, O., "A novel waveguide polarization mode splitter using refractive index changes induced by superlattice disordering," *IEEE J. Quantum Electron.,* vol. QE-30, no. 8, pp. 1794-1800, 1994.

- Svedin, J. A. M., "A numerically efficient finite element formulation for the general waveguide problem without spurious modes," *IEEE Trans. Microwave Theory Tech.*, vol. MTT-37, no. 11, pp. 1708-1715, 1989.

- Takada, K., Yamada, H., and Inoue, Y., "Optical low coherence method for characterizing silica-based arrayed-waveguide grating multiplexers," *J. Lightwave Technol.,* vol. 14, no. 7, pp. 1677-1689, 1996.

- Takada, K. and Mitachi, S., "Polarization crosstalk dependence on length in silica-based waveguides measured by using optical low coherence interference," *J. Lightwave Technol.,* vol. 16, no. 8, pp. 1413-1422, 1998.

- Takada, K., Abe, M., Shibata, M., Ishii, M., and Okamoto, K., "Low-crosstalk 10-GHz-spaced 512-channel arrayed-waveguide grating multi/demultiplexer fabricated on a 4-in wafer," *IEEE Photon. Technol. Lett.,* vol. 13, no. 11, pp. 1182-1184, 2001.

- Takahashi, H., Suzuki, S., Kato, K., and Nishi, I., "Arrayed waveguide grating for wavelength division multi/demultiplexer with nanometer resolution," *Electron. Lett.,* vol. 26, no. 2, pp. 87-88, 1990.

- Tamir, T., (Ed.), *Guided wave optoelectronics,* New York: Springer-Verlag, 1990.

- Tien, P. K., "Light waves in thin films and integrated optics," *Appl. Opt.,* vol. 10, no. 11, pp. 2395-2413, 1971.

- Toba, H., Oda, K., Nakanishi, K., Shibata, N., Nosu, K., Takato, N., and Fukuda, M., "100-channel optical FDM transmission/distribution at 622 Mb/s over 50 km," in *Proc. Conf. Optical Fibre Communication (OFC),* Paper PD1-1, 1990.

- Tsuji, Y. and Koshiba, M., "A finite element beam propagation method for strongly guiding and longitudinally varying optical waveguides," *J. Lightwave Technol.,* vol. 14, no. 2, pp. 217-222, 1996.

- Tzolov, V. P. and Fontaine, M., "A passive polarization converter free of longitudinally periodic structure," *Opt. Commun.,* vol. 127, no.1-3, pp. 7-13, 1996.

- Van Dam, C., Spiekman, L. H., van Ham, F. P. G. M., Groen, F. H., Van Der Tol, J. J. G. M., Moerman, Pascher, I., W. W., Hamacher, M., Heidrich, H., Weinert, C. M., and Smit, M. K., "Novel compact polarization converters based on ultra short bends," *IEEE Photon. Technol. Lett.,* vol. 8, no. 10, pp. 1346-1348, 1996.

- Van Der Tol, J. J. G. M. and Baken, N. H. G., "Correction to effective index method for rectangular dielectric waveguides," *Electron. Lett.,* vol. 24, no. 4, pp. 207-208, 1988.

- Van Der Tol, J. J. G. M., F. Hakimzadeh, F., Pederson, J. W., Li, D., and Van Brug, H., "A new short and low-loss passive polarization converter on InP," *IEEE Photon. Technol. Lett.,* vol. 7, no. 1, pp. 32-34, 1995.

- Van de Velde, K., Thienpont, H., and Van Green, R., "Extending the effective index method for arbitrarily shaped inhomogeneous optical waveguides," *J. Lightwave Technol.,* vol.6, no. 6, pp. 1153-1159, 1988.

- Vassalo, C., "1993-1995 optical mode solvers," *Opt. Quantum Electron.,* vol. 29, no. 2, pp. 95-114, 1997.

- Walker, N. G., Walker, G. R., and Davidson, J., "Endless polarization control using an integrated optic Lithium Niobate device," *Electron. Lett.,* vol. 24, no. 5, pp. 266-268, 1988.

- Walker, G. R. and Walker, N. G., "Rugged all-fibre endless polarization controller," *Electron. Lett.,* vol. 24, no. 22, pp. 1353-1354, 1988.

- Wei, P. K. and Wang, W. S., "A TE-TM mode splitter on Lithium Niobate using Ti, Ni, and MgO diffusions," *IEEE Photon. Technol. Lett.,* vol. 6, no. 2, pp. 245-248, 1994.

- Weinert, C. M. and Heidrich, H., "Vectorial simulation of passive TE/TM mode converter devices on InP," *IEEE Photon. Technol. Lett.,* vol. 5, no. 3, pp. 324-326, 1993.

- Wu, R. B. and Chen, C. H., "A variational analysis of dielectric waveguide by the conformal mapping technique," *IEEE Trans. Microwave Theory Tech.,* vol. MTT-33, no. 8, pp. 681-685, 1985.

- Yariv, A. and Yeh, P., *"Optical waves in crystals,"* New York: Wiley Interscience, 1984.

- Yeh, C., Ha, K., Dong, S. B., and Brown, W. P., "Single-mode optical waveguides," *Appl. Opt.,* vol. 18, no. 10, pp. 1490-1504, 1979.

- Young, T. P., "Design of integrated optical circuits using finite elements," *IEE Proc.,* pt. A, vol. 135, no. 3, pp. 135-144, 1988.

- Zienkiewicz, O. C., *The finite element method,* 3rd edition, McGraw-Hill, UK, 1977.